nanomaterials

Special Issue Reprint

Semiconductor Quantum Dots

Synthesis, Properties and Applications

Edited by
Donghai Feng, Guofeng Zhang and Yang Li

mdpi.com/journal/nanomaterials

MDPI

Semiconductor Quantum Dots:
Synthesis, Properties and Applications

Semiconductor Quantum Dots: Synthesis, Properties and Applications

Guest Editors

Donghai Feng
Guofeng Zhang
Yang Li

MDPI

Basel • Beijing • Wuhan • Barcelona • Belgrade • Novi Sad • Cluj • Manchester

Guest Editors
Donghai Feng
State Key Laboratory of Precision Spectroscopy
East China Normal University
Shanghai
China

Guofeng Zhang
State Key Laboratory of Quantum Optics Technologies and Devices
Shanxi University
Taiyuan
China

Yang Li
School of Physics and Optoelectronic Engineering
Hangzhou Institute for Advanced Study
University of Chinese Academy of Sciences
Hangzhou
China

Editorial Office
MDPI AG
Grosspeteranlage 5
4052 Basel, Switzerland

This is a reprint of the Special Issue, published open access by the journal *Nanomaterials* (ISSN 2079-4991), freely accessible at: https://www.mdpi.com/journal/nanomaterials/special_issues/semiconductor_quantum_dots.

For citation purposes, cite each article independently as indicated on the article page online and as indicated below:

Lastname, A.A.; Lastname, B.B. Article Title. *Journal Name* **Year**, *Volume Number*, Page Range.

ISBN 978-3-7258-4457-9 (Hbk)
ISBN 978-3-7258-4458-6 (PDF)
https://doi.org/10.3390/books978-3-7258-4458-6

Contents

nanomaterials

Editorial

Semiconductor Quantum Dots: Synthesis, Properties and Applications

Donghai Feng [1,*], Guofeng Zhang [2,*] and Yang Li [3,*]

[1] State Key Laboratory of Precision Spectroscopy, East China Normal University, Shanghai 200241, China
[2] State Key Laboratory of Quantum Optics and Quantum Optics Devices, Institute of Laser Spectroscopy, Collaborative Innovation Center of Extreme Optics, Shanxi University, Taiyuan 030006, China
[3] Hangzhou Institute for Advanced Study, University of Chinese Academy of Sciences, Hangzhou 310024, China
* Correspondence: dhfeng@phy.ecnu.edu.cn (D.F.); guofeng.zhang@sxu.edu.cn (G.Z.); ly@ucas.ac.cn (Y.L.)

Semiconductor nanoparticles of sizes smaller than exciton Bohr diameters undergo quantum confinement and are called quantum dots (QDs), which exhibit size-dependent physicochemical properties. For the discovery and synthesis of QDs, three pioneers—Moungi G. Bawendi, Louis E. Brus, and Alexei I. Ekimov—have been awarded the 2023 Nobel Prize in Chemistry [1]. Since the discovery of QDs in the early 1980s [2], the synthesis, properties, and applications of QDs have been extensively investigated [3,4]. Various strategies, including physical, chemical, and biological approaches, have been developed to develop QDs with controllable sizes, compositions, and structures [5–8]. QDs have superior optoelectronic properties, including wide tunability, narrow emission bandwidth, high brightness, and high efficiency, and offer a wide range of potential device applications in solar energy harvesting [9], lighting [10], displays [11], detectors [12], biomedical imaging [13], and quantum information technology [14].

This Special Issue includes eight contributions, comprising seven research articles and one review article, dedicated to the synthesis, properties, and applications of QDs with diverse components and structures. These studies involve the investigation of the size uniformity in $CsPbBr_3$ perovskite QDs via appropriate manganese doping [15], cost-effective magnetic carbon QDs/FeO_x photocatalytic composites [16], the effects of surface plasmon coupling on the color conversion from quantum wells into QDs [17], temperature- and size-dependent photoluminescence spectroscopy study on $CuInS_2$ QDs [18], methods for obtaining one single Larmor frequency in the coherent spin dynamics of colloidal CdSe and CdS QDs [19], room temperature coherent spin dynamics in $CsPbBr_3$ perovskite QDs [20], high-quality CdSe/CdS/ZnS QD-based aptasensors for the simultaneous detection of two different Alzheimer's disease core biomarkers [21], and a review on advances in solution-processed blue QD light-emitting diodes [22]. Research on the synthesis, properties, and applications of QDs will continue to be rigorous and of high interest. Closely following the prominent event of the 2023 Nobel Prize in Chemistry, our Special Issue highlights the development of QDs and will be of interest to general readers of *Nanomaterials*.

Author Contributions: D.F., G.Z. and Y.L. wrote this Editorial Letter. All authors have read and agreed to the published version of the manuscript.

Funding: This work was supported by the National Nature Science Foundation of China (Grants No. 12174108, 62127817, 62075120); the Basic Public Research Program of Zhejiang Province (LGF22B010004); Research Funds of Hangzhou Institute for Advanced Study, UCAS (2024HIAS-Y008); the Shanxi Province Science and Technology Innovation Talent Team (No. 202204051001014); and the Science and Technology Cooperation Project of Shanxi Province (202104041101021).

Acknowledgments: The Guest Editors express the deepest gratitude to all the authors for contributing their valuable work to the Special Issue. Special thanks to all the reviewers for their work in

participating in the peer-review process of the submitted manuscripts and enhancing the papers' quality and impact.

Conflicts of Interest: The authors declare no conflicts of interest.

References

1. Available online: https://www.nobelprize.org/prizes/chemistry/2023/summary/ (accessed on 2 November 2024).
2. Efros, A.L.; Brus, L.E. Nanocrystal quantum dots: From discovery to modern development. *ACS Nano* **2021**, *15*, 6192–6210. [CrossRef] [PubMed]
3. Ciftja, O. *Quantum Dots: Applications, Synthesis, and Characterization*; Nova Science Publishers: New York, NY, USA, 2012.
4. Masumoto, Y.; Takagahara, T. *Semiconductor Quantum Dots: Physics, Spectroscopy and Applications, Nanoscience and Technology Series*; Springer: Berlin/Heidelberg, Germany, 2002.
5. García de Arquer, F.P.; Talapin, D.V.; Klimov, V.I.; Arakawa, Y.; Bayer, M.; Sargent, E.H. Semiconductor quantum dots: Technological progress and future challenges. *Science* **2021**, *373*, eaaz8541. [CrossRef] [PubMed]
6. Reiss, P.; Carriere, M.; Lincheneau, C.; Vaure, L.; Tamang, S. Synthesis of semiconductor nanocrystals, focusing on nontoxic and earth-abundant materials. *Chem. Rev.* **2016**, *116*, 10731–10819. [CrossRef] [PubMed]
7. Zhou, J.; Yang, Y.; Zhang, C.y. Toward biocompatible semiconductor quantum dots: From biosynthesis and bioconjugation to biomedical application. *Chem. Rev.* **2015**, *115*, 11669–11717. [CrossRef] [PubMed]
8. Li, Y.; Hou, X.; Shen, Y.; Dai, N.; Peng, X. Tuning the reactivity of indium alkanoates by tertiary organophosphines for the synthesis of indium-based quantum dots. *Chem. Mater.* **2021**, *33*, 9348–9356. [CrossRef]
9. Carey, G.H.; Abdelhady, A.L.; Ning, Z.; Thon, S.M.; Bakr, O.M.; Sargent, E.H. Colloidal quantum dot solar cells. *Chem. Rev.* **2015**, *115*, 12732–12763. [CrossRef] [PubMed]
10. Won, Y.H.; Cho, O.; Kim, T.; Chung, D.Y.; Kim, T.; Chung, H.; Jang, H.; Lee, J.; Kim, D.; Jang, E. Highly efficient and stable InP/ZnSe/ZnS quantum dot light-emitting diodes. *Nature* **2019**, *575*, 634–638. [CrossRef] [PubMed]
11. Shu, Y.; Lin, X.; Qin, H.; Hu, Z.; Jin, Y.; Peng, X. Quantum dots for display applications. *Angew. Chem.* **2020**, *132*, 22496–22507. [CrossRef]
12. Nakotte, T.; Munyan, S.G.; Murphy, J.W.; Hawks, S.A.; Kang, S.; Han, J.; Hiszpanski, A.M. Colloidal quantum dot based infrared detectors: Extending to the mid-infrared and moving from the lab to the field. *J. Mater. Chem.* **2022**, *10*, 790–804. [CrossRef]
13. Gil, H.M.; Price, T.W.; Chelani, K.; Bouillard, J.S.G.; Calaminus, S.D.; Stasiuk, G.J. NIR-quantum dots in biomedical imaging and their future. *iScience* **2021**, *24*, 102189. [CrossRef] [PubMed]
14. Kagan, C.R.; Bassett, L.C.; Murray, C.B.; Thompson, S.M. Colloidal quantum dots as platforms for quantum information science. *Chem. Rev.* **2021**, *121*, 3186–3233. [CrossRef] [PubMed]
15. Zhang, M.; Han, X.; Yang, C.; Zhang, G.; Guo, W.; Li, J.; Chen, Z.; Li, B.; Chen, R.; Qin, C.; et al. Size uniformity of $CsPbBr_3$ perovskite quantum dots via manganese-doping. *Nanomaterials* **2024**, *14*, 1284. [CrossRef] [PubMed]
16. Ying, W.; Liu, Q.; Jin, X.; Ding, G.; Liu, M.; Wang, P.; Chen, S. Magnetic carbon quantum dots/iron oxide composite based on waste rice noodle and iron oxide scale: Preparation and photocatalytic capability. *Nanomaterials* **2023**, *13*, 2506. [CrossRef] [PubMed]
17. Yang, S.; Feng, H.Y.; Lin, Y.S.; Chen, W.C.; Kuo, Y.; Yang, C.C. Effects of surface plasmon coupling on the color conversion of an InGaN/GaN quantum-well structure into colloidal quantum dots inserted into a nearby porous structure. *Nanomaterials* **2023**, *13*, 328. [CrossRef]
18. Korepanov, O.; Kozodaev, D.; Aleksandrova, O.; Bugrov, A.; Firsov, D.; Kirilenko, D.; Mazing, D.; Moshnikov, V.; Shomakhov, Z. Temperature-and size-dependent photoluminescence of $CuInS_2$ quantum dots. *Nanomaterials* **2023**, *13*, 2892. [CrossRef] [PubMed]
19. Jiang, M.; Zhang, Y.; Hu, R.; Men, Y.; Cheng, L.; Liang, P.; Jia, T.; Sun, Z.; Feng, D. Methods for obtaining one single larmor frequency, either v_1 or v_2, in the coherent spin dynamics of colloidal quantum dots. *Nanomaterials* **2023**, *13*, 2006. [CrossRef]
20. Meliakov, S.R.; Zhukov, E.A.; Kulebyakina, E.V.; Belykh, V.V.; Yakovlev, D.R. Coherent spin dynamics of electrons in $CsPbBr_3$ perovskite nanocrystals at room temperature. *Nanomaterials* **2023**, *13*, 2454. [CrossRef] [PubMed]
21. Lu, X.; Hou, X.; Tang, H.; Yi, X.; Wang, J. A high-quality CdSe/CdS/ZnS quantum-dot-based FRET aptasensor for the simultaneous detection of two different alzheimer's disease core biomarkers. *Nanomaterials* **2022**, *12*, 4031. [CrossRef]
22. Li, S.N.; Pan, J.L.; Yu, Y.J.; Zhao, F.; Wang, Y.K.; Liao, L.S. Advances in solution-processed blue quantum dot light-emitting diodes. *Nanomaterials* **2023**, *13*, 1695. [CrossRef]

nanomaterials

MDPI

Article

Size Uniformity of $CsPbBr_3$ Perovskite Quantum Dots via Manganese-Doping

Mi Zhang [1], Xue Han [1], Changgang Yang [1], Guofeng Zhang [1,*], Wenli Guo [1], Jialu Li [1], Zhihao Chen [1], Bin Li [1], Ruiyun Chen [1], Chengbing Qin [1], Jianyong Hu [1], Zhichun Yang [1], Ganying Zeng [1], Liantuan Xiao [1,2,*] and Suotang Jia [1]

[1] State Key Laboratory of Quantum Optics and Quantum Optics Devices, Institute of Laser Spectroscopy, Collaborative Innovation Center of Extreme Optics, Shanxi University, Taiyuan 030006, China; z15034657487@163.com (M.Z.); hanxuechn@163.com (X.H.); changgang.yang@sxu.edu.cn (C.Y.); guowenlisx@163.com (W.G.); jialu-li@outlook.com (J.L.); chenzhihaochn@163.com (Z.C.); libin@sxnu.edu.cn (B.L.); chenry@sxu.edu.cn (R.C.); chbqin@sxu.edu.cn (C.Q.); jyhu@sxu.edu.cn (J.H.); yangzhichun@sxu.edu.cn (Z.Y.); zengganying@sxu.edu.cn (G.Z.); tjia@sxu.edu.cn (S.J.)

[2] College of Physics, Taiyuan University of Technology, Taiyuan 030006, China

* Correspondence: guofeng.zhang@sxu.edu.cn (G.Z.); xlt@sxu.edu.cn (L.X.)

Abstract: The achievement of size uniformity and monodispersity in perovskite quantum dots (QDs) requires the implementation of precise temperature control and the establishment of optimal reaction conditions. Nevertheless, the accurate control of a range of reaction variables represents a considerable challenge. This study addresses the aforementioned challenge by employing manganese (Mn) doping to achieve size uniformity in $CsPbBr_3$ perovskite QDs without the necessity for the precise control of the reaction conditions. By optimizing the Mn:Pb ratio, it is possible to successfully dope $CsPbBr_3$ QDs with the appropriate concentrations of Mn^{2+} and achieve a uniform size distribution. The spectroscopic measurements on single QDs indicate that the appropriate Mn^{2+} concentrations can result in a narrower spectral linewidth, a longer photoluminescence (PL) lifetime, and a reduced biexciton Auger recombination rate, thus positively affecting the PL properties. This study not only simplifies the size control of perovskite QDs but also demonstrates the potential of Mn-doped $CsPbBr_3$ QDs for narrow-linewidth light-emitting diode applications.

Keywords: $CsPbBr_3$ perovskite quantum dots; manganese-doping; size uniformity; single quantum-dot spectroscopy; narrow-linewidth

1. Introduction

Cesium lead halide ($CsPbX_3$, where X = Cl, Br, or I) perovskite quantum dots (QDs) display a range of advantageous properties, including high photoluminescence (PL) quantum yields, tunable PL spectra, high defect tolerance, and large carrier diffusion lengths [1–4]. These excellent properties have led to $CsPbX_3$ perovskite QDs having considerable potential in a wide range of applications, including light-emitting diodes (LEDs) [5,6], photovoltaics [7], lasers [8,9], photodetectors [10,11], and quantum light sources [12]. Nevertheless, the properties and applications of nanoscale perovskite QDs are strongly dependent on their size uniformity and monodispersity. As the sizes of the QDs are smaller than their Bohr diameters, the energy levels are quantized due to quantum confinement effects. As the size of the QD decreases, the confinement of the carriers becomes stronger, leading to an increase in the energy spacing between the discrete energy levels [13,14]. Consequently, the optical and electronic properties of QDs are highly sensitive to their sizes. The non-uniformity of the size of QDs typically leads to the broadening of the PL spectra, which in turn affects the performance of QD-based devices [15–18]. Consequently, size uniformity is of paramount importance in determining the performance, stability, and controllability of QD-based applications. This ensures consistency in optical, electronic, and assembly properties, thereby improving the functionality and reliability of devices in a range of fields. Nevertheless, the production of perovskite QDs with high size uniformity using colloidal methods remains a significant challenge.

A variety of synthesis methods and strategies have been employed to achieve size uniformity and monodispersity in perovskite QDs. For example, precursor stoichiometry control has been used to precisely tune precursor ratios to influence nucleation and growth kinetics, resulting in uniform perovskite QD sizes [19,20]. The precise control of temperature and reaction time has been employed to regulate synthesis conditions, resulting in the formation of smaller, more uniform perovskite QDs [21,22]. Furthermore, solvent engineering has been utilized to optimize solubility and growth kinetics, thereby improving size control [23,24]. The use of ligands such as oleic acid or oleylamine in surfactant engineering has been employed to stabilize the perovskite QDs and enhance size uniformity [25,26]. However, maintaining precise temperature control and appropriate reaction conditions can be challenging, resulting in variations in perovskite QD size and uniformity.

In this study, we demonstrate the successful achievement of the size uniformity and monodispersity of $CsPbBr_3$ perovskite QDs through the incorporation of manganese (Mn) doping. This method does not necessitate the precise control of various reaction conditions for the synthesis of $CsPbBr_3$ perovskite QDs. It has been demonstrated that Mn doping in perovskite QDs can stabilize the crystal structure, effectively reduce the defect density, and improve the lattice ordering [26]. By optimizing the Mn:Pb ratio in the precursor, it was possible to successfully introduce appropriate concentrations of Mn^{2+} into the $CsPbBr_3$ perovskite QDs. The introduction of Mn^{2+} greatly optimizes the size distribution of $CsPbBr_3$ perovskite QDs. Single QD spectroscopy measurements demonstrate that the incorporation of Mn^{2+} at appropriate concentrations has a positive effect on the PL properties of $CsPbBr_3$ perovskite QDs.

2. Materials and Methods

All materials were purchased from Aladdin and used as received without further purification. The materials used in the experiments include cesium carbonate (Cs_2CO_3, 99.9%, metals basis), lead bromide ($PbBr_2$, 99.0%), zinc bromide ($ZnBr_2$, 99.9%, metals basis), manganese (II) bromide ($MnBr_2$, 98.0%), oleylamine (OAm, C18:80–90%), oleic acid (OA, AR), 1-octadecene (ODE, >90.0%(GC)), and hexane (>99%(GC)).

In this study, $CsPbBr_3$ perovskite QDs were synthesized by suitably modifying the previously reported hot injection synthesis method [19]. Stoichiometric mixtures of different ratios of $PbBr_2$ and $MnBr_2$ were used for the synthesis of Mn-doped $CsPbBr_3$ perovskite QDs with different doping concentrations. The Cs precursor solution was prepared by reacting 0.25 g of Cs_2CO_3 powder with 0.9 mL of OA and 9 mL of ODE in a 50 mL three-necked flask. This reaction was conducted at 150 °C under a nitrogen (N_2) atmosphere. A separate solution was then prepared by mixing 75 mg of $PbBr_2$, together with $ZnBr_2$ (acting as a Br^- supplementation source) and $MnBr_2$ (acting as a dopant) with 5 mL of ODE, 2 mL of OA, and 2 mL of OAm in a separate 50 mL round-bottomed three-necked flask; the mass and molar ratios of $PbBr_2$, $MnBr_2$ and $ZnBr_2$ at different doping concentrations are given in Table S1. The aforementioned mixture was maintained at 120 °C under an N_2 atmosphere for one hour to ensure thorough mixing and solubilization. Once the requisite temperature was reached, 0.4 mL of the previously prepared Cs precursor solution was rapidly injected into the flask containing the $PbBr_2$ mixture. This injection initiated the nucleation and subsequent growth of the $CsPbBr_3$ perovskite QDs. To promptly terminate the reaction, the flask was immersed in an ice bath after 5 s. After the reaction, the $CsPbBr_3$ perovskite QDs were separated from the reaction mixture by high-speed centrifugation. Methyl acetate was used as an antisolvent to precipitate the perovskite QDs, which were then redispersed in hexane. Unreacted salts and impurities were removed as precipitates through centrifugation at 4000 rpm, and the supernatant, containing the dispersed perovskite QDs, was collected for further use. During the synthesis of the Mn-doped QDs, $ZnBr_2$ was used to maintain a constant total amount of Br^- to ensure that the sizes of the QDs were not affected by the amount of Mn doping. ICP-MS analyses showed that the concentration of Zn^{2+} was extremely low, which indicated that Zn^{2+} was not effectively doped into the QDs [19].

For single QD measurements, the hexane solution of perovskite QDs was mixed with 1 wt.% polystyrene solution. The mixture was then spin-coated onto clean glass coverslips at 3000 rpm for one minute to form a polystyrene film to protect the perovskite QDs. The size of the perovskite QDs was measured from the TEM image using a JEM-2100 microscope (JEOL, Tokyo, Japan). The absorption, excitation, and PL emission spectra of the perovskite QDs in hexane were measured using a PerkinElmer Lambda 950 UV–VISNIR spectrometer (PerkinElmer, Hopkinton, MA, USA) and a Cary Eclipse Fluorescence Spectrophotometer (Agilent, Santa Clara, CA, USA), respectively. X-ray diffraction (XRD) patterns of the perovskite QDs were obtained using a D2 PHASER diffractometer (Bruker, Billerica, MA, USA). The elemental concentrations of Mn-doped perovskite QDs were determined using a NexION350 series inductively coupled plasma mass spectrometer (ICP-MS) (PerkinElmer, MA, USA).

A confocal fluorescence microscopy system was home-built to collect the PL photons emitted from single QDs [27,28]. A pulsed laser emitting at 439 nm (EXW-12, NKT) with a pulse duration of 50 to 100 ps and a repetition rate of 5 MHz was used for excitation. The system incorporated an Olympus oil immersion objective with a high magnification of 100× and a numerical aperture (NA) of 1.3, which not only facilitated the precise focusing of the laser beam onto the QD samples but also efficiently collects the emitted PL photons. The collected PL photons were initially filtered through a dichroic mirror (Semrock, IDEX, Northbrook, IL, USA) and a long-pass filter (Semrock, IDEX, IL, USA) to eliminate any background noise that might otherwise interfere with the analysis. Subsequently, a spatial filtering step using a 100 μm pinhole was employed to reject out-of-focus photons, thereby ensuring that only the desired PL photons were processed. A 50/50 beam-splitter cube was then used to divide the filtered PL photons into two equal beams. Each beam was then detected by a highly sensitive single-photon avalanche diode detector (SPCM-AQR-15, PerkinElmer, MA, USA), which is capable of rapidly responding to individual photons. The detected signals were accurately recorded by a time-tagged, time-resolved (TTTR), time-correlated single-photon counting (TCSPC) data acquisition card (HydraHarp 400, PicoQuant, Berlin, Germany), which provides a temporal resolution of 1 ps. Of note, all measurements were conducted at room temperature in order to ensure reproducibility and comparability with other experiments. The described setup and procedures adhere to standard practices in fluorescence microscopy and single-photon detection, thus ensuring the reliability and accuracy of the data obtained for the investigation of the PL properties of perovskite QDs.

3. Results and Discussion

The synthesis of the Mn-doped $CsPbBr_3$ perovskite QDs was successfully accomplished using $MnBr_2$ as a dopant. The doping concentrations of the QDs were 4.7%, 20.4%, and 42.9%, with the undoped QDs serving as a control. The Mn^{2+} concentration was accurately determined by inductively coupled plasma mass spectrometry (ICP-MS) analysis, as shown in Table S2. Taking the undoped and the 4.7% Mn-doped $CsPbBr_3$ perovskite QDs as examples, the solution PL quantum yield (QY) of the undoped QDs is about 80%, and the PLQY of the 4.7% doped QDs is about 70%. The transmission electron microscopy (TEM) images presented in Figure 1a,b illustrate the distinct morphological discrepancies between the undoped and the 4.7% Mn-doped perovskite QDs. Following the incorporation of 4.7% Mn doping, notable improvements in both the size distribution and morphology of the perovskite QDs were observed. In particular, these QDs exhibit a strikingly uniform size distribution, with a significant reduction in the full width at half maximum (FWHM) of the size distribution from 2 nm to 1.2 nm (Figure 1c,d), which highlights the high level of control over the size uniformity obtained by Mn doping. Furthermore, the original cubic morphology becomes more distinct and well-defined, indicating an improvement in crystallinity. The size narrowing can be attributed to the effective modulation of QD surface defects by Mn doping [26,29]. Mn doping has the effect of reducing surface defects by increasing the defect formation energy while avoiding the introduction of deep traps into the band gap. The reduction in surface defects not only improves the short-range ordering of the lattice but also brings the local structural ordering closer to the ideal homogeneous state. At the same time, this optimization is reflected in the emission spectrum of the perovskite QDs, where the FWHM of the emission spectrum is significantly narrowed from 34.5 nm to 24.1 nm (Figure 1e), representing a 30.3% reduction as compared to the original width. This indicates a more homogeneous energy distribution and the improved optical properties of the doped perovskite QDs, which can be attributed to the profound effect of Mn doping in regulating and reducing surface defects on the QD surfaces. Conventionally, during the growth process of perovskite QDs, the presence of unpaired chemical bonds leads to the formation of surface defects with high free energy, acting as non-radiative recombination centers that deteriorate the optical performance. However, the introduction of Mn^{2+} as a dopant effectively mitigates this issue by increasing the defect formation energy barrier, thereby suppressing the formation of such defects and avoiding the introduction of deep traps within the band gap. This mechanism not only enhances the short-range order of the crystal lattice but also brings the local structural order closer to an ideal state of uniformity, as evidenced by the improved optical properties [26,29]. Furthermore, the substitution of Pb^{2+}, which possesses a larger ionic radius, by the equivalent but smaller Mn^{2+}, lead to a contraction of the lattice. This lattice contraction not only contributes to the observed reduction in the average edge length of the perovskite QDs from 6.41 nm to 6.08 nm (Figure 1c,d), but also affects the electronic structure. Specifically, the enhancement of the coordination field around Mn^{2+} due to lattice contraction results in a narrowing of the band gap between the $^4T_1$ and $^6A_1$ energy levels of Mn^{2+}, leading to a slight redshift in the position of the PL excitation and emission peaks (Figures 1e and S1) [30]. This effect, coupled with the reduced surface defects, underscores the beneficial role of Mn doping in enhancing the optical properties of the perovskite QDs. Additionally, the monotonic shift of the peaks in the X-ray diffraction (XRD) patterns by 0.18° toward higher angles (Figure 1f,g) provides further evidence of the lattice contraction induced by Mn doping. The XRD plots of perovskite QDs with different doping concentrations, along with comparisons to the standard phase, are provided in Supplementary Materials Figure S2. The observed improvements in energy distribution, optical properties, and structural order of the doped perovskite QDs provide compelling evidence that Mn doping effectively regulates and reduces surface defects, leading to enhanced performance. These findings not only validate the successful doping of the perovskite QDs but also highlight the potential of Mn^{2+} as a powerful dopant for improving the properties of semiconductor nanomaterials.

As the doping concentration is increased from 4.7% to 20.4%, a slight blue shift in the absorption edge can be observed, accompanied by a corresponding shift in the PL peak from 496.6 nm to 486.6 nm. When the doping concentration exceeds 42.9%, the size distribution and morphology of the perovskite QDs deteriorate, resulting in a reverse redshift of the characteristic spectra (Figure S3g,h and Table S3). Furthermore, it was observed that the Mn-doped perovskite QDs did not exhibit Mn-related PL in the visible spectral region at room temperature due to the low energy of the excitonic transition [30–32].

In order to investigate the impact of doping on $CsPbBr_3$ perovskite QDs, we conducted single-dot PL spectroscopy on undoped and 4.7% Mn-doped $CsPbBr_3$ perovskite QDs under identical excitation conditions. The excitation condition $\langle N \rangle$ represents the average number of photons absorbed per QD per pulse. $\langle N \rangle = \sigma \cdot j_{exc}$, where j_{exc} is the per-pulse photon fluence, and σ is the QD absorption cross section [4,33]. The estimation of $\langle N \rangle$ and the calculation of the absorption cross section σ can be found in the Supplementary Materials. The average values of σ for the undoped $CsPbBr_3$ perovskite QDs and the 4.7% Mn-doped $CsPbBr_3$ perovskite QDs are 3.52×10^{-14} cm^2 and 2.97×10^{-14} cm^2, respectively (Figure S4), which is consistent with the findings of previous research [4]. Figure 2a,b illustrate the typical PL intensity trajectories for single undoped and 4.7% Mn-doped perovskite QDs under low excitation ($\langle N \rangle = 0.2$). The corresponding PL intensity histograms are shown in the right panels. From the figures, it can be observed that the PL intensity trajectory of the single 4.7% Mn-doped QD remains essentially unchanged as compared to that of the undoped QD. However, as the doping concentration increases, the PL trajectories of the perovskite QDs deteriorate, exhibiting a decrease in intensity and an increase in blinking (Figure S5). By applying a single exponential fit to each 10 ms time bin of the PL trajectories, fluorescence lifetime-intensity distribution (FLID) maps can be derived, which provide valuable insights into the PL properties of the QDs [34,35]. Prior to and following doping, the PL intensity of single $CsPbBr_3$ perovskite QDs exhibits a linear correlation with their lifetimes, indicating that PL blinking in both the undoped and Mn-doped QDs is primarily dominated by band-edge carrier (BC) blinking (Figure 2c,d). This implies that the moderate amount of Mn doping did not alter the blinking mechanism of the perovskite QDs.

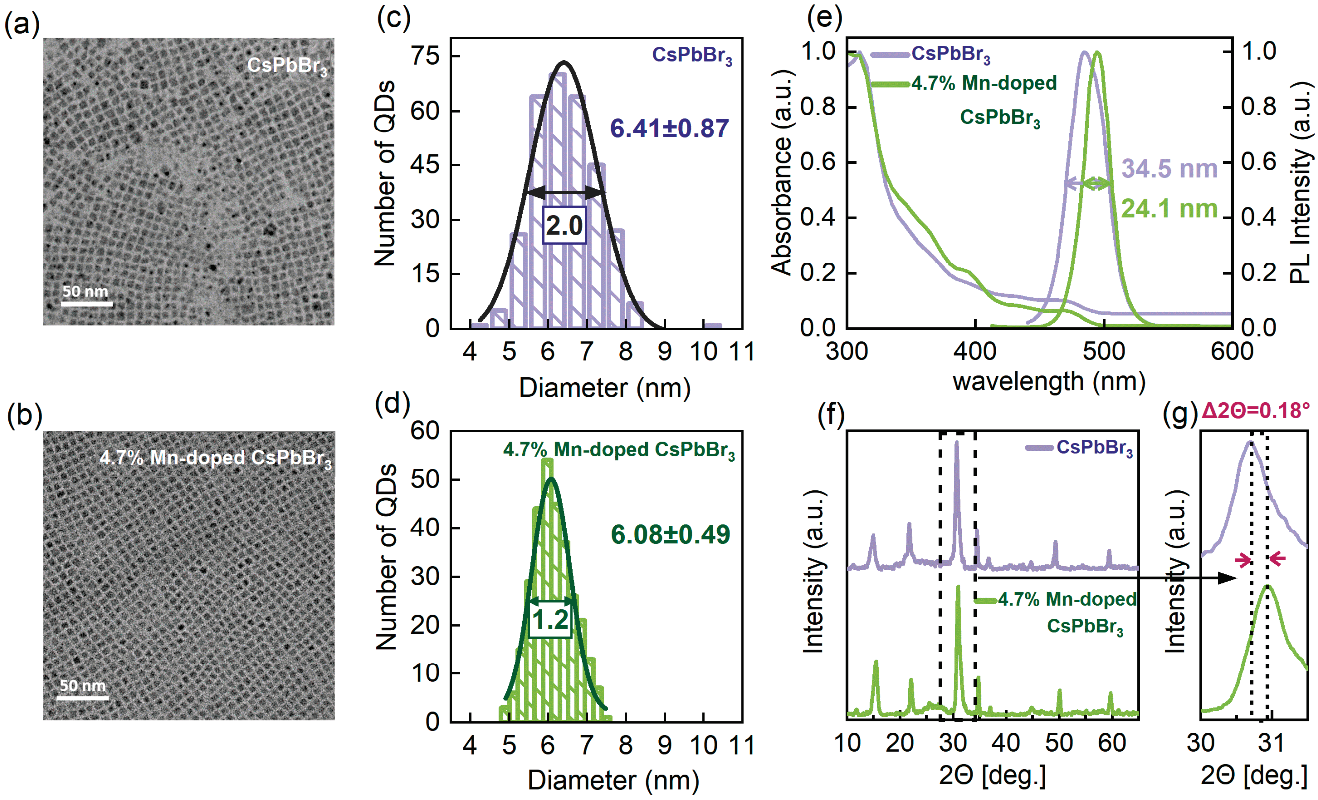

Figure 1. Morphological, spectral, and structural characterization of undoped and 4.7% Mn-doped $CsPbBr_3$ perovskite quantum dots (QDs). (**a**,**b**) Transmission electron microscopy (TEM) images of undoped and Mn-doped $CsPbBr_3$ perovskite QDs. (**c**,**d**) Histograms depicting the distribution of edge lengths for undoped and Mn-doped perovskite QDs. (**e**) Absorption and PL emission spectra of undoped and Mn-doped perovskite QDs, demonstrating that Mn-doped perovskite QDs exhibit a narrower linewidth. (**f**) X-ray diffraction (XRD) patterns of perovskite QDs with different Mn doping concentrations, demonstrating the preservation of the cubic phase upon Mn doping. (**g**) A magnified view shows a subtle but monotonic shift in the XRD peak toward higher 2θ angles, indicating a progressive contraction of the lattice with Mn doping.

The corresponding PL decay trajectories, extracted from the bright- and dim-state PL regions, are presented in Figure 2e,f, respectively. The decay curves can be fitted by mono-exponential functions to obtain the bright- and dim-state lifetimes. The radiative lifetime scaling can be calculated based on the bright- and dim-state lifetimes and the corresponding PL intensities of the bright- and dim-state. The radiative lifetime scaling for both the undoped and 4.7% Mn-doped $CsPbBr_3$ perovskite QDs is approximately 1.0

(details of the scaling calculations can be found in the Supplementary Materials), which further confirms that both undoped and Mn-doped perovskite QDs adhere to the BC blinking mechanism [36,37]. This BC blinking behavior indicates that the blinking of the undoped and Mn-doped perovskite QDs is primarily attributed to the surface-shallow trap states. Given the analogous energy level structure of the Mn and $CsPbBr_3$ perovskite QDs, doping Mn^{2+} does not introduce deep trap states and thus does not alter the carrier trapping and de-trapping rates. The corresponding second-order correlation function ($g^{(2)}$) curves depicted in Figure 2g,h show very low values of $g^{(2)}(0)$, well below 0.5. This observation suggests that the investigated perovskite QDs are single QDs [38] and also indicates that Mn doping does not appear to alter the photon statistical properties of the QDs.

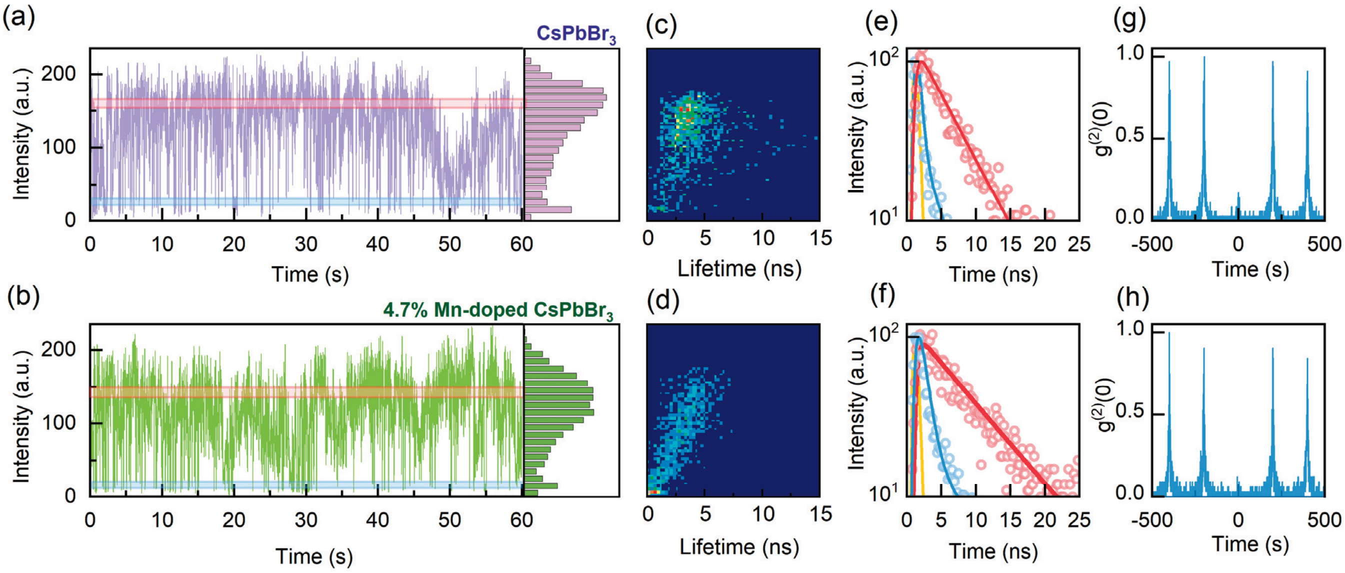

Figure 2. (**a**,**b**) Typical PL intensity time trajectories for single undoped and 4.7% Mn-doped $CsPbBr_3$ perovskite QDs. The corresponding PL intensity histograms are presented in the right panels. (**c**,**d**) Corresponding fluorescence lifetime–intensity distribution (FLID) maps. The color change from blue to red indicates an increase in the probability of occurrence of a given state in the intensity–lifetime space. (**e**,**f**) Corresponding PL decay trajectories obtained from the bright- and dim-state PL regions marked in respective colors on the PL intensity trajectories of (**a**,**b**). The solid red and blue lines represent mono-exponential fits, and the solid yellow lines in the figures represent the instrument response function (IRF) of the system. (**g**,**h**) Corresponding second-order correlation function ($g^{(2)}$) curves of the bright-state PL regions for single undoped and 4.7% Mn-doped $CsPbBr_3$ perovskite QDs.

In order to gain further insight into the impact of Mn doping on $CsPbBr_3$ perovskite QDs, a statistical analysis was conducted on the single-exciton lifetimes of both single undoped and Mn-doped $CsPbBr_3$ perovskite QDs. The single-exciton lifetime can be determined by fitting the bright state of the PL intensity trajectory. The histograms of single-exciton lifetimes are presented in Figure 3a,b, and the results were obtained from approximately 100 QDs in each case. The average lifetime value of 4.7% Mn-doped $CsPbBr_3$ perovskite QDs is 5.37 ns, which is larger than the average lifetime value of undoped $CsPbBr_3$ perovskite QDs (4.93 ns). This increase in the lifetime value indicates that the doping of Mn^{2+} favors the suppression of defect recombination [29].

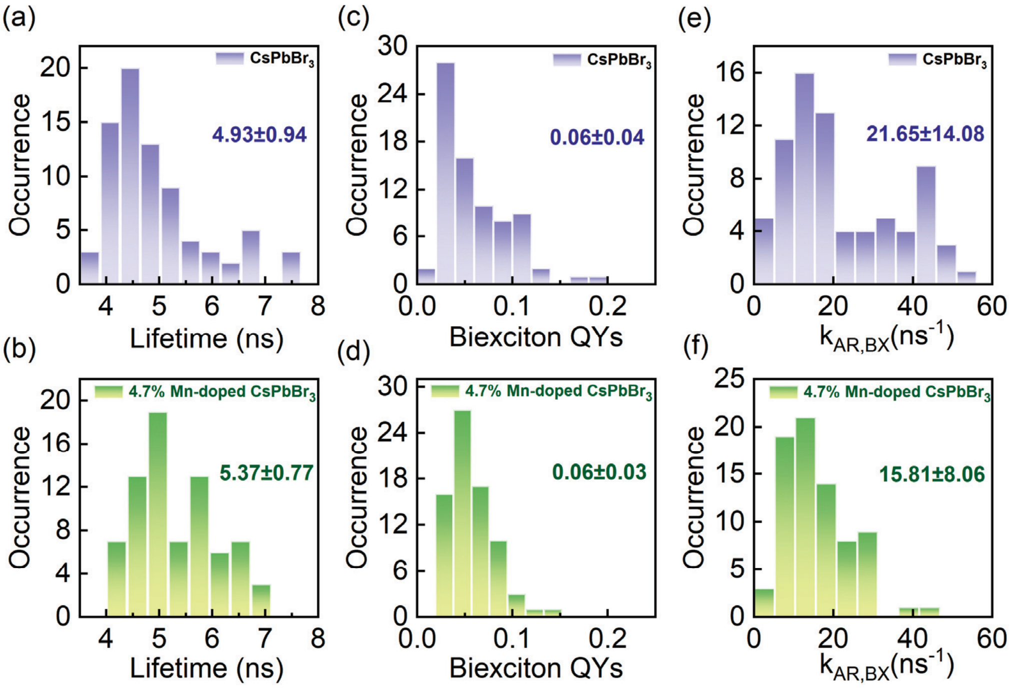

Figure 3. (**a**,**b**) Histograms of single-exciton lifetimes for single undoped and 4.7% Mn-doped $CsPbBr_3$ perovskite QDs. (**c**,**d**) Histograms of biexciton quantum yields (QYs) for single undoped and Mn-doped $CsPbBr_3$ perovskite QDs. (**e**,**f**) Histograms of biexciton Auger recombination rates ($k_{AR,BX}$) for single undoped and Mn-doped $CsPbBr_3$ perovskite QDs.

Furthermore, we conducted a detailed investigation into the impact of doping on the biexciton quantum yields (QYs) and biexciton Auger recombination rates ($k_{AR,BX}$) in perovskite QDs. In the case of weak excitation conditions with $\langle N \rangle = 0.2$, the biexciton QYs can be calculated using the Equation (1) [39,40]:

$$QY_{BX} = g^{(2)}(0) \times QY_X \tag{1}$$

where QY_{BX} and QY_X are the biexciton QY and the single-exciton QY, respectively. It is assumed that the single-exciton QY of the on-state PL intensity trajectory is unity for single QDs [39]. According to the values of $g^{(2)}(0)$, the biexciton QYs of single undoped and Mn-doped $CsPbBr_3$ perovskite QDs can be obtained by Equation (1). The histograms of the biexciton QYs in the two cases are presented in Figure 3c,d, respectively, and the average values are calculated to be 0.06 and 0.06, respectively. This suggests that Mn doping has a minimal impact on the biexciton QYs of perovskite QDs.

When the excitation condition $\langle N \rangle \ll 1$, the relationship of $g^{(2)}(0)$ to the biexciton and single-exciton lifetimes of a single perovskite QD can be expressed by Equation (2) [16,40,41]:

$$g^{(2)}(0) = 4\frac{\tau_{BX}}{\tau_X} \tag{2}$$

where τ_{BX} and τ_X are the biexciton and single-exciton lifetimes, respectively. The biexciton QY can be expressed by Equation (3) [40]:

$$QY_{BX} = \frac{k_{r,BX}}{k_{r,BX} + k_{AR,BX}} = \frac{k_{r,BX}}{1/\tau_{BX}} \tag{3}$$

where $k_{r,BX}$ and $k_{AR,BX}$ represent the biexciton radiative rate and the biexciton Auger recombination rate, respectively. According to Equations (2) and (3), $k_{AR,BX}$ can be obtained. Histograms of $k_{AR,BX}$ for single undoped and Mn-doped $CsPbBr_3$ perovskite QDs are shown in Figure 3e,f. The $k_{AR,BX}$ values for undoped perovskite QDs exhibit a relatively wide distribution, reflecting the non-uniform size distribution of the undoped QDs (Figure 3e). The mean value of $k_{AR,BX}$ is 21.65 ns^{-1}. In contrast, the distribution of $k_{AR,BX}$ of the Mn-doped perovskite QDs is more concentrated (Figure 3f). This is primarily attributed to the enhancement of their size uniformity and the significant reduction in size dispersion achieved by Mn doping. The average value of $k_{AR,BX}$ is 15.81 ns^{-1} for the Mn-doped QDs, which is smaller than that of the undoped QDs. This evidence demonstrates that the incorporation of Mn effectively mitigates the discreteness of the $k_{AR,BX}$. The reduction in the $k_{AR,BX}$ achieved by minimizing non-radiative recombination processes leads to an increase in the radiative recombination fraction. At the same time, the reduced $k_{AR,BX}$ indicates that the quantum confinement on the carriers is reduced, creating favorable conditions for the overall enhancement of the LED device performance. A summary table of photophysical parameters for the Mn-doped QDs obtained in this work is presented in Table S3, and results from the other literature used for comparison are also included in Table S3. In addition, the 4.7% Mn-doped QDs met our expectations, so we did not attempt to prepare QDs with small changes in the Mn concentration.

One of the key challenges in the advancement of QD LED (QLED) technology is the relatively wide emission spectra, which affects the color purity of the emitted light from LEDs [42,43]. To further validate the feasibility of Mn-doped $CsPbBr_3$ perovskite QDs for LED applications, we employed undoped and 4.7% Mn-doped $CsPbBr_3$ perovskite QDs as down-conversion phosphors. The $CsPbBr_3$ perovskite QDs were thoroughly mixed with a 1wt% polystyrene (PS)-toluene solution to improve the stability. The resulting mixture was then applied to a 395 nm UV chip and allowed to dry in air for one hour, resulting in the fabrication of the QLED device. As illustrated in Figure 4a,b, at a driving voltage of 3 V, the FWHM of the light emission of the QLED based on Mn-doped $CsPbBr_3$ perovskite QDs is 24.3 nm, which is smaller than that of the undoped QDs (31.5 nm). The green light purity of the two QLEDs is expressed in CIE coordinates as (0.26, 0.54) for the undoped perovskite QDs and (0.18, 0.62) for the 4.7% Mn-doped perovskite QDs, as shown in Figure 4c. Notably, the QLED based on the Mn-doped QDs exhibit color coordinates that are closer to the ideal green LED coordinates in the 1931 color space (0.170, 0.797) [44] and exhibit a higher degree of color purity, which highlights the great potential of doped perovskite QDs for LED fabrication.

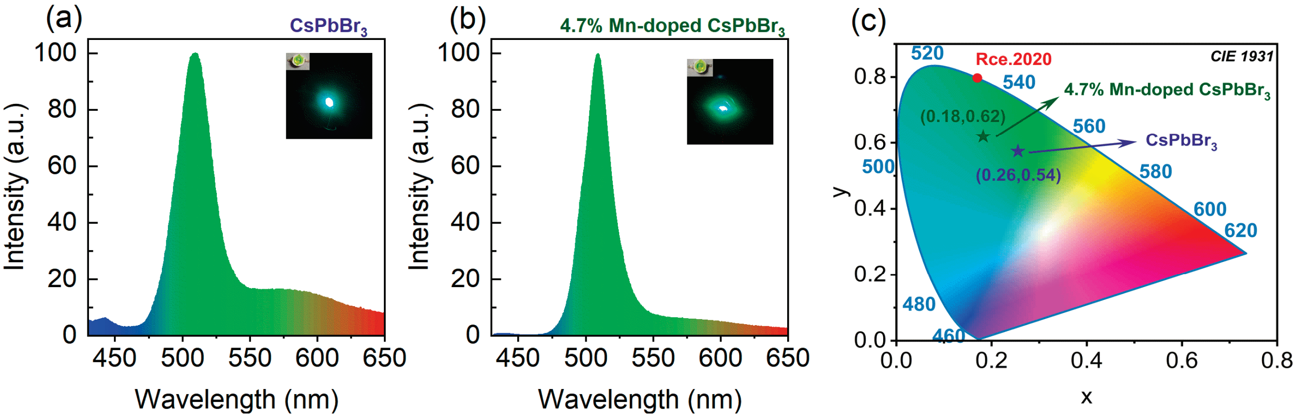

Figure 4. (**a**,**b**) Light-emitting diode (LED) emission spectra of the undoped and 4.7% Mn-doped $CsPbBr_3$ perovskite QDs. Insets: Optical images corresponding to the LED. (**c**) Chromaticity coordinates.

4. Conclusions

Mn-doped $CsPbBr_3$ perovskite QDs were successfully prepared by introducing an appropriate amount of Mn^{2+} into the QDs. The study demonstrates that Mn doping significantly increases the defect formation energy, which promotes the formation of nearly uniform local structural order in the perovskite QDs, leading to improved size uniformity and monodispersity. The FWHM of the size distribution of the perovskite QDs was reduced from 2 nm to 1.2 nm, with a 30.3% reduction in the PL emission linewidth as compared to the undoped QDs, indicating a more homogeneous energy distribution and improved optical properties. The study reveals that the optimal doping effect is achieved when the Mn doping concentration of perovskite QDs is set at 4.7% among four different doping concentrations. This doping process does not result in the introduction of deep trap states within the band gap and instead improves the size uniformity. Furthermore, the improvement in PL properties is evidenced by the narrowing of the spectral linewidths, the increase in PL lifetime, and the reduction in the Auger recombination rate. Additionally, a 23% reduction in linewidth was observed for the 4.7% doped QLEDs, with a CIE color coordinate of (0.18, 0.62) that is closer to the ideal coordinates for green LEDs, further demonstrating their potential for LED applications. This work offers an effective strategy for enhancing the color purity of perovskite QD-based LEDs.

Supplementary Materials: The following supporting information can be downloaded at https://www.mdpi.com/article/10.3390/nano14151284/s1: Estimation of $\langle N \rangle$ and calculation of the absorption cross section; BC blinking determined by radiative lifetime scaling; Figure S1: excitation spectra of PL for undoped and 4.7% Mn-doped perovskite CsPbBr3 QDs; Figure S2: X-ray diffraction (XRD) patterns of perovskite QDs with different Mn doping concentrations; Figure S3: morphological and structural characterizations of undoped and Mn-doped CsPbBr3 perovskite QDs with various doping concentrations; Figure S4: histograms of the absorption cross sections (σ) of undoped and 4.7% Mn-doped CsPbBr3 perovskite QDs; Figure S5: typical PL intensity time trajectory for single CsPbBr3 perovskite QDs with different doping concentrations; Table S1: mass and molar ratios of PbBr2, MnBr2 and ZnBr2 at different doping concentrations; Table S2: quantitative elemental scanning ICP-OES analysis of Mn-doped CsPbBr3 QDs under different doping concentrations; and Table S3: a summary table of photophysical parameters for the Mn-doped QDs obtained in this work and results from other literature used for comparison. References [45–47] are cited in the Supplementary Materials.

Author Contributions: Conceptualization, G.Z. (Guofeng Zhang) and L.X.; data curation, M.Z. and X.H.; formal analysis, C.Y., J.L., W.G., Z.C. and B.L.; visualization, M.Z. and G.Z. (Guofeng Zhang); funding acquisition, G.Z. (Guofeng Zhang), R.C., C.Q., J.H., Z.Y., G.Z. (Ganying Zeng), L.X. and S.J.; writing—original draft, M.Z. and G.Z. (Guofeng Zhang); writing—review and editing, G.Z. (Guofeng Zhang), R.C., C.Q., J.H., Z.Y., G.Z. (Ganying Zeng), L.X. and S.J. All authors have read and agreed to the published version of the manuscript.

Funding: The authors acknowledge financial support from the National Key Research and Development Program of China (No. 2022YFA1404201), the Natural Science Foundation of China (Nos. 62127817, U22A2091, U23A20380, 62075120, 62222509, 62075122, 62205187, 62105193, 62305201, and 62305200), NSFC-STINT (No. 62011530133), the Program for Changjiang Scholars and the Innovative Research Team (No. IRT_17R70), the China Postdoctoral Science Foundation (No. 2022M722006), the Fundamental Research Program of Shanxi Province (No. 202303021222031, 202103021223032, 202103021223254), the Shanxi Province Science and Technology Innovation Talent Team (No. 202204051001014), the Shanxi Province Science and Technology Major Special Project (No. 202201010101005), the Science and Technology Cooperation Project of Shanxi Province (No. 202104041101021), the Shanxi "1331 Project", and 111 Project (No. D18001).

Data Availability Statement: Data underlying the results are contained within the article or the Supplementary Materials.

Conflicts of Interest: The authors declare no conflicts of interest.

References

1. Tang, Y.; Tang, S.; Luo, M.; Guo, Y.; Zheng, Y.; Lou, Y.; Zhao, Y. All-inorganic lead-free metal halide perovskite quantum dots: Progress and prospects. *Chem. Commun.* **2021**, *57*, 7465–7479. [CrossRef] [PubMed]
2. Wu, X.; Ji, H.; Yan, X.; Zhong, H. Industry outlook of perovskite quantum dots for display applications. *Nat. Nanotechnol.* **2022**, *17*, 813–816. [CrossRef] [PubMed]
3. Li, B.; Zhang, G.; Gao, Y.; Chen, X.; Chen, R.; Qin, C.; Hu, J.; Wu, R.; Xiao, L.; Jia, S. Single quantum dot spectroscopy for exciton dynamics. *Nano Res.* **2024**. [CrossRef]
4. Li, B.; Huang, H.; Zhang, G.; Yang, C.; Guo, W.; Chen, R.; Qin, C.; Gao, Y.; Biju, V.P.; Rogach, A.L.; et al. Excitons and biexciton dynamics in single $CsPbBr_3$ perovskite quantum dots. *J. Phys. Chem. Lett.* **2018**, *9*, 6934–6940. [CrossRef] [PubMed]

5. Li, Y.; Du, K.; Zhang, M.; Gao, X.; Lu, Y.; Yao, S.; Li, C.; Feng, J.; Zhang, H. Tunable ultra-uniform Cs_4PbBr_6 perovskites with efficient photoluminescence and excellent stability for high-performance white light-emitting diodes. *J. Mater. Chem.* **2021**, *9*, 12811–12818. [CrossRef]
6. He, X.; Li, T.; Liang, Z.; Liu, R.; Ran, X.; Wang, X.; Guo, L.; Pan, C. Enhanced cyan photoluminescence and stability of $CsPbBr_3$ quantum dots via surface engineering for white light-emitting diodes. *Adv. Opt. Mater.* **2024**, *12*, 2302726. [CrossRef]
7. Liu, Y.; Yuan, S.; Zheng, H.; Wu, M.; Zhang, S.; Lan, J.; Li, W.; Fan, J. Structurally dimensional engineering in perovskite photovoltaics. *Adv. Energy Mater.* **2023**, *13*, 2300188. [CrossRef]
8. Chen, L.J.; Dai, J.H.; Lin, J.D.; Mo, T.S.; Lin, H.P.; Yeh, H.C.; Chuang, Y.C.; Jiang, S.A.; Lee, C.R. Wavelength-tunable and highly stable perovskite-quantum-dot-doped lasers with liquid crystal lasing cavities. *ACS Appl. Mater. Interfaces* **2018**, *10*, 33307–33315. [CrossRef] [PubMed]
9. Nguyen, T.; Tan, L.Z.; Baranov, D. Tuning perovskite nanocrystal superlattices for superradiance in the presence of disorder. *J. Chem. Phys.* **2023**, *159*, 204703. [CrossRef] [PubMed]
10. Lin, L.; Liu, Y.; Wu, W.; Huang, L.; Zhu, X.; Xie, Y.; Liu, H.; Zheng, B.; Liang, J.; Sun, X. Self-powered perovskite photodetector arrays with asymmetric contacts for imaging applications. *Adv. Electron. Mater.* **2023**, *9*, 2300106. [CrossRef]
11. Pan, X.; Ding, L. Application of metal halide perovskite photodetectors. *J. Semicond.* **2022**, *43*, 020203. [CrossRef]
12. Ma, J.; Zhang, J.; Horder, J.; Sukhorukov, A.A.; Toth, M.; Neshev, D.N.; Aharonovich, I. Engineering quantum light sources with flat optics. *Adv. Mater.* **2024**, *36*, 2313589. [CrossRef] [PubMed]
13. Kulkarni, S.A.; Yantara, N.; Tan, K.S.; Mathews, N.; Mhaisalkar, S.G. Perovskite nanostructures: Leveraging quantum effects to challenge optoelectronic limits. *Mater. Today* **2020**, *33*, 122–140. [CrossRef]
14. Lu, X.; Hou, X.; Tang, H.; Yi, X.; Wang, J. A high-quality CdSe/CdS/ZnS quantum-dot-based FRET aptasensor for the simultaneous detection of two different Alzheimer's disease core biomarkers. *Nanomaterials* **2022**, *12*, 4031. [CrossRef] [PubMed]
15. Chen, M.; Shen, G.; Guyot-Sionnest, P. Size distribution effects on mobility and intraband gap of HgSe quantum dots. *J. Phys. Chem. C* **2020**, *124*, 16216–16221. [CrossRef]
16. Yang, C.; Zhang, G.; Gao, Y.; Li, B.; Han, X.; Li, J.; Zhang, M.; Chen, Z.; Wei, Y.; Chen, R. Size-dependent photoluminescence blinking mechanisms and volume scaling of biexciton Auger recombination in single $CsPbI_3$ perovskite quantum dots. *J. Chem. Phys.* **2024**, *160*, 174505. [CrossRef] [PubMed]
17. Bai, X.; Li, H.; Peng, Y.; Zhang, G.; Yang, C.; Guo, W.; Han, X.; Li, J.; Chen, R.; Qin, C.; et al. Role of aspect ratio in the photoluminescence of single CdSe/CdS dot-in-rods. *J. Phys. Chem. C* **2022**, *126*, 2699–2707. [CrossRef]
18. Korepanov, O.; Kozodaev, D.; Aleksandrova, O.; Bugrov, A.; Firsov, D.; Kirilenko, D.; Mazing, D.; Moshnikov, V.; Shomakhov, Z. Temperature-and size-dependent photoluminescence of $CuInS_2$ quantum dots. *Nanomaterials* **2023**, *13*, 2892. [CrossRef] [PubMed]
19. Dong, Y.; Qiao, T.; Kim, D.; Parobek, D.; Rossi, D.; Son, D.H. Precise control of quantum confinement in cesium lead halide perovskite quantum dots via thermodynamic equilibrium. *Nano Lett.* **2018**, *18*, 3716–3722. [CrossRef] [PubMed]
20. Larson, H.; Cossairt, B.M. Indium-poly (carboxylic acid) ligand interactions modify InP quantum dot nucleation and growth. *Chem. Mater.* **2023**, *35*, 6152–6160. [CrossRef]
21. Paik, T.; Greybush, N.J.; Najmr, S.; Woo, H.Y.; Hong, S.V.; Kim, S.H.; Lee, J.D.; Kagan, C.R.; Murray, C.B. Shape-controlled synthesis and self-assembly of highly uniform upconverting calcium fluoride nanocrystals. *Inorg. Chem. Front.* **2024**, *11*, 278–285. [CrossRef]
22. Chen, J.; Zhang, L.; Li, S.; Jiang, F.; Jiang, P.; Liu, Y. Cu-deficient cuinse quantum dots for "turn-on" detection of adenosine triphosphate in living cells. *ACS Appl. Nano Mater.* **2021**, *4*, 6057–6066. [CrossRef]
23. Akkerman, Q.A.; Park, S.; Radicchi, E.; Nunzi, F.; Mosconi, E.; De Angelis, F.; Brescia, R.; Rastogi, P.; Prato, M.; Manna, L. Nearly monodisperse insulator Cs_4PbX_6 (X = Cl, Br, I) nanocrystals, their mixed halide compositions, and their transformation into $CsPbX_3$ nanocrystals. *Nano Lett.* **2017**, *17*, 1924–1930. [CrossRef] [PubMed]
24. Kirakosyan, A.; Kim, Y.; Sihn, M.R.; Jeon, M.G.; Jeong, J.R.; Choi, J. Solubility-controlled room-temperature synthesis of cesium lead halide perovskite nanocrystals. *ChemNanoMat* **2020**, *6*, 1863–1869. [CrossRef]
25. Manoli, A.; Papagiorgis, P.; Sergides, M.; Bernasconi, C.; Athanasiou, M.; Pozov, S.; Choulis, S.A.; Bodnarchuk, M.I.; Kovalenko, M.V.; Othonos, A. Surface functionalization of $CsPbBr_3$ nanocrystals for photonic applications. *ACS Appl. Nano Mater.* **2021**, *4*, 5084–5097. [CrossRef]
26. Yong, Z.; Guo, S.; Ma, J.; Zhang, J.; Li, Z.; Chen, Y.; Zhang, B.; Zhou, Y.; Shu, J.; Gu, J.; et al. Doping-enhanced short-range order of perovskite nanocrystals for near-unity violet luminescence quantum yield. *J. Am. Chem. Soc.* **2018**, *140*, 9942–9951. [CrossRef] [PubMed]
27. Li, J.; Wang, D.; Zhang, G.; Yang, C.; Guo, W.; Han, X.; Bai, X.; Chen, R.; Qin, C.; Hu, J.; et al. The role of surface charges in the blinking mechanisms and quantum-confined stark effect of single colloidal quantum dots. *Nano Res.* **2022**, *15*, 7655–7661. [CrossRef]
28. Li, B.; Gao, Y.; Wu, R.; Miao, X.; Zhang, G. Charge and energy transfer dynamics in single colloidal quantum dots/monolayer MoS_2 heterostructures. *Phys. Chem. Chem. Phys.* **2023**, *25*, 8161–8167. [CrossRef]
29. Bi, C.; Wang, S.; Li, Q.; Kershaw, S.V.; Tian, J.; Rogach, A.L. Thermally stable copper(II)-doped cesium lead halide perovskite quantum dots with strong blue emission. *J. Phys. Chem. Lett.* **2019**, *10*, 943–952. [CrossRef] [PubMed]
30. Mir, W.J.; Mahor, Y.; Lohar, A.; Jagadeeswararao, M.; Das, S.; Mahamuni, S.; Nag, A. Postsynthesis doping of Mn and Yb into $CsPbX_3$ (X = Cl, Br, or I) perovskite nanocrystals for downconversion emission. *Chem. Mater.* **2018**, *30*, 8170–8178. [CrossRef]

31. Liu, W.; Lin, Q.; Li, H.; Wu, K.; Robel, I.; Pietryga, J.M.; Klimov, V.I. Mn^{2+}-doped lead halide perovskite nanocrystals with dual-color emission controlled by halide content. *J. Am. Chem. Soc.* **2016**, *138*, 14954–14961. [CrossRef] [PubMed]
32. Yun, R.; Yang, H.; Sun, W.; Zhang, L.; Liu, X.; Zhang, X.; Li, X. Recent advances on Mn^{2+}-doping in diverse metal halide perovskites. *Laser Photonics Rev.* **2023**, *17*, 2200524. [CrossRef]
33. Hu, F.; Zhang, H.; Sun, C.; Yin, C.; Lv, B.; Zhang, C.; Yu, W.W.; Wang, X.; Zhang, Y.; Xiao, M. Superior optical properties of perovskite nanocrystals as single photon emitters. *ACS Nano* **2015**, *9*, 12410–12416. [CrossRef] [PubMed]
34. Han, X.; Zhang, G.; Li, B.; Yang, C.; Guo, W.; Bai, X.; Huang, P.; Chen, R.; Qin, C.; Hu, J. Blinking mechanisms and intrinsic quantum-confined stark effect in single methylammonium lead bromide perovskite quantum dots. *Small* **2020**, *16*, 2005435. [CrossRef] [PubMed]
35. Yang, C.; Li, Y.; Hou, X.; Zhang, M.; Zhang, G.; Li, B.; Guo, W.; Han, X.; Bai, X.; Li, J. Conversion of photoluminescence blinking types in single colloidal quantum dots. *Small* **2023**, *20*, 2309134. [CrossRef] [PubMed]
36. Podshivaylov, E.A.; Kniazeva, M.A.; Tarasevich, A.O.; Eremchev, I.Y.; Naumov, A.V.; Frantsuzov, P.A. A quantitative model of multi-scale single quantum dot blinking. *J. Mater. Chem.* **2023**, *11*, 8570–8576. [CrossRef]
37. Yuan, G.; Gómez, D.E.; Kirkwood, N.; Boldt, K.; Mulvaney, P. Two mechanisms determine quantum dot blinking. *ACS Nano* **2018**, *12*, 3397–3405. [CrossRef] [PubMed]
38. Li, B.; Zhang, G.; Yang, C.; Li, Z.; Chen, R.; Qin, C.; Gao, Y.; Huang, H.; Xiao, L.; Jia, S. Fast recognition of single quantum dots from high multi-exciton emission and clustering effects. *Opt. Express* **2018**, *26*, 4674. [CrossRef]
39. Nair, G.; Zhao, J.; Bawendi, M.G. Biexciton quantum yield of single semiconductor nanocrystals from photon statistics. *Nano Lett.* **2011**, *11*, 1136–1140. [CrossRef] [PubMed]
40. Guo, W.; Tang, J.; Zhang, G.; Li, B.; Yang, C.; Chen, R.; Qin, C.; Hu, J.; Zhong, H.; Xiao, L.; et al. Photoluminescence blinking and biexciton Auger recombination in single colloidal quantum dots with sharp and smooth core/shell interfaces. *J. Phys. Chem. Lett.* **2021**, *12*, 405–412. [CrossRef] [PubMed]
41. Park, Y.; Bae, W.K.; Padilha, L.A.; Pietryga, J.M.; Klimov, V.I. Effect of the core/shell interface on Auger recombination evaluated by single-quantum-dot spectroscopy. *Nano Lett.* **2014**, *14*, 396–402. [CrossRef] [PubMed]
42. Zhuang, X.; Liang, B.; Jiang, C.; Wang, S.; Bi, H.; Wang, Y. Narrow band organic emitter for pure green solution-processed electroluminescent devices with CIE coordinate y of 0.77. *Adv. Opt. Mater.* **2024**, *12*, 2400490. [CrossRef]
43. Li, S.; Pan, J.; Yu, Y.; Zhao, F.; Wang, Y.; Liao, L. Advances in solution-processed blue quantum dot light-emitting diodes. *Nanomaterials* **2023**, *13*, 1695. [CrossRef] [PubMed]
44. Kumar, S.; Jagielski, J.; Kallikounis, N.; Kim, Y.; Wolf, C.; Jenny, F.; Tian, T.; Hofer, C.J.; Chiu, Y.; Stark, W.J.; et al. Ultrapure green light-emitting diodes using two-dimensional formamidinium perovskites: Achieving recommendation 2020 color coordinates. *Nano Lett.* **2017**, *17*, 5277–5284. [CrossRef] [PubMed]
45. Duan, W.; Hu, L.; Zhao, W.; Zhang, X. Rare-earth ion-doped perovskite quantum dots: Synthesis and optoelectronic properties. *J. Mater. Sci. Mater. Electron.* **2022**, *33*, 19019–19025. [CrossRef]
46. Biswas, A.; Bakthavatsalam, R.; Kundu, J. Efficient exciton to dopant energy transfer in Mn^{2+}-doped $(C_4H_9NH_3)_2PbBr_4$ two-dimensional (2D) layered perovskites. *Chem. Mater.* **2017**, *29*, 7816–7825. [CrossRef]
47. Zeng, F.; Tan, Y.; Hu, W.; Tang, X.; Zhang, X.; Yin, H. A facile strategy to synthesize high colour purity blue luminescence aluminium-doped CsPbBr3 perovskite quantum dots. *J. Lumin.* **2022**, *245*, 118788. [CrossRef]

nanomaterials

MDPI

Article

Magnetic Carbon Quantum Dots/Iron Oxide Composite Based on Waste Rice Noodle and Iron Oxide Scale: Preparation and Photocatalytic Capability

Wanying Ying, Qing Liu, Xinyan Jin, Guanzhi Ding, Mengyu Liu, Pengyu Wang and Shuoping Chen *

College of Materials Science and Engineering, Guilin University of Technology, Guilin 541004, China;
2120210327@glut.edu.cn (W.Y.); 2120220336@glut.edu.cn (Q.L.); 2120200261@glut.edu.cn (X.J.);
1020220195@glut.edu.cn (G.D.); 2120210291@glut.edu.cn (M.L.); 2120220368@glut.edu.cn (P.W.)
* Correspondence: 2012014@glut.edu.cn

Abstract: To provide an economical magnetic photocatalyst and introduce an innovative approach for efficiently utilizing discarded waste rice noodle (WRN) and iron oxide scale (IOS), we initially converted WRN into carbon quantum dots (CQDs) using a hydrothermal method, simultaneously calcining IOS to obtain iron oxide (FeO_x). Subsequently, we successfully synthesized a cost-effective, magnetic CQDs/FeO_x photocatalytic composite for the first time by combining the resulting CQDs and FeO_x. Our findings demonstrated that calcining IOS in an air atmosphere enhanced the content of photocatalytically active α-Fe_2O_3, while incorporating WRN-based CQDs into FeO_x improved the electron-hole pair separation, resulting in increased O_2 reduction and H_2O oxidation. Under optimized conditions (IOS calcination temperature: 300 °C; carbon loading: 11 wt%), the CQDs/FeO_x composite, utilizing WRN and IOS as its foundation, exhibited exceptional and reusable capabilities in photodegrading methylene blue and tetracycline. Remarkably, for methylene blue, it achieved an impressive degradation rate of 99.30% within 480 min, accompanied by a high degradation rate constant of 5.26×10^{-3} min^{-1}. This composite demonstrated reusability potential for up to ten photocatalytic cycles without a significant reduction in the degradation efficiency, surpassing the performance of IOS and FeO_x without CQDs. Notably, the composite exhibited strong magnetism with a saturation magnetization strength of 34.7 emu/g, which enables efficient and convenient recovery in photocatalytic applications. This characteristic is highly advantageous for the large-scale industrial utilization of photocatalytic water purification.

Keywords: waste rice noodle; iron oxide scale; carbon quantum dots/iron oxide composite; photocatalytic capability; magnetic

1. Introduction

In recent years, there has been growing interest in using semiconductor materials [1–3] as photocatalysts [4,5] for degrading low concentrations of organic and inorganic molecules in freshwater treatment [6], environmental remediation [7,8], industrial [9], and health applications [10,11]. Various types of semiconductors, such as TiO_2 [12], ZnO [13], ZnS [14], CdS [15], and others, have been reported for photocatalytic decontamination over the past two decades. However, one major challenge encountered with most photocatalysts in powder form is their non-magnetic nature, making them difficult to separate from the purified solution. To address this issue, coupling [16–19] magnetic particles with non-magnetic semiconductor photocatalysts appears to be the most logical solution. By incorporating magnetic particles into the hybrid photocatalysts, an external magnetic field can be used to easily separate them after the photocatalytic process, ensuring reusability and offering a promising approach for environmental pollution control. Among the various magnetic particles, iron oxides—such as Fe_3O_4 [16,20], α-Fe_2O_3 [21], β-Fe_2O_3 [22], γ-Fe_2O_3 [23], FeO [24], and spinel ferrites (MFe_2O_4 [25])—have garnered significant attention in the field of photocatalysis due to their low cost, strong magnetism, environmental friendliness, and stability. However, in comparison to classical photocatalysts like TiO_2 and ZnO, iron oxides do not demonstrate outstanding photocatalytic efficiency. Consequently, it has become essential to explore certain degrees of doping or composite modification to enhance their performance [26–28]. Among these, the composition of carbon quantum dots (CQDs) has proven to be an effective means of enhancing the photocatalytic performance of iron oxide materials [29–34]. There have been reports demonstrating that carbon quantum dots/iron oxide photocatalytic materials can efficiently degrade water-soluble organic pollutants such as methylene blue. For instance, Sun et al. prepared quantum dots using glucose as a carbon source and combined them with commercially-available magnetic Fe_3O_4 nanoparticles to create CQDs/Fe_3O_4 composite material. This composite achieved an 83% degradation rate of alkaline methylene blue solution within 30 min [29]. Additionally, Zhang et al. reported the synthesis of CQDs/MIL-101(Fe)/g-C_3N_4 composite photocatalytic material, using $FeCl_3$ as the iron source and citric acid and ethylenediamine as carbon sources. This composite achieved a photocatalytic rate of 99.3% for methylene blue within 120 min [34]. However, it is worth noting that the CQDs/iron oxide photocatalytic materials reported to date have typically used commercially available iron and carbon sources, resulting in relatively high synthesis costs, which may pose challenges for large-scale commercialization.

The improper disposal of cooking waste has the potential to introduce pollutants into the soil and water ecosystems, posing a considerable urban governance dilemma [35]. The contemporary methods employed for the management of cooking waste in commercial settings [36,37] predominantly encompass techniques like anaerobic digestion [38], aerobic composting [39], landfill deposition [40], incineration [41], and the creation of forage [42]. Despite enabling the large-scale industrial treatment of cooking waste, these strategies are accompanied by notable limitations [43], including substantial land utilization, substantial capital investment in equipment, diminished product profit margins, and the potential for generating secondary pollutants like greenhouse gas emissions and leachates. In order to address these issues, our previous investigation proposed a novel approach to utilizing cooking waste, specifically waste rice noodle (WRN), with starch as the main component. This approach involved first hydrothermal carbonizing the WRN to create a solution of CQDs, which was then combined with specific inorganic nano powders like TiO_2 or ZnO to produce CQDs/TiO_2 [44] or CQDs/ZnO [45] photocatalytic composites for water pollution control. The CQDs/inorganic oxide composites derived from WRN displayed remarkable photocatalytic degradation efficiency, outperforming commercial TiO_2 or ZnO, particularly under visible light illumination, for a range of water-soluble dyes. This conversion strategy of WRN to CQDs/TiO_2 [44] or CQDs/ZnO [45] composites added significant value and offered promising prospects for industrialization, potentially providing a new method for cooking waste recycling. However, although both catalysts could be recycled and reused multiple times without significantly reducing their photocatalytic degradation capacity, each recycling step requires careful centrifugation, washing, and drying. This process posed significant challenges when applied to large-scale wastewater treatment in practical settings.

On the other hand, iron oxide scale (IOS [46]) is formed on the surface of steel during the steel rolling process when the steel is rapidly cooled with water, resulting in iron-containing oxides. If not properly treated, significant amounts of IOS may be released into the environment, potentially causing severe pollution to water bodies, soil, and other natural surroundings [47]. At present, the primary method for handling waste IOS is to reintroduce it into the metallurgical industry, where it is used in the smelting of steel [48]. This well-established approach is suitable for large-scale production, but it requires significant investments in terms of funds, equipment, land, and labor. Furthermore, there is the possibility that waste IOS may contain Ca, Mg, P, and Si, providing an alternative pathway for reusing it as fertilizer [49]. However, such fertilizers can only utilize a small fraction of the effective components present in the IOS, leading to generally low fertilizer efficiency.

Considering these limitations, it is essential to explore novel approaches that utilize waste IOS as a raw material to produce high-tech, high-value functional materials.

Based on previous research, our goal is to design and synthesize a new functional material derived from waste that boasts lower production costs and enhanced recyclability. We proposed integrating two types of waste materials, namely rice noodle waste (WRN) and iron oxide scale (IOS), as the raw materials. Firstly, the WRN underwent a hydrothermal process to convert it into CQDs, while the IOS was calcined to obtain iron oxides (FeO_x). Subsequently, we combined the CQDs from WRN with the FeO_x from IOS, achieving the pioneering synthesis of a cost-effective magnetic CQDs/FeO_x photocatalytic composite material without the need for additional synthetic agents (see Figure 1). This material exhibited a good photocatalytic performance and could be effectively separated using magnets, showcasing its commendable recyclability and reusability. Our research delves into the material's structure, photocatalytic performance, and photocatalytic mechanism, as well as thoroughly analyzing the effects of IOS calcination and CQDs combination on the material's properties.

Figure 1. Formation process of CQDs/FeO_x composite using WRN and IOS as raw materials.

2. Experiment Section

2.1. Materials

The waste rice noodle (WRN) was obtained from the canteen located at the Guilin University of Technology in Guilin, China, with its primary organic components including starch (21.36 g/100 g), protein (1.91 g/100 g), and fat (0.4 g/100 g). The waste iron oxide scale (IOS, 200 mesh, main element content: Fe 71.09 wt%, O 27.41 wt%, Si 0.47 wt%, Ca 0.42 wt%, Mn 0.38 wt%, Al 0.23 wt%) was obtained from Valin Lianyuan Iron and Steel Co. Ltd. in Hunan, China. The tetracycline hydrochloride (98% purity), methylene blue (98.5% purity), nano ZnO (99% purity), nano TiO_2 (99% purity), 1,4-benzoquinone (BQ, 98% purity), 2-propanol (IPA, 99% purity), ethylenediaminetetraacetic acid disodium salt (EDTA–2Na, 98% purity), as well as dimethyl pyridine N-oxide (DMPO, 99% purity), were procured from Macklin Reagent (Shanghai, China) and were used as received, without undergoing additional purification steps.

2.2. Synthesis

To initiate the process, the formulation of the CQDs solution commenced via a hydrothermal treatment applied to the WRN, adhering to the methodology outlined in our earlier research [44,45]. In the standard synthesis protocol, 100 g of WRN underwent thorough grinding to yield a consistent paste using a mortar. Subsequently, this paste was combined with 200 g of deionized water. The ensuing mixture underwent heating within a 500 mL Teflon-lined autoclave, where it was subjected to a temperature of 200 °C for a duration of 10 h. A brown CQDs solution, accompanied by black-gray sediment, was successfully acquired. Employing vacuum filtration, the brown CQDs solution was isolated, intended for subsequent fabrication of CQDs/FeO_x photocatalytic composites, while the solid portion was separated to yield hydrothermal carbon (HTC) powder, which could be further treated to produce activated carbon [44]. Simultaneously, the IOS powder underwent calcination at various temperatures (100 °C, 200 °C, 300 °C, 400 °C, 500 °C) in an air atmosphere using a SGM6812CK tube furnace (Sigma, Luoyang, China) for 4 h, producing FeO_x as a brown powder.

Next, a volume of 40 mL from the CQDs solution was skillfully combined with an appropriate quantity of FeO_x, choosing from three different amounts (0.25 g, 0.5 g, 1 g), in precisely measured proportions. Through meticulous magnetic stirring at room temperature for a duration of 0.5 h, a consistent and homogenous suspension was created. Subsequently, this well-mixed composition was placed into a 50 mL Teflon-lined autoclave, undergoing heating at a temperature of 85 °C for a span of 3 h to facilitate the formation of the composite structure. Following this process, the composite material was retrieved and subjected to centrifugation, followed by thorough triple washing with distilled water. Upon being subjected to vacuum drying at 60 °C, the resulting product emerged as the CQDs/FeO_x photocatalytic composite material, taking the form of a deep brown powder. The samples were labeled as CQDs/FeO_x–1 to CQDs/FeO_x–7 based on the calcination temperature of the IOS and the amount of FeO_x used. The relevant formulation design and elemental composition are presented in Table 1.

Table 1. Formulation design of CQDs/FeO_x composites.

Serial Number	Calcination Temperature of IOS (°C)	Dosage of FeO_x (g)	Elemental Composition (wt%)						
			Fe	O	C	Mn	Al	Si	Ca
CQDs/FeO_x–1	100	0.5	63.17	24.36	11.23	0.19	0.41	0.35	0.29
CQDs/FeO_x–2	200	0.5	62.75	24.66	11.34	0.2	0.42	0.36	0.27
CQDs/FeO_x–3	300	0.5	62.6	24.94	11.14	0.21	0.44	0.35	0.32
CQDs/FeO_x–4	400	0.5	62.91	24.87	10.89	0.23	0.44	0.34	0.32
CQDs/FeO_x–5	500	0.5	62.95	24.58	11.24	0.22	0.39	0.33	0.29
CQDs/FeO_x–6	300	0.25	56.24	22.38	20.21	0.19	0.4	0.32	0.26
CQDs/FeO_x–7	300	1	65.88	26.2	6.56	0.22	0.46	0.35	0.33

2.3. General Characterization and Measurement of Photocatalytic Performance

The characterizations and photocatalytic degradation experiments of the CQDs/FeO_x composite material were conducted following the methods outlined in our previous reports [44,45]. For in-depth details, please refer to Supplementary Materials S1 and S2 in the ESI.

3. Result and Discussion

3.1. Structural Characterization

The PXRD analysis of the CQDs/FeO_x composite (CQDs/FeO_x–3 sample), FeO_x powder (achieved through the calcination of IOS at 300 °C), and IOS (raw material) is depicted in Figure 2. Evidently, the waste IOS contained two main phases. Among them, the characteristic peaks at 30.0°, 35.4°, 37.0°, 43.1°, 56.9°, and 62.5° corresponded to the (220), (311), (222), (400), (511), and (440) crystal planes, respectively, which could be attributed to magnetite (Fe_3O_4, JCPDS card no. 19-0629). Additionally, the characteristic peaks at 33.1° and 35.6° could be attributed to the (104) and (110) crystal planes of hematite (α-Fe_2O_3, JCPDS card no. 33-0664). This indicated that the IOS mainly contained Fe_3O_4 and α-Fe_2O_3, with Fe_3O_4 being dominant. Combining this with the results of the elemental composition analysis (See Table 2), the Fe/O mass ratio in the IOS was 2.59, and it could be calculated that there was only about 10.8% of α-Fe_2O_3 in the mixed phase of iron oxide. Typically, the band gap of magnetite (Fe_3O_4) was too small to exhibit an effective photocatalytic ability. As a result, the iron oxide photocatalytic component was mainly α-Fe_2O_3. Therefore, it was foreseeable that the waste IOS could not be directly used as a photocatalytic material or directly combined with CQDs due to the low content of α-Fe_2O_3, making calcination treatment necessary to enhance its photocatalytic potential.

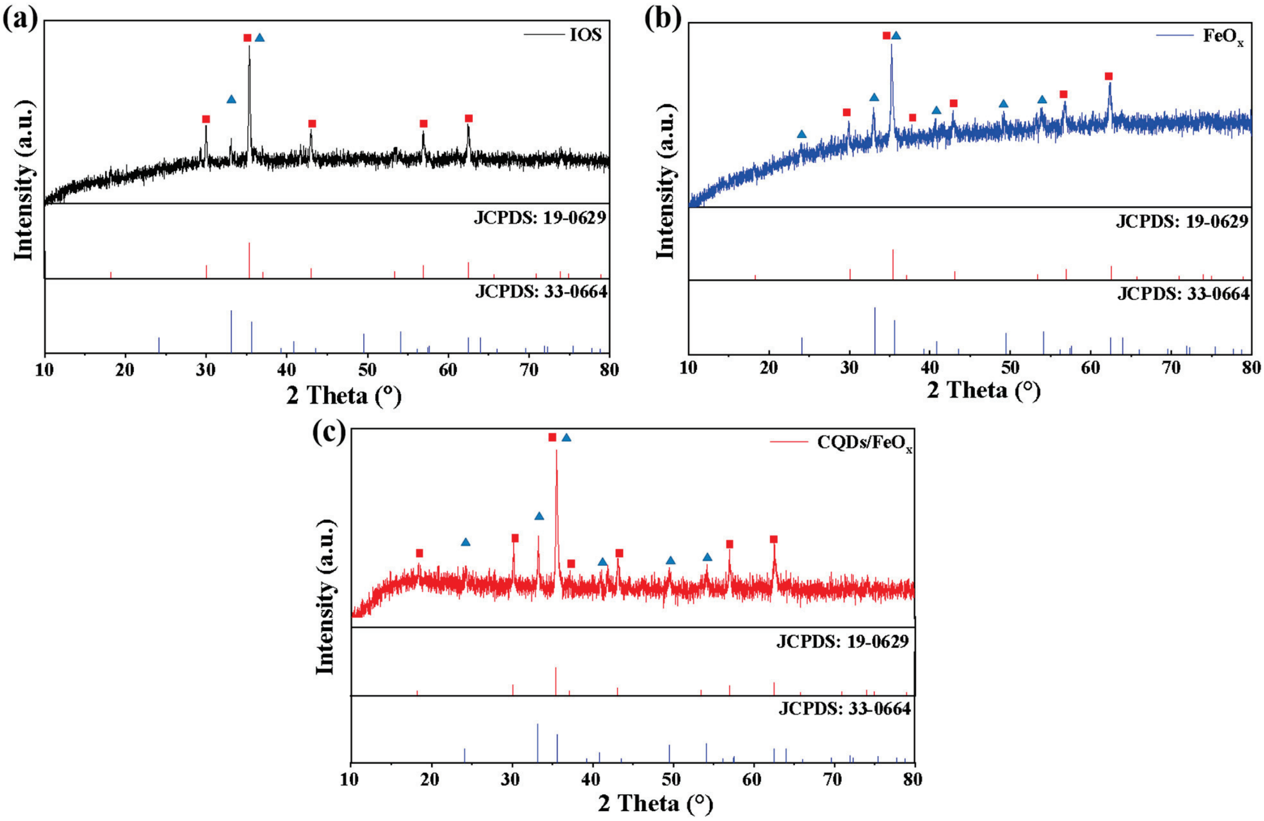

Figure 2. PXRD pattern of IOS (**a**), FeO_x (**b**) and CQDs/FeO_x composite (**c**). The red square and blue triangle represent the diffraction peaks of Fe_3O_4 and α-Fe_2O_3, respectively.

Table 2. Comparison of composition element content of CQDs/FeO_x composite, FeO_x and IOS.

Serial Number	Elemental Composition (wt%)						
	Fe	O	C	Al	Si	Ca	Mn
IOS	71.09	27.41	-	0.23	0.47	0.42	0.38
FeO_x [a]	70.46	28.05	-	0.21	0.49	0.4	0.39
CQDs/FeO_x composite [b]	62.6	24.94	11.14	0.21	0.44	0.35	0.32

[a] calcining IOS at 300 °C in an air atmosphere for 4 h; [b] CQDs/FeO_x–3 sample.

Comparing the PXRD pattern of the FeO_x powders obtained through the calcination of IOS at 300 °C with that of IOS, it was evident that the diffraction peaks of the α-Fe_2O_3 were significantly enhanced after calcination. The characteristic peaks at 24.1°, 33.1°, 35.6°, 40.9°, 49.5°, and 54.1° corresponded to the (012), (104), (110), (113), (024), and (116) crystal planes of α-Fe_2O_3, respectively. Additionally, based on compositional analysis, the Fe/O mass ratio decreased to 2.51, indicating that the FeO_x powder contained 43.3% of α-Fe_2O_3. This transformation implied that calcination in air could convert a portion of the initially non-photocatalytic Fe_3O_4 into photocatalytically active α-Fe_2O_3, which laid the foundation for obtaining practical photocatalytic materials after the composite with CQDs. The PXRD patterns of the CQDs/FeO_x composite and FeO_x exhibited resemblances; however, the diffraction peaks corresponding to the CQDs within the composite were not prominently discernible due to their relatively modest concentration.

The results of the particle size distribution testing indicated that the obtained CQDs/FeO_x composite (CQDs/FeO_x–3 sample) exhibited a Z-average particle size value of 127.8 ± 63.26 nm (refer to Figure S1 in ESI). The outcomes of the TEM analysis for the CQDs/FeO_x composite (CQDs/FeO_x–3 sample) are visually depicted in Figure 3a. It could be observed that the CQDs/FeO_x composites exhibited an irregular lamellar structure, with uniformly dispersed spherical CQDs particles on the FeO_x surface. In Figure 3b, the HRTEM image vividly revealed the intricate lattice arrangement of the FeO_x and CQDs. The lattice stripes, exhibiting spacings of 0.185 nm, 0.198 nm, and 0.271 nm, corresponded, respectively, to the (104), (110), and (024) crystal planes of α-Fe_2O_3. Furthermore, discernible lattice stripes with spacings of 0.103 nm and 0.168 nm aligned with the (111) and (220) crystal planes of Fe_3O_4. These observations indicated that the obtained FeO_x was primarily a mixture of magnetite (Fe_3O_4) and hematite (α-Fe_2O_3), which aligned with the PXRD results. Moreover, crystalline planes with a lattice spacing of about 0.283 nm, corresponding to the (020) crystalline planes of CQDs [50,51], were also observed, confirming the successful combination of the WRN-based CQDs and FeO_x in the resulting composite.

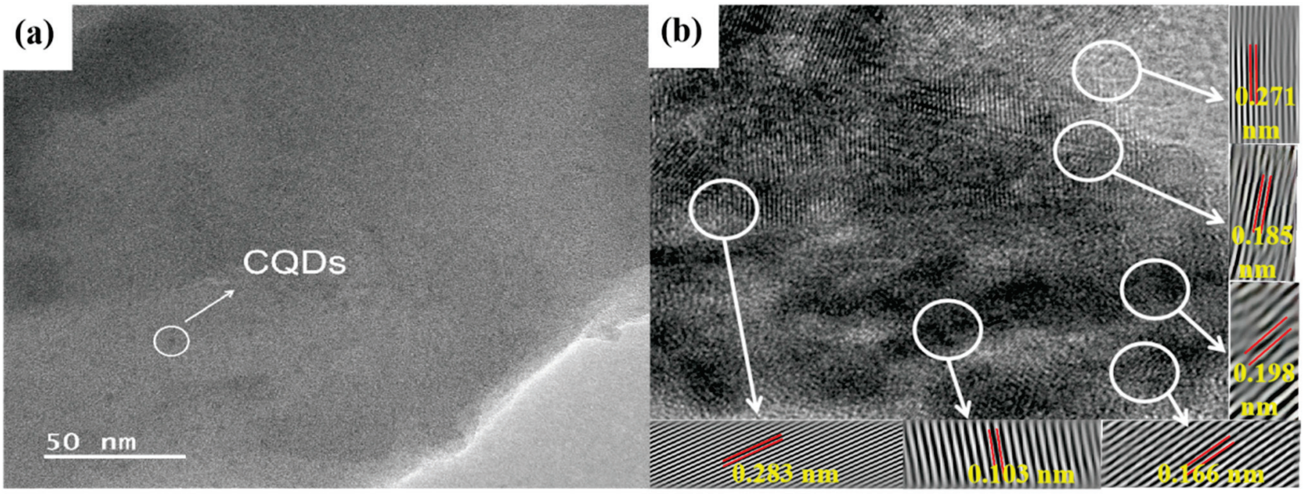

Figure 3. The TEM image (**a**) and HRTEM image (**b**) of CQDs/FeO_x composite based on WRN and IOS.

The XPS spectra of both the CQDs/FeO_x composite and FeO_x powders are displayed in Figure 4 and summarized in Table 3. Figure 4a highlights the elemental presence of Fe, O, and C within the CQDs/FeO_x composite. Notably, Figure 4b and Table 2 elucidate that the Fe 2p spectra disclosed characteristic peaks at 724.67 and 710.49 eV, corresponding to the Fe($2p_{1/2}$) and Fe($2p_{3/2}$) signals, respectively. A noteworthy separation of divalent and trivalent iron signals was discernible within the Fe($2p_{3/2}$) signal, indicative of the presence of both Fe^{2+} and Fe^{3+} ions in the resulting CQDs/FeO_x composite. In the high-resolution spectrum of O 1s, the CQDs/FeO_x complex displayed distinct Fe–O and C–O bonds, hosting characteristic signals positioned at 530.71 and 528.29 eV, respectively. In contrast, the O 1s spectrum of the FeO_x calcined at 300 °C displayed two distinct peaks at 530.5 and 529.38 eV, attributing them to the Fe–O bond and the hydroxyl group present on the FeO_x surface, respectively. This led to the inference that the interaction between CQDs and FeO_x involved the carboxyl group within the CQDs and the Fe–OH group on the surface of the

FeO_x, leading to the vanishing of the surface hydroxyl signal and the emergence of the C–O bond signal, as indicated in Figure 4c and Table 3. Additionally, in the high-resolution C 1s spectrum of the CQDs/FeO_x composite, the peak at 283.69 eV could be attributed to the C–C bond within the CQDs. Simultaneously, the signals centered at 285.03 and 287.51 eV corresponded to the C–O and C=C bonds of CQDs, respectively, confirming the successful integration of the CQDs and FeO_x within the resultant composites.

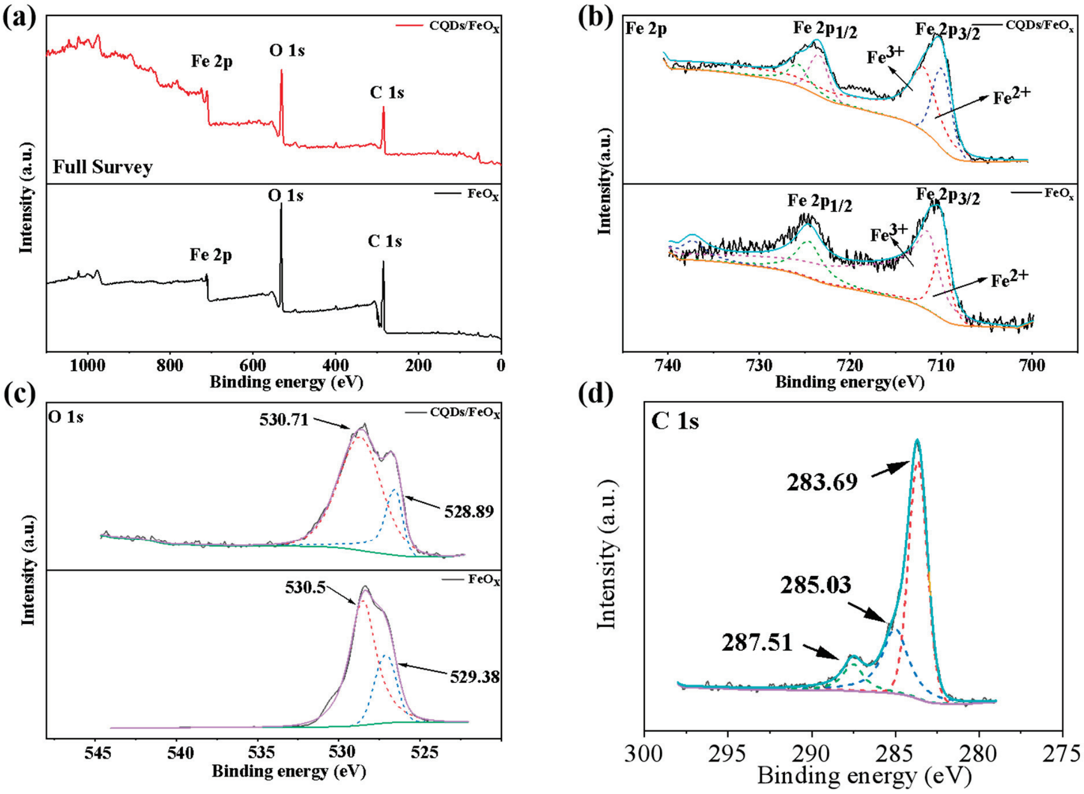

Figure 4. The full XPS (**a**), as well as Fe 2p ((**b**), black: original data, blue: overall fitting curve, green: Fe^{3+} curve at Fe $2p_{1/2}$, purple: Fe^{2+} curve at Fe $2p_{1/2}$, red: Fe^{3+} curve at Fe $2p_{3/2}$, navy blue: Fe^{2+} curve at Fe $2p_{3/2}$, orange curve: bottom line), O 1s ((**c**), black: original data, purple: overall fitting curve, red and blue: peak fitting, green: bottom line) and C 1s ((**d**), CQDs/FeO_x composite only, black: original data, blue: overall fitting curve, red and green: peak fitting, purple: bottom line) high-resolution spectrum of FeO_x powder and CQDs/FeO_x composite.

Table 3. XPS peak distribution of FeO_x powder and CQDs/ FeO_x composite based on waste rice noodle.

Photocatalyst	Element	Peak (eV)	Surface Group	Assignment
CQDs/FeO_x composite [a]	C 1s	283.69	C	Graphitic carbon
		285.03	C–O	Alcoholic or etheric structure in CQDs
		287.51	C=C	Aromatic ring of CQDs
	O 1s	530.71	Fe–O	Oxygen bonded to iron
		528.29	C–O	Oxygen singly bonded to CQDs
	Fe 2p	710.49	Fe	Fe ($2p_{3/2}$)
		724.67	Fe	Fe ($2p_{1/2}$)
FeO_x [b]	O 1s	530.5	Fe–O	Oxygen bonded to iron
		529.38	Fe–OH	Surface hydroxyl group of FeO_x
	Fe 2p	710.35	Fe	Fe ($2p_{3/2}$)
		724.71	Fe	Fe ($2p_{1/2}$)

[a] CQDs/FeO_x–3 sample; [b] calcining IOS at 300 °C in an air atmosphere for 4 h.

As shown in Figure 5a, without the combination of CQDs, the IOS and FeO_x exhibited an obvious Fe–OH stretching vibration peak at around 880 cm^{-1} in their IR spectra. However, this peak disappeared after the composite of FeO_x with CQDs. Paired with the XPS findings, it is conceivable that the intricate interplay between the CQDs and FeO_x constituted a response involving the carboxyl group within the CQDs and the hydroxyl group located on the FeO_x surface. Furthermore, characteristic absorption peaks of CQDs were observed in the IR spectra of the CQDs/FeO_x composites, including the stretching vibration (3422 cm^{-1}) and bending vibration (1620 cm^{-1}) of the O–H bond on the CQDs, and the stretching vibration (1063 cm^{-1}) of the C–O bond, etc. In addition, due to the presence of organic groups such as hydroxyl and carboxyl groups in the CQDs, the PZC value of the CQDs/FeO_x composites (8.46) was higher than that of the non-composite FeO_x powder (7.98) (See Figure 5b). In addition, due to larger feedstock particles, the CQDs/FeO_x composite exhibited a relatively low specific surface area (2.28 m^2 g^{-1}) compared with the CQDs/TiO_2 [44] and CQDs/ZnO [45] photocatalytic composites in our previous report; however, it was still slightly higher than that of the non-composite FeO_x powder (1.57 m^2 g^{-1}) (See Figure 5c).

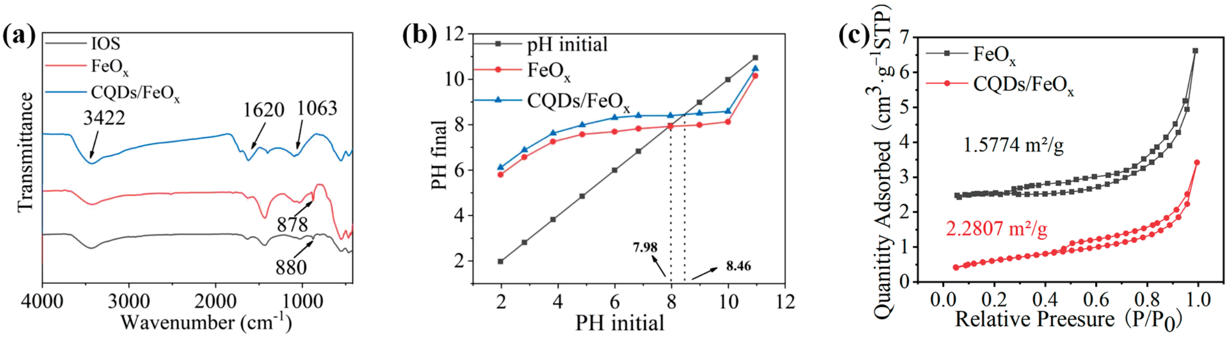

Figure 5. (**a**) IR spectra of IOS, FeO_x powder and CQDs/FeO_x composite; (**b**,**c**) The PZC value (**b**) and BET (**c**) of FeO_x powder and CQDs/FeO_x composite.

3.2. Photocatalytic Performance of CQDs/FeO_x Composites

The resulting CQDs/FeO_x composite exhibited excellent photocatalytic degradation efficiency towards various organic pollutants. Figure 6a underscores the formidable challenge of degrading methylene blue, a prevalent and highly toxic pollutant in dyeing wastewater, using 405 nm visible purple light. In the absence of a catalyst, its degradation rate remained at a mere 2.3%, even after an extended duration of 8 h (480 min). Due to its non-photocatalytic Fe_3O_4 component, the IOS itself lacked the ability for photocatalytic degradation to methylene blue, as its degradation rate was only 4.9% after 480 min of light irradiation, which was almost indistinguishable from the degradation without the catalyst. However, after calcination at 300 °C, a portion of the Fe_3O_4 in the IOS was converted into α-Fe_2O_3, resulting in the FeO_x with a certain photocatalytic degradation ability. The degradation rate of the FeO_x towards methylene blue reached 41.8% after 480 min of light irradiation, with an apparent degradation rate constant of 1.03×10^{-3} min^{-1}. However, complete degradation could not be achieved under these conditions. In contrast, the catalytic effect of the CQDs/FeO_x composite (CQDs/FeO_x–3 sample) on methylene blue significantly improved after incorporating the WRN-based CQDs into the FeO_x. The composite demonstrated a good photocatalytic degradation rate (up to 99.30% within 480 min) and a relatively high degradation rate constant (5.26×10^{-3} min^{-1}), enabling the complete degradation of methylene blue (See Figure S2 in ESI).

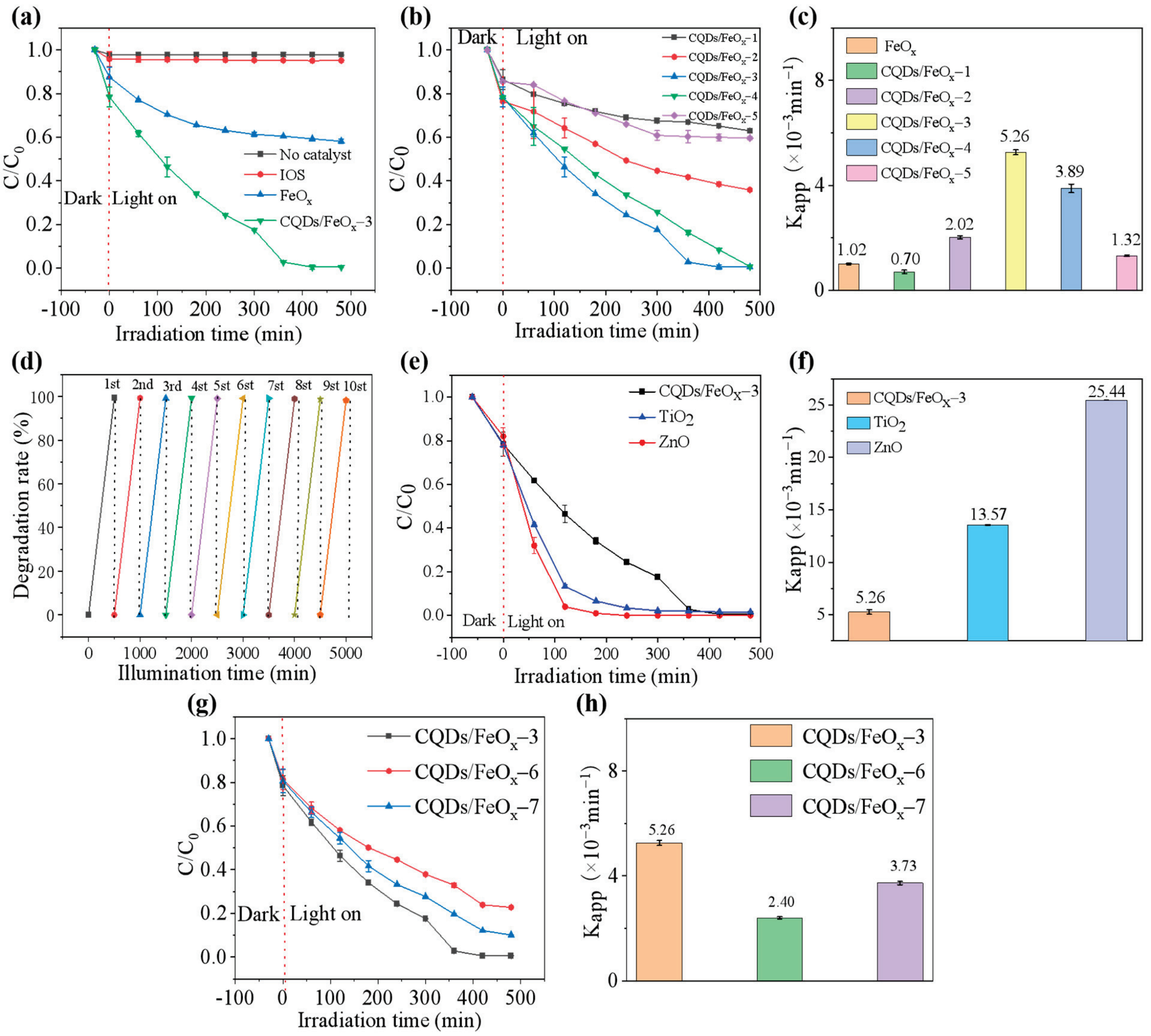

Figure 6. (**a**) Photocatalytic degradation rates of IOS, FeO_x powder and $CQDs/FeO_x$ composites ($CQDs/FeO_x$–3 sample) at 405 nm purple light for methylene blue at different irradiation times; (**b**) Photocatalytic degradation rates of $CQDs/FeO_x$ composites prepared at different calcination temperatures for methylene blue at 405 nm purple light at different irradiation times; (**c**) Apparent degradation rate constants (K_{app}) of $CQDs/FeO_x$ composites and FeO_x powder prepared at different calcination temperatures; (**d**) Photocatalytic degradation performance of $CQDs/FeO_x$ composites across varying photocatalytic cycles employing a 500-min operational cycle; (**e**,**f**) The photocatalytic degradation rates (**e**) and apparent degradation rate constant (K_{app}, (**f**)) of $CQDs/FeO_x$–3 sample, commercial TiO_2 and ZnO; (**g**,**h**) Photocatalytic degradation rates (**g**) and apparent degradation rate constant (K_{app}, (**h**)) of $CQDs/FeO_x$ composites with different carbon contents.

It was found that achieving a good photocatalytic performance for the $CQDs/FeO_x$ composite required the appropriate calcination of the IOS in an air atmosphere to enhance the content of α-Fe_2O_3. The degradation rates of methylene blue for $CQDs/FeO_x$ composite materials obtained at different calcination temperatures (samples $CQDs/FeO_x$–1 to $CQDs/FeO_x$–5) are shown in Figure 6b,c. Combined with the results of the phase and elemental composition, it was observed that without proper high-temperature calcination to increase the content of α-Fe_2O_3, even with the incorporation of CQDs, the catalytic effect could hardly be improved. For instance, the $CQDs/FeO_x$–1 sample obtained by heating the IOS at 100 °C had a Fe/O mass ratio of 2.59 due to the relatively low calcination temperature. It was found that only about 10.9% of α-Fe_2O_3 was present in the mixed FeO_x phase, similar to the IOS as a raw material. Consequently, despite containing CQDs, the photocatalytic degradation of CQDs/FeO_x–1 remained poor. After 480 min of light exposure, its degradation rate to methylene blue was only 35.79%, and the degradation rate constant was merely 7.04×10^{-4} min^{-1}, which is even worse than the FeO_x sample without CQDs but calcined at 300 °C. There are reports indicating that, when heated in air at an appropriate temperature (around 300 °C), Fe_3O_4 exhibits a tendency to transform into α-Fe_2O_3 [52–54]. As shown in Table 1, with enhancing the calcination temperature, the Fe/O mass ratio of the composite FeO_x material showed a trend of initially decreasing and then increasing, indicating that the content of α-Fe_2O_3 first increased and then decreased. Among them, the CQDs/FeO_x–3 sample prepared with IOS calcined at 300 °C had the smallest Fe/O mass ratio (2.51), which corresponded to the highest α-Fe_2O_3 content (44%). Therefore, it exhibited the best photocatalytic performance and achieved the complete degradation of methylene blue within 480 min, with a degradation rate constant of 5.26×10^{-3} min^{-1}. Furthermore, the material demonstrated excellent recyclability, and its degradation rate remained above 98% even after ten cycles of photocatalysis (See Figure 6d). However, when compared to commercially available nanoscale TiO_2 or ZnO, the photocatalytic degradation efficiency of the obtained CQDs/FeO_x photocatalytic material was relatively low (See Figure 6e,f). Nevertheless, due to its complete reliance on waste materials as feedstock, the cost of the CQDs/FeO_x photocatalytic material is significantly lower. Additionally, it possesses strong magnetism, unlike commercial TiO_2 or ZnO, enabling convenient recovery. Therefore, it may present a more competitive option for large-scale water purification.

Additionally, the loading amount of CQDs also affects the photocatalytic degradation capability of the CQDs/FeO_x composite material. As shown in Figure 6g,h, at lower carbon contents, the photocatalytic degradation efficiency of the CQDs/FeO_x composite material improved with the increasing carbon content. The CQDs/FeO_x composite material with a carbon content of approximately 11 wt% (CQDs/FeO_x–3 sample) exhibited the best photocatalytic performance, with a degradation rate constant of 5.26×10^{-3} min^{-1} for methylene blue. However, it was found that further increasing the loading amount of CQDs may have an adverse effect on the photocatalytic performance. For example, in the case of the CQDs/FeO_x–7 sample featuring a carbon content of 20.2 wt%, a comparatively reduced degradation rate constant of 3.73×10^{-3} min^{-1} was observed for methylene blue degradation. This phenomenon could be attributed to the potential shielding influence stemming from the presence of carbon-based constituents [55].

The obtained CQDs/FeO_x composite material could also be utilized for controlling antibiotic residues, as shown in Figure 7. Under 405 nm purple light, the CQDs/FeO_x composite (CQDs/FeO_x–3 sample) could degrade 98.21% of tetracycline within 320 min, with an apparent degradation rate constant of 3.73×10^{-3} min^{-1}. In comparison, under the same conditions, the FeO_x powder without CQDs could only degrade 40.45% of tetracycline, with an apparent degradation rate constant of 1.29×10^{-3} min^{-1}.

Compared with other CQDs/iron oxide composites using different iron and carbon sources (Table 4), the CQDs/FeO_x composite reported in this paper demonstrated a comparably good photocatalytic performance. Moreover, due to the complete utilization of waste materials (IOS and WRN) as raw sources, the synthesis cost of this material was significantly reduced compared to other CQDs/iron oxide composites [29–34]. This complete conversion of waste to treasure makes it more environmentally friendly and exhibits outstanding sustainability, making it more suitable for large-scale, industrial applications in water purification projects. In comparison to our previous reports on CQDs/TiO_2 and CQDs/ZnO composites based on WRN, the CQDs/FeO_x composite exhibited a weaker photocatalytic performance (See Table 5). However, due to the presence of magnetic Fe_3O_4 components, it offers the advantage of simplified recovery procedures while ensuring high recyclability. Additionally, as the oxide component is derived from waste IOS, it eliminates the need for commercial reagents, further reducing the costs and promoting environmental friendliness.

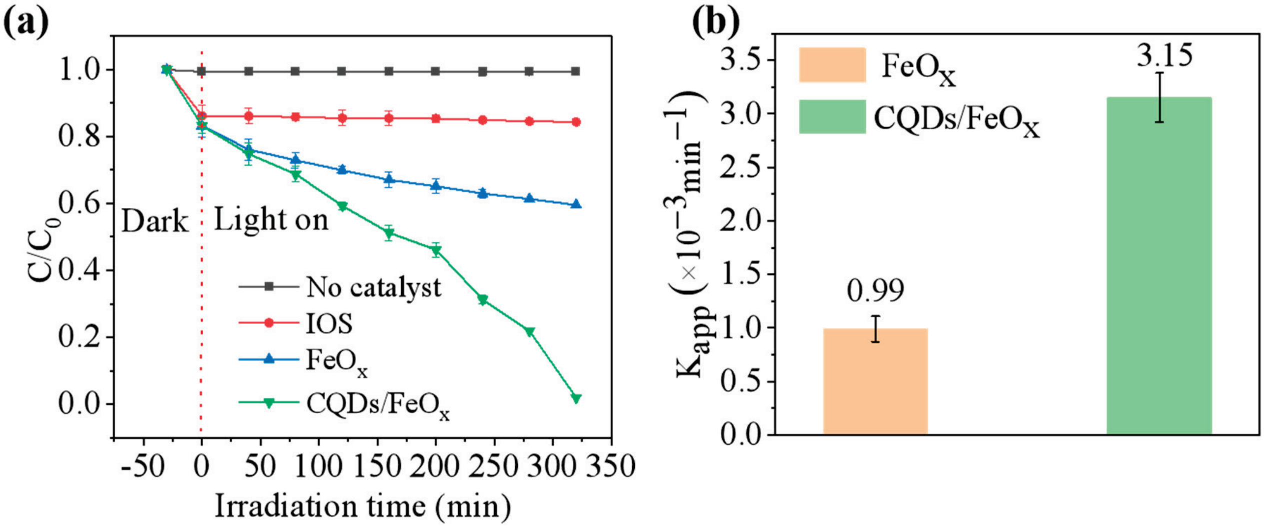

Figure 7. (**a**) Photocatalytic degradation rates of IOS, FeOx powder and CQDs/FeOx composite (CQDs/FeO$_x$–3 sample) at 405 nm purple light for tetracycline hydrochloride at different irradiation times; (**b**) Apparent degradation rate constants (K_{app}) of CQDs/FeOx composite (CQDs/FeO$_x$–3 sample) and FeO$_x$ powder.

3.3. Magnetic Properties of CQDs/FeO$_x$ Composites

In addition to exhibiting efficient photocatalytic degradation to various organic pollutants, the resulting CQDs/FeO$_x$ composite also demonstrated outstanding magnetic properties. The magnetization curves of the CQDs/FeO$_x$ composite and the raw IOS were tested and are shown in Figure 8a. The IOS powder exhibited remarkable soft ferromagnetism at room temperature, characterized by a low coercivity of 97.4 Oe, a low residual magnetization intensity of 5.2 emu/g, and a high saturation magnetization intensity of 5.8 emu/g, primarily attributed to the abundance of Fe_3O_4 particles in the material.

As mentioned earlier, after the process of calcination and compounding, the magnetic properties of the CQDs/FeO$_x$ composites slightly weakened due to the reduced Fe_3O_4 content. Nevertheless, its saturation magnetization intensity remained at approximately 54.6 emu/g, along with low coercivity (117.1 Oe) and residual magnetization intensity (5.8 emu/g). Therefore, the CQDs/FeO$_x$ composite still exhibits exceptional soft magnetic characteristics, making it a promising candidate for various magnetic applications.

Table 4. Photocatalytic degradation performance of CQDs/iron oxide composites utilizing various iron and carbon sources.

Iron Source	Carbon Source of CQDs	Light Source	Pollutant	Pollutant Concentration	Photocatalyst Dosage (g/L)	Irradiation Times (min)	Degradation Rate (%)	Reference
Waste IOS	WRN	Purple light lamp (20 W, wavelength: 405 nm)	methylene blue tetracycline	20 mg/L 20 mg/L	2 2	480 320	99.30 98.21	This work
Commercially-available magnietic Fe_3O_4 nanoparticles	Glucose	Xe lamp (400 W, wavelength > 420 nm)	methylene blue (in NaOH solution)	1×10^{-3} mol/L	1	30	83	[29]
Commercial γ-Fe_2O_3	Glucose	Xe lamp (300 W, wavelength: 455 nm)	sulfamethoxazole (SMX)	10 mg/L	0.2	120	95	[30]
$FeSO_4 \cdot 7H_2O$	Citric acid	Xe lamp with a 420 nm cutoff filter (350 W)	tetracycline, (0.50 mM of H_2O_2 was added)	20 mg/L	0.25	60	93	[31]
$Fe(NO_3)_3 \cdot 9H_2O$	Citric acid	HPMVL visible light lamp (250 W)	Oxytetracycline	10 mg/L	0.2	100	98	[32]
$FeSO_4 \cdot 7H_2O$	Citric acid	Xe lamp (300 W, wavelength > 420 nm)	Metronidazole	30 mg/L	0.2	45	99.36	[33]
$FeCl_3 \cdot 6H_2O$	Citric acid and Ethylenediamine	Xe lamp (300 W, wavelength: 420 nm)	Methylene blue	20 mg/L	0.5	120	99.3	[34]

Table 5. Photocatalytic degradation performance of different CQDs/metal oxide composites based on WRN.

Metal Source	Carbon Source of CQDs	Light Source	Pollutant	Pollutant Concentration	Photocatalyst Dosage (g/L)	Irradiation Times (min)	Degradation Rate (%)	Reference
Waste IOS	WRN	Purple light lamp (20 W, wavelength: 405 nm)	methylene blue tetracycline	20 mg/L 20 mg/L	2 2	480 320	99.30 98.21	This work
Commercial TiO_2	WRN	Purple light lamp (20 W, wavelength: 405 nm)	methylene blue	20 mg/L	4	80	99.87	[44]
Commercial ZnO	WRN	Purple light lamp (20 W, wavelength: 405 nm)	methylene blue tetracycline	20 mg/L 20 mg/L	2 2	10 10	98.88 98.21	[45]

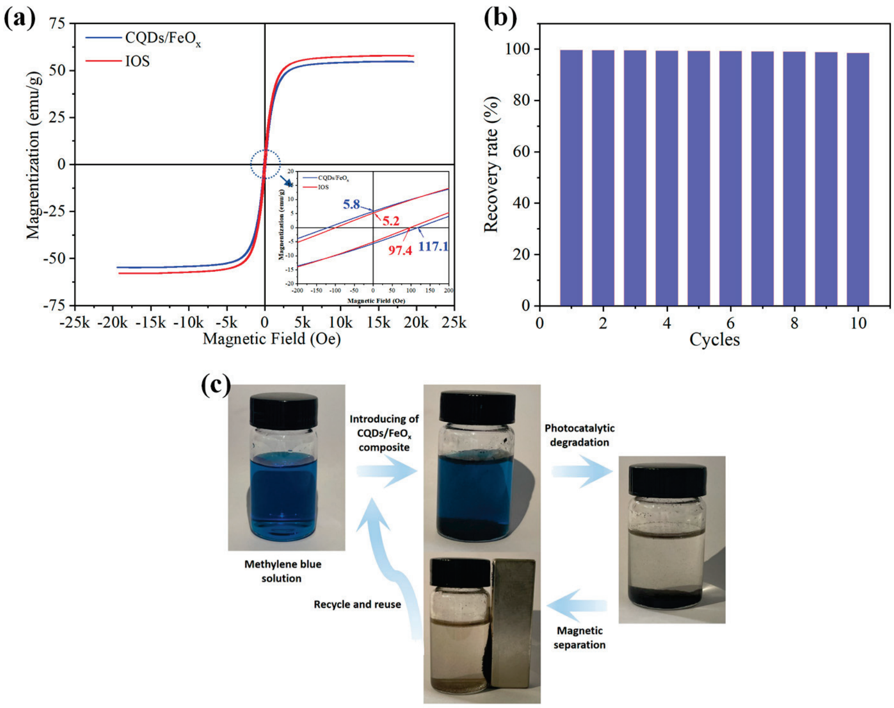

Figure 8. (**a**) Magnetization curves of IOS and CQDs/FeO$_x$ composite (CQDs/FeO$_x$–3 sample); (**b**) Mass recovery rate of CQDs/FeO$_x$ composite (CQDs/FeO$_x$–3 sample) across varying photocatalytic cycles; (**c**) Schematic illustration of the recycle and reuse of CQDs/FeO$_x$ composite using magnetic separation.

As depicted in Figure 8b,c, the magnetic properties of the CQDs/FeO$_x$ composite material enable efficient and convenient recyclability in photocatalytic applications. Following the photocatalytic process, the CQDs/FeO$_x$ composite can be effortlessly separated using a magnetic field, achieving a mass recovery rate of 99.62% after the initial photocatalytic cycle and 98.45% after ten cycles of photocatalysis. Additionally, iron oxide photocatalysts have demonstrated excellent environmental compatibility, with minimal toxicity to fish and algae [56–58]. Consequently, the resulting CQDs/FeO$_x$ photocatalyst holds significant promise for large-scale industrial water purification.

3.4. Photocatalytic Mechanism of CQDs/FeO$_x$ Composites

To delve deeper into the photocatalytic mechanism of the resulting CQDs/FeO$_x$ composite, the UV-VIS diffuse reflectance spectra of both the FeO$_x$ and the CQDs/FeO$_x$ composite are illustrated in Figure 9a. Evidently, even after calcination at 300 °C, the main energy absorption region of the FeO$_x$ inorganic phase was in the ultraviolet region, with almost no absorption in the visible wavelength range above 380 nm. In contrast, the CQDs/FeO$_x$ composite material exhibited strong absorption throughout the entire visible light region, indicating that the introduction of CQDs enabled the composite material to utilize the energy in the visible light region more effectively, thereby generating more electron-hole pairs. Moreover, the determination of band gaps for the FeO$_x$ and CQDs/FeO$_x$ samples was performed through the application of the Tauc plot method [59,60], as depicted in Figure 9b. The band gap of the FeO$_x$ was 2.17 eV, but after introducing CQDs, the band gap of the CQDs/FeO$_x$ composite material was further reduced to 1.40 eV. This narrower band gap allowed for more the effective utilization of energy in the visible light region, significantly promoting electron transitions and enhancing the photocatalytic degradation performance.

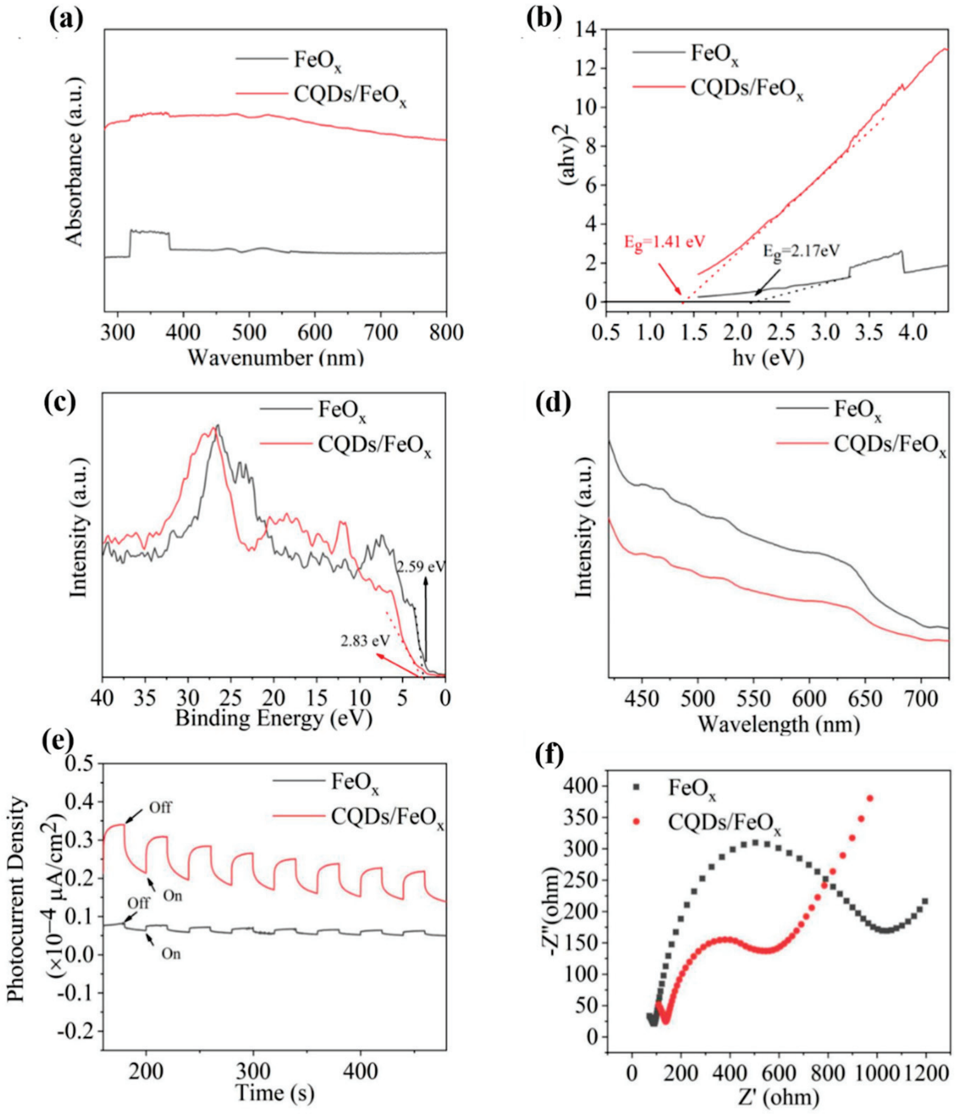

Figure 9. The UV-vis absorption spectra (**a**), Tauc plot curves (**b**), VB XPS spectra (**c**), PL spectra (**d**), PCR (**e**) and EIS (**f**) of the CQDs/FeO$_x$ composite and FeO$_x$.

The valence band (VB) potentials of the CQDs/FeO$_x$ composite and FeO$_x$ powder are determined using XPS valence spectra. As shown in Figure 9c, due to the presence of Fe_2O_3, the VB potential of the FeO$_x$ powder was 2.59 eV, which was more positive than $E^0(\cdot OH, H^+/H_2O)$ (2.38 eV vs. NHE). This suggested that the FeO$_x$ powder could oxidize water to generate hydroxyl radical (·OH). However, the conduction band (CB) potential ($E_{CB} = E_{VB} - E_g$) of the FeO$_x$ was determined to be 0.42 eV, which was more positive than the standard electrode potential $E^0(O_2, H^+/\cdot O_2H)$ for superoxide radicals (−0.046 eV vs. NHE). This indicated that the FeO$_x$ powder could not reduce oxygen in water to produce superoxide radical ($O_2{}^{\cdot-}$). On the other hand, the introduction of CQDs raised the VB potential of the CQDs/FeO$_x$ composite material to 2.83 eV, enabling better oxidation of water to form photocatalytically active hydroxyl radical. Combining its own band gap (1.40 eV) and the band gap of CQDs (2.14 eV), the CB potential was calculated to be −0.08 eV, which was lower than $E^0(O_2, H^+/\cdot O_2H)$ for superoxide radicals (−0.046 eV vs. NHE). This indicated that the CQDs/FeO$_x$ composite material could reduce oxygen in water to generate photocatalytically active superoxide radical.

The photoluminescence emission profiles of both the CQDs/FeO$_x$ composite material and FeO$_x$ are presented in Figure 9d. The fluorescence emission intensity exhibited by the CQDs/FeO$_x$ composite material was notably subdued in comparison to that of the

FeO_x. This observation implies that the incorporation of CQDs could proficiently curtail the recombination of photogenerated electron-hole pairs, thereby significantly contributing to the enhancement of the photocatalytic degradation efficacy. The enhanced mechanism of the CQDs/FeO_x composite material on the catalytic performance of the FeO_x was also demonstrated through transient photocurrent response (PCR) under visible light irradiation and electrochemical impedance spectra (EIS). As shown in Figure 9e, under purple light illumination, the photocurrent intensity of the CQDs/FeO_x composite material was approximately 11 times that of the FeO_x without CQDs, indicating that the CQDs/FeO_x composite could achieve a more efficient interface charge transfer and more effective electron-hole pair separation. The lower probability of photogenerated electron-hole recombination resulted in a significant improvement in the photocatalytic degradation performance. Additionally, the Nyquist plot of the CQDs/FeO_x composite displayed a smaller semicircle diameter than that of the FeO_x powder, indicating that the resulting CQDs/FeO_x composite exhibited lower charge transfer resistance than the FeO_x powder. This ensured a more efficient interface charge transfer and more effective electron-hole pair separation, consistent with the photocurrent analysis results (see Figure 9f).

The impacts of distinct quenching agents (EDTA–2Na, BQ and IPA) on the photodegradation process of methylene blue are elucidated in Figure 10a,b. Notably, the introduction of EDTA–2Na marginally curtailed the photocatalytic degradation efficacy of the CQDs/FeO_x composite material, yielding a photocatalytic efficiency of 93.44% in comparison to the absence of quenching agents. This observation underscores that photogenerated holes (h+) played a minor role and were not the primary drivers of the photocatalytic activity. In contrast, the incorporation of BQ or IPA substantially impeded the degradation efficiency, yielding photocatalytic efficiencies of 40.75% and 60.15%, respectively, as opposed to the scenario without quenching agents. This phenomenon implies that both superoxide radicals ($O_2^{\cdot-}$) and hydroxyl radicals (·OH) stood as the predominant active species in the photocatalytic degradation mechanism, with $O_2^{\cdot-}$ playing a more pronounced role. Furthermore, using DMPO as a radical trapping agent, electron spin resonance spectroscopy (ESR) was carried out to study the active oxygen species generated by the CQDs/FeO_x composite and FeO_x. As shown in Figure 10c–f, the addition of the CQDs/FeO_x composite resulted in strong characteristic peaks of both superoxide radical ($O_2^{\cdot-}$) and hydroxyl radical (·OH). This indicates that the CQDs/FeO_x composite material could reduce adsorbed O_2 to form superoxide radical ($O_2^{\cdot-}$) and oxidize adsorbed H_2O to form hydroxyl radical (·OH) under light irradiation. In contrast, under the same test conditions, the FeO_x powder could not generate superoxide radical ($O_2^{\cdot-}$) effectively, while its signal of hydroxyl radicals was weak.

As shown in Figure 10g, the possible photocatalytic mechanism of the CQDs/FeO_x composite material was similar to that of the CQDs/TiO_2 [44] and CQDs/ZnO [45] composites in our previous report. Upon exposure to visible light, the CQDs/FeO_x composite undergoes a dynamic process: the CQDs become readily excited by photogenerated electrons situated in the conduction band (CB), leaving behind holes in the valence band (VB). This excitation triggers rapid spatial electron transfer between the CQDs and FeO_x particles, effectively suppressing recombination and yielding the enhanced separation of electron-hole pairs. As a result, photogenerated electrons amass in the CB of the CQDs, while the holes populate the VB of FeO_x, with each entity primed for their distinct roles in photocatalytic reactions. Photogenerated holes engage with H_2O to yield a profusion of ·OH radicals, while photogenerated electrons react with O_2, leading to an abundant production of $O_2^{\cdot-}$ radicals. These generated $O_2^{\cdot-}$ and ·OH radicals collectively orchestrate the degradation of diverse organic pollutants, thereby showcasing exceptional prowess in the realm of photocatalytic degradation activity.

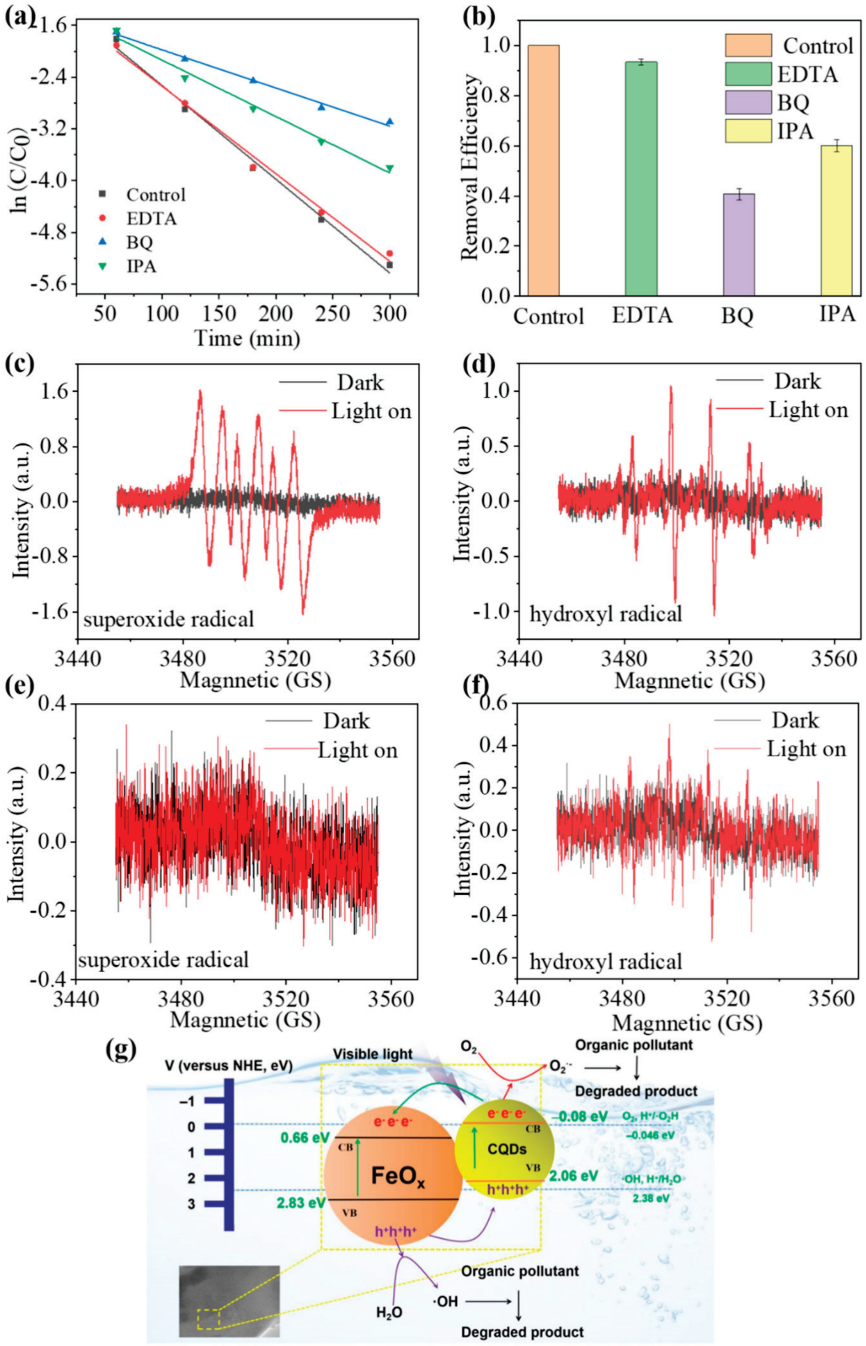

Figure 10. (**a**,**b**) Impact of various quenching agents (EDTA–2Na, BQ or IBA) on the photodegradation of methylene blue under 405 nm purple light. (**c**,**d**) ESR spectra of the CQDs/FeO_x composite in methanol (**c**) and water (**d**) using DMPO as a radical trapping agent. (**e**,**f**) ESR spectra of FeO_x in methanol (**e**) and water (**f**) using DMPO as a radical trapping agent. (**g**) Diagram illustrating the photocatalytic mechanism of the CQDs/FeO_x composite.

4. Conclusions

In this study, we successfully synthesized low-cost CQDs/FeO_x composites by combining waste rice noodle (WRN) and iron oxide scale (IOS) and assessed their photocatalytic performance. The key steps in our synthesis strategy were identified: first, calcining IOS in an air atmosphere to enhance the photocatalytically active α-Fe_2O_3 content; second, incorporating WRN-based CQDs into FeO_x to enhance the electron-hole pair separation, leading to increased O_2 reduction and H_2O oxidation. This significantly improved the photocatalytic performance. The resulting CQDs/FeO_x composites efficiently degraded various organic pollutants under purple light irradiation and had superior magnetic properties, allowing for easy separation and reuse.

Our CQDs/FeO_x composite achieved the 100% conversion of WRN and IOS waste into high-value functional materials without additional synthetic additives. Compared to other reported photocatalytic composites, such as the CQDs/TiO_2 and CQDs/ZnO from our previous work and other CQDs/iron oxide composites using synthetic reagents, our CQDs/FeO_x composite is more cost-effective, environmentally friendly, and sustainable. Its magnetic properties enable rapid separation and efficient reuse, making it a promising candidate for large-scale, low-cost photocatalytic water purification with commercial potential. Furthermore, our approach to transform WRN and IOS into a CQDs/FeO_x composite opens new possibilities for the combined utilization of waste.

Supplementary Materials: The following supporting information can be downloaded at: https://www.mdpi.com/article/10.3390/nano13182506/s1. S1: General characterization; S2: Measurement of photocatalytic performance; Figure S1: The particle size distribution; Figure S2 Comparative images of photocatalytic degradation of methylene blue; Figures S3–S6: The kinetic fitting of photocatalytic degradation; Figure S7: The emission spectrum of the 405 nm purple light lamp; Tables S1 to S2: The kinetic parameters of photocatalytic degradation.

Author Contributions: Conceptualization, methodology and writing (original draft preparation): W.Y.; Software: Q.L.; Investigation: X.J.; Resources: G.D.; Formal Analysis: M.L.; Data curation: P.W.; Writing (review and editing), project administration, funding acquisition and supervision: S.C. All authors have read and agreed to the published version of the manuscript.

Funding: This work was supported by grants from the National Nature Science Foundation of China (No. 51763007) and Guangxi Natural Science Foundation Program (No. 2015GXNSFBA139033).

Institutional Review Board Statement: Not applicable.

Informed Consent Statement: Not applicable.

Data Availability Statement: Not applicable.

Conflicts of Interest: The authors declare no conflict of interest.

Abbreviations

WRN	Waste rice noodle
IOS	Iron oxide scale
CQDs	Carbon quantum dots
Symbols	
CQDs/FeO_x-x	Samples of CQDs/FeO_x composites with different calcination temperatures (x = 1, 2, 3, 4, 5) and different carbon contents (x = 3, 6, 7)

References

1. Zong, X.; Wang, L. Ion-exchangeable semiconductor materials for visible light-induced photocatalysis. *J. Photochem. Photobiol. C Photochem. Rev.* **2014**, *18*, 32–49. [CrossRef]
2. Xia, G.M. Interdiffusion in group IV semiconductor material systems: Applications, research methods and discoveries. *Sci. Bull.* **2019**, *64*, 1436–1455. [CrossRef] [PubMed]
3. Guo, Y.; Xu, Z.; Curto, A.G.; Zeng, Y.-J.; Van Thourhout, D. Plasmonic semiconductors: Materials, tunability and applications. *Prog. Mater. Sci.* **2023**, *138*, 101158. [CrossRef]
4. Dharani, S.; Vadivel, S.; Gnanasekaran, L.; Rajendran, S. S-scheme heterojunction photocatalysts for hydrogen production: Current progress and future prospects. *Fuel* **2023**, *349*, 128688. [CrossRef]
5. Wang, J.; Wang, Z.; Dai, K.; Zhang, J. Review on inorganic–organic S-scheme photocatalysts. *J. Mater. Sci. Technol.* **2023**, *165*, 187–218. [CrossRef]
6. Ruziwa, D.T.; Oluwalana, A.E.; Mupa, M.; Meili, L.; Selvasembian, R.; Nindi, M.M.; Sillanpaa, M.; Gwenzi, W.; Chaukura, N. Pharmaceuticals in wastewater and their photocatalytic degradation using nano-enabled photocatalysts. *J. Water Process Eng.* **2023**, *54*, 103880. [CrossRef]

7. Yue, C.; Zhu, L.; Qiu, Y.; Du, Z.; Qiu, J.; Liu, F.; Wang, F. Recent advances of plasmonic elemental Bi based photocatalysts in environmental remediation and energy conversion. *J. Clean. Prod.* **2023**, *392*, 136017. [CrossRef]
8. Noureen, L.; Wang, Q.; Humayun, M.; Shah, W.A.; Xu, Q.; Wang, X. Recent advances in structural engineering of photocatalysts for environmental remediation. *Environ. Res.* **2023**, *219*, 115084. [CrossRef]
9. Shubha, J.P.; Roopashree, B.; Patil, R.C.; Khan, M.; Shaik, M.R.; Alaqarbeh, M.; Alwarthan, A.; Mahmoud Karami, A.; Adil, S.F. Facile synthesis of ZnO/CuO/Eu heterostructure photocatalyst for the degradation of industrial effluent. *Arab. J. Chem.* **2023**, *16*, 104547. [CrossRef]
10. Wang, M.; Xu, Z.; Qi, Z.; Cai, Y.; Li, G.; Choi, W.; An, T. Repeated photocatalytic inactivation of *E. coli* by UV + Ni foam@TiO_2: Performance and photocatalyst deactivation. *Chem. Eng. J.* **2023**, *468*, 143680. [CrossRef]
11. Lu, Y.; Chen, R.; Wu, F.; Gan, W.; Zhao, Z.; Chen, L.; Zhang, M.; Sun, Z. A novel SiP/TiO_2 S-scheme heterojunction photocatalyst for efficient degradation of norfloxacin. *Sep. Purif. Technol.* **2023**, *324*, 124572. [CrossRef]
12. Sadikin, S.N.; Ridwan, J.; Umar, M.I.A.; Raub, A.A.M.; Yunas, J.; Hamzah, A.A.; Dahlan, D.; Rahman, M.Y.A.; Umar, A.A. Photocatalytic activity and stability properties of porous TiO_2 film as photocatalyst for methylene blue and methylene orange degradation. *Int. J. Electrochem. Sci.* **2023**, *18*, 100246. [CrossRef]
13. Bi, T.; Du, Z.; Chen, S.; He, H.; Shen, X.; Fu, Y. Preparation of flower-like ZnO photocatalyst with oxygen vacancy to enhance the photocatalytic degradation of methyl orange. *Appl. Surf. Sci.* **2023**, *614*, 156240. [CrossRef]
14. Sharma, K.; Raizada, P.; Hasija, V.; Singh, P.; Bajpai, A.; Nguyen, V.-H.; Rangabhashiyam, S.; Kumar, P.; Nadda, A.K.; Kim, S.Y.; et al. ZnS-based quantum dots as photocatalysts for water purification. *J. Water Process Eng.* **2021**, *43*, 102217. [CrossRef]
15. Ullah, H.; Haneef, Z.; Ahmad, A.; Butler, I.S.; Nasir Dara, R.; Rehman, Z. MoS_2 and CdS photocatalysts for water decontamination: A review. *Inorg. Chem. Commun.* **2023**, *153*, 110775. [CrossRef]
16. López, J.; Rey, A.; Viñuelas-Zahinos, E.; Álvarez, P.M. Preparation of a new green magnetic Fe_3O_4 @TiO_2-P25 photocatalyst for solar advanced oxidation processes in water. *J. Environ. Chem. Eng.* **2023**, *11*, 109999. [CrossRef]
17. Waheed, I.F.; Hamad, M.A.; Jasim, K.A.; Gesquiere, A.J. Degradation of methylene blue using a novel magnetic $CuNiFe_2O_4$/g-C_3N_4 nanocomposite as heterojunction photocatalyst. *Diam. Relat. Mater.* **2023**, *133*, 109716. [CrossRef]
18. Jiang, Z.; Zou, Y.; Hao, Y.; Xu, L.; Liu, C.; Su, H.; Gong, S. Magnetic recyclable ZnO/$SrFe_{12}O_{19}$ photocatalyst for effective photodegradation of rhodamine B under simulated sunlight. *Int. J. Hydrog. Energy* **2022**, *47*, 34387–34396. [CrossRef]
19. Rafieezadeh, M.; Kianfar, A.H. Fabrication of heterojunction ternary Fe_3O_4/TiO_2/$CoMoO_4$ as a magnetic photocatalyst for organic dyes degradation under sunlight irradiation. *J. Photochem. Photobiol. A Chem.* **2022**, *423*, 113596. [CrossRef]
20. Dulyasucharit, R.; Wongkasemjit, S.; Nanan, S.; Intharaksa, O.; Masingboon, C. Magnetic Fe_3O_4/$Bi_2O_2(OH)(NO_3)$ as a sunlight-driven photocatalyst for rhodamine B degradation. *J. Solid State Chem.* **2023**, *319*, 123784. [CrossRef]
21. Li, X.; Qiu, Y.; Zhu, Z.; Chen, T.; Zhang, H.; Yin, D. Construction of magnetically separable dual Z-scheme g-C_3N_4/α-Fe_2O_3/Bi_3TaO_7 photocatalyst for effective degradation of ciprofloxacin under visible light. *Chem. Eng. J.* **2022**, *440*, 135840. [CrossRef]
22. Mohan, H.; Ramasamy, M.; Ramalingam, V.; Natesan, K.; Duraisamy, M.; Venkatachalam, J.; Shin, T.; Seralathan, K.K. Enhanced visible light-driven photocatalysis of iron-oxide/titania composite: Norfloxacin degradation mechanism and toxicity study. *J. Hazard. Mater.* **2021**, *412*, 125330. [CrossRef] [PubMed]
23. Subha, N.; Mahalakshmi, M.; Monika, S.; Senthil Kumar, P.; Preethi, V.; Vaishnavi, G.; Rajabhuvaneswari, A. Heterostructured γ-Fe_2O_3/$FeTiO_3$ magnetic nanocomposite: An efficient visible-light-driven photocatalyst for the degradation of organic dye. *Chemosphere* **2022**, *306*, 135631. [CrossRef] [PubMed]
24. Hayati, F.; Moradi, S.; Farshineh Saei, S.; Madani, Z.; Giannakis, S.; Isari, A.A.; Kakavandi, B. A novel, Z-scheme ZnO@AC@FeO photocatalyst, suitable for the intensification of photo-mediated peroxymonosulfate activation: Performance, reactivity and bisphenol A degradation pathways. *J. Environ. Manag.* **2022**, *321*, 115851. [CrossRef] [PubMed]
25. Mishra, S.; Acharya, R. Recent updates in modification strategies for escalated performance of Graphene/MFe_2O_4 heterostructured photocatalysts towards energy and environmental applications. *J. Alloys Compd.* **2023**, *960*, 170576. [CrossRef]
26. Sanei, A.; Dashtian, K.; Yousefi Seyf, J.; Seidi, F.; Kolvari, E. Biomass derived reduced-graphene-oxide supported α-Fe_2O_3/ZnO S-scheme heterostructure: Robust photocatalytic wastewater remediation. *J. Environ. Manag.* **2023**, *332*, 117377. [CrossRef]
27. Liu, Z.; Luo, M.; Yuan, S.; Meng, L.; Ding, W.; Su, S.; Cao, Y.; Wang, Y.; Li, X. Boron-doped graphene quantum dot/bismuth molybdate composite photocatalysts for efficient photocatalytic nitrogen fixation reactions. *J. Colloid Interface Sci.* **2023**, *650*, 1301–1311. [CrossRef]
28. Mohamed, M.M.; Bayoumy, W.A.; Goher, M.E.; Abdo, M.H.; Mansour El-Ashkar, T.Y. Optimization of α-Fe_2O_3@Fe_3O_4 incorporated N-TiO_2 as super effective photocatalysts under visible light irradiation. *Appl. Surf. Sci.* **2017**, *412*, 668–682. [CrossRef]
29. Sun, A.-C. Synthesis of magnetic carbon nanodots for recyclable photocatalytic degradation of organic compounds in visible light. *Adv. Powder Technol.* **2018**, *29*, 719–725. [CrossRef]
30. Li, Y.; Xiang, W.; Zhou, T.; Huang, M.; Wang, C.; Wu, X.; Mao, J.; Wang, P. Visible light induced efficient activation of persulfate by a carbon quantum dots (CQDs) modified g-Fe_2O_3 catalyst. *Chin. Chem. Lett.* **2020**, *31*, 2757–2761. [CrossRef]
31. Huang, S.; Zhang, Q.; Liu, P.; Ma, S.; Xie, B.; Yang, K.; Zhao, Y. Novel up-conversion carbon quantum dots/α-FeOOH nanohybrids eliminate tetracycline and its related drug resistance in visible-light responsive Fenton system. *Appl. Catal. B Environ.* **2020**, *263*, 118336. [CrossRef]

32. Mmelesi, O.K.; Ammar-Merah, S.; Nkambule, T.T.I.; Kefeni, K.K.; Kuvarega, A.T. Synergistic role of N-doped carbon quantum dots on Zn-doped cobalt ferrite (N-CQDs/ZnCF) for the enhanced photodegradation of oxytetracycline under visible light. *Mater. Sci. Eng. B* **2023**, *294*, 116538. [CrossRef]
33. Wu, X.; Wang, X.; Lynch, I.; Guo, Z.; Zhang, P.; Wu, L.; Ning, P.; Ren, N. Exceptional photo-elimination of antibiotic by a novel Z-scheme heterojunction catalyst composed of nanoscale zero valent iron embedded with carbon quantum dots (CQDs)-black TiO_2. *J. Hazard. Mater.* **2023**, *304*, 132323. [CrossRef] [PubMed]
34. Zhang, J.; Liu, R.; Kuang, M.; Xie, S.; Wang, J.; Ji, Z. Constructing CQDs/MIL-101(Fe)/g-C_3N_4 photocatalyst and its enhancement to the photocatalytic activity. *Mater. Lett.* **2023**, *167*, 135004. [CrossRef]
35. Li, Y.; Jin, Y.; Li, J.; Chen, Y.; Gong, Y.; Li, Y.; Zhang, J. Current situation and development of kitchen waste treatment in China. *Procedia Environ. Sci.* **2016**, *31*, 40–49. [CrossRef]
36. Deng, Y.; Chen, X.; Adam, N.G.T.S.; Xu, J. A multi-objective optimization approach for clean treatment of food waste from an economic-environmental-social perspective: A case study from China. *J. Clean. Prod.* **2022**, *357*, 131559. [CrossRef]
37. Farahdiba, A.U.; Warmadewanthi, I.D.A.A.; Fransiscus, Y.; Rosyidah, E.; Hermana, J.; Yuniarto, A. The present and proposed sustainable food waste treatment technology in Indonesia: A review. *Environ. Technol. Innov.* **2023**, *32*, 103256. [CrossRef]
38. Wang, B.; Ma, J.; Zhang, L.; Su, Y.; Xie, Y.; Ahmad, Z.; Xie, B. The synergistic strategy and microbial ecology of the anaerobic co-digestion of food waste under the regulation of domestic garbage classification in China. *Sci. Total Environ.* **2021**, *765*, 144632. [CrossRef]
39. Gao, X.; Yang, F.; Yan, Z.; Zhao, J.; Li, S.; Nghiem, L.; Li, G.; Luo, W. Humification and maturation of kitchen waste during indoor composting by individual households. *Sci. Total Environ.* **2022**, *814*, 152509. [CrossRef]
40. Li, P.; Ma, J.; Li, L.; Han, Y.; Zheng, T.; Wang, Y.; Chai, F.; Liu, J. Emission behavior and impact assessment of gaseous volatile compounds in two typical rural domestic waste landfills. *J. Environ. Manag.* **2023**, *325*, 116659. [CrossRef]
41. Liu, B.; Han, Z.; Liang, X. Dioxin emissions from municipal solid waste incineration in the context of waste classification policy. *Atmos. Pollut. Res.* **2023**, *14*, 101842. [CrossRef]
42. Mohanakrishna, G.; Sneha, N.P.; Rafi, S.M.; Sarkar, O. Dark fermentative hydrogen production: Potential of food waste as future energy needs. *Sci. Total Environ.* **2023**, *888*, 163801. [CrossRef]
43. Kumar, V.; Sharma, N.; Umesh, M.; Selvaraj, M.; Al-Shehri, B.M.; Chakraborty, P.; Duhan, L.; Sharma, S.; Pasrija, R.; Awasthi, M.K.; et al. Emerging challenges for the agro-industrial food waste utilization: A review on food waste biorefinery. *Bioresour. Technol.* **2022**, *362*, 127790. [CrossRef]
44. Jin, X.; Che, R.; Yang, J.; Liu, Y.; Chen, X.; Jiang, Y.; Liang, J.; Chen, S.; Su, H. Activated Carbon and Carbon Quantum Dots/Titanium Dioxide Composite Based on Waste Rice Noodles: Simultaneous Synthesis and Application in Water Pollution Control. *Nanomaterials* **2022**, *12*, 472. [CrossRef] [PubMed]
45. Jin, X.Y.; Ying, W.Y.; Che, R.J.; Xiao, P.; Zhou, Y.Q.; Liu, Y.; Liu, M.Y.; Chen, S.P. CQDs/ZnO composites based on waste rice noodles: Preparation and photocatalytic capability. *RSC Adv.* **2022**, *12*, 23692–23703. [CrossRef] [PubMed]
46. Jjagwe, J.; Olupot, P.W.; Carrara, S. Iron oxide nanoparticles/nanocomposites derived from steel and iron wastes for water treatment: A review. *J. Environ. Manag.* **2023**, *343*, 118236. [CrossRef] [PubMed]
47. Yu, J.; Xu, R.; Zhang, J.; Zheng, A. A review on reduction technology of air pollutant in current China's iron and steel industry. *J. Clean. Prod.* **2023**, *414*, 137659. [CrossRef]
48. Hao, J.; Dou, Z.-H.; Zhang, T.-A.; Jiang, B.-C.; Wang, K.; Wan, X.-Y. Manufacture of wear-resistant cast iron and copper-bearing antibacterial stainless steel from molten copper slag via vortex smelting reduction. *J. Clean. Prod.* **2022**, *375*, 134202. [CrossRef]
49. Rai, S.K.; Mukherjee, A.K. Optimization for production of liquid nitrogen fertilizer from the degradation of chicken feather by iron-oxide (Fe_3O_4) magnetic nanoparticles coupled β-keratinase. *Biocatal. Agric. Biotechnol.* **2015**, *4*, 632–644. [CrossRef]
50. Cui, F.; Zhou, S.; Wang, D.; Tan, X.; Li, Q.; Li, T.; Li, J. Preparation and antibacterial properties of amino functionalized antibacterial carbon quantum dots. *Packag. Eng.* **2023**, *44*, 121–129.
51. Wang, L.; Lu, T.; Ruan, F.; Deng, D.; Xu, S. Synthesis of photoluminescent carbon nanoparticlesby hydrothermal method. *Chin. J. Lumin.* **2014**, *35*, 706–709. [CrossRef]
52. Graham, M.J.; Hussey, R.J. The growth and structure of oxide films on Fe. I. oxidation of (001) and (112) Fe at 200–300 °C. *Oxid. Met.* **1981**, *15*, 407–420. [CrossRef]
53. Chen, R.Y.; Yuen, W.Y.D. Review of the high-temperature oxidation of iron and carbon steels in air or oxygen. *Oxid. Met.* **2003**, *59*, 433–468. [CrossRef]
54. Atkinson, A. Transport processes during the growth of oxide films at elevated temperature. *Rev. Mod. Phys.* **1985**, *57*, 437–470. [CrossRef]
55. Guo, P.; Shi, W.; Wang, H.; Han, M.; Li, H.; Hui, H.; Liu, Y.; Kang, Z. Facile fabrication of a CoO/g-C_3N_4 p–n heterojunction with enhanced photocatalytic activity and stability for tetracycline degradation under visible light. *Catal. Sci. Technol.* **2017**, *7*, 3225–3331. [CrossRef]
56. Swedha, M.; Okla, M.; Abdel-Maksoud, M.; Kokilavani, S.; Kamwilaisak, K.; Sudheer Khan, S. Photo-Fenton system Fe_3O_4/$NiCu_2S_4$ QDs towards bromoxynil and cefixime degradation: A realistic approach. *Surf. Interfaces* **2023**, *38*, 102764. [CrossRef]

57. Harikumar, B.; Okla, M.; Kokilavani, S.; Almunqedhi, B.; Alshuwaish, R.; Abdel-Maksoud, M.; El-Tayeb, M.; Sudheer Khan, S. Insights into oxygen defect enriched and non-metal dopant co modulated Fe_3O_4 nanospheres embedded WO_3 nanorods for ameliorated photodegradation of doxycycline, Cr(VI) reduction and its genotoxicity. *J. Clean. Prod.* **2023**, *398*, 136549. [CrossRef]
58. Alexpandi, R.; Abirami, G.; Murugesan, B.; Durgadevi, R.; Swasthikka, R.P.; Cai, Y.; Ragupathi, T.; Ravi, A.V. Tocopherol-assisted magnetic Ag-Fe_3O_4-TiO_2 nanocomposite for photocatalytic bacterial-inactivation with elucidation of mechanism and its hazardous level assessment with zebrafish model. *J. Hazard. Mater.* **2023**, *442*, 130044. [CrossRef]
59. Jubu, P.R.; Yam, F.K.; Igba, V.M.; Beh, K.P. Tauc-plot scale and extrapolation effect on bandgap estimation from UV–vis–NIR data–A case study of β-Ga_2O_3. *J. Solid State Chem.* **2020**, *290*, 121576. [CrossRef]
60. Jubu, P.R.; Obaseki, O.S.; Nathan-Abutu, A.; Yam, F.K.; Yusof, Y.; Ochang, M.B. Dispensability of the conventional Tauc's plot for accurate bandgap determination from UV–vis optical diffuse reflectance data. *Results Opt.* **2022**, *9*, 100273. [CrossRef]

nanomaterials

Article

Effects of Surface Plasmon Coupling on the Color Conversion of an InGaN/GaN Quantum-Well Structure into Colloidal Quantum Dots Inserted into a Nearby Porous Structure

Shaobo Yang [1], His-Yu Feng [1], Yu-Sheng Lin [1], Wei-Cheng Chen [1], Yang Kuo [2] and Chih-Chung (C. C.) Yang [1,*]

[1] Institute of Photonics and Optoelectronics, and Department of Electrical Engineering, National Taiwan University, No. 1, Section 4, Roosevelt Road, Taipei 10617, Taiwan
[2] Department of Energy and Refrigerating Air-Conditioning Engineering, Tungnan University, 152 Beishen Road, Section 3, New Taipei City 22202, Taiwan
* Correspondence: ccycc@ntu.edu.tw

Abstract: To further enhance the color conversion from a quantum-well (QW) structure into a color-converting colloidal quantum dot (QD) through Förster resonance energy transfer (FRET), we designed and implemented a device structure with QDs inserted into a GaN nano-porous structure near the QWs to gain the advantageous nanoscale-cavity effect. Additionally, surface Ag nanoparticles were deposited for inducing surface plasmon (SP) coupling with the QW structure. Based on the measurements of time-resolved and continuous-wave photoluminescence spectroscopies, the FRET efficiency from QW into QD is enhanced through the SP coupling. In particular, performance in the polarization perpendicular to the essentially extended direction of the fabricated pores in the nano-porous structure is more strongly enhanced when compared with the other linear polarization. A numerical simulation study was undertaken, and showed consistent results with the experimental observations.

Keywords: surface plasmon coupling; color conversion; colloidal quantum dot; Förster resonance energy transfer; porous structure; nanoscale-cavity effect

1. Introduction

Photon color conversion is a useful process for color display application. The performance of such a process relies on the efficiencies of two mechanisms, including the energy transfer from the energy donor into the acceptor and the acceptor emission. If the distance between the donor and acceptor is smaller than several tens nm, the Förster resonance energy transfer (FRET) can lead to a high efficiency of energy transfer [1]. Based on the electromagnetic theory, FRET can be regarded as a process of the acceptor absorption of the near-field energy produced by the donor [2,3]. In other words, donor energy is effectively transferred into the acceptor without the far-field process of photon emission-absorption. The near field distribution produced by the donor is affected by its surrounding structure. When the donor is placed near a nanoscale cavity, the near field distribution in a certain portion of the cavity can be enhanced [4]. Therefore, by placing the acceptor inside the nanoscale cavity, the energy absorbed by the acceptor or FRET efficiency can be enhanced [4,5]. In such a structure, the emission efficiency of the acceptor can also be increased through the nanoscale-cavity effect. The increased emission efficiency of a light emitter inside a nanoscale cavity is caused by the modification of the near field distribution through the Purcell effect [6], which can enhance the far-field radiated power. Hence, through the nanoscale-cavity effect, either the energy transfer from the donor into acceptor or the acceptor emission efficiency can be enhanced, leading to an improved color conversion process.

Nanomaterials **2023**, *13*, 328. https://doi.org/10.3390/nano13020328

A surface plasmon (SP) resonance on a metal nanostructure can couple with a light emitter to enhance its emission efficiency and to produce strong electromagnetic field distributions around the metal nanostructure and light emitter [7,8]. If the acceptor in a FRET process is placed within such a field distribution produced by the SP-coupled donor, the energy absorbed by the acceptor or the FRET efficiency can be increased [9,10]. However, the SP coupling can also enhance donor emission that reduces the available energy for transferring into the acceptor. Therefore, whether SP coupling can enhance the efficiency of an FRET process depends on the SP coupling condition [11]. If the SP coupling condition can be properly designed, both FRET efficiency and acceptor emission efficiency can be enhanced through SP coupling, leading to an effective color conversion process. In particular, by applying SP coupling to a color conversion system with a nanoscale cavity, the color conversion efficiency can be further enhanced.

In this paper, we studied the behaviors of the color conversion from a blue-emitting InGaN/GaN quantum-well (QW) structure into the emission of a colloidal quantum dot (QD), which is inserted into a GaN porous structure (PS) near the QW structure [12–14], under the condition of SP coupling. Both green-emitting QD (GQD) and red-emitting QDs (RQD) were used in this study. The SP coupling is induced by depositing Ag nanoparticles (NPs) onto the top surface of a sample. The color conversion behaviors were investigated with the measurements of continuous-wave (CW) and time-resolved (TR) photoluminescence (PL) spectroscopies. The results of a simulation study well support the experimentally observed enhancement of color conversion through the SP coupling. In Section 2 of this paper, the sample structures, their fabrication procedures, and the optical measurement methods are described. The optical measurement results are presented in Section 3. The simulation study is reported in Section 4. Further discussions about the results are made in Section 5. Finally, conclusions are drawn in Section 6.

2. Sample Structures, Fabrication Procedures, and Measurement Methods

Figure 1a schematically illustrates the sample structure under study, in which a PS layer of 200 nm in thickness was fabricated in the grown highly Si-doped GaN (n^+-GaN) layer. On the top surface, Ag NPs are deposited for inducing the SP coupling with the QW structure. To prepare such a QW template, first a 200-nm n^+-GaN layer with the Si doping concentration at ~2×10^{19} cm^{-3} was grown on a ~3-μm un-doped GaN (u-GaN) layer, followed by the deposition of a ~50 nm n-GaN layer with the Si doping concentration at ~5×10^{18} cm^{-3}. The growth temperatures for the n^+-GaN, n-GaN, and u-GaN layers are the same at 1040 °C. Then, a 5-period InGaN/GaN QW structure was grown at the temperatures of 695 and 793 °C for the InGaN well layers and GaN barrier layers, respectively. The QW structure was capped by a u-GaN layer of ~30 nm in thickness. At room temperature, the emission peak wavelength of the QW structure lies between 450 and 460 nm. To blue-shift the localized surface plasmon (LSP) resonance feature of the surface Ag NPs such that it is close to the QW emission peak wavelength, a ~5-nm SiO_2 layer was coated onto the top surface before Ag NP deposition [15,16]. GQDs and RQDs were inserted into the nanoscale cavities of the PS layer for studying their emission behaviors. CdZnSeS/ZnS GQDs and RQDs were purchased from Taiwan Nanocrystals Inc. Hsinchu, Taiwan. They are capped with an amphiphilic polymer, i.e., poly(isobutylene-alt-maleic anhydride), and hence are negatively charged with zeta potentials between −40 and −50 mV [17]. Including the capped amphiphilic polymer, the size of a GQD or RQD ranges from 8 through 10 nm. The emission wavelengths of GQD and RQD are ~530 and ~625 nm, respectively.

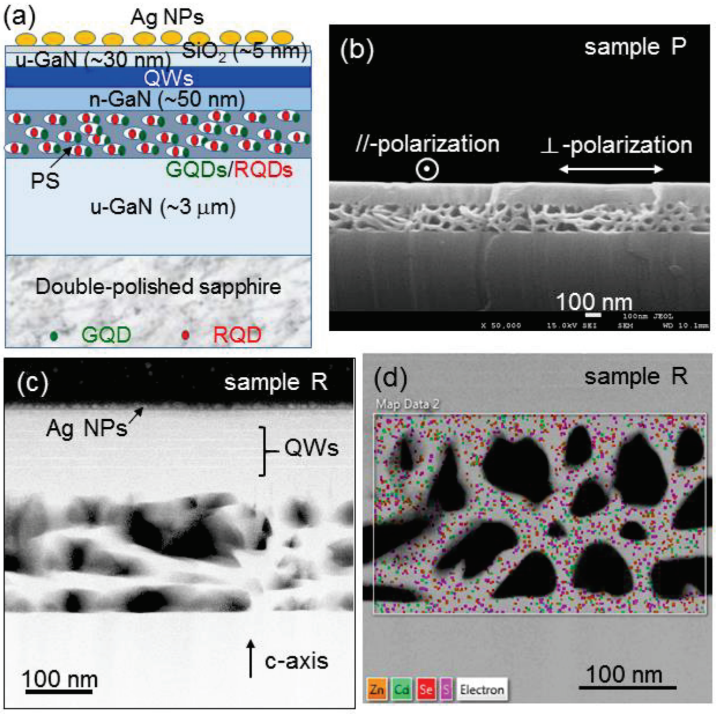

Figure 1. (**a**) Schematic illustration for the sample structure. The PS was fabricated in the grown n$^+$-GaN layer for accommodating GQD and/or RQD. Surface Ag NPs were deposited to induce the SP coupling with the QW structure. (**b**) Cross-sectional SEM image showing the PS in sample P. The directions of the two polarizations are defined in this figure. (**c**) Cross-sectional TEM image of sample R. (**d**) EDX mapping result in a TEM image of sample R showing the distributions of the four composition elements of RQD.

Five samples were prepared for comparing their emission performances, including samples A and P without QD, and samples G, R, and G+R with designated QDs. Without a PS in sample A, surface Ag NPs were deposited for observing the SP coupling effect on QW emission. With a PS and surface Ag NPs in sample P, the results show the SP coupling effect on the QW emission when a nearby PS exists. In samples G, R, and G+R, GQD only, RQD only, and GQD plus RQD, respectively, were inserted into the individual PSs for studying the SP coupling effects of surface Ag NPs on the FRETs from QW into QD and QD emission. The electrochemical etching conditions for fabricating a PS include 15 V in applied voltage, 5 wt% for the HNO$_3$ electrolyte concentration, and 5.5 min for the etching duration. In the etching process, the sample was electrically connected with an indium ball as the anode and a Pt plate was used as the cathode. Figure 1b shows the cross-sectional scanning electron microscopy (SEM) image of the PS in sample P. We can see that the whole n$^+$-GaN layer has been etched to become a PS. The cross-sectional facet in this image is perpendicular to the direction of current injection in the electrochemical process. On the sample top surface, the direction along (perpendicular to) this facet is designated as the perpendicular, i.e., ⊥, (parallel, i.e., //,) polarization in optical measurements because the fabricated nano-pores essentially extend along the direction perpendicular to this facet. Basically, the electrochemical etching path follows the flow direction of injected electric current. Therefore, the pore extension essentially follows the injected current direction. However, because it is difficult to well control the current flow path inside a sample, the PS anisotropy in the lateral dimension is quite weak. Nevertheless, as shown in the following discussions, we can still clearly observe the anisotropic optical properties in a sample with QDs inserted into a PS and/or Ag NPs on the top surface due to the anisotropic nanoscale-cavity effect. It is noted that although the LSP resonance of surface Ag NPs is polarization-independent, the SP coupling is polarization-dependent due to the anisotropic PS in a sample, which results in a polarization-dependent nanoscale-cavity effect.

To insert QDs into a PS, we fabricated a linear array of surface hole of 300 μm in diameter and ~450 nm in depth. After a droplet of the ethanol solution of QD was applied to the sample surface, the solution could flow into the PS through the surface holes. For spreading the QD solution laterally in the PS, the sample was spun at 300 rpm in speed for 30 min. To focus the study on the emission behaviors of the QDs inserted into the subsurface PS, we cleaned the sample's surface with wet cotton swabs to remove the QDs remained on the surface. The sample's surface was then examined with SEM to make sure that it was indeed clean. Figure 1c shows the cross-sectional dark-field transmission electron microscopy (TEM) image of sample R. In this image, above the PS, we can see five bright stripes, which correspond to the five QWs. On the top surface, Ag NPs can be observed. In the PS, the foggy regions correspond to the distributions of QD. Due to the surface coating of the amphiphilic polymer, the particle-like image of a QD becomes blurred in the TEM image. However, the scanning image of energy-dispersive X-ray spectroscopy (EDX) in Figure 1d can prove the distribution of QD in the PS. In this image, the yellow, green, red, and pink dots show the distributions of elements Zn, Cd, Se, and S, respectively.

The surface Ag NPs were fabricated by depositing Ag of 1.8 nm in thickness onto the SiO$_2$-coated sample surface at room temperature. Without a thermal annealing process, the deposited Ag naturally formed an NP distribution on the sample surface, as illustrated with the SEM image (sample P) in the inset of Figure 2. The three surface nano-holes in this SEM image were formed during the electrochemical etching process. These surface nano-holes help in directing the electrolyte into the n$^+$-GaN layer and letting out the gases (N$_2$ and O$_2$) produced during the electrochemical etching process. The main body of Figure 2 shows the normalized transmission spectra of the five samples under study. They were obtained by using the individual transmission spectra before Ag NP deposition as the normalization baselines. Here, the transmission depressions correspond to the LSP resonance features of the surface Ag NPs with the resonance peaks all around 465 nm. In Figure 2, the three vertical dashed lines indicate the emission peak wavelengths of the QW structure, GQD, and RQD. We can see that the LSP resonance peaks are close to the QW emission peak wavelength for producing strong SP coupling with the QW structure. At the GQD emission wavelength, the LSP resonance is still quite strong. However, because the distance between the surface Ag NPs and the GQD distribution in the PS is quite large (>160 nm), their SP coupling is expected to be weak. The fabrication of samples G, R, or G+R followed the procedure of PS fabrication, QD insertion, and then Ag NP deposition.

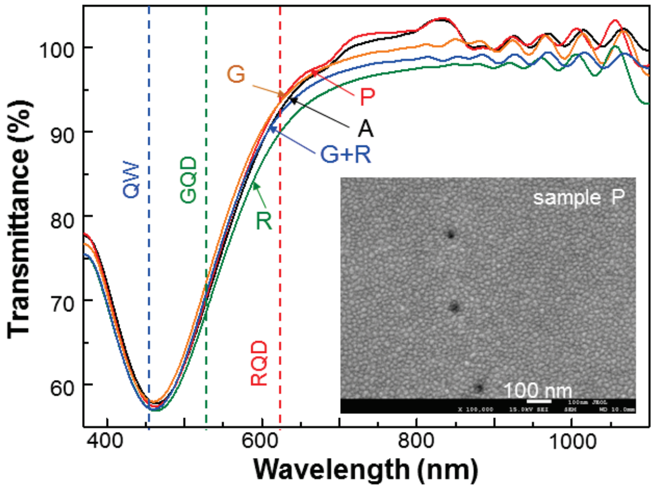

Figure 2. Normalized transmission spectra of the five samples under study after surface Ag NPs were deposited. The three vertical dashed lines indicate the emission peak wavelengths of the QW structure, GQD, and RQD. The inset shows the SEM image of sample P after surface Ag NPs were deposited.

3. Optical Characterization Results

The CWPL measurement was excited by an InGaN laser diode of 405 nm in wavelength and 6 mW in output power. The TRPL measurement was excited by the second-harmonic (390 nm in wavelength and ~1.5 mW in power) of a femtosecond Ti:sapphire laser (MIRA 900, pumped by VERDI-8W, Coherent, USA) with the pulse repetition rate at 76 MHz. The signals were monitored with a photon-counting system (the time-correlated single photon-counting solution delivered by Becker & Hickl). The temporal resolution of this system was higher than 0.1 ns. The method for calibrating the decay time of a PL decay profile has been reported in a previous publication [18]. Figure 3a shows the normalized CWPL spectra of sample A at 10 and 300 K before (labeled by "intrinsic" or "I") and after (labeled by "Ag NP" or "NP") surface Ag NP deposition. The internal quantum efficiency (IQE) of a QW structure is defined as the ratio of the integrated intensity at 300 K over that at a low temperature, i.e., 10 K in this study. The IQEs for sample A before and after Ag NP deposition are also shown in Figure 3a. The IQE is increased from the intrinsic value of 57.8% to 63.8% after Ag NP deposition. The SP coupling indeed enhances the IQE by a significant amount. Figure 3b shows that the results of sample P are similar to those in Figure 3a for sample A. However, one more set of data obtained at the stage after PS fabrication but before Ag NP deposition (labeled by "PS") was added. Here, we can see that after PS fabrication, the PL spectral peaks are blue-shifted at either temperature. As also shown in the figure, the IQE of this sample increases from the intrinsic value of 57.4% to 67.2% after PS fabrication, and then to 69.4% after Ag NP deposition. The IQE increase after PS fabrication is caused by the strain relaxation and hence the weakening of the quantum-confined Stark effect (QCSE) in the QW structure [19]. The weakened QCSE leads to the increase of radiative recombination or IQE and the blue-shift of the emission spectrum. Figure 3c,d show the results of samples G and R, respectively, similar to Figure 3a,b. We can again see that after PS fabrication, the IQE is increased and the emission spectrum is blue-shifted. It is noted that the evaluation for QW IQE based on the PL measurements at 10 and 300 K becomes unreliable after QDs are inserted into the PS of a sample. This is because the inserted QDs absorb the QW emission and distort the measurement of its intensity. The behaviors of the normalized CWPL spectra in sample G+R are similar to those in either sample G or R and are not shown in this paper. Nevertheless, the variation of its IQE will be given later.

Figure 4 shows the normalized blue-light PL decay profiles of samples A and P at different fabrication stages. After PS fabrication in sample P, the PL decay rate significantly increased, which is consistent with the increase of IQE. After Ag NP deposition (labeled by "SP") in sample A, the PL decay rate is also increased that is again consistent with the increase of IQE after SP coupling was introduced. In sample P, after Ag NP deposition, the PL decay rate in either polarization is also enhanced. Although the decay profiles in the two polarizations are close to each other, the decay rate in the ⊥-polarization is slightly higher. Figure 5 shows the normalized blue-light PL decay profiles of sample G+R at different fabrication stages. Here, we can see that after PS fabrication, the decay rate is increased. After QD insertion but before Ag NP deposition (w/o SP), the QW PL decay rate is further increased in either polarization due to the FRET from QW into QD. The PL decay profiles in the two polarizations almost coincide with each other. Then, after Ag NP deposition (SP), the PL decay rate is further increased in either polarization due to SP coupling. With SP coupling, the PL decay profiles in the two polarizations become clearly separated. The decay rate in the ⊥-polarization is higher.

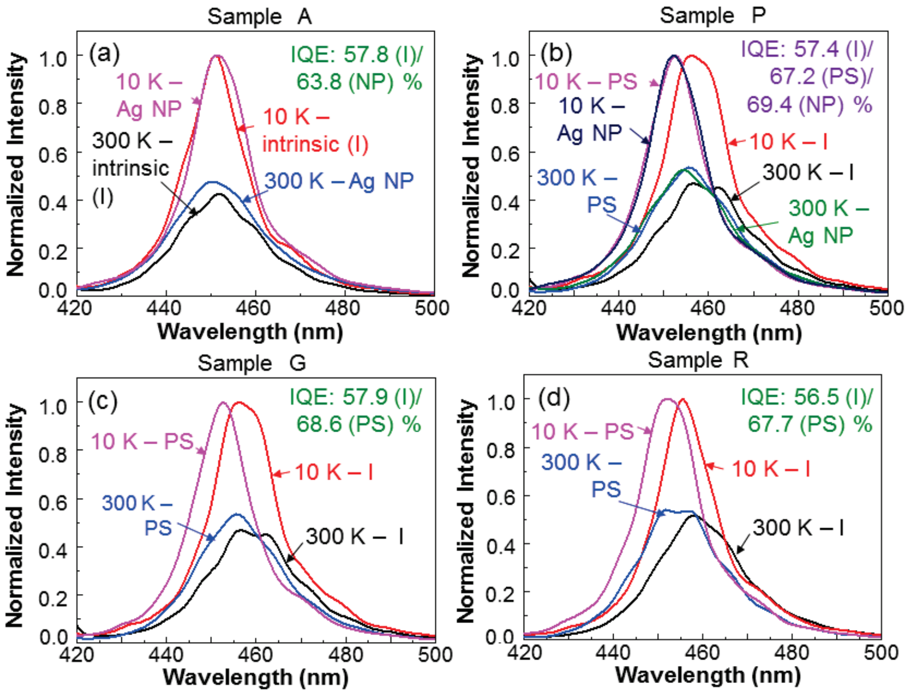

Figure 3. (**a**–**d**): Normalized QW CWPL spectra in different fabrication stages at 10 and 300 K for samples A, P, G, and R, respectively. I: intrinsic condition; PS: after PS fabrication; NP: after surface Ag NP deposition.

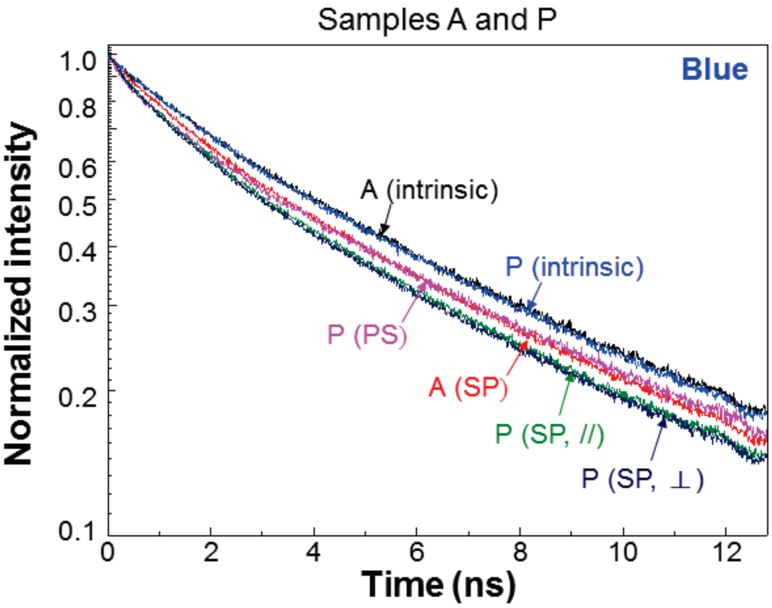

Figure 4. Normalized blue-light PL decay profiles of samples A and P at different fabrication stages. PS: after PS fabrication; SP: after surface Ag NP deposition for inducing SP coupling.

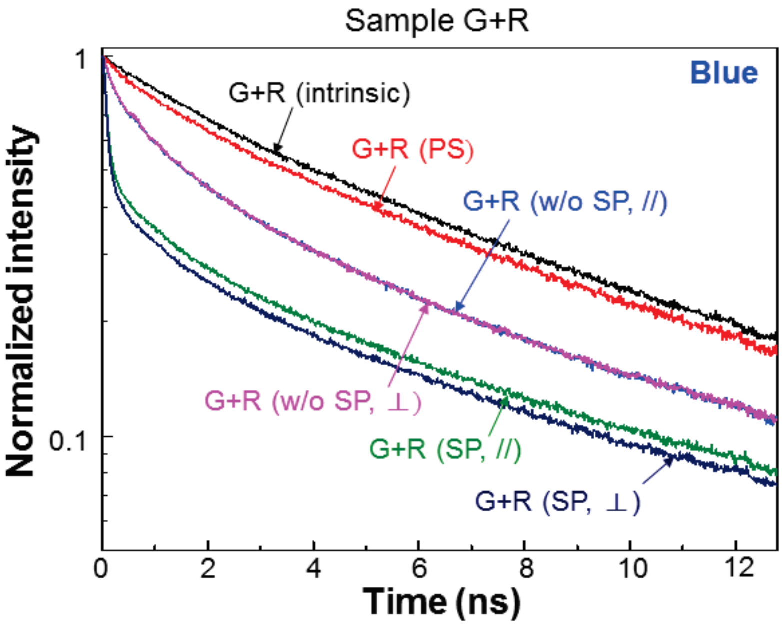

Figure 5. Normalized blue-light PL decay profiles of sample G+R at different fabrication stages in the two polarizations. PS: after PS fabrication; w/o SP: after QD insertion but before Ag NP deposition; SP: after QD insertion and Ag NP deposition.

Figures 6 and 7 show the normalized green- (red-) light PL decay profiles of samples G (R) and G+R in the cases with and without SP coupling for the two polarizations. For comparison, that of GQD (RQD) placed on the top surface of a GaN template, which does not contain a QW structure, is also shown, as labeled by “GQD (intrinsic)” (“RQD (intrinsic)”). Compared with the intrinsic GQD decay profile, the green-light decay rate in either polarization is decreased when GQD is inserted into the PS of sample G. This decrease of decay rate is caused by the FRET from QW into GQD. After SP coupling is introduced, the green-light decay rate is further decreased in sample G, indicating that the SP coupling can enhance the FRET from QW into GQD. Although the decay profiles for the two polarizations are close to each other in either case with or without SP coupling, we can still see the higher decay rate in the ⊥-polarization. In sample G+R, generally the green-light decay rates are significantly increased, when compared with those in sample G, due to the FRET from GQD into RQD in the PS. In this sample, SP coupling can also enhance the FRET from QW into GQD such that the green-light decay rate is slightly reduced. Here, the green-light decay profiles in the two polarizations are clearly separated. As shown in Figure 7, the red-light decay rates in sample R are also reduced, when compared with the intrinsic case, due to the FRET from QW into RQD. In this sample, the SP coupling effect for enhancing the FRET from QW into RQD is weak. Additionally, the difference between the two polarizations is small. Then, in sample G+R, the red-light decay rate is further reduced because RQD receives energy from GQD through the FRET from GQD into RQD. In this sample, the SP coupling can further reduce the red-light decay rate. In either case, with or without SP coupling, again, the difference between the two polarizations is small.

In Table 1, we show the decay times of the QW structure at different fabrication stages in the five samples under study. The numbers inside the curly brackets show the corresponding IQE values. The numbers inside the parentheses show the FRET efficiencies in the corresponding FRET processes. The FRET efficiency, η, is defined as $\eta = 1-\tau_{DA}/\tau_D$, where τ_{DA} (τ_D) is the PL decay time of the energy donor when the acceptor is present (absent) [11]. Here, in each sample, the QW PL decay time decreases after PS fabrication, after QD insertion, or after Ag NP deposition. The decay time in the ⊥-polarization is always shorter than that in the //-polarization. A shorter decay time always corresponds to a higher IQE. In sample G, the FRET efficiency increases from 11.92 (12.91%) at the stage after QD insertion, but before Ag NP deposition, to 19.70 (23.51%) after Ag NP deposition in the //-(⊥-) polarization. In sample R, the FRET efficiency increases from 17.89 (19.06%) at the stage after QD insertion but before Ag NP deposition to 22.41 (24.92%) after Ag NP deposition in the //- (⊥-) polarization. Then, in sample G+R, the FRET efficiency increases from 37.50 (37.67%) at the stage after QD insertion but before Ag NP deposition to 60.33 (64.67%) after Ag NP deposition in the //-(⊥-) polarization. We can see that SP coupling can indeed enhance FRET efficiency. In particular, the FRET efficiency enhancement through SP coupling is stronger in the ⊥-polarization. The FRET efficiencies in sample R are generally higher than those in sample G. However, the SP coupling effect for enhancing FRET efficiency is weaker in sample R, when compared with sample G. With both FRETs from QW into GQD and RQD, the overall FRET efficiencies in sample G+R are higher than those in the other two QD samples.

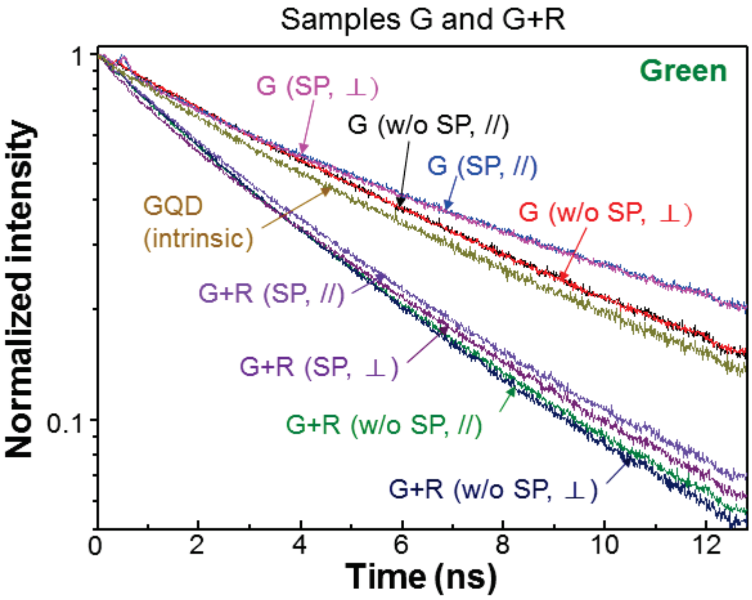

Figure 6. Normalized green-light PL decay profiles of samples G and G+R at different fabrication stages in the two polarizations.

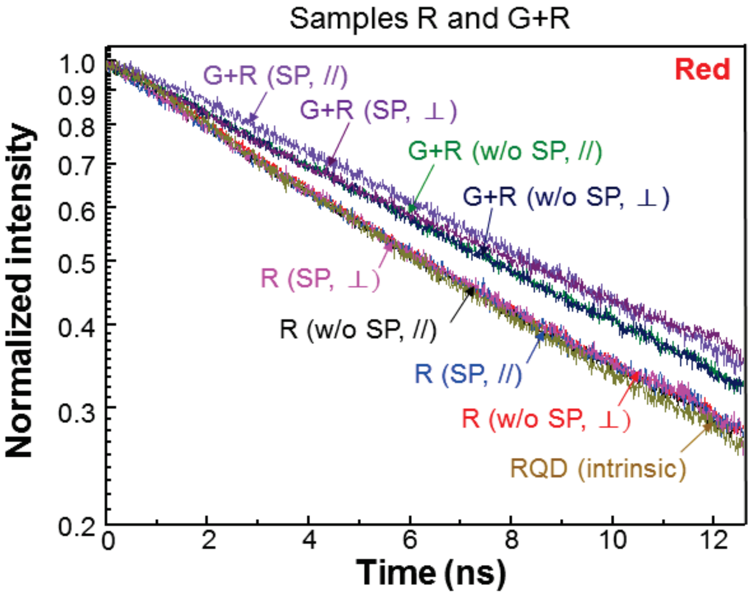

Figure 7. Normalized red-light PL decay profiles of samples R and G+R at different fabrication stages in the two polarizations.

Table 1. Blue-light PL decay times (in ns) in the five samples under study at different fabrication stages. The numbers inside the curly brackets show the corresponding IQEs. The numbers inside the parentheses show the corresponding FRET efficiencies.

Sample		**A**	**P**	**G**	**R**	**G+R**
Intrinsic		6.48 {57.8%}	6.36 {57.4%}	6.65 {57.9%}	6.67 {56.5%}	6.46 {57.7%}
After PS fabrication		—	5.89 {67.2%}	6.04 {68.6%}	5.98 {67.7%}	6.00 {68.1%}
After QD insertion	//	—	—	5.32 (11.92%)	4.91 (17.89%)	3.75 (37.50%)
	⊥	—	—	5.26 (12.91%)	4.84 (19.06%)	3.74 (37.67%)
After Ag NP deposition	//	5.71 {63.8%}	5.33 {69.4%}	4.85 (19.70%)	4.64 (22.41%)	2.38 (60.33%)
	⊥		5.23	4.62 (23.51%)	4.49 (24.92%)	2.12 (64.67%)

In Rows 3 and 4 of Table 2, we show the green- and red-light decay times, respectively, in the two polarizations under the conditions with and without SP coupling for the three QD samples. For comparison, the intrinsic PL decay times of GQD and RQD, i.e., 5.78 and 8.95 ns, respectively, are shown inside the curly brackets in Row 1. For the green light in the //-(⊥-) polarization, through the FRET from QW into GQD, the decay time increases from the intrinsic value of 5.78 ns to 6.26 (6.22) ns in the case without SP coupling, and then to 6.57 (6.48) ns under the condition of SP coupling in sample G. For the red light in the //-(⊥-) polarization, through the FRET from QW into RQD, the decay time increases from the intrinsic value of 8.95 ns to 9.27 (9.23) ns in the case without SP coupling, and then to 9.43 (9.39) ns under the condition of SP coupling in sample R. In sample G+R, for the green light in the //-(⊥-) polarization, the decay time decreases to 3.73 (3.69) ns in the case without SP coupling through the FRET from GQD into RQD, but returns to 3.98 (3.80) ns under the condition of SP coupling. On the other hand, for the red light in the //-(⊥-) polarization in this sample, the decay time increases to 11.15 (11.09) ns in the case without SP coupling, and further increases to 11.87 (11.84) ns under the condition of SP coupling.

Table 2. Green- and red-light PL decay times for samples G, R, and G+R in the two polarizations before (w/o SP) and after (SP) Ag NP deposition. The intrinsic PL decay times of GQD and RQD are shown inside the curly brackets in row 1. Also shown in this table are the color ratios, i.e., G/B and R/B ratios, and the polarization ratios (PRs) for the three color components.

Sample	**G (//, ⊥) {5.78 ns}**		**R (//, ⊥) {8.95 ns}**		**G+R (//, ⊥)**	
SP condition	w/o SP	SP	w/o SP	SP	w/o SP	SP
Green decay time (ns)	6.26, 6.22	6.57, 6.48	—	—	3.73, 3.69	3.98, 3.80
Red decay time (ns)	—	—	9.27, 9.23	9.43, 9.39	11.15, 11.09	11.87, 11.84
G/B ratio	0.107, 0.137	0.172, 0.225	—	—	0.114, 0.146	0.174, 0.213
R/B ratio	—	—	0.365, 0.412	0.371, 0.447	0.530, 0.694	0.696, 0.850
Blue PR	0.948	0.901	0.933	0.897	0.914	0.902
Green PR	1.217	1.179	—	—	1.169	1.103
Red PR	—	—	1.084	1.090	1.197	1.102

Figure 8a–c show the normalized CWPL spectra in the two polarizations under the conditions with and without SP coupling for samples G, R, and G+R, respectively. In each sample, under either condition with or without SP coupling, the spectra of the two polarizations are normalized with respect to the blue intensity peak in the //-polarization. Here, one can see that in either the green- or red-light component, the intensity in the ⊥-polarization is always higher than that in the //-polarization. However, the blue-light intensity in the ⊥-polarization is always lower than that in the //-polarization. These results clearly indicate that the FRET from QW into QD in the ⊥-polarization is stronger. The results in Figure 8 also show that the SP coupling can indeed enhance the green- and red-light intensity ratios with respect to the blue-light intensity. In Rows 5 and 6 of Table 2, we show the ratios of the integrated intensities of green and red lights over those of the corresponding blue lights, i.e., the G/B and R/B ratios, respectively, in the two polarizations under the conditions with and without SP coupling. The blue-, green-, and red-light components in a spectrum are separated by dividing the spectrum at 510 and 580 nm in wavelength. Under either condition with or without SP coupling, either the G/B or R/B ratio in the ⊥-polarization is always larger than the corresponding value in the //-polarization for each sample. By introducing SP coupling to a sample, either the G/B or R/B ratio in each polarization is increased. In the last three rows of Table 2, we show the polarization ratios of the three samples under the conditions with and without SP coupling. A polarization ratio is defined as the ratio of the integrated intensity in the ⊥-polarization over that in the //-polarization. We can see that all the green- and red-light (blue-light) polarization ratios are larger (smaller) than unity. In each sample, the SP coupling can reduce the blue-light polarization ratio because it enhances the FRET more effectively from QW into QD in the ⊥-polarization, when compared with the //-polarization. The SP-coupling effect also reduces the polarization ratios of either green or red light in samples G and G+R.

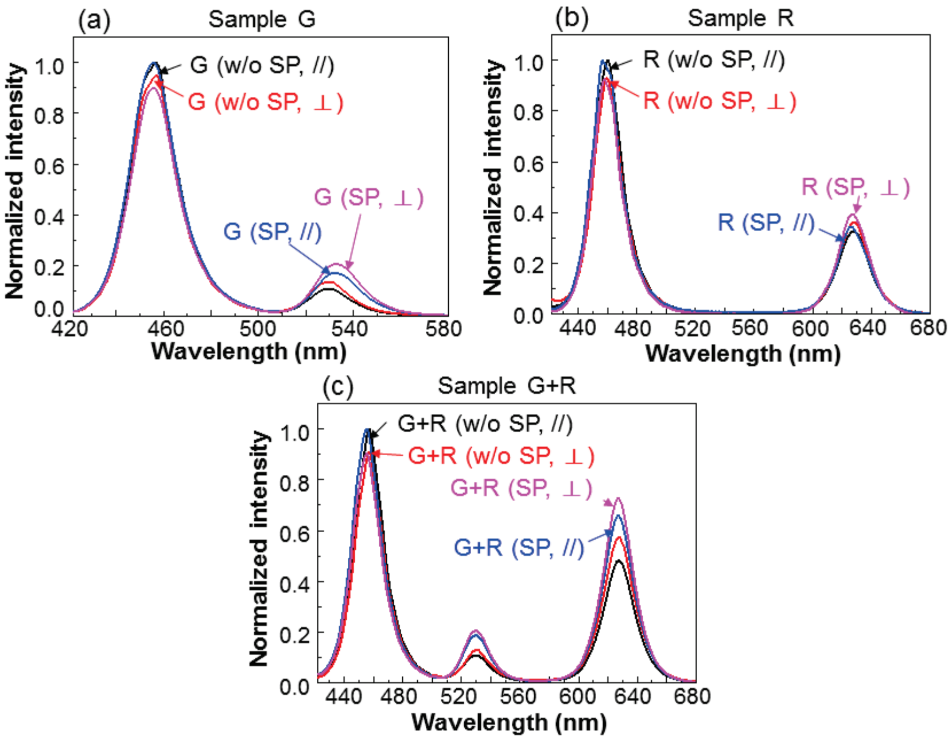

Figure 8. (**a**–**c**): Normalized CWPL spectra before (w/o SP) and after (SP) Ag NP deposition in the two polarizations for samples G, R, and G+R, respectively.

4. Simulation Study

To further understand the mechanism of color conversion enhancement in the sample structure, a numerical simulation study was undertaken. The simulation structures are schematically illustrated in Figure 9a–c. In Figure 9a for structure S with SP coupling, an infinitely-long empty nano-tube with the radius at r_0 = 30 nm was horizontally embedded in a QW template. The QW is represented by a dipole, denoted by the blue arrow, which serves as the donor in the FRET to be studied. A QD was placed inside the nano-tube and serves as the acceptor of the FRET from QW into QD. A 5-nm SiO_2 layer (refractive index at 1.5) was placed between the surface Ag NP and the QW template. It is assumed that the center of the Ag NP, the QW-dipole donor, and the QD-acceptor are vertically aligned. All of them lie in a vertical plane passing the axis of the embedded nano-tube. The distance between the QW-dipole donor and the top surface of the QW template (the upper boundary of the nano-tube) is d = 60 nm (s = 60 nm). The distance between the QD-acceptor and the upper boundary of the nano-tube is t = 10 nm. As illustrated in Figure 9b, the surface Ag NP is a truncated ellipsoid in geometry with the horizontal semi-axis of b = 21.8 nm, the height of h = 30 nm, and the radius of the circular contact interface of 18.9 nm. For comparison, in the reference structure (structure SR), as illustrated in Figure 9c, the Ag NP and SiO_2 layer are removed to show the results without SP coupling. The numerical simulation method has been described in a few earlier publications [7,16]. In numerical computations, the refractive index of GaN is set at 2.399. Additionally, the experimental data were used for the wavelength-dependent dielectric constant of Ag [20]. To evaluate the radiation behavior of a dipole, we first computed its radiated electromagnetic field when it was placed in a homogeneous spherical background space. Then, the total field was evaluated in the real structure for simulation based on the commercial software of COMSOL. By subtracting the radiated field of the dipole from the total field, we obtained the scattered field, which was used for evaluating the feedback effect on the dipole radiation behavior from the surrounding structure. With the obtained scattered field, the optical Bloch equations were solved to give the strength and orientation of the dipole modified by the feedback effect. Based on the modified dipole, the final electromagnetic field distribution and the total radiated power can be computed. With the feedback process, the effect of the scattered field caused by the nano-tube on the radiation behavior of the dipole was included. In other words, the Purcell effect was practically taken into account [6].

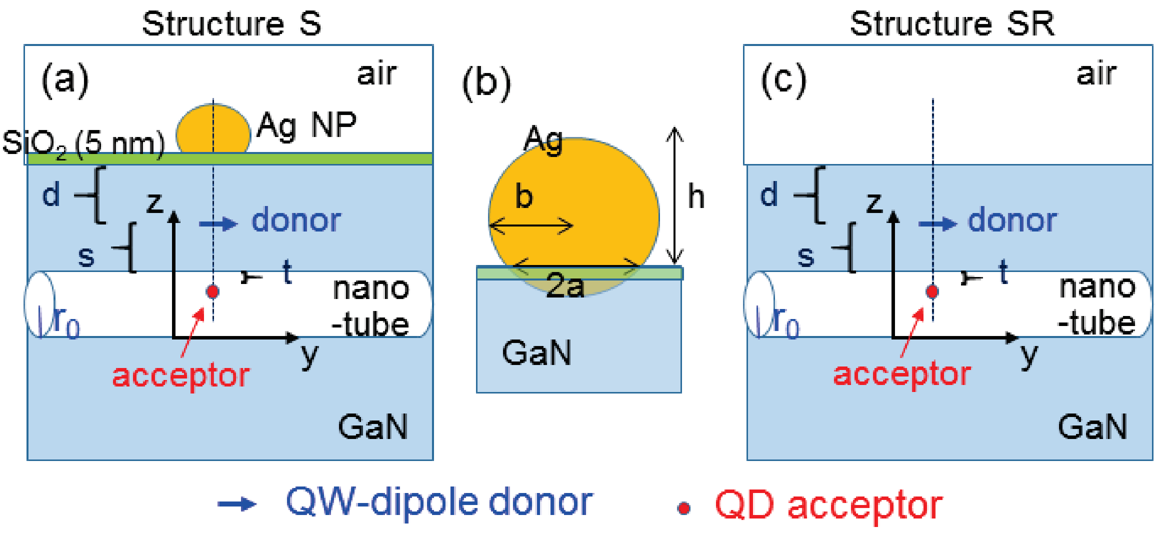

Figure 9. (**a**): Illustration of structure S used in the simulation, including a surface Ag NP for inducing the SP coupling with the QW-dipole donor and a QD-acceptor inside an embedded nano-tube. (**b**) Geometry illustration of the surface Ag NP. (**c**): Illustration of the reference structure SR for simulation.

Based on the simulation study, Figure 10a,b show the y-z-plane distributions of electric field strength (norm) at 455 nm in structures S and SR, respectively, produced by an x-oriented donor dipole. This radiating dipole is located at the center (marked by "x") of the white circular region, in which no field distribution is shown because of the extremely strong field there. Here, we can see that inside the nano-tube, the electromagnetic field is significantly stronger in structure S, when compared with structure SR, even though Figure 10a,b is plotted in the log scale, indicating the SP-coupling effect induced by the surface Ag NP.

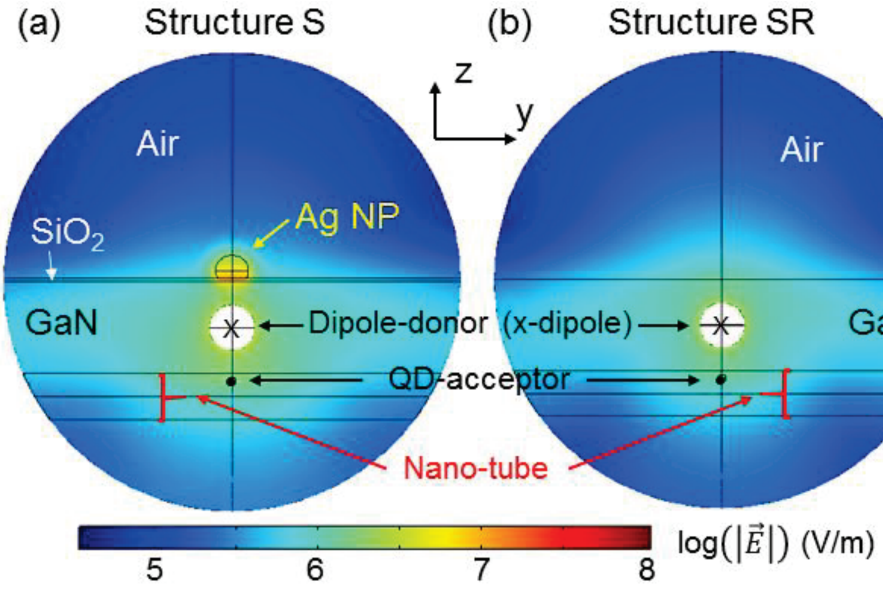

Figure 10. (**a**,**b**): y-z-plane distributions of electric field strength (norm) at 455 nm in structures S and SR, respectively, produced by an x-oriented donor dipole.

Figure 11a shows the normalized field intensity produced by the QW-dipole donor at the position of the QD acceptor under the conditions with (structure S) and without (structure SR) SP coupling in the cases of x- and y-dipole. The results here are normalized with respect to the corresponding field intensities in a structure without the Ag NP, SiO$_2$ layer, and the embedded nano-tube, i.e., an air/GaN half-space structure. For either the x- or y-dipole in structure S, we can see an intensity peak around 460 nm, which is caused by the SP-coupling effect, confirming that the SP coupling can indeed enhance the donor field intensity inside the nano-tube. Without SP coupling in structure SR, the donor intensity inside the nano-tube can also be enhanced due to the nanoscale-cavity effect for the x-dipole, which corresponds to the $\perp$-polarization in the experimental study reported earlier in this paper. The vertical dashed line in Figure 11a indicates the experimental QW emission peak wavelength at 455 nm. Figure 11b shows the normalized radiated powers of the QD-acceptor in structures S and SR for the x- and y-dipole. The results are normalized with respect to the radiated power in a homogeneous space of air. Here, except for the depressions around 460 nm, the results in structures S and SR are close to each other for either dipole orientation. The depressions are caused by the SP coupling between the QD-acceptor and the LSP resonance of the surface Ag NP. In other words, based on our simulation model, with the distance between the QD-acceptor and the bottom face of the Ag NP at 135 nm, the SP coupling leads to an emission suppression around the LSP resonance peak wavelength of the surface Ag NP. However, this behavior is unimportant in our numerical study because we are mainly concerned with the acceptor emissions in the green and red spectral ranges, particularly at 530 and 625 nm in wavelength, as indicated by the vertical dashed lines in Figure 11b. The larger-than-unity results shown in Figure 11b indicate that the emission efficiency of a QD inside a nanoscale cavity can indeed be enhanced, particularly in the polarization perpendicular to the nano-tube axis (the x-dipole). Rows 2 and 3 of Table 3 show the normalized donor intensities at the position of the acceptor in structures S and SR, respectively, for the x- and y-dipole at the wavelength of 455 nm. The donor intensities are stronger for the x-dipole. Rows 4 and 5 (6 and 7) of Table 3 show the normalized radiated powers of the acceptor in structures S and SR, respectively, for the x- and y-dipole at the wavelength of 540 (625) nm. The dipole polarization dependencies can also be observed.

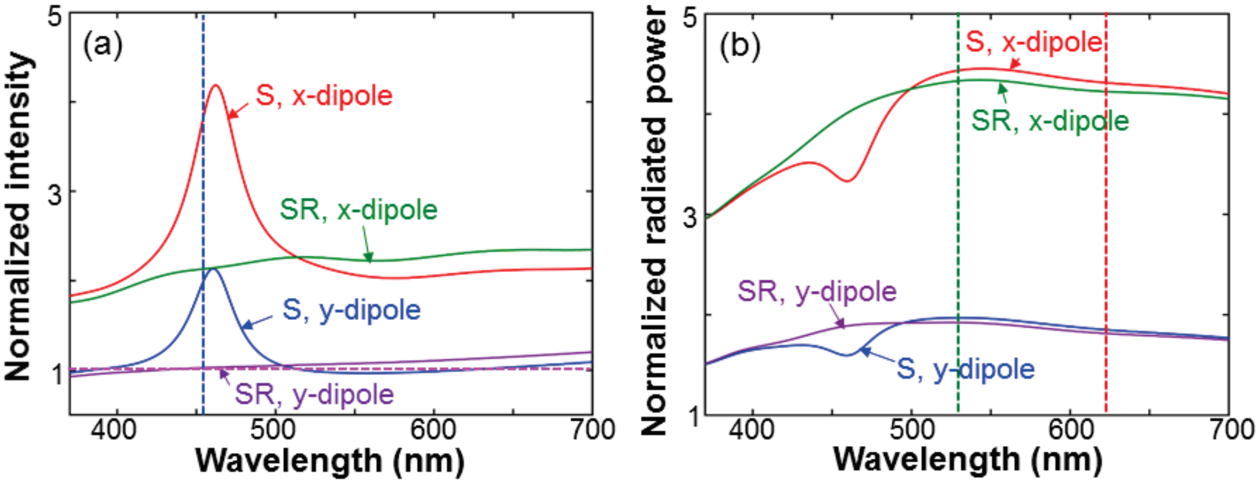

Figure 11. (**a**): Normalized intensity spectra produced by the QW-dipole donor at the position of the QD-acceptor in structures S and SR for the two dipole orientations. (**b**): Normalized radiated power spectra of the QD-acceptor in structures S and SR for the two dipole orientations.

Table 3. Simulation results obtained from Figures 11 and 12 at 455, 530, and 625 nm in wavelength for the two dipole orientations, including the results of donor intensity, acceptor radiated power, and color conversion enhancement factor.

	x-Dipole	y-Dipole
Normalized donor intensity at 455 nm (S)	3.872	2.016
Normalized donor intensity at 455 nm (SR)	2.132	1.027
Normalized acceptor radiated power at 530 nm (S)	4.435	1.970
Normalized acceptor radiated power at 530 nm (SR)	4.331	1.922
Normalized acceptor radiated power at 625 nm (S)	4.309	1.847
Normalized acceptor radiated power at 625 nm (SR)	4.222	1.811
Donor intensity ratio at 455 nm (S/SR)	1.816	1.963
Acceptor radiative power ratio at 530 nm (S/SR)	1.024	1.025
Acceptor radiative power ratio at 625 nm (S/SR)	1.021	1.020
Color conversion enhancement factor from 455 into 530 nm (S/SR)	1.860	2.012
Color conversion enhancement factor from 455 into 625 nm (S/SR)	1.854	2.002

Figure 12 shows the ratios of the intensity produced by the donor at the position of the acceptor and the radiated power of the acceptor in structure S over the corresponding values in structure SR. These ratios show the enhancements of those two parameters through SP coupling. We can see that although the SP coupling produces weak effects on the emissions of GQD and RQD because their emission wavelengths are far away from the LSP resonance peak, it can effectively increase the donor field intensity inside the nano-tube. In Rows 8–10 of Table 3, we show the donor intensity ratios at 455 nm and the acceptor radiated power ratios at 530 and 625 nm, respectively, for the x- and y-dipole. The multiplication of the donor intensity ratio at 455 nm by the acceptor radiated power ratio at 530 (625) nm corresponds to the enhancement ratio of the color conversion efficiency from QW into GQD (RQD), as shown in Row 11 (12) of Table 3. Although the SP coupling does not produce a significant change of the emission efficiency of a QD inside the nanoscale cavity, it does enhance the donor intensity at the position of the QD, i.e., the FRET from QW into QD, resulting in a significant enhancement of the color conversion efficiency.

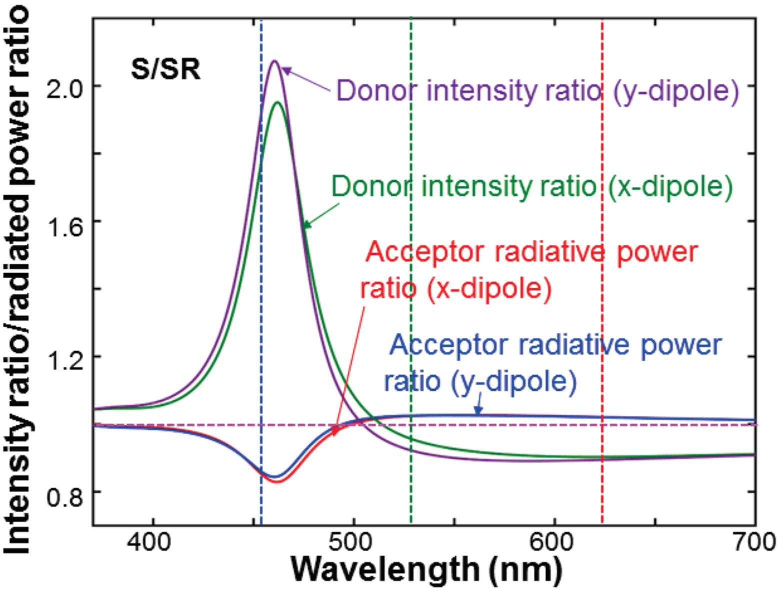

Figure 12. Ratios of the donor intensity and acceptor radiated power in structure S over the corresponding values in structure SR for the two dipole orientations.

5. Discussions

As shown in Row 7 of Table 2, the SP coupling leads to the decrease of blue-light polarization ratio in each sample due to the stronger SP-coupling enhancement of the FRET from QW into QD in the ⊥-polarization. In this situation, we may expect the larger polarization ratios for green and red lights because the GQD and RQD receive more energy from the QW structure through FRET in the ⊥-polarization. However, as shown in Rows 8 and 9 of Table 2, after the SP coupling effect is introduced, the green- and red-light polarization ratios are decreased except for that in sample R, even though they are still larger than unity. This result may have two attributions. First, in the CWPL measurement, the obtained PL intensities include the contribution of the far-field process of photon emission–absorption–reemission, besides that of the near-field process of FRET. The far-field process is more weakly polarization-dependent, when compared with the near-field process. Second, the non-resonant scattering of the surface Ag NP distribution can also weaken the polarization dependence of the measured CWPL intensity for green or red light. It is noted that in our simulation model we did not really evaluate the transferred power from the donor into the acceptor and hence we could not observe such an experimental result in the simulation study.

In Figure 8, we can see that certain spectral peaks are shifted after the SP coupling effects are introduced to the samples. Those of blue light in all the three samples are blue-shifted after the SP coupling effects are included. This is because the SP coupling and hence the FRET from QW into QD are stronger on the long-wavelength side of the QW emission spectrum, as shown in Figure 2, such that the QW emission on the long-wavelength side becomes weaker. Therefore, the QW emission peak is effectively blue-shifted. The reason for the noticeable red-shift of the green-light peak in sample G is complicated. It can be caused by the non-uniform GQD emission wavelength. It can also be attributed to the wavelength-dependent nanoscale-cavity and SP-coupling effects.

6. Conclusions

In summary, we have designed and implemented a device structure for improving the color conversion performance from a QW structure into QDs inserted into a nearby subsurface GaN PS by introducing the SP coupling between the QW structure and the LSP resonance on surface Ag NPs to the device. Based on TRPL and CWPL measurements, we observed the enhanced FRET efficiencies from QW into QD through SP coupling. The SP-coupling induced enhancement was stronger in the polarization perpendicular to the essentially extended direction of the pores in the fabricated PS. The results of a numerical simulation study well supported the experimental observations. The encouraging results in this paper can help us in improving the color conversion efficiency in a light-emitting device.

Author Contributions: Conceptualization, S.Y. and C.-C.Y.; methodology, S.Y. and H.-Y.F.; software, Y.K.; formal analysis, Y.-S.L. and W.-C.C.; resources, C.-C.Y.; writing—original draft preparation, S.Y.; writing—review and editing, C.-C.Y.; supervision, C.-C.Y.; project administration, C.-C.Y.; funding acquisition, C.-C.Y. All authors have read and agreed to the published version of the manuscript.

Funding: This research was funded by the Ministry of Science and Technology, Taiwan, The Republic of China, under the grants of MOST 111-2221-E-002-073, MOST 110-2221-E-002-131, and MOST 109-2221-E-002-194.

Data Availability Statement: All the data supporting reported results can be found in the text of this paper.

Acknowledgments: The assistances of Chen-Hua Chen, Sheng-Yang Kuo, and Zong-Han Li in sample fabrication, that of Shung-Hsiang Wu in optical characterization, that of Hao-Yu Hsieh in material analysis, and those of Chia-Hao Li and Jun-Chen Chen in simulation study are all acknowledged.

Conflicts of Interest: The authors declare no conflict of interest.

References

1. Förster, T. Energy transport and fluorescence. *Naturwissenschaften* **1946**, *33*, 166–175.
2. Hsu, L.Y.; Ding, W.; Schatz, G.C. Plasmon-coupled resonance energy transfer. *J. Phys. Chem. Lett.* **2017**, *8*, 2357–2367. [CrossRef] [PubMed]
3. Kuo, Y.; Shih, C.Y.; Yang, C.C. Simulation study of the effect of surface plasmon coupling on Förster resonance energy transfer behavior. *Plasmonics* **2022**, *17*, 989–1000. [CrossRef]
4. Kuo, Y.; Lu, Y.J.; Shih, C.Y.; Yang, C.C. Simulation study on the enhancement of resonance energy transfer through surface plasmon coupling in a GaN porous structure. *Opt. Express* **2021**, *29*, 43182–43192. [CrossRef]
5. Huang, Y.Y.; Li, Z.H.; Lai, Y.C.; Chen, J.C.; Wu, S.H.; Yang, S.; Kuo, Y.; Yang, C.C.; Hsu, T.C.; Lee, C.L. Nanoscale-cavity enhancement of color conversion with colloidal quantum dots embedded in the surface nano-holes of a blue-emitting light-emitting diode. *Opt. Express* **2022**, *30*, 31322–31335. [CrossRef] [PubMed]
6. Purcell, E.M. Spontaneous emission probabilities at radio frequencies. *Phys. Rev.* **1946**, *69*, 681.
7. Kuo, Y.; Ting, S.Y.; Liao, C.H.; Huang, J.J.; Chen, C.Y.; Hsieh, C.; Lu, Y.C.; Chen, C.Y.; Shen, K.C.; Lu, C.F.; et al. Surface plasmon coupling with radiating dipole for enhancing the emission efficiency of a light-emitting diode. *Opt. Express* **2011**, *19*, A914–A929. [CrossRef] [PubMed]
8. Wu, R.N.; Ni, C.C.; Yang, S.; Kuo, Y.; Chang, W.Y.; Su, Y.C.; Kuo, S.Y.; Yang, C.C. Surface plasmon coupling of Ag nanoparticles with InGaN/GaN quantum wells for enhancing the emission efficiency of light-emitting devices. *ACS Appl. Nano Mater.* **2022**, *5*, 8288–8297. [CrossRef]
9. Ni, C.C.; Kuo, S.Y.; Li, Z.H.; Wu, S.H.; Wu, R.N.; Chen, C.Y.; Yang, C.C. Förster resonance energy transfer in surface plasmon coupled color conversion processes of colloidal quantum dots. *Opt. Express* **2021**, *29*, 4067–4081. [CrossRef] [PubMed]
10. Chen, Y.P.; Ni, C.C.; Wu, R.N.; Kuo, S.Y.; Su, Y.C.; Huang, Y.Y.; Chen, J.W.; Hsu, Y.C.; Wu, S.H.; Chen, C.Y.; et al. Combined effects of surface plasmon coupling and Förster resonance energy transfer on the light color conversion behaviors of colloidal quantum dots on an InGaN/GaN quantum-well nanodisk structure. *Nanotechnology* **2021**, *32*, 135206. [CrossRef] [PubMed]
11. Ghenuche, P.; Mivelle, M.; de Torres, J.; Moparthi, S.B.; Rigneault, H.; Van Hulst, N.F.; García-Parajó, M.F.; Wenger, J. Matching nanoantenna field confinement to FRET distances enhances Forster energy transfer rates. *Nano Lett.* **2015**, *15*, 6193–6201. [CrossRef] [PubMed]
12. Chen, D.; Xiao, H.; Han, J. Nanopores in GaN by electrochemical anodization in hydrofluoric acid: Formation and mechanism. *J. Appl. Phys.* **2012**, *112*, 064303. [CrossRef]
13. Griffin, P.; Oliver, R. Porous nitride semiconductors reviewed. *J. Phys. D Appl. Phys.* **2020**, *53*, 383002. [CrossRef]

14. Schwab, M.J.; Chen, D.; Han, J.; Pfefferle, L.D. Aligned mesopore arrays in GaN by anodic etching and photoelectrochemical surface etching. *J. Phys. Chem. C* **2013**, *117*, 16890–16895. [CrossRef]
15. Lin, C.H.; Su, C.Y.; Kuo, Y.; Chen, C.H.; Yao, Y.F.; Shih, P.Y.; Chen, H.S.; Hsieh, C.; Kiang, Y.W.; Yang, C.C. Further reduction of efficiency droop effect by adding a lower-index dielectric interlayer in a surface plasmon coupled blue light-emitting diode with surface metal nanoparticles. *Appl. Phys. Lett.* **2014**, *105*, 101106. [CrossRef]
16. Kuo, Y.; Chang, W.Y.; Lin, C.H.; Yang, C.C.; Kiang, Y.W. Evaluating the blue-shift behaviors of the surface plasmon coupling of an embedded light emitter with a surface Ag nanoparticle by adding a dielectric interlayer or coating. *Opt. Express* **2015**, *23*, 30709–30720. [CrossRef] [PubMed]
17. Lin, C.A.J.; Sperling, R.A.; Li, J.K.; Yang, T.Y.; Li, P.Y.; Zanella, M.; Chang, W.H.; Parak, W.J. Design of an amphiphilic polymer for nanoparticle coating and functionalization. *Small* **2008**, *4*, 334–341. [CrossRef] [PubMed]
18. Chen, C.Y.; Ni, C.C.; Wu, R.N.; Kuo, S.Y.; Li, C.H.; Kiang, Y.W.; Yang, C.C. Surface plasmon coupling effects on the Förster resonance energy transfer from quantum dot into rhodamine 6G. *Nanotechnology* **2021**, *32*, 295202. [CrossRef] [PubMed]
19. Chen, H.S.; Yeh, D.M.; Lu, Y.C.; Chen, C.Y.; Huang, C.F.; Tang, T.Y.; Yang, C.C.; Wu, C.S.; Chen, C.D. Strain relaxation and quantum confinement in InGaN/GaN nanoposts. *Nanotechnology* **2006**, *17*, 1454–1458. [CrossRef]
20. Palik, E.D. *Handbook of Optical Constants of Solids*; Academic Press: New York, NY, USA, 1998; Volume 3.

nanomaterials

Article

Temperature- and Size-Dependent Photoluminescence of $CuInS_2$ Quantum Dots

Oleg Korepanov [1,*], Dmitriy Kozodaev [1,2], Olga Aleksandrova [1], Alexander Bugrov [3], Dmitrii Firsov [1], Demid Kirilenko [4], Dmitriy Mazing [1], Vyacheslav Moshnikov [1] and Zamir Shomakhov [5]

[1] Micro- and Nanoelectronics Department, Saint Petersburg Electrotechnical University "LETI", 197022 Saint Petersburg, Russia; kozodaev@ntmdt.nl (D.K.); oaaleksandrova@gmail.com (O.A.); d.d.firsov@gmail.com (D.F.); dmazing@yandex.ru (D.M.); vamoshnikov@mail.ru (V.M.)
[2] NT-MDT BV, 7335 Apeldoorn, The Netherlands
[3] Department of Physical Chemistry, Saint Petersburg Electrotechnical University "LETI", 197022 Saint Petersburg, Russia; anbugrov@etu.ru
[4] Ioffe Institute, 194021 Saint Petersburg, Russia; zumsisai@gmail.com
[5] Institute of Informatics, Electronics and Robotics, Kabardino-Balkarian State University, n.a. Kh.M. Berbekov, 360004 Nalchik, Russia; shozamir@yandex.ru
* Correspondence: okrpnv@gmail.com

Abstract: We present the results of a temperature-dependent photoluminescence (PL) spectroscopy study on $CuInS_2$ quantum dots (QDs). In order to elucidate the influence of QD size on PL temperature dependence, size-selective precipitation was used to obtain several nanoparticle fractions. Additionally, the nanoparticles' morphology and chemical composition were studied using transmission electron microscopy, X-ray diffraction, and X-ray photoelectron spectroscopy. The obtained QDs showed luminescence in the visible–near infrared range. The PL energy, linewidth, and intensity were studied within an 11–300 K interval. For all fractions, a temperature decrease led to a shift in the emission maximum to higher energies and pronounced growth of the PL intensity down to 75–100 K. It was found that for large particle fractions, the PL intensity started to decrease, with temperature decreasing below 75 K, while the PL intensity of small nanoparticles remained stable.

Keywords: quantum dots; $CuInS_2$; temperature-dependent photoluminescence

1. Introduction

Quantum dots (QDs) are nanocrystals composed of semiconductor materials that exhibit photoluminescent properties, making them increasingly popular in research and development. Their unique optoelectronic properties make them highly attractive for numerous applications. QDs come in various sizes, shapes, and chemical compositions, and can be employed in a number of different spheres, from solid-state lighting and photovoltaics to life science applications, such as imaging, sensing, medical diagnostics, and photodynamic therapy. With current research focusing on the use of nanocrystals with dimensions of less than 10 nm, these materials offer size-dependent absorption and emission energy tunability that is beneficial for development of bio-labeling reagents, as well as photonic devices such as liquid-crystal displays, QD-solar cells, light-emitting diodes (LEDs), and photodetectors [1–5].

QDs composed of group II–VI elements, e.g., cadmium and lead chalcogenides, have become the most popular choice due to their tunable absorption onset and strong fluorescence. However, the obvious toxicity of these materials has limited their use in some areas [6,7]. Thus, binary compound semiconductors (e.g., InP and ZnS) [8], elemental semiconductors (e.g., Si, C) [9], and ternary chalcogenides [10], which offer comparable optical features and tunable emission and absorption wavelengths, without the same level of toxicity, have been explored. The search for safer and earth-abundant QD materials is a current research topic. This includes ternary nanocrystals such as the $CuInS(Se)_2$ and $AgInS(Se)_2$, as well as the quaternary nanocrystals Zn-Cu-In-S(Se) and Zn-Ag-In-S(Se).

$CuInS_2$ is a ternary I–III–VI semiconductor with direct transition bandgap energy of 1.53 eV. $CuInS_2$ and $AgInS_2$ nanocrystals have broad photoluminescence (PL) spectra with a full width at half maximum (FWHM) of around 0.4 eV. Their PL quantum yields (PLQY) can be enhanced through composition control, while their absorption and emission spectra show a blue shift with decreasing particle size [11]. Recent advancements have demonstrated potential for ternary and quaternary nanocrystals based on I–III–VI semiconductors in novel applications such as photovoltaics and photocatalysis, as well as biomedicine (e.g., multimodal imaging, drug delivery, theranostics, etc.) [12–14].

While the most common approach to QD preparation is synthesis in organic solvents, yielding hydrophobic QDs with nonpolar surface ligands, ternary and quaternary QDs can be synthesized in water. Rendering QDs synthesized in nonpolar medium dispersible in water could be performed via a ligand exchange process; however, this can have detrimental effects on the photophysical properties of nanocrystals, inducing the formation of new trap states that promote the nonradiative recombination of charge carriers, and thus, leading to photoluminescence quenching. Aqueous techniques become even more relevant in the case of I–III–VI nanocrystals, which are typically synthesized in nonpolar media employing aliphatic thiols as coordinating ligands, resulting in the strong coordination of surface groups and hindering ligand exchange. The synthesis of ternary and quaternary QDs in aqueous medium can be achieved using a various types of capping ligands such as thiols [15,16], amino-acids [17–19], polymers [20,21], etc., providing excellent long-term colloidal stability.

Luminescence thermometry is a flexible optical method that measures local temperatures, where temperature-dependent changes function as indicators or probes. Rare-earth ion-doped luminescent compounds have become a popular alternative for making temperature-dependent sensors [22,23]. The single emission center that the phosphor-based optical temperature detector relies on makes it unstable and inaccurate due to variations in excitation power [24]. Compared to rare-earth ion-doped phosphors, QDs demonstrate high sensitivity and photostability, although the potential application of QDs in optical temperature sensing, as well as the underlying mechanisms, require further investigation.

Several studies discuss the impact of particle size and low temperatures on the optical characteristics of QDs [25–27]. However, the correlation between particle size and temperature dependence remains inconclusive. In this study, $CuInS_2$ QDs were synthesized and separated according to size, and temperature curves were obtained within the range of room temperature to 11 K.

2. Materials and Methods

2.1. Chemicals

Indium(III) chloride ($InCl_3$, 99.999%) and 3-Mercaptopropionic acid ($C_3H_6O_2S$, 99%) were purchased from Sigma Aldrich (St. Louis, MO, USA). Copper(II) acetate ($Cu(CH_2COO)_2$, 99%), sodium sulfide ($Na_2S{\cdot}9H_2O$, 98%), and sodium hydroxide (NaOH) were provided by Vekton (St. Petersburg, Russia). All chemicals were used without additional purification.

2.2. Synthesis of $CuInS_2$ QDs

In the presented work, MPA was used as a stabilizer. A distinctive feature of MPA is its relatively small molecule size compared to known surfactants used in the synthesis of I–III–VI QDs (L-Glutathione, polymers, etc.). The use of short-chain molecules makes it possible to reduce the distance between QDs, which leads to an increase in charge transfer efficiency.

The photoluminescent quantum yield and photostability of ternary QDs can be adjusted through composition variation. Generally, the highest PL quantum yield and photostability observed in I–III–VI QDs are achieved at a molar ratio of [I]:[III] = 1:4 [28,29].

$CuInS_2$ QDs were synthesized in an aqueous solution. Under magnetic stirring, 0.1 mmol of $Cu(CH_2COO)_2$, 0.4 mmol of $InCl_3$, and 2 mmol of MPA were dissolved in 5 mL of deionized water. The pH of the solution was adjusted to 7.00 using 0.1 M NaOH; then, a freshly prepared aqueous solution containing 0.5 mmol of $Na_2S{\cdot}9H_2O$ was added. The solution was heated to 95 °C for 300 min.

QDs of different sizes were obtained via n steps of size-selective precipitation, where n represents the fraction number. Precipitation was achieved through the addition of isopropanol, and separation was performed via centrifugation.

2.3. Methods

Transmission electron microscopy (TEM) studies were performed using a JEOL JEM-2100F microscope, JEOL, Akishima, Japan (accelerating voltage 200 kV, point resolution 0.19 nm). Specimens for the TEM were prepared via wetting of a conventional copper TEM grid covered with a carbon lacey film in suspension and its subsequent drying in air.

X-ray diffraction measurements of the samples were carried out using a Rigaku SmartLab diffractometer (Rigaku Corporation, Tokyo, Japan) in a 2θ angle range of 15 to 60° with a scanning rate of 1° per minute using CuK_α radiation at 40.0 kV and 30.0 mA. Qualitative X-ray phase analysis of the QDs was performed by comparing the experimental diffraction patterns with the cards of the International Centre for Diffraction Data's PDF databases using the Crystallographica Search-Match program. The average size of the coherent scattering regions was calculated through the broadening of X-ray diffraction lines using the Rigaku SmartLab Studio II software package version 2.0.

X-ray photoelectron spectroscopy (XPS) spectra were recorded using a "K-Alpha" Thermo Scientific system (Waltham, MA, USA) equipped with an Al-K_α (1486.6 eV) X-ray source. The sample was outgassed to less than 4.5×10^{-9} mbar. The background subtraction of secondary electrons was performed using the Shirley method. The spectrometer energy scale was calibrated with Au $4f_{7/2}$, Cu $2p_{3/2}$, and Ag $3d_{5/2}$ lines at 84.2, 367.9, and 932.4 eV, respectively.

The infrared transmission measurements were performed using a Vertex 80 Fourier transform infrared (FTIR) spectrometer (Bruker Optics, Ettlingen, Germany) equipped with a SiC globar as the IR radiation source, a KBr beamsplitter, and a pyroelectric deuterated L-alanine-doped triglycine sulphate (DLaTGS) photodetector. A PL measurement setup [30] based on the same FTIR spectrometer (equipped instead with a CaF_2 beamsplitter and a Si diode photodetector) was employed to obtain the temperature dependences of the PL spectra. The samples were placed into a Janis CCS-150 closed-cycle helium cryostat, and a 405 nm semiconductor laser diode was used as an excitation source. Nanoparticle samples were dried, powdered, and made into transparent films by mixing them with KBr. The QD solutions were poured into quartz cuvettes and measurements were performed using the same PL spectra measurement setup without cryostat implementation.

Absorption spectra of QD solutions were acquired using a PE-5400UV UV-vis spectrophotometer ("Ekohim" LLC, St. Petersburg, Russia) in quartz cuvettes.

3. Results and Discussion

3.1. Structure Characterization

In order to establish the morphology and structure of the $CuInS_2$ QDs, TEM and XRD studies were performed.

The X-ray diffraction pattern (Figure 1a) contains at least three broad peaks in the 2θ angle ranges of 23–34°, 42–50°, and 52–58°, which indicates the presence of a crystalline structure in the sample. The observed Bragg peaks are in good agreement with the (112), (200), (204), (220), and (312) planes of $CuInS_2$ (JCPDS 65-2732) with the chalcopyrite structure, which indicates that the resulting QDs are nuclei of the tetragonal crystalline phase $CuInS_2$ (Figure 1a). In this case, characteristic reflections of the hexagonal Cu_2S phase (JCPDS 84-0208) are not observed in the sample. The average size of the coherent scattering regions (D) of $CuInS_2$, calculated using the Rigaku SmartLab Studio II program through the broadening of X-ray maxima, is approximately 1.5 nm. The average QD size of 2 nm, estimated via XRD, is in an agreement with the TEM results. According to TEM results (Figure 1b), chalcopyrite planes corresponding to (112) with a period of 0.32 nm are observed, and the QDs have an average diameter of 2 ± 0.5 nm. The average size of the obtained QDs is less than the Bohr radius of exciton in $CuInS_2$, which means that the nanoparticles are in a strong confinement regime.

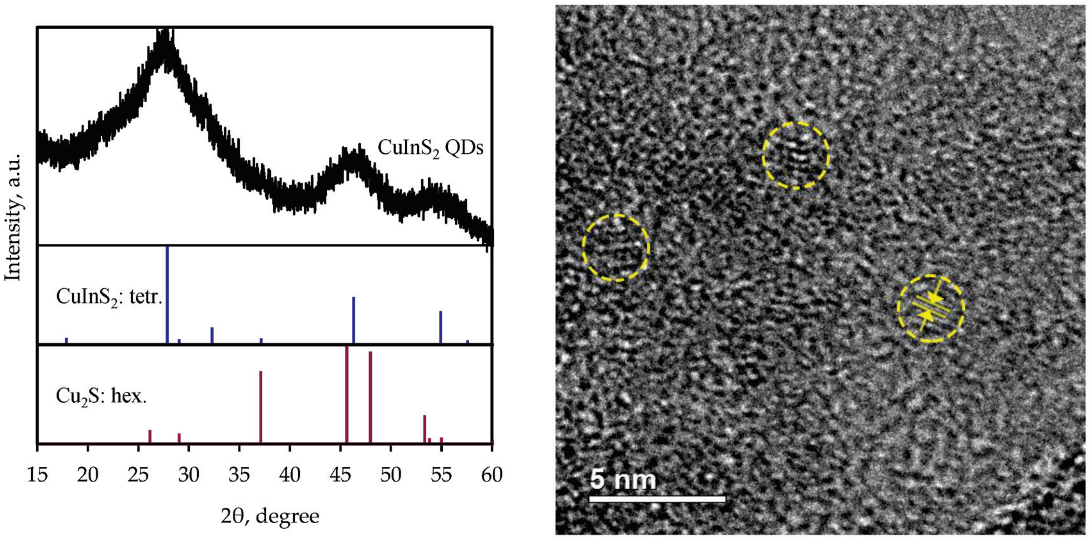

(**a**) (**b**)

Figure 1. (**a**) XRD patterns and (**b**) TEM image of obtained samples. In (**b**), several quantum dots are encircled in yellow, while the interplanar spacing is indicated by the arrows.

Figure 2 shows the XPS spectra of the $CuInS_2$ QDs.

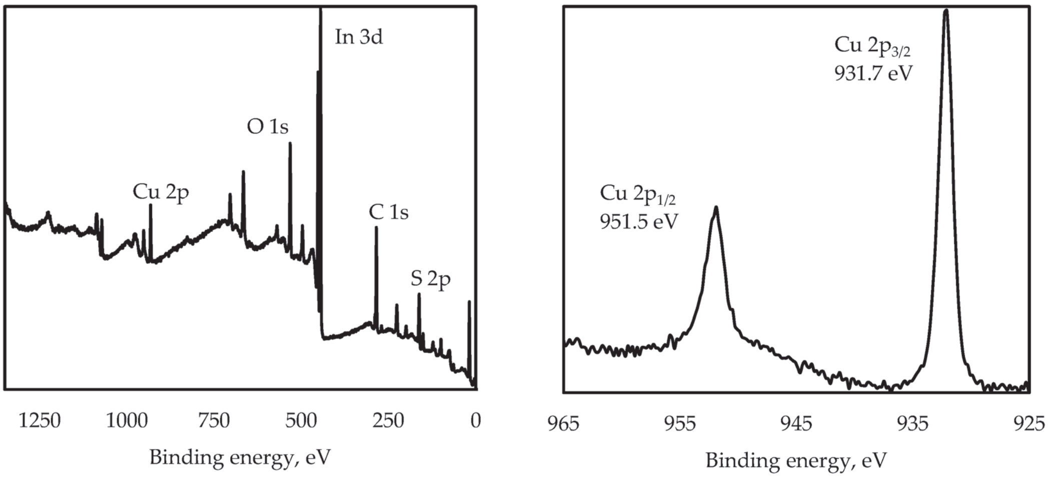

(**a**) (**b**)

Figure 2. *Cont.*

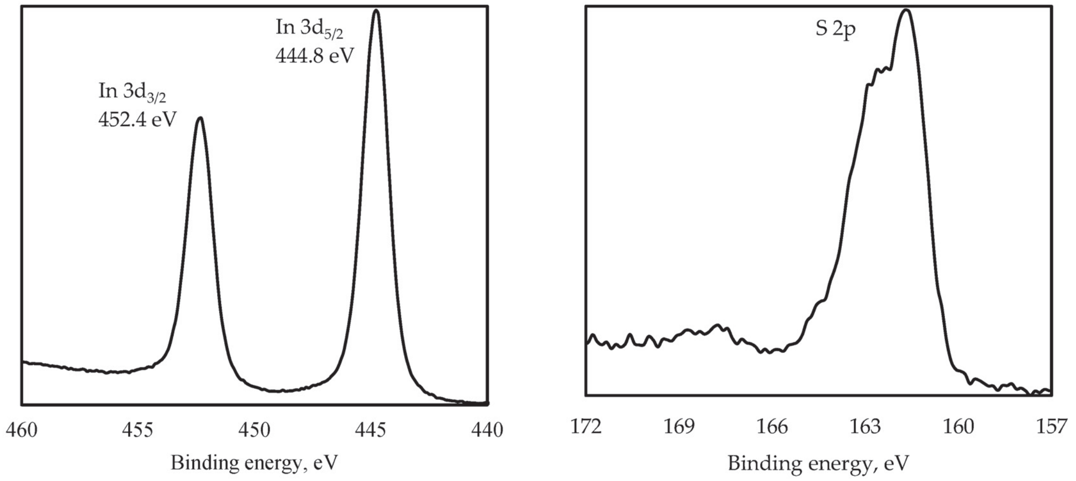

(**c**) (**d**)

Figure 2. XPS spectra of $CuInS_2$ QDs: survey (**a**), Cu 2p (**b**), In 3d (**c**), S 2p (**d**).

From Figure 2, it can be seen that Cu 2p peaks are found at 931.7 eV (Cu $2p_{3/2}$) and 951.5 eV (Cu $2p_{1/2}$), In 3d peaks are found at 444.8 eV (In $3d_{5/2}$) and 452.4 eV (In $3d_{3/2}$), and an S 2p peak is found at 161.7 eV. C and O elements comprising MPA ligands are detected, as well (Figure 2a). In Figure 2b, the Cu 2p line is split into Cu $2p_{3/2}$ and Cu $2p_{1/2}$ (splitting value is 19.8 eV), with no distinguishable Cu^{2+} peak at about 942 eV. In Figure 3a, the kinetic energy of the Cu LMM Auger transition (916.6 eV), corresponding to Cu_2O, suggests that the copper is in the Cu^+ state in this sample. The In 3d line is split into In $3d_{5/2}$ and In $3d_{3/2}$, with splitting energy of 7.6 eV (Figure 3b). Two peaks, In $3d_{5/2}$ and In $3d_{3/2}$, and the kinetic energy of the In $M_4N_{45}N_{45}$ Auger transition of 407.2 eV (Figure 3b) are assigned to In^{3+} in the $CuInS_2$ QDs. Two distinct peaks at binding energies of 161.7 and 162.8 eV are assigned to S $2p_{3/2}$ and S $2p_{1/2}$, which is consistent with the values for S^{2-} [31].

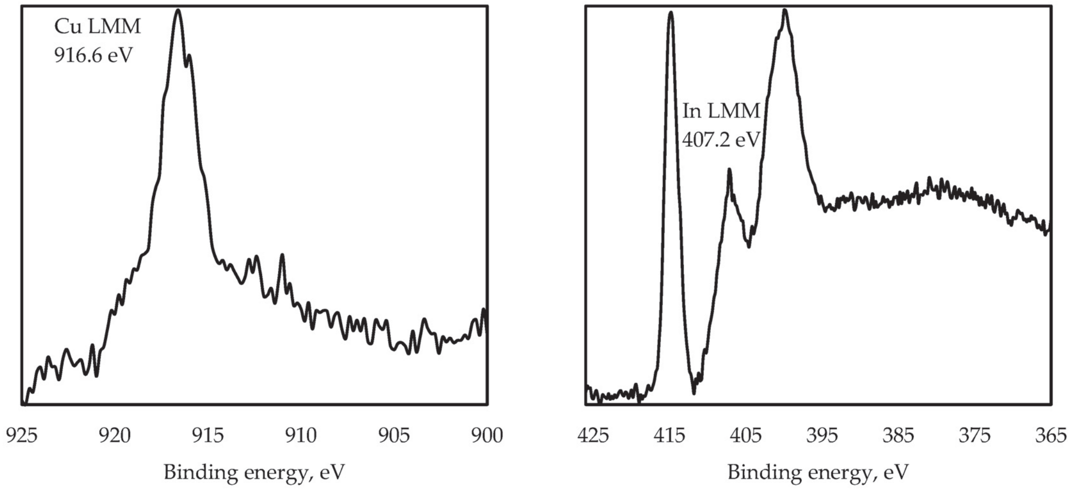

(**a**) (**b**)

Figure 3. XPS signal corresponding to Cu LMM (**a**) and In LMM (**b**) Auger transitions of $CuInS_2$ QDs.

3.2. Absorption and PL Spectra

Figure 4 shows the PL spectrum of the obtained $CuInS_2$ QD aqueous solution at room temperature and its deconvolution result, as well as the absorption spectrum of the same solution.

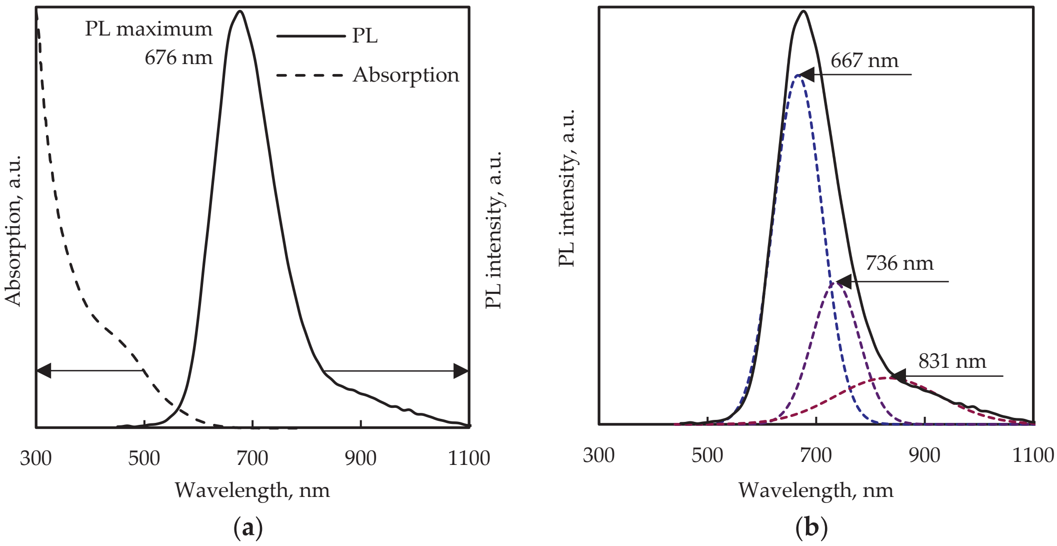

Figure 4. PL (solid line) and absorption spectra (dash line) of the $CuInS_2$ QD stock solution (**a**) and PL spectrum deconvolution result (**b**).

The obtained sample shows features common to I-III-VI QDs, such as the absence of an absorption exciton peak and a broad PL band with a large Stokes shift. The PL curve, represented by a peak with a maximum at about 676 nm and an FWHM parameter at about 115 nm, can be qualitatively decomposed as the sum of three Gaussian functions with maxima at about 667, 736, and 831 nm. It can be assumed that the radiative recombination in the studied sample is due to three mechanisms. The large Stokes shift, which is about 290 meV, indicates the emission mechanism associated with defects, and the absence of the interband radiative recombination component. There are several main theories under consideration for the observed characteristic of PL in Cu-In-S nanocrystals. In the first model, emission is associated with the trapping of photoexcited charge carriers on donor and acceptor defects, followed by radiative recombination (a mechanism involving donor–acceptor pairs) [32]. The transition energy in this case also depends on the Coulomb interaction of ionized defects, and hence, on their relative spatial localization, which is a source of additional broadening of the PL spectrum. The acceptor levels can be represented by point defects (e.g., V_{Cu}) and even group I atom centers in their regular lattice positions (Cu^+, Cu^{2+}), and the donor levels of In_{Cu}, V_S, In_i. According to this approach, the two emission channels can correspond to the donor–acceptor pairs V_{Cu}–In_{Cu} (relatively short wavelength band) and V_{Cu}–V_S (long wavelength band). Another approach to explaining the optical properties of Cu-In-S nanocrystals involves photoexcited hole trapping at Cu^+ sites followed by recombination with a delocalized photoexcited electron [33]. In this case, the Stokes shift is governed by the strong electron–phonon interaction, and the dependence of the transition energy on the crystal size can be easily explained by the change in the energy of the LUMO orbital due to quantum confinement. This model is in good agreement with the results of cyclic voltammetry studies and time-resolved absorption spectroscopy [33,34]. It cannot be ruled out that both mechanisms coexist simultaneously. States associated with surface defects may also be involved in the process of radiative recombination.

The PL spectra of the size-dependent $CuInS_2$ QDs are shown in Figure 5.

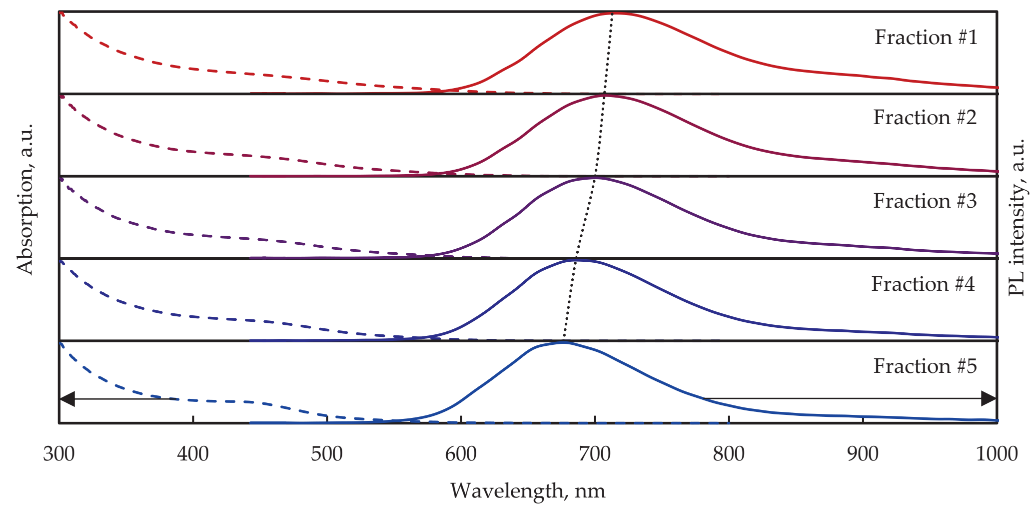

Figure 5. PL (solid lines) and absorption spectra (dash lines) of size-selected $CuInS_2$ QDs in aqueous solution.

Each consecutive precipitation yields a smaller average size fraction (designated fraction ordered from the largest (#1) to the smallest (#5), leading to a blue shift in the PL spectrum (from 713 nm to 677 nm), which, assuming that PL occurs via recombination of the localized hole with the delocalized electron, is caused by a rise in the conduction band bottom due to the effect of spatial quantization [35]. There is a tail extending from 850 nm on the PL spectra of every sample caused by emission through the surface states. According to the TEM images (Figure S1), the particles in fraction #1 are noticeably larger, with sizes from around 4 nm; in fraction #5, the particles do not exceed 3 nm.

3.3. Temperature-Dependent Photoluminescence

Nanoparticle samples were dried, powdered, and made into transparent films by mixing them with KBr. Figure 6 shows the PL spectra of the $CuInS_2$ QDs of separated fractions at room temperature and 11 K.

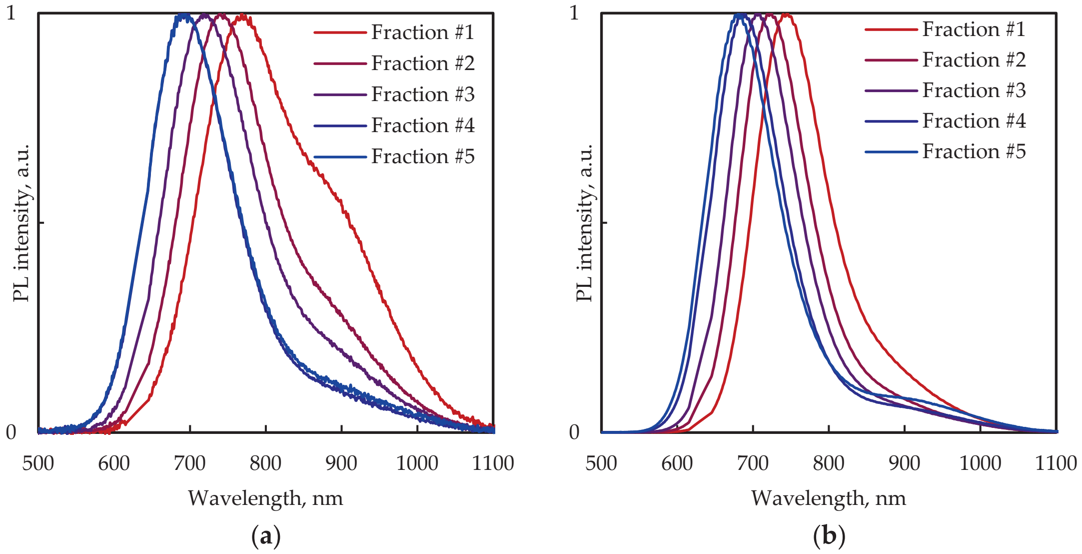

(**a**) (**b**)

Figure 6. Normalized PL spectra of size-selected $CuInS_2$ QDs in KBr pellets at 300 K (**a**) and 11 K (**b**).

The PL spectra of size-selected $CuInS_2$ QDs in KBr pellets at 300 K have at least two PL bands in range of 690–770 nm and around 900 nm. For fractions #1 and #2 (large particles) at room temperature, the shoulder at around 900 nm is more pronounced than for fractions

#3–#5. In contrast, the shoulder becomes more distinct with decreasing temperature for fractions #4 and #5.

The general trend of the blue shift of PL spectra with decreasing QD size is retained for the samples prepared in a KBr pellet. The PL peak position shifts from around 1.61 eV for fraction #1 to 1.78 eV for fraction #5 at room temperature (Figure 6a) and from 1.66 eV to 1.82 eV at 11 K (Figure 6b). The PL spectra curves of fractions #4 and #5 of the $CuInS_2$ QDs in the KBr pellet almost coincide at room temperature. Upon cooling down to 11 K the PL maximum positions of these fractions slightly diverge and the PL spectra of these fractions are well resolved (Figure 7).

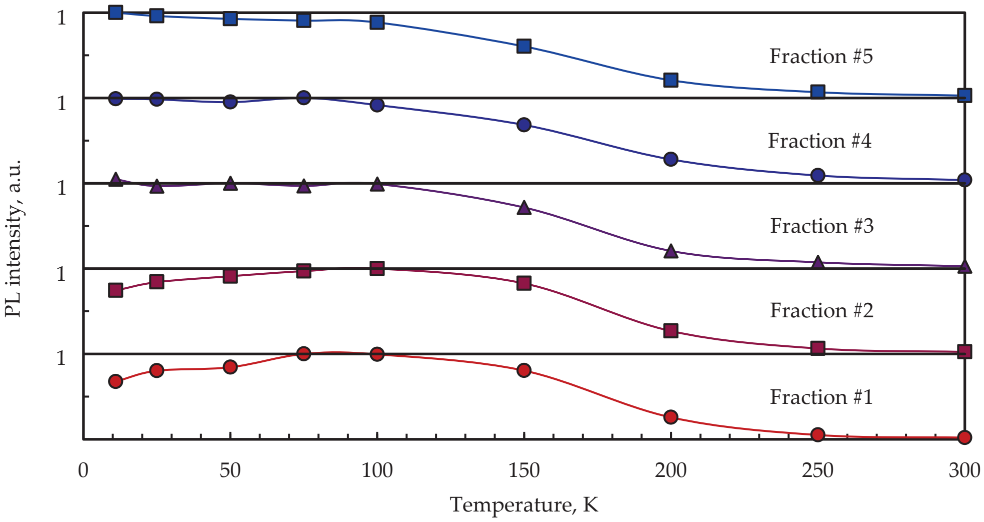

Figure 7. Temperature dependence of the PL integral intensity of size-selected $CuInS_2$ QDs in KBr pellets.

The profile of the PL spectra of the $CuInS_2$ QD samples exhibits strong temperature dependence in the range of 11–300 K. The temperature decrease leads to a shift in the emission maximum to higher energies and pronounced growth of the PL intensity up to 75–100 K. A further decrease in PL intensity with decreasing temperature occurs for fractions #1 and #2 (large particles), while no such trend is observed for fractions #3, #4, and #5 (small particles), which does not experience PL intensity change below 75 K.

The temperature dependence of the integral PL intensity could be associated with the recombination rate (Equation (1)). The thermal dependence of the recombination rate has an activation characteristic and includes the radiative and nonradiative parts (Equation (2)). As the nonradiative component of the decay rate goes down with decreasing temperature, the intensity dependence reaches saturation below 100 K (becoming solely a function of the radiative decay rate, which is temperature-independent).

$$I(t) = \sum_{i=1}^{3} a_i e^{\left(-\frac{t}{\tau_i}\right)}, \tag{1}$$

$$\frac{1}{\tau(T)} = \frac{1}{\tau_r} + \frac{1}{\tau_{nr}(0)} e^{\left(-\frac{E_a}{k_B T}\right)}, \tag{2}$$

In the above equations, τ_r and τ_{nr} are the radiative and nonradiative decay times, respectively, E_a is the thermal activation energy, and k_B is the Boltzmann constant.

The observed decrease in PL intensity below 100 K in larger fractions of QDs of the I–III–VI ternary systems may be explained in view of the assumption that the radiative decay time increases with increasing nanocrystal size due to an increasing ligand-to-QD ratio. In our case, molecules up to 700 MPA can coordinate QDs from a small fraction, and molecules up to 1200 MPA can bind to QDs from a large fraction. An increased ligand-to-

QD ratio resulted in a higher probability of the charge carrier trapping process occurring, which, for small QDs, leads to decreasing PL lifetimes.

Assuming the DAP emission model, the radiative recombination rate ($1/\tau_r$) should depend on the distance between the donor and acceptor centers. Given that there are numerous emission channels with different rates, the PL decay profile is multiexponential. In [36], the authors analyzed the temperature dependence of the PL of silicon nanoparticles of different sizes in a temperature range of 5–300 K. The authors also observed a decrease in PL intensity with decreasing temperature below 70 K. A less pronounced decrease in PL intensity was registered for small nanoparticles. The authors also provided time-resolved PL measurements for the samples, and found a correlation between particle size and PL quenching rate. At a certain temperature, the large crystals experienced a greater saturation effect than the smaller ones due to their longer PL lifetime. In $CuInS_2$ QDs, the decay time of PL similarly decreased with decreasing particle size [37]. Accordingly, these considerations could be applied to explain the temperature dependence of integral PL intensity in our samples.

Figure 8 shows the temperature-dependent PL emission maximum shift for five size-selected samples of $CuInS_2$ QDs embedded in KBr. As the temperature increases, all the samples show a decrease in emission energy of several tens of meV. A similar trend was observed in nanocrystalline binary systems [38–40] and self-assembled QDs [41,42], as well. This effect could be attributed to thermally induced population redistribution across inhomogeneously broadened states.

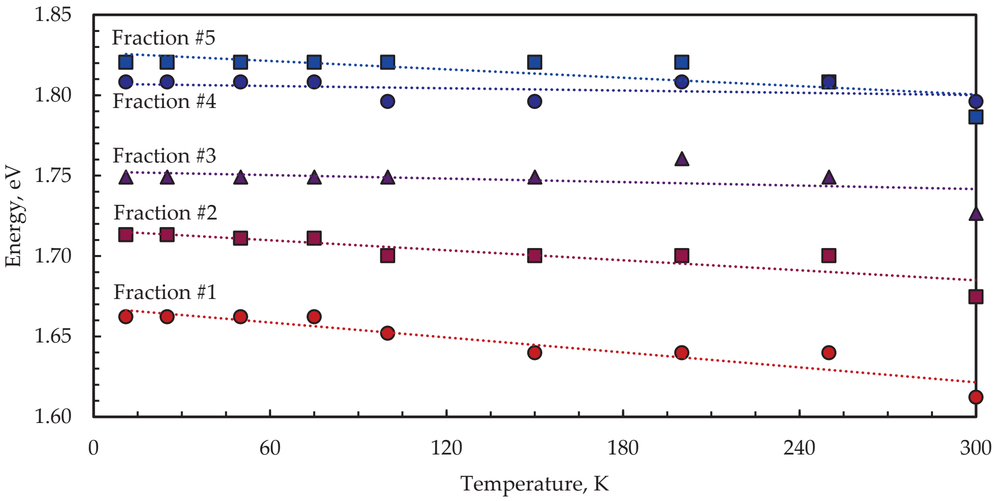

Figure 8. Temperature dependence of the PL peak maximum of size-selected $CuInS_2$ QDs in KBr pellets.

The energy of the PL peak intensity of the transitions E_{max} is determined via the convolution of the density of states (DOS) and the state population functions. The temperature dependence of E_{max} is given by the following expression:

$$E_{max}(T) = E_0(0) - \frac{\alpha T^2}{\beta + T} - \frac{\sigma^2}{(kT)}, \quad (3)$$

where $E_0(0)$ is the DOS maximum energy at 0 K, α and β are the Varshni parameters, σ is the dispersion of the DOS function, and k is the Boltzmann constant. According to (3), if an ensemble of states is broadened with the dispersion σ, the peak energy E_{max} is shifted by $-\sigma^2/kT$ relative to E_0.

The direct band-to-band transition is not a determinant of the PL properties, and $CuInS_2$ QD emission occurs due to the involvement of copper-related levels [34]. The optical properties of $CuInS_2$ QDs thus strongly resemble those of copper-doped binary

II–VI and III–V QDs [43]. The copper centers form optically active levels within the bandgap near the valence band edge in binary II–VI systems, e.g., ZnS, ZnSe CdS, and CdSe [44–47]. Notably, according to [44], in ZnS:Cu^{2+}, copper levels shift with the valence band as the temperature changes, which allows us to assume that Varshni's law, with some modification, is applicable to the temperature-dependent PL characterization of $CuInS_2$ QDs.

Figure 9 shows the PL FWHM temperature dependence of $CuInS_2$ QDs in KBr pellets for five different QD sizes. In a lower temperature range below 120 K, the dependence of FWHM on temperature is weak. A further temperature increase leads to PL curve broadening for all fractions, so that the difference between FWHMs becomes negligible at room temperature. Emission FWHM analysis with temperature variation provides information about the exciton–phonon interaction in QDs. The experimental data could be modeled using Equation (4), defining the temperature dependence of exciton peak broadening in bulk semiconductors. The total emission width is described as the sum of an inhomogeneous broadening term, which is connected with QD size distribution and terms representing homogeneous broadening, mainly due to optical phonon–exciton interactions.

$$\Gamma(T) = \Gamma_{inh} + \Gamma_{LO}\left(e^{\frac{E_{LO}}{kT}} - 1\right)^{-1} \tag{4}$$

Γ_{inh}—the temperature-independent intrinsic inhomogeneous line width;
Γ_{LO}—the longitudinal optical (LO) phonon–exciton coupling coefficient;
E_{LO}—the LO phonon energy.

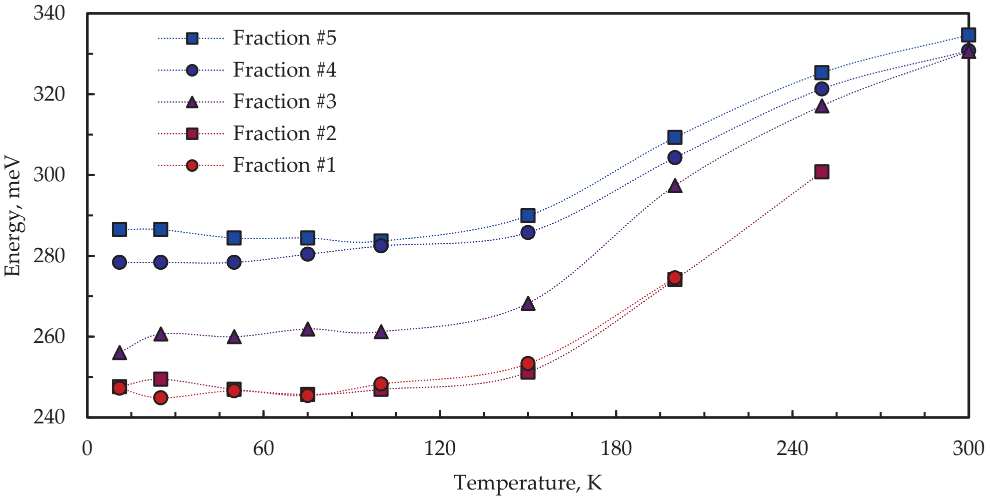

Figure 9. Temperature dependence of PL FWHM of size-selected $CuInS_2$ QDs in KBr pellets.

Applying a numerical value of E_{LO} equal to 36 meV obtained via Raman spectroscopy in [48,49], the authors of [27] determined the values of Γ_{inh} and Γ_{LO} to be 320 meV and 0.1 meV for the whole $CuInS_2$ QD stock ensemble. In our case, the values of Γ_{inh} and Γ_{LO} varied with fraction size in the ranges 245–280 meV and 80–110 meV, respectively. The assessed Γ_{LO} values appear to be too high. The broadening of the PL curve with increasing temperature is likely more complex than being attributed to electron–phonon coupling, potentially necessitating the consideration of various thermally activated emission centers. The narrowing of the PL curve with decreasing temperature may be linked to the influence of surface ligands.

In [50], the authors suggested that thiol groups could influence the PL emission properties of aqueous I–III–VI QDs through the transfer of a hole to the redox level of surface-bound disulfides formed via ligand oxidation. In our previous work [21], though, we observed very little narrowing of the PL curve with decreasing temperature for non-thiol

(thiol-less) PVP-capped $AgInS_2$ QDs. It is likely that the stabilization mechanism of these QDs is based on the interaction of oxygen from PVP with the QD surface. Given the higher electronegativity of oxygen, its electron-donating ability is weaker, thus making ligand oxidation (hole trapping) less probable. For the smallest QDs (fraction #5), in contrast to other fractions, the FWHM slightly increased below 100 K, which could be due to the exciton leakage effect [51].

4. Conclusions

In conclusion, $CuInS_2$ quantum dots (QDs) were synthesized in aqueous solution utilizing MPA as a ligand. For our studies, nanoparticles of different sizes were obtained via size-selective precipitation. The temperature-dependent photoluminescence (PL) spectra of $CuInS_2$ QDs were examined in the temperature range of 11–300 K. It was found that the temperature decrease led to a shift in the emission maximum to higher energies and a decrease in PL intensity down to 75–100 K, with a further decrease observed for larger nanoparticles below 75 K, whereas small nanoparticles did not display any alteration in PL intensity at lower temperatures. The shift in the PL peak towards higher energies with decreasing temperature was linked to the change in the convolution of the density of states and the state population functions. The observed PL line broadening with increasing temperature was associated with the influence of surface thiol ligands. It was discovered that the intricate relationship between integral intensity and temperature involves the size of $CuInS_2$ QDs. A temperature sensor design based on QDs should consider both the dimensions and size distribution of the QDs employed. Our observations could be useful for better understanding the luminescence mechanism in $CuInS_2$ QDs.

Supplementary Materials: The following supporting information can be downloaded at: https://www.mdpi.com/article/10.3390/nano13212892/s1, Figure S1: TEM image of the fraction #1 (a) and fraction #5 (b) of $CuInS_2$ QDs; Table S1: PL parameters of size-selected QDs in solution; Table S2: Γ_{inh} and Γ_{LO} values calculated using Formula (4) for the different fractions; Figure S2: Normalized PL spectra of size-selected $CuInS_2$ QDs in KBr pellets in temperature range of 11–300 K. Fractions #1–#5 presented in (a–e). Temperature dependence of the PL integral intensity of the same samples (f).

Author Contributions: Conceptualization, O.K.; absorption spectra measurements, O.K.; TEM measurements, D.K. (Demid Kirilenko); XRD measurements, A.B.; XPS measurements, Z.S.; PL measurements, D.F.; writing—original draft preparation, O.K.; data curation, O.K., O.A., A.B., Z.S. and D.M.; writing—review and editing, O.K. and D.K. (Dmitriy Kozodaev); visualization, O.K.; supervision, O.K., V.M. and D.K. (Dmitriy Kozodaev); resources, V.M. and D.K. (Dmitriy Kozodaev); project administration, O.K. All authors have read and agreed to the published version of the manuscript.

Funding: The APC was funded by NT-MDT BV.

Data Availability Statement: The data that support the findings of this study are available from the corresponding author upon reasonable request.

Acknowledgments: TEM tests were performed using equipment of the Federal Joint Research Center "Material science and characterization in advanced technology", supported by the Ministry of Science and Higher Education of the Russian Federation. X-ray diffraction experiments were performed using Engineering Center equipment of the St. Petersburg State Technological Institute (Technical University).

Conflicts of Interest: The authors declare no conflict of interest.

References

1. Yin, X.; Zhang, C.; Guo, Y.; Yang, Y.; Xing, Y.; Que, W. PbS QD-Based Photodetectors: Future-Oriented near-Infrared Detection Technology. *J. Mater. Chem. C* **2021**, *9*, 417–438. [CrossRef]
2. Matea, C.; Mocan, T.; Tabaran, F.; Pop, T.; Mosteanu, O.; Puia, C.; Iancu, C.; Mocan, L. Quantum Dots in Imaging, Drug Delivery and Sensor Applications. *IJN* **2017**, *12*, 5421–5431. [CrossRef] [PubMed]
3. Reshma, V.G.; Mohanan, P.V. Quantum Dots: Applications and Safety Consequences. *J. Lumin.* **2019**, *205*, 287–298. [CrossRef]

4. Bera, D.; Qian, L.; Tseng, T.-K.; Holloway, P.H. Quantum Dots and Their Multimodal Applications: A Review. *Materials* **2010**, *3*, 2260–2345. [CrossRef]
5. Liu, Z.; Lin, C.-H.; Hyun, B.-R.; Sher, C.-W.; Lv, Z.; Luo, B.; Jiang, F.; Wu, T.; Ho, C.-H.; Kuo, H.-C.; et al. Micro-Light-Emitting Diodes with Quantum Dots in Display Technology. *Light Sci. Appl.* **2020**, *9*, 83. [CrossRef]
6. Kauffer, F.-A.; Merlin, C.; Balan, L.; Schneider, R. Incidence of the Core Composition on the Stability, the ROS Production and the Toxicity of CdSe Quantum Dots. *J. Hazard. Mater.* **2014**, *268*, 246–255. [CrossRef]
7. Zhang, Y.; Chen, W.; Zhang, J.; Liu, J.; Chen, G.; Pope, C. In Vitro and In Vivo Toxicity of CdTe Nanoparticles. *J. Nanosci. Nanotechnol.* **2007**, *7*, 497–503. [CrossRef]
8. Tarantini, A.; Wegner, K.D.; Dussert, F.; Sarret, G.; Beal, D.; Mattera, L.; Lincheneau, C.; Proux, O.; Truffier-Boutry, D.; Moriscot, C.; et al. Physicochemical Alterations and Toxicity of InP Alloyed Quantum Dots Aged in Environmental Conditions: A Safer by Design Evaluation. *NanoImpact* **2019**, *14*, 100168. [CrossRef]
9. Liu, N.; Tang, M. Toxicity of Different Types of Quantum Dots to Mammalian Cells in Vitro: An Update Review. *J. Hazard. Mater.* **2020**, *399*, 122606. [CrossRef]
10. Girma, W.M.; Fahmi, M.Z.; Permadi, A.; Abate, M.A.; Chang, J.-Y. Synthetic Strategies and Biomedical Applications of I–III–VI Ternary Quantum Dots. *J. Mater. Chem. B* **2017**, *5*, 6193–6216. [CrossRef]
11. Zhong, H.; Bai, Z.; Zou, B. Tuning the Luminescence Properties of Colloidal I–III–VI Semiconductor Nanocrystals for Optoelectronics and Biotechnology Applications. *J. Phys. Chem. Lett.* **2012**, *3*, 3167–3175. [CrossRef] [PubMed]
12. Huang, W.-T.; Yoon, S.-Y.; Wu, B.-H.; Lu, K.-M.; Lin, C.-M.; Yang, H.; Liu, R.-S. Ultra-Broadband near-Infrared Emission $CuInS_2/ZnS$ Quantum Dots with High Power Efficiency and Stability for the Theranostic Applications of Mini Light-Emitting Diodes. *Chem. Commun.* **2020**, *56*, 8285–8288. [CrossRef] [PubMed]
13. Chetty, S.S.; Praneetha, S.; Vadivel Murugan, A.; Govarthanan, K.; Verma, R.S. Human Umbilical Cord Wharton's Jelly-Derived Mesenchymal Stem Cells Labeled with Mn^{2+} and Gd^{3+} Co-Doped $CuInS_2$–ZnS Nanocrystals for Multimodality Imaging in a Tumor Mice Model. *ACS Appl. Mater. Interfaces* **2020**, *12*, 3415–3429. [CrossRef] [PubMed]
14. Gao, X.; Liu, Z.; Lin, Z.; Su, X. CuInS2 Quantum Dots/Poly(l-Glutamic Acid)–Drug Conjugates for Drug Delivery and Cell Imaging. *Analyst* **2014**, *139*, 831. [CrossRef] [PubMed]
15. Korepanov, O.A.; Mazing, D.S.; Aleksandrova, O.A.; Moshnikov, V.A. Synthesis and Study of Colloidal Nanocrystals Based on Ternary Chalcogenides for Active Media of Heavy Metal Ions Sensors. In Proceedings of the 2019 IEEE Conference of Russian Young Researchers in Electrical and Electronic Engineering (EIConRus), Saint Petersburg/Moscow, Russia, 28–31 January 2019; IEEE: Saint Petersburg and Moscow, Russia, 2019; pp. 771–773.
16. Jain, S.; Bharti, S.; Bhullar, G.K.; Tripathi, S.K. Synthesis, Characterization and Stability Study of Aqueous MPA Capped $CuInS_2/ZnS$ Core/Shell Nanoparticles. *J. Lumin.* **2022**, *252*, 119279. [CrossRef]
17. Mazing, D.S.; Chernaguzov, I.S.; Shulga, A.I.; Korepanov, O.A.; Aleksandrova, O.A.; Moshnikov, V.A. Synthesis of Ternary Chalcogenide Colloidal Nanocrystals in Aqueous Medium. *J. Phys. Conf. Ser.* **2018**, *1038*, 012050. [CrossRef]
18. Liu, Z.; Ma, Q.; Wang, X.; Lin, Z.; Zhang, H.; Liu, L.; Su, X. A Novel Fluorescent Nanosensor for Detection of Heparin and Heparinase Based on $CuInS_2$ Quantum Dots. *Biosens. Bioelectron.* **2014**, *54*, 617–622. [CrossRef]
19. An, X.; Zhang, Y.; Wang, J.; Kong, D.; He, X.; Chen, L.; Zhang, Y. The Preparation of $CuInS_2$-ZnS-Glutathione Quantum Dots and Their Application on the Sensitive Determination of Cytochrome *c* and Imaging of HeLa Cells. *ACS Omega* **2021**, *6*, 17501–17509. [CrossRef]
20. Amaral-Júnior, J.C.; Mansur, A.A.P.; Carvalho, I.C.; Mansur, H.S. Tunable Luminescence of Cu-In-S/ZnS Quantum Dots-Polysaccharide Nanohybrids by Environmentally Friendly Synthesis for Potential Solar Energy Photoconversion Applications. *Appl. Surf. Sci.* **2021**, *542*, 148701. [CrossRef]
21. Korepanov, O.; Aleksandrova, O.; Firsov, D.; Kalazhokov, Z.; Kirilenko, D.; Kozodaev, D.; Matveev, V.; Mazing, D.; Moshnikov, V. Polyvinylpyrrolidone as a Stabilizer in Synthesis of $AgInS_2$ Quantum Dots. *Nanomaterials* **2022**, *12*, 2357. [CrossRef]
22. Haouari, M.; Maaoui, A.; Saad, N.; Bulou, A. Optical Temperature Sensing Using Green Emissions of Er^{3+} Doped Fluoro-Tellurite Glass. *Sens. Actuators A Phys.* **2017**, *261*, 235–242. [CrossRef]
23. Meert, K.W.; Morozov, V.A.; Abakumov, A.M.; Hadermann, J.; Poelman, D.; Smet, P.F. Energy Transfer in Eu^{3+} Doped Scheelites: Use as Thermographic Phosphor. *Opt. Express* **2014**, *22*, A961. [CrossRef] [PubMed]
24. Zhong, J.; Chen, D.; Peng, Y.; Lu, Y.; Chen, X.; Li, X.; Ji, Z. A Review on Nanostructured Glass Ceramics for Promising Application in Optical Thermometry. *J. Alloys Compd.* **2018**, *763*, 34–48. [CrossRef]
25. Iida, K.; Kim, D. Temperature-Dependent Photoluminescence Properties of Water-Soluble $CuInS_2$ and $CuInS_2/ZnS$ Quantum Dots. *J. Appl. Phys.* **2022**, *132*, 194306. [CrossRef]
26. Xia, C.; Wu, W.; Yu, T.; Xie, X.; Van Oversteeg, C.; Gerritsen, H.C.; De Mello Donega, C. Size-Dependent Band-Gap and Molar Absorption Coefficients of Colloidal $CuInS_2$ Quantum Dots. *ACS Nano* **2018**, *12*, 8350–8361. [CrossRef]
27. Shi, A.; Wang, X.; Meng, X.; Liu, X.; Li, H.; Zhao, J. Temperature-Dependent Photoluminescence of $CuInS_2$ Quantum Dots. *J. Lumin.* **2012**, *132*, 1819–1823. [CrossRef]
28. Mir, I.A.; Das, K.; Akhter, T.; Ranjan, R.; Patel, R.; Bohidar, H.B. Eco-Friendly Synthesis of $CuInS_2$ and $CuInS_2$@ZnS Quantum Dots and Their Effect on Enzyme Activity of Lysozyme. *RSC Adv.* **2018**, *8*, 30589–30599. [CrossRef]

29. Speranskaya, E.S.; Sevrin, C.; De Saeger, S.; Hens, Z.; Goryacheva, I.Y.; Grandfils, C. Synthesis of Hydrophilic $CuInS_2$/ZnS Quantum Dots with Different Polymeric Shells and Study of Their Cytotoxicity and Hemocompatibility. *ACS Appl. Mater. Interfaces* **2016**, *8*, 7613–7622. [CrossRef]
30. Firsov, D.D.; Komkov, O.S.; Solov'ev, V.A.; Kop'ev, P.S.; Ivanov, S.V. Temperature-Dependent Photoluminescence of InSb/InAs Nanostructures with InSb Thickness in the above-Monolayer Range. *J. Phys. D Appl. Phys.* **2016**, *49*, 285108. [CrossRef]
31. Landry, C.C.; Barron, A.R. Synthesis of Polycrystalline Chalcopyrite Semiconductors by Microwave Irradiation. *Science* **1993**, *260*, 1653–1655. [CrossRef]
32. Chen, B.; Zhong, H.; Zhang, W.; Tan, Z.; Li, Y.; Yu, C.; Zhai, T.; Bando, Y.; Yang, S.; Zou, B. Highly Emissive and Color-Tunable $CuInS_2$-Based Colloidal Semiconductor Nanocrystals: Off-Stoichiometry Effects and Improved Electroluminescence Performance. *Adv. Funct. Mater.* **2012**, *22*, 2081–2088. [CrossRef]
33. Berends, A.C.; Rabouw, F.T.; Spoor, F.C.M.; Bladt, E.; Grozema, F.C.; Houtepen, A.J.; Siebbeles, L.D.A.; de Mello Donegá, C. Radiative and Nonradiative Recombination in $CuInS_2$ Nanocrystals and $CuInS_2$-Based Core/Shell Nanocrystals. *J. Phys. Chem. Lett.* **2016**, *7*, 3503–3509. [CrossRef]
34. Fuhr, A.S.; Yun, H.J.; Makarov, N.S.; Li, H.; McDaniel, H.; Klimov, V.I. Light Emission Mechanisms in $CuInS_2$ Quantum Dots Evaluated by Spectral Electrochemistry. *ACS Photonics* **2017**, *4*, 2425–2435. [CrossRef]
35. Zang, H.; Li, H.; Makarov, N.S.; Velizhanin, K.A.; Wu, K.; Park, Y.-S.; Klimov, V.I. Thick-Shell $CuInS_2$/ZnS Quantum Dots with Suppressed "Blinking" and Narrow Single-Particle Emission Line Widths. *Nano Lett.* **2017**, *17*, 1787–1795. [CrossRef] [PubMed]
36. Rinnert, H.; Jambois, O.; Vergnat, M. Photoluminescence Properties of Size-Controlled Silicon Nanocrystals at Low Temperatures. *J. Appl. Phys.* **2009**, *106*, 023501. [CrossRef]
37. Sun, J.; Ikezawa, M.; Wang, X.; Jing, P.; Li, H.; Zhao, J.; Masumoto, Y. Photocarrier Recombination Dynamics in Ternary Chalcogenide $CuInS_2$ Quantum Dots. *Phys. Chem. Chem. Phys.* **2015**, *17*, 11981–11989. [CrossRef]
38. Kalytchuk, S.; Zhovtiuk, O.; Kershaw, S.V.; Zbořil, R.; Rogach, A.L. Temperature-Dependent Exciton and Trap-Related Photoluminescence of CdTe Quantum Dots Embedded in a NaCl Matrix: Implication in Thermometry. *Small* **2016**, *12*, 466–476. [CrossRef]
39. Jing, P.; Zheng, J.; Ikezawa, M.; Liu, X.; Lv, S.; Kong, X.; Zhao, J.; Masumoto, Y. Temperature-Dependent Photoluminescence of CdSe-Core CdS/CdZnS/ZnS-Multishell Quantum Dots. *J. Phys. Chem. C* **2009**, *113*, 13545–13550. [CrossRef]
40. Joshi, A.; Narsingi, K.Y.; Manasreh, M.O.; Davis, E.A.; Weaver, B.D. Temperature Dependence of the Band Gap of Colloidal CdSe/ZnS Core/Shell Nanocrystals Embedded into an Ultraviolet Curable Resin. *Appl. Phys. Lett.* **2006**, *89*, 131907. [CrossRef]
41. Alphandéry, E.; Nicholas, R.J.; Mason, N.J.; Lyapin, S.G.; Klipstein, P.C. Photoluminescence of Self-Assembled InSb Quantum Dots Grown on GaSb as a Function of Excitation Power, Temperature, and Magnetic Field. *Phys. Rev. B* **2002**, *65*, 115322. [CrossRef]
42. Eliseev, P.G.; Osinski, M.; Lee, J.; Sugahara, T.; Sakai, S. Band-Tail Model and Temperature-Induced Blue-Shift in Photoluminescence Spectra of $In_xGa_{1-x}N$ Grown on Sapphire. *J. Elec. Mater.* **2000**, *29*, 332–341. [CrossRef]
43. Knowles, K.E.; Nelson, H.D.; Kilburn, T.B.; Gamelin, D.R. Singlet–Triplet Splittings in the Luminescent Excited States of Colloidal Cu^+:CdSe, Cu^+:InP, and $CuInS_2$ Nanocrystals: Charge-Transfer Configurations and Self-Trapped Excitons. *J. Am. Chem. Soc.* **2015**, *137*, 13138–13147. [CrossRef]
44. Bol, A.A.; Ferwerda, J.; Bergwerff, J.A.; Meijerink, A. Luminescence of Nanocrystalline ZnS:Cu^{2+}. *J. Lumin.* **2002**, *99*, 325–334. [CrossRef]
45. Suyver, J.F.; van der Beek, T.; Wuister, S.F.; Kelly, J.J.; Meijerink, A. Luminescence of Nanocrystalline ZnSe:Cu. *Appl. Phys. Lett.* **2001**, *79*, 4222–4224. [CrossRef]
46. Stouwdam, J.W.; Janssen, R.A.J. Electroluminescent Cu-Doped CdS Quantum Dots. *Adv. Mater.* **2009**, *21*, 2916–2920. [CrossRef]
47. Meulenberg, R.W.; van Buuren, T.; Hanif, K.M.; Willey, T.M.; Strouse, G.F.; Terminello, L.J. Structure and Composition of Cu-Doped CdSe Nanocrystals Using Soft X-Ray Absorption Spectroscopy. *Nano Lett.* **2004**, *4*, 2277–2285. [CrossRef]
48. Uehara, M.; Watanabe, K.; Tajiri, Y.; Nakamura, H.; Maeda, H. Synthesis of $CuInS_2$ Fluorescent Nanocrystals and Enhancement of Fluorescence by Controlling Crystal Defect. *J. Chem. Phys.* **2008**, *129*, 134709. [CrossRef] [PubMed]
49. Courtel, F.M.; Paynter, R.W.; Marsan, B.; Morin, M. Synthesis, Characterization, and Growth Mechanism of n-Type $CuInS_2$ Colloidal Particles. *Chem. Mater.* **2009**, *21*, 3752–3762. [CrossRef]
50. Miropoltsev, M.; Wegner, K.D.; Häusler, I.; Hodoroaba, V.-D.; Resch-Genger, U. Influence of Hydrophilic Thiol Ligands of Varying Denticity on the Luminescence Properties and Colloidal Stability of Quaternary Semiconductor Nanocrystals. *J. Phys. Chem. C* **2022**, *126*, 20101–20113. [CrossRef]
51. Karczewski, G.; Maćkowski, S.; Kutrowski, M.; Wojtowicz, T.; Kossut, J. Photoluminescence Study of CdTe/ZnTe Self-Assembled Quantum Dots. *Appl. Phys. Lett.* **1999**, *74*, 3011–3013. [CrossRef]

nanomaterials

MDPI

Article

Methods for Obtaining One Single Larmor Frequency, Either v_1 or v_2, in the Coherent Spin Dynamics of Colloidal Quantum Dots

Meizhen Jiang [1,†], Yuanyuan Zhang [1,†], Rongrong Hu [2,*], Yumeng Men [1], Lin Cheng [1], Pan Liang [3], Tianqing Jia [1], Zhenrong Sun [1] and Donghai Feng [1,4,*]

[1] State Key Laboratory of Precision Spectroscopy, East China Normal University, Shanghai 200241, China; 52200920010@stu.ecnu.edu.cn (M.J.); 52170920029@stu.ecnu.edu.cn (Y.Z.); 52250920010@stu.ecnu.edu.cn (Y.M.); 51210920033@stu.ecnu.edu.cn (L.C.); tqjia@phy.ecnu.edu.cn (T.J.); zrsun@phy.ecnu.edu.cn (Z.S.)
[2] College of Sciences, Shanghai Institute of Technology, Shanghai 201418, China
[3] College of Arts and Sciences, Shanghai Dianji University, Shanghai 201306, China; liangp@sdju.edu.cn
[4] Collaborative Innovation Center of Extreme Optics, Shanxi University, Taiyuan 030006, China
* Correspondence: hrr92@sit.edu.cn (R.H.); dhfeng@phy.ecnu.edu.cn (D.F.)
† These authors contributed equally to this work.

Abstract: The coexistence of two spin components with different Larmor frequencies in colloidal CdSe and CdS quantum dots (QDs) leads to the entanglement of spin signals, complicating the analysis of dynamic processes and hampering practical applications. Here, we explored several methods, including varying the types of hole acceptors, air or anaerobic atmosphere and laser repetition rates, in order to facilitate the obtention of one single Larmor frequency in the coherent spin dynamics using time-resolved ellipticity spectroscopy at room temperature. In an air or nitrogen atmosphere, manipulating the photocharging processes by applying different types of hole acceptors, e.g., Li[Et$_3$BH] and 1-octanethiol (OT), can lead to pure spin components with one single Larmor frequency. For as-grown QDs, low laser repetition rates favor the generation of the higher Larmor frequency spin component individually, while the lower Larmor frequency spin component can be enhanced by increasing the laser repetition rates. We hope that the explored methods can inspire further investigations of spin dynamics and related photophysical processes in colloidal nanostructures.

Keywords: colloidal quantum dots; spin dynamics; time-resolved spectroscopy; hole acceptors

1. Introduction

The electron spin in semiconductors is a promising candidate for quantum bits which are the elementary units for quantum information processing [1–3]. It is of fundamental importance to understand electron spin properties and further control the spins. Compared with bulk semiconductors, the confined electrons in quantum dots (QDs) are more adaptable to quantum information science, due to the less efficient spin–orbit interaction and longer spin dephasing times [4]. Over the past two decades, many efforts have been dedicated to investigating the spin properties and the spin manipulation in colloidal QDs grown using wet chemical approaches, obtaining long spin dephasing times up to few nanoseconds even at room temperature [5–7]. The open surface and surrounding matrix of colloidal QDs provide convenience for optical and chemical manipulation of electron spin [8–12]. In addition, colloidal QDs have the advantages of low cost and easily controlled shapes, sizes and structures. Since it was first reported by J. A. Gupta et al. that ensembles of colloidal CdSe QDs show two distinct spin components in the coherent dynamics, which differ in g factors and Larmor frequencies [13], colloidal CdS QDs [10] were also found to have similar phenomena. The coexistence of two spin components with different Larmor frequencies (referred to below as v_1 and v_2) entangles the spin signals and complicates the investigation of their origins and the related spin relaxation mechanisms. For instance, in ensembles of colloidal CdSe QDs, the v_1 and v_2 spins with spin dephasing times up to hundreds of picoseconds were assigned to the electron and exciton, respectively (electron–exciton model) [5], which is, however, contradictory to the fact that exciton spin relaxation times are short and have around a subpicosecond time scale [14]. Recently, the two spin components were redemonstrated to both belong to electrons in photocharged QDs, which have different wave function spreads, which were either confined by the QD potential (corresponding to the v_1 component) or additionally localized in the surface vicinity (corresponding to the v_2 component) [11]. Similarly, for CdSe nanocrystals embedded in a glass matrix, a solely detected Larmor precession frequency (corresponding to the v_2 component in solution-grown colloidal CdSe QDs) was also determined to arise from resident electrons localized in the vicinity of the surface [15]. However, a systematic investigation of separation and manipulation of the two spin components is still lacking. Obtaining one pure spin component is not only important for deeper understanding of the underlining spin relaxation mechanism and related photophysics but also crucial for the practical applications of quantum bits.

In this work, we investigated the spin signals of colloidal CdSe and CdS QDs in toluene using time-resolved ellipticity spectroscopy under different photocharging conditions, such as addition of different types of hole acceptors, changing laser repetitions as well as air and nitrogen (N_2) atmospheres. We systematically studied the methods that can contribute to obtaining or enhancing one single Larmor frequency, either v_1 or v_2, in the coherent spin dynamics. In a N_2 atmosphere, the addition of hole acceptor, either Li[Et_3BH] or 1-octanethiol (OT), is beneficial to obtain the spin signal of the v_1 component, while adding the OT hole acceptor in an air atmosphere usually brings the v_2 spin component into being separately. High laser repetition rates can enhance the spin signal of the v_1 component, whereas low laser repetition rates are convenient for obtaining the v_2 component alone.

2. Materials and Methods

2.1. Sample Preparation

Octadecylamine-stabilized colloidal CdSe (average diameter: 6.5 nm, estimated from the first exciton absorption peak [16]) and oleic-acid-stabilized CdS QDs (average diameter: 5.3 nm) in toluene solution were commercially obtained from Hangzhou Najing Technology Co., Ltd. (Hangzhou, China) The corresponding absorption spectra are shown in Figure 1. The mass concentration of all obtained QD samples is 5 mg/mL. For photocharging experiments, the well-known OT hole acceptor [17] or Li[Et_3BH] [18], purchased from Sigma Aldrich, was mixed with toluene solutions of CdSe or CdS QDs in an airtight quartz cuvette with a thickness of 1 mm. For Li[Et_3BH], the sample preparation was performed in a glove box in a N_2 atmosphere. The OT hole acceptor was mixed with QDs in either a N_2 or air atmosphere. The final concentrations of all samples in the measurements were kept the same at 2.5 mg/mL.

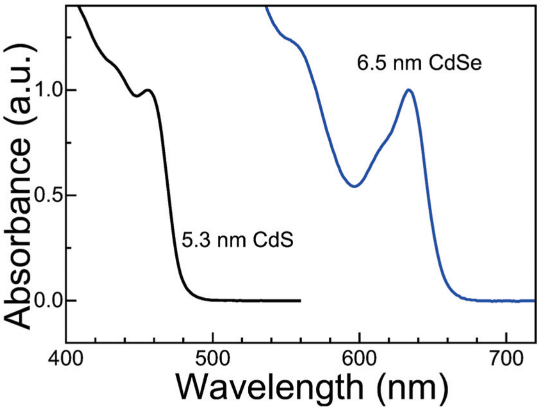

Figure 1. Absorption spectra of as-grown colloidal 6.5 nm CdSe and 5.3 nm CdS QDs. The intensity of the first absorption peak of CdSe and CdS QDs is normalized.

2.2. Setup for the Measurements of Coherent Electron Spin Dynamics

The coherent spin dynamics of colloidal QDs were measured using time-resolved ellipticity spectroscopy [11,19,20]. The experimental configuration depicted in Figure 2 is based on a ytterbium-doped potassium gadolinium tungstate (Yb-KGW) regenerative amplifier (PHAROS, Light Conversion Ltd; the central wavelength is 1026 nm, and the pulse duration is ~270 fs), combined with an optical parametric amplifier (OPA). The laser repetition rates of the OPA outputs are tunable and up to 50 kHz. All the measurements were performed at room temperature and in a transverse external magnetic field provided by an electromagnet with iron poles.

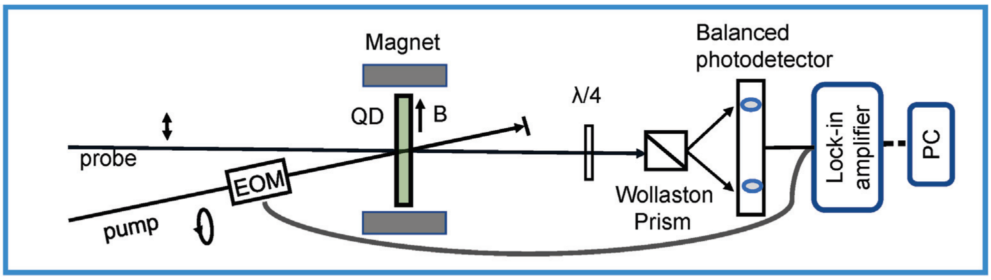

Figure 2. Setup schematic of time-resolved ellipticity measurements.

In the pump—probe measurements as shown in Figure 2, the pump and probe pulses are wavelength-degenerate and emitted from the OPA with their wavelength tuned at the low energy side of the first exciton absorption band. The circularly polarized pump pulses generate the spin polarization in the QD samples, while the subsequent dynamics of this spin polarization are monitored by the change of ellipticity of the linearly polarized probe pulses. The linearly polarized probe pulses become partially elliptically polarized after transmitting through the spin-polarized QDs because of the absorption difference of left- and right-circularly polarized light. The time delay between the pump and probe pulses is adjusted by a mechanical delay line.

3. Results

3.1. Spin Dynamics of As-Grown CdSe and CdS Colloidal QDs with Native Ligands

As-grown colloidal CdSe and CdS QDs with native ligands normally have two spin Larmor frequencies in coherent spin dynamics measured at high laser repetition rates. As shown in Figure 3, time-resolved ellipticity signals of as-grown colloidal CdSe and CdS QDs are measured in a transverse magnetic field B of 500 and 300 mT, respectively. The corresponding fast Fourier transform (FFT) spectra are shown in the right panels of Figure 3. Figure 3c is the fast Fourier transform (FFT) spectrum of the spin dynamics of CdSe QDs, which shows two Larmor precession frequencies of v_1 = 7.32 GHz and v_2 = 11.11 GHz. Two g factor values of g_1 = 1.05 and g_2 = 1.59 are correspondingly derived from these frequencies by the equation $g = hv_\mathrm{L}/(\mu_B B)$, where h, v_L and μ_B are the Planck constant, Larmor precession frequency and Bohr magneton, respectively. Both g factor values are in line with the size dependence of g factors reported in the literature [11]. Similarly, Figure 3d shows two Larmor precession frequencies and the corresponding g factors of CdS QDs of v_1 = 7.73 GHz, g_1 = 1.85, and v_2 = 8.12 GHz, g_2 = 1.93. Despite the FFT amplitudes and spin dynamic curves of CdSe and CdS QDs being distinctly different, both the spin signals comprise two Larmor frequencies (the smaller one refers to the v_1 component, and the larger one is the v_2 component). The FFT amplitude of the v_1 component is much smaller than that of the v_2 component in CdSe QDs, while it is the opposite in CdS QDs. The difference of relative FFT amplitudes may result from different surface ligands and their interactions with the QDs. It has been shown in the literature that the v_1 component is stronger than the v_2 component for as-grown 6 nm CdSe QDs with stearic acid stabilizing ligands [21], while the v_1 component is significantly weaker than the v_2 component for 6.1 nm CdSe QDs with octadecylamine stabilizing ligands [22]. In the following, we will provide appropriate methods which selectively bring one of the two spin components into being, or purposefully enhance one of them and suppress the other.

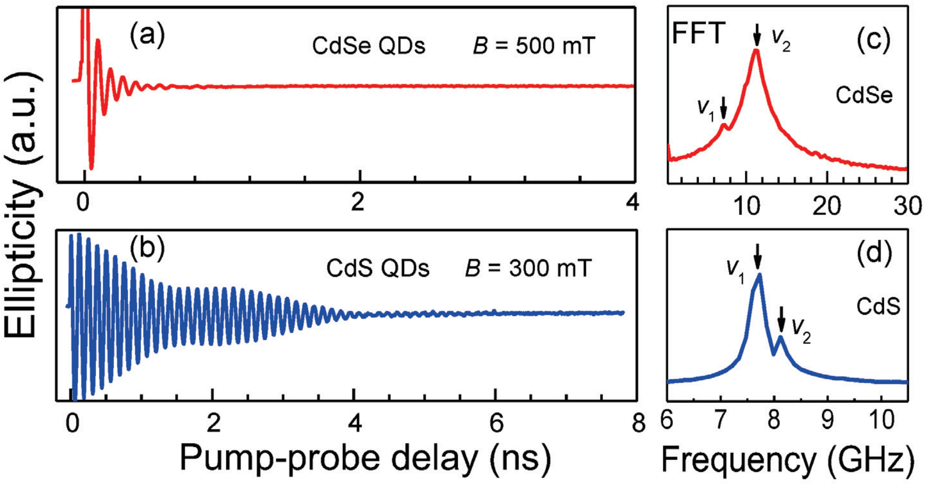

Figure 3. Time-resolved ellipticity signals in as-grown colloidal (**a**) CdSe and (**b**) CdS QDs. (**c**) and (**d**) are the fast Fourier transform (FFT) spectra of panel (**a**) and (**b**), respectively. The laser repetition rate is 50 kHz.

3.2. Methods to Individually Obtain the v_1 Component

Adding hole acceptors to the QD solutions is helpful in manipulating the spin signals. Figure 4a,b show time-resolved ellipticity signals in as-grown colloidal CdSe and CdS QDs and QDs with Li[Et$_3$BH] hole acceptors prepared in a N_2 atmosphere. The presence of the hole acceptor Li[Et$_3$BH] strongly increases the ellipticity signals both for CdSe and CdS QDs. As depicted in the insets of Figure 4a,b, actually only the v_1 component is remarkably enhanced, while the v_2 component disappears. This indicates that addition of Li[Et$_3$BH] hole acceptors in a N_2 atmosphere is conducive to separating the entangled spin signals by increasing the v_1 component and suppressing the v_2 component. The reason is that the Li[Et$_3$BH] hole acceptor, as a strong chemical reducing agent, can capture the photogenerated holes and leave the electrons in the dot core (corresponding to photocharging state of the v_1 component [11]). With enough Li[Et$_3$BH] molecules, all QDs could be charged to this state, and the spin signal of the v_2 component (which corresponds to another charging state [11]) is thus suppressed. With the removal of the influence of oxygen (as electron scavengers [23,24]) in a N_2 atmosphere, the photodoped electrons in the dot core are long-lived [18]. Under the irradiation of ambient room light and pump/probe pulses, the spin amplitudes of CdSe and CdS QDs with Li[Et$_3$BH] remain almost the same after two hours as shown in Figure 4c, indicating that stable photocharging can be obtained in CdSe and CdS QDs. Stable charging means that the generation of photocharging states can adequately compensate for their decay, which requires appropriate Li[Et$_3$BH] concentrations and appropriate light illumination conditions.

Consequently, an effective strategy to achieve pure states of the v_1 component is to modify colloidal QDs with Li[Et$_3$BH] hole acceptors in an anaerobic atmosphere. The spin signals of the v_1 component are considerably amplified, which also improves the signal-to-noise ratio significantly.

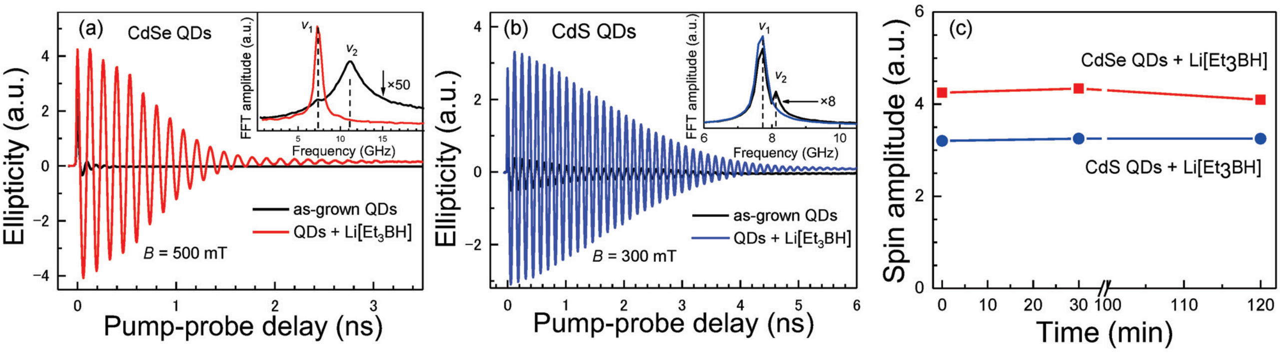

Figure 4. (**a**,**b**) Time-resolved ellipticity signals in as-grown colloidal CdSe and CdS QDs and QDs with Li[Et$_3$BH] prepared in a N_2 atmosphere. The insets are the corresponding FFT spectra of panel a and b. The FFT spectra of as-grown CdSe and CdS QDs are multiplied by 50 and 8, respectively, for better distinction of the two observed Larmor frequencies. (**c**) Spin amplitudes in CdSe and CdS QDs with Li[Et$_3$BH] as a function of time under ambient room light illumination. The molar ratio of Li[Et$_3$BH] to CdSe and CdS QDs is 500 and 10, respectively. The laser repetition rate is 50 kHz.

3.3. Methods to Individually Obtain the v_2 Component

Inspired by the success of individually obtainment of the v_1 spin component by modifying QDs surface with an appropriate hole acceptor in a N_2 atmosphere, we investigated the effect of adding another OT hole acceptor to QDs prepared in an air atmosphere. The comparison of the time-resolved ellipticity signals of CdSe QDs with and without OT prepared in an air atmosphere is shown in Figure 5a. Adding OT, the spin signal of the v_2 component increases to about 8 times that of as-grown QDs. The inset of Figure 5a shows that the FFT amplitude of v_2 enlarges, while v_1 disappears. A similar phenomenon can be found in the measurements in as-grown CdS QDs and QDs with OT prepared in an air atmosphere, as depicted in Figure 5b. The spin amplitude of the v_2 component significantly increases and brings the v_2 component into being separately. Note that the laser repetition for CdS QDs with OT is 10 kHz. Since with the higher laser repetition, i.e., with 50 kHz laser repetition, the spin signal of the v_1 component is apparent as a result of the pile-up effect from previous pulses. The v_1 component can appear at high laser repetition rates, and the higher the laser repetition rate, the stronger the intensity of the v_1 component, which will be illustrated below. For measurements with different laser repetition rates, a normalization of both pulse energies and laser powers is requisite. The spin signal of CdS QDs with OT measured at 10 kHz laser repetition rates in the main panel has already been multiplied by a factor of 5; equivalently, both the pulse energy and laser power are normalized to be the same between the measurements with 10 and 50 kHz laser repetition rates.

The following are possible reasons that account for the selective enhancement of the v_2 spin component by using OT hole acceptors. OT molecules are linked to the QD surface by replacing native ligands and capture the photogenerated holes in QDs. Therefore, the captured holes are still in nearby the QD surface. Due to the Coulombic attraction, the electron also tends to stay at nearby the QD surface. This charging state contributes to the spin signal of the v_2 component [11] and can be enhanced by addition of enough OT molecules. Meanwhile, the charging state corresponding to the v_1 component is totally inhibited due to the presence of oxygen. Those results suggest that addition of OT with an appropriate molar ratio to QDs in an air atmosphere may provide an approach to obtaining the spin signal of the v_2 component solely.

Note that modifying the QDs surface with an OT hole acceptor prepared in a N_2 atmosphere can also provide an effective strategy to boost the spin signal of the v_1 component. The spin dynamics of CdSe QDs with and without an OT hole acceptor prepared in a N_2 atmosphere are shown in Figure 6a. Via adding OT, the total spin amplitudes of CdSe QDs are considerably enhanced. The FFT amplitudes of the v_1 component are relatively weak in both as-grown CdSe QDs and QDs with OT (OT/QDs = 7000) compared with those of the

v_2 component as shown in Figure 6b. However, increasing the molar ratio of OT to QDs to 70,000, the FFT amplitude of the v_1 component is increased significantly, while the v_2 component is reduced. For CdS QDs, some similar phenomena also occur, e.g., addition of OT enhances the total spin signal, but some details are different. Figure 6c,d show the spin signals of colloidal CdS QDs and QDs with OT prepared in a N_2 atmosphere and the corresponding FFT spectra. When the molar ratio of OT to QDs is 100, there is only one frequency of the v_1 component, while the v_2 component disappears. However, increasing the molar ratio of OT to QDs to 5000, the v_2 component emerges again. The anaerobic conditions also help the enhancements of the v_1 component with addition of OT hole acceptors in both CdSe and CdS QDs. In some cases, with appropriate OT concentrations, even a pure v_1 spin component could be achieved.

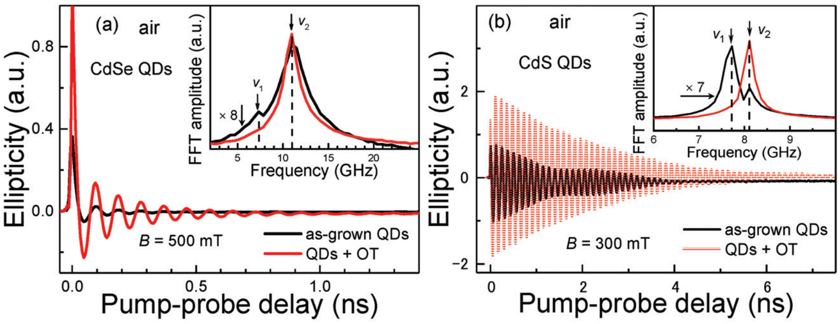

Figure 5. (**a**) Time-resolved ellipticity signals of as-grown colloidal CdSe QDs and QDs with 1-octanethiol (OT) prepared in an air atmosphere. The inset is the corresponding FFT spectra. The FFT spectroscopy of as-grown CdSe QDs is multiplied by 8 for clarity. The molar ratio of OT to CdSe QDs is 11,000. The laser repetition rate is 50 kHz. (**b**) Spin signals of as-grown colloidal CdS QDs and QDs with OT prepared in an air atmosphere. The inset is the corresponding FFT spectra. The FFT spectroscopy of as-grown CdS QDs is multiplied by 7 for clarity. The molar ratio of OT to CdS QDs is 5000. The laser repetition rates for as-grown CdS QDs and QDs with OT are 50 and 10 kHz, respectively.

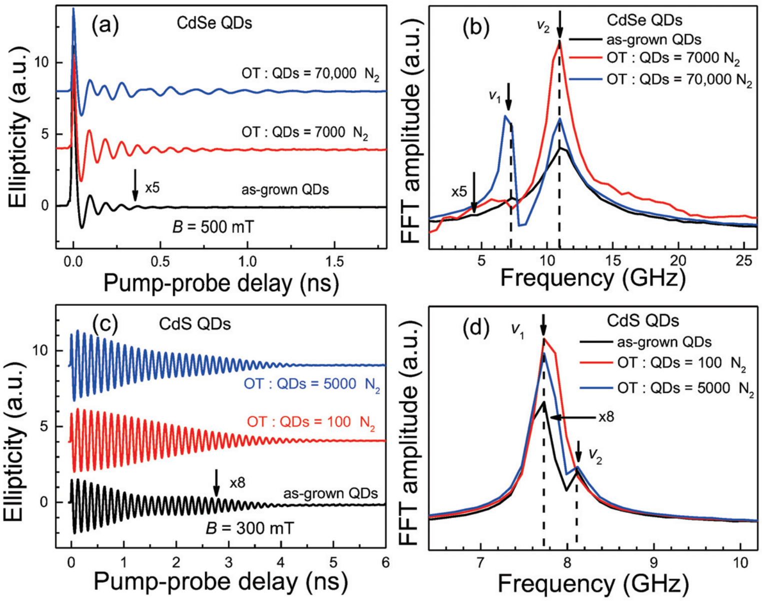

Figure 6. (**a**) Time-resolved ellipticity signals in as-grown colloidal CdSe QDs and QDs with OT prepared in a N_2 atmosphere. (**b**) The corresponding FFT spectra of panel a. The spin signal and its FFT spectroscopy of as-grown CdSe QDs are both multiplied by 5 for better clarity. The laser repetition rate is 50 kHz. (**c**) Spin signals of colloidal CdS QDs and QDs with OT prepared in a N_2 atmosphere. (**d**) The corresponding FFT spectra of panel c. The spin signal and its FFT spectroscopy of as-grown CdS QDs are both multiplied by 8. The laser repetition rate is 50 kHz. The plots in panel a and c are offset for clarity.

3.4. Influence of Laser Repetition Rates on Spin Signals

Figure 7 shows the spin dynamics of as-grown CdSe and CdS QDs (with native ligands at an air atmosphere) at different laser repetition rates and the corresponding FFT spectra. At a high laser repetition rate of 50 kHz, spin dynamics of colloidal QDs, either CdSe or CdS QDs, exhibit two distinct spin components with different Larmor precession frequencies, which is similar to the results shown in Figure 3. As the laser repetition rate decreases from 50 to 1 kHz, the spin amplitude reduces slightly, and the v_1 component gradually disappears in CdSe QDs as shown in Figure 7a,b. At the laser repletion rate of 1 kHz, only the v_2 component is shown in the coherent spin dynamics. The amplitudes of the v_2 component show almost no change when altering the laser repetition rates. As-grown CdS QDs exhibited similar experimental phenomena when reducing laser repetition rates from 50 to 0.5 kHz. Decreasing the laser repetition rates can also apparently decrease the spin signals of the v_1 component but have negligible effects on the v_2 component. This suggests that the charging state of the v_1 component is long-lived and subject to pile-up effects from previous pulses at high laser repetition rates. Decreasing the laser repetition rates decreases the pile-up effects. When pile-up effects are equal to or less important than the oxygen-induced electron removing, the v_1 component disappears. The results in Figure 7 also imply that the charging state of the v_2 component is short-lived and has no pile-up effects from previous pulses. The influence of laser repetition rates demonstrated here explains the fact that, in the literature, only one single Larmor frequency (corresponding to v_2) was observed for pump–probe measurements with low laser repetition rates [7,25,26], while two Larmor frequencies were typically detected for the measurements with high laser repetition rates [5,13,22]. Accordingly, decreasing laser repetition rates is an effective way to isolate the spin signal of the v_2 component. If a stronger spin signal of the v_1 component is required, then high laser repetition rates must be used for the measurements.

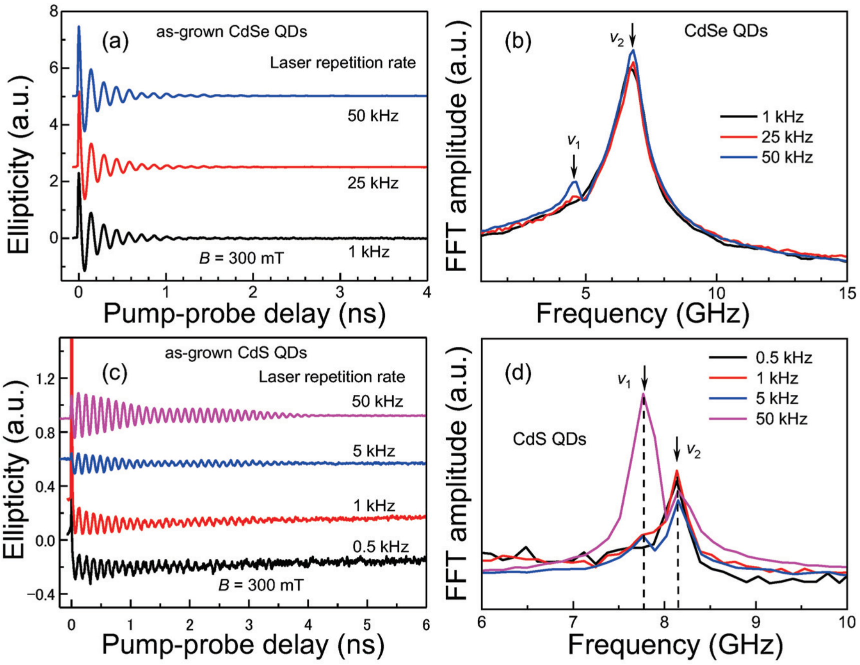

Figure 7. (**a**) Time-resolved ellipticity signals of CdSe QDs at laser repetition rates of 1, 25 and 50 kHz, respectively. (**b**) The corresponding FFT spectra of panel a. (**c**) Electron spin dynamics of CdS QDs with different laser repetition rates. (**d**) The corresponding FFT spectra of panel c.

For convenience, we summarize the methods that facilitate the acquisition of one single Larmor frequency, either the v_1 or v_2 component, in spin coherent measurements of our samples as follows:

(1) Addition of an appropriate molar ratio of hole acceptors, Li[Et$_3$BH] or OT, in a N$_2$ atmosphere is beneficial to obtain the pure spin signal of the v_1 component.
(2) Modifying colloidal QDs with an OT hole acceptor prepared in an air atmosphere provides advantages on the selection of the v_2 spin component.
(3) Low laser repetition rates are convenient for the appearance of merely the v_2 component, whereas the spin signals of the v_1 component rise effectively when applying high laser repetition rates.

4. Conclusions

In conclusion, the coherent spin dynamics of CdSe and CdS colloidal QDs were studied using time-resolved ellipticity spectroscopy. Two spin components with different Larmor frequencies typically coexist in QDs with native ligands when measured at high laser repetition rates. In the presence of appropriate hole acceptors, e.g., Li[Et$_3$BH] and OT, with a proper molar ratio in N$_2$ or air atmosphere, the two spin components can be selectively enhanced or suppressed, leaving one pure spin component. Low laser repetition rates are beneficial to the appearance of the v_2 component solely. Higher laser repetition rates significantly contribute to the enhancement of the v_1 spin component. Consequently, those results imply that addition of hole acceptors either in an air or anaerobic atmosphere and adjusting laser repetition rates provide effective strategies to manipulate the spin signals in colloidal QDs, which is helpful for in-depth investigation of spin dynamics and practical applications.

Author Contributions: Conceptualization, T.J., Z.S. and D.F.; Data curation, M.J., Y.Z., R.H. and D.F.; Formal analysis, M.J., Y.Z. and R.H.; Investigation, M.J., Y.Z., R.H., Y.M., L.C. and P.L.; Writing—original draft, R.H. and D.F.; Writing—review and editing, R.H. and D.F. All authors have read and agreed to the published version of the manuscript.

Funding: This work was supported by the National Natural Science Foundation of China (Grants No 12174108, 91950112, 12104311, 12004239, 12074123 and 12034008).

Data Availability Statement: The data that support the findings of this study are available from the corresponding author upon reasonable request.

Conflicts of Interest: The authors declare no conflict of interest.

References

1. Loss, D.; DiVincenzo, D.P. Quantum Computation with Quantum Dots. *Phys. Rev. A At. Mol. Opt. Phys.* **1998**, *57*, 120–126. [CrossRef]
2. Awschalom, D.D.; Bassett, L.C.; Dzurak, A.S.; Hu, E.L.; Petta, J.R. Quantum Spintronics: Engineering and Manipulating Atom-Like Spins in Semiconductors. *Science* **2013**, *339*, 1174–1179. [CrossRef]
3. Hanson, R.; Awschalom, D.D. Coherent Manipulation of Single Spins in Semiconductors. *Nature* **2008**, *453*, 1043–1049. [CrossRef]
4. Khaetskii, A.V.; Nazarov, Y.V. Spin Relaxation in Semiconductor Quantum Dots. *Phys. Rev. B Condens. Matter Mater. Phys.* **2000**, *61*, 12639–12642. [CrossRef]
5. Gupta, J.A.; Awschalom, D.D.; Efros, A.L.; Rodina, A.V. Spin Dynamics in Semiconductor Nanocrystals. *Phys. Rev. B Condens. Matter Mater. Phys.* **2002**, *66*, 125307. [CrossRef]
6. Janßen, N.; Whitaker, K.M.; Gamelin, D.R.; Bratschitsch, R. Ultrafast Spin Dynamics in Colloidal ZnO Quantum Dots. *Nano Lett.* **2008**, *8*, 1991–1994.
7. Feng, D.H.; Li, X.; Jia, T.Q.; Pan, X.Q.; Sun, Z.R.; Xu, Z.Z. Long-Lived, Room-Temperature Electron Spin Coherence in Colloidal CdS Quantum Dots. *Appl. Phys. Lett.* **2012**, *100*, 122406. [CrossRef]
8. Biadala, L.; Shornikova, E.V.; Rodina, A.V.; Yakovlev, D.R.; Siebers, B.; Aubert, T.; Nasilowski, M.; Hens, Z.; Dubertret, B.; Efros, A.L.; et al. Magnetic Polaron on Dangling-Bond Spins in CdSe Colloidal Nanocrystals. *Nat. Nanotechnol.* **2017**, *12*, 569–574. [CrossRef]
9. Hu, R.R.; Wu, Z.; Zhang, Y.Y.; Yakovlev, D.R.; Liang, P.; Qiang, G.; Guo, J.X.; Jia, T.Q.; Sun, Z.R.; Bayer, M.; et al. Long-Lived Negative Photocharging in Colloidal CdSe Quantum Dots Revealed by Coherent Electron Spin Precession. *J. Phys. Chem. Lett.* **2019**, *10*, 4994–4999. [CrossRef]
10. Feng, D.H.; Yakovlev, D.R.; Pavlov, V.V.; Rodina, A.V.; Shornikova, E.V.; Mund, J.; Bayer, M. Dynamic Evolution from Negative to Positive Photocharging in Colloidal CdS Quantum Dots. *Nano Lett.* **2017**, *17*, 2844–2851. [CrossRef]

11. Hu, R.R.; Yakovlev, D.R.; Liang, P.; Qiang, G.; Chen, C.; Jia, T.Q.; Sun, Z.R.; Bayer, M.; Feng, D.H. Origin of Two Larmor Frequencies in the Coherent Spin Dynamics of Colloidal CdSe Quantum Dots Revealed by Controlled Charging. *J. Phys. Chem. Lett.* **2019**, *10*, 3681–3687. [CrossRef] [PubMed]
12. Li, X.; Feng, D.H.; Tong, H.F.; Jia, T.Q.; Deng, L.; Sun, Z.R.; Xu, Z.Z. Hole Surface Trapping Dynamics Directly Monitored by Electron Spin Manipulation in CdS Nanocrystals. *J. Phys. Chem. Lett.* **2014**, *5*, 4310–4316. [CrossRef] [PubMed]
13. Gupta, J.A.; Awschalom, D.D.; Peng, X.; Alivisatos, A.P. Spin Coherence in Semiconductor Quantum Dots. *Phys. Rev. B Condens. Matter Mater. Phys.* **1999**, *59*, R10421–R10424. [CrossRef]
14. Huxter, V.M.; Kovalevskij, V.; Scholes, G.D. Dynamics within the Exciton Fine Structure of Colloidal CdSe Quantum Dots. *J. Phys. Chem. B* **2005**, *109*, 20060–20063. [CrossRef] [PubMed]
15. Qiang, G.; Zhukov, E.A.; Evers, E.; Yakovlev, D.R.; Golovatenko, A.A.; Rodina, A.V.; Onushchenko, A.A.; Bayer, M. Electron Spin Coherence in CdSe Nanocrystals in a Glass Matrix. *ACS Nano* **2022**, *16*, 18838–18848. [CrossRef]
16. Yu, W.W.; Qu, L.; Guo, W.; Peng, X. Experimental Determination of the Extinction Coefficient of CdTe, CdSe, and CdS Nanocrystals. *Chem. Mater.* **2003**, *15*, 2854–2860. [CrossRef]
17. McArthur, E.A.; Morris-Cohen, A.J.; Knowles, K.E.; Weiss, E.A. Charge Carrier Resolved Relaxation of the First Excitonic State in CdSe Quantum Dots Probed with Near-Infrared Transient Absorption Spectroscopy. *J. Phys. Chem. B* **2010**, *114*, 14514–14520. [CrossRef]
18. Rinehart, J.D.; Schimpf, A.M.; Weaver, A.L.; Cohn, A.W.; Gamelin, D.R. Photochemical Electronic Doping of Colloidal CdSe Nanocrystals. *J. Am. Chem. Soc.* **2013**, *135*, 18782–18785. [CrossRef]
19. Zhang, Y.Y.; Jiang, M.Z.; Wu, Z.; Yang, Q.; Men, Y.M.; Cheng, L.; Liang, P.; Hu, R.R.; Jia, T.Q.; Sun, Z.R.; et al. Hyperfine-Induced Electron-Spin Dephasing in Negatively Charged Colloidal Quantum Dots: A Survey of Size Dependence. *J. Phys. Chem. Lett.* **2021**, *12*, 9481–9487. [CrossRef]
20. Wu, Z.; Zhang, Y.Y.; Hu, R.R.; Jiang, M.Z.; Liang, P.; Yang, Q.; Deng, L.; Jia, T.Q.; Sun, Z.R.; Feng, D.H. Hole-Acceptor-Manipulated Electron Spin Dynamics in CdSe Colloidal Quantum Dots. *J. Phys. Chem. Lett.* **2021**, *12*, 2126–2132. [CrossRef]
21. Stern, N.P.; Poggio, M.; Bartl, M.H.; Hu, E.L.; Stucky, G.D.; Awschalom, D.D. Spin Dynamics in Electrochemically Charged CdSe Quantum Dots. *Phys. Rev. B* **2005**, *72*, 161303(R). [CrossRef]
22. Fumani, A.K.; Berezovsky, J. Magnetic-Field-Dependent Spin Decoherence and Dephasing in Room-Temperature CdSe Nanocrystal Quantum Dots. *Phys. Rev. B Condens. Matter Mater. Phys.* **2013**, *88*, 155316. [CrossRef]
23. Schimpf, A.M.; Gunthardt, C.E.; Rinehart, J.D.; Mayer, J.M.; Gamelin, D.R. Controlling Carrier Densities in Photochemically Reduced Colloidal ZnO Nanocrystals: Size Dependence and Role of the Hole Quencher. *J. Am. Chem. Soc.* **2013**, *135*, 16569–16577. [CrossRef] [PubMed]
24. van Dijken, A.; Meulenkamp, E.A.; Vanmaekelbergh, D.; Meijerink, A. Influence of Adsorbed Oxygen on the Emission Properties of Nanocrystalline ZnO Particles. *J. Phys. Chem. B* **2000**, *104*, 4355–4360. [CrossRef]
25. Feng, D.H.; Shan, L.F.; Jia, T.Q.; Pan, X.Q.; Tong, H.F.; Deng, L.; Sun, Z.R.; Xu, Z.Z. Optical Manipulation of Electron Spin Coherence in Colloidal CdS Quantum Dots. *Appl. Phys. Lett.* **2013**, *102*, 062408. [CrossRef]
26. Zhang, Z.B.; Jin, Z.M.; Ma, H.; Xu, Y.; Lin, X.; Ma, G.H.; Sun, X.L. Room-Temperature Spin Coherence in Zinc Blende CdSe Quantum Dots Studied by Time-Resolved Faraday Ellipticity. *Phys. E Low-Dimens. Syst. Nanostructures* **2014**, *56*, 85–89. [CrossRef]

nanomaterials

MDPI

Article

Coherent Spin Dynamics of Electrons in $CsPbBr_3$ Perovskite Nanocrystals at Room Temperature

Sergey R. Meliakov [1,*], Evgeny A. Zhukov [1,2], Evgeniya V. Kulebyakina [1], Vasilii V. Belykh [2] and Dmitri R. Yakovlev [1,2,*]

[1] P.N. Lebedev Physical Institute of the Russian Academy of Sciences, 119991 Moscow, Russia
[2] Experimentelle Physik 2, Technische Universität Dortmund, 44227 Dortmund, Germany
* Correspondence: meliakov.sr@phystech.edu (S.R.M); dmitri.yakovlev@tu-dortmund.de (D.R.Y.)

Abstract: Coherent spin dynamics of charge carriers in $CsPbBr_3$ perovskite nanocrystals are studied in a temperature range of 4–300 K and in magnetic fields of up to 500 mT using time-resolved pump-probe Faraday rotation and differential transmission techniques. We detect electron spin Larmor precession in the entire temperature range. At temperatures below 50 K, hole spin precession is also observed. The temperature dependences of spin-related parameters, such as Landè g-factor and spin dephasing time are measured and analyzed. The electron g-factor increases with growing temperature, which can not be described by the temperature-induced band gap renormalization. We find that photocharging of the nanocrystals with either electrons or holes depends on the sample cooling regime, namely the cooling rate and illumination conditions. The type of the charge carrier provided by the photocharging can be identified via the carrier spin Larmor precession.

Keywords: perovskite nanocrystals; $CsPbBr_3$; coherent spin dynamics; electron and hole g-factors; time-resolved Faraday rotation

1. Introduction

Lead halide perovskite semiconductors are the focus of research interest due to their exceptional photovoltaic efficiency and optoelectronic properties [1–3]. The simple fabrication technology makes them attractive for applications as solar cells, light emitting devices, radiation detectors, etc. They also demonstrate remarkable spin properties, facilitating spintronic applications [3–6]. Colloidal nanocrystals (NCs), which have been successfully synthesized from the lead halide perovskite, greatly increase the possibilities for tailoring of the material properties [7,8]. Among them, the fully-inorganic $CsPbBr_3$ NCs are mostly investigated and appreciated for their stability.

The spin physics of halide perovskite semiconductors is an emerging research field, which exploits experimental techniques and physical concepts developed for spins in conventional semiconductors [9,10]. Most of the optical techniques developed for the investigation of spin properties and spin dependent phenomena work well for perovskite crystals, polycrystalline films, nanocrystals, and two-dimensional materials. These are optical orientation [11–13], optical alignment [12], polarized emission in magnetic field [14–16], time-resolved Faraday/Kerr rotation [17,18], time-resolved differential transmission [11,19,20], spin-flip Raman scattering [21,22], and optically-detected nuclear magnetic resonance [23–25]. The reported spin dynamics cover huge time ranges from a few picoseconds at room temperature [11,19] up to tens of nanoseconds for spin coherence [25] and spin dephasing [23] times and further up to sub-millisecond times for longitudinal spin relaxation times [24] at cryogenic temperatures.

Experiments on coherent spin dynamics by means of time-resolved pump-probe Faraday/Kerr rotation reveal signals from electrons and holes provided by photocharging in $CsPbBr_3$ NCs [26]. The hole spin coherence has been observed up to room temperature [27], and its optical manipulation has been implemented [28]. The electron spin coherence has not been demonstrated so far for perovskite NCs at room temperature. The spin mode-locking effect reported recently for $CsPb(Cl,Br)_3$ NCs in a glass matrix demonstrates that the elaborated protocols of coherent spin synchronization can be implemented in perovskite NCs [25]. Still, the understanding of spin relaxation and spin decoherence mechanisms is far from being complete.

The Landè g-factor controlling the Zeeman splitting of charge carriers and excitons is a key parameter in spin physics. We have recently shown that the universal dependences of the electron, hole, and exciton g-factors on the band gap energy are predicted in bulk lead halide perovskites [21,29]. Theoretical analysis predicts that, in NCs, additional mixing of the band states provides a considerable contribution to the electron g-factor by deviating it from the universal dependence for bulk; however, the mixing has only a weak effect on the hole g-factor [30]. We have confirmed this through low-temperature measurements of $CsPbI_3$ NCs in glass. The temperature dependence of the carrier g-factors in perovskite NCs has not been studied so far. Based on this simple approach, one expects that g-factor is controlled by the temperature shift of the band gap energy. However, it has been shown for GaAs and CdTe semiconductors that temperature dependence of the electron g-factor may have other strong contributions [31–34], which have an origin that is not yet fully clarified, even for conventional semiconductors. This motivates us to examine this problem for perovskite NCs.

In this paper, we study the coherent spin dynamics of carriers in perovskite $CsPbBr_3$ NCs by time-resolved pump-probe Faraday rotation and differential transmission techniques. The spin dynamics are measured in the temperature range of 4–300 K, where the carrier g-factors and spin relaxation times are evaluated. We find an unexpected temperature dependence for the electron g-factor. Although at room temperature we observe only electron spin precession, at low temperatures, the hole component may appear. We demonstrate that the photocharging of the NCs with either electrons or holes depends on the sample cooling regime, namely cooling rate and illumination conditions.

2. Materials and Methods

2.1. Samples

For this study, we use solution-grown lead halide perovskite $CsPbBr_3$ NCs with two sizes of 4.60 nm (sample #1) and 4.74 nm (sample #2). The NCs were synthesized using a procedure described in Refs. [35,36]. A total of 1–1.5 mg of the obtained NCs were dissolved in 60 μL of 3.3 wt% polysterene solution in toluene, and 10 μL of the obtained solution were drop-casted on 5×5 mm glass substrate and dried at room temperature overnight.

2.2. Photoluminescence and Optical Transmission

For optical experiments the samples were placed in a helium-flow cryostat, where the temperature was varied from $T = 4$ K up to 300 K. Photoluminescence (PL) was excited by a continuous-wave laser with a photon energy of 3.061 eV (wavelength of 405 nm) and a power of 1.2 mW (excitation density of 1 W/cm^2). The PL spectra were measured with an 0.5 m spectrometer and a charge-coupled device (CCD) camera. Optical transmission was measured with a halogen lamp. The transmitted signal was normalized to the intensity of the light sent directly to the detector. The PL and transmission spectra were recorded from the sample area with a diameter of approximately 300 μm.

2.3. Time-Resolved Faraday Rotation

To study the coherent spin dynamics of carriers, we used the time-resolved pump-probe technique with detection of the Faraday rotation (FR) [37]. This technique was successfully used for investigation of bulk perovskite semiconductors [17,18,21,23,38] and $CsPbBr_3$ NCs [26–28]. Spin-oriented electrons and holes were generated by circularly polarized pump pulses. The laser system used (light conversion) generated 1.5 ps pulses with spectral width of about 1 meV at a repetition rate of 25 kHz (repetition period 40 μs). The laser beam was split into pump and probe beams, which had coinciding photon energies. The time delay between the pump and probe pulses was controlled by a mechanical delay line. The pump beam was modulated with an electro-optical modulator between σ^+ and σ^- circular polarizations at a frequency of 26 kHz. The probe beam was linearly polarized. The Faraday rotation angle of the probe beam, which was proportional to the carrier spin polarization, was measured as a function of the delay between the pump and probe pulses using a balanced photodetector connected to a lock-in amplifier synchronized with the modulator. The pump power density was tuned to the range P_{pump} = 3.8–12.7 W/cm^2 and the probe power density was P_{probe} = 3.8–10 W/cm^2. The probe beam spot size on the sample was slightly smaller than the size of the pump beam spot, which was about 100 µm in diameter. For the time-resolved FR measurements, the samples were placed in a helium-flow optical cryostat and the temperature was varied in the range of 4–300 K. A magnetic field up to 500 mT was applied perpendicular to the laser wave vector (Voigt geometry, $\mathbf{B} \perp \mathbf{k}$) by means of an electromagnet.

2.4. Time-Resolved Differential Transmission

We used a time-resolved differential transmission (DT, $\Delta T/T$) technique to study population and spin dynamics of charge carriers and excitons at room temperature and zero magnetic field. For measuring the population dynamics, the pump and probe beams were linearly polarized. The pump beam intensity was modulated with an electro-optical modulator at a frequency of 26 kHz. The probe beam transmitted through the sample and the reference laser beam were sent to the balanced photodetector connected with the lock-in amplifier synchronized with the modulator.

For measuring the spin dynamics, circularly polarized pump and probe beams were used. This allowed us to measure the dynamics of the optical spin orientation degree (P_{oo}) at a picosecond time resolution. The pump beam had σ^+ circular polarization. The probe beam was polarized either σ^+ or σ^-, and its intensity was modulated with a mechanical chopper at a frequency of 2 kHz synchronized with the lock-in amplifier. The optical orientation degree is calculated for the σ^+ polarized pump with:

$$P_{\text{oo}}(t) = \frac{I^+(t) - I^-(t)}{I^+(t) + I^-(t)}\,. \tag{1}$$

Here, $I^+(t)$ and $I^-(t)$ are the signal intensities measured at σ^+ and σ^- polarizations of the probe beam, respectively.

3. Results and Discussion

3.1. Photoluminescence and Transmission

Photoluminescence and transmission spectra of sample #1 measured at a room temperature are shown in Figure 1a. The minimum in the transmission spectrum at 2.610 eV corresponds to the exciton resonance in CsPbBr$_3$ NCs. The emission band is Stokes shifted from this energy, having a maximum at 2.520 eV. The PL line full width at a half maximum of 130 meV is determined by inhomogeneous broadening of the NC ensemble due to NC size dispersion.

Sample #2 has very similar PL and transmission spectra with exciton resonance slightly shifted to lower energies due to larger NC size compared to the sample #1 (see Figure 3a,b). Their evolution with the temperature in the range of 5.4–300 K is shown in the Supplementary Materials, Figure S1. We use it for evaluation of the temperature shift of the band gap energy involved in the discussion of the temperature dependence of the electron g-factor given below.

It is worthwhile to note, that the exciton binding energy in bulk CsPbBr$_3$ amounts to 31.5 meV [39,40], which provides exciton stability in a wide temperature range. In NCs, this energy increases with decreasing the NC size [41,42].

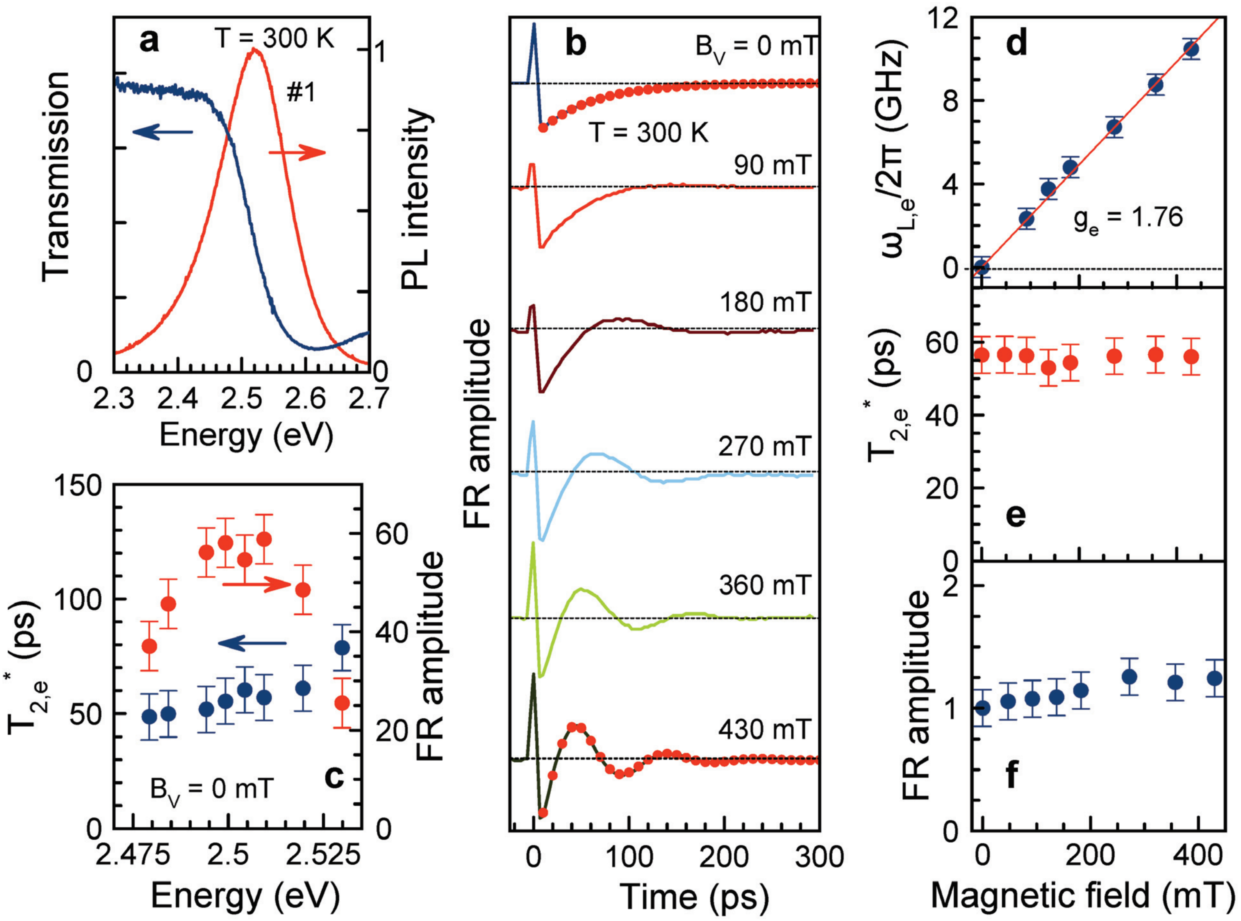

Figure 1. Electron spin dynamics in CsPbBr$_3$ NCs (sample #1) measured at $T = 300$ K. (**a**) Photoluminescence (red line) and transmission (blue line) spectra. (**b**) FR dynamics at different magnetic fields. Fits of the data at $B_V = 0$ and 430 mT with Equation (2) are shown by red dots. Pump power density $P_{\text{pump}} = 8.4\ \text{W/cm}^2$. Laser photon energy $E_L = 2.509$ eV. (**c**) Amplitude of FR signal (red dots) and spin relaxation time (blue dots) as a function of the laser energy near the exciton resonance. $B_V = 0$ mT. (**d**–**f**) Magnetic field dependences of the Larmor frequency (red line shows linear fit), spin dephasing time $T_{2,e}^*$, and FR amplitude.

3.2. Time-Resolved Faraday Rotation

Figure 1b shows the coherent spin dynamics measured by time-resolved FR in the sample #1 at room temperature. The dynamics are measured at the laser energy of $E_L = 2.509$ eV, which corresponds to the maximum of the spectral dependence of the FR signal amplitude at a zero magnetic field, see Figure 1c. This maximum is shifted to lower energies with respect the exciton transmission minimum, as is expected for the photogeneration of the spin coherence for the resident carriers via the charged exciton (trion) resonances [26,37].

The FR dynamics (Figure 1b) are shown for transversal magnetic fields B_V (Voigt geometry) varied from 0 up to 430 mT. The FR signals have one rapidly decaying oscillating component, which we assign to the Larmor precession of a charge carrier spins in a magnetic field. We evaluate the spin dephasing time (T_2^*), amplitude (A_0), and Larmor precession frequency (ω_L) by fitting these dynamics with [37]:

$$A_{\text{FR}}(t) = \sum_{\text{e,h}} A_{0,\text{e(h)}} \exp\left(-\frac{t}{T^*_{2,\text{e(h)}}}\right) \cos(\omega_{\text{L,e(h)}} t). \tag{2}$$

Note that this equation accounts for contributions of both electrons (e) and holes (h), as both of them are typically present in the spin dynamics of bulk perovskites and their nanocrystals at cryogenic temperatures [18,26]. For fitting room temperature dynamics, we use only one contribution, and for fitting nonoscillating signal at zero magnetic field, the Larmor frequency is set to zero. Examples of the fits for magnetic fields $B_V = 0$ and 430 mT are shown by the red dots. The evaluated parameters and their magnetic field dependences are shown in Figure 1d–f.

The dependence of the Larmor precession frequency on the magnetic field (Figure 1d) is a linear function without offset at zero field. From its slope, we evaluate the Landè factor $g_e = 1.76 \pm 0.03$ using the following expression:

$$|g_{e(h)}| = \frac{\hbar \omega_{L,e(h)}}{\mu_B B}. \tag{3}$$

Here, $\hbar$ is the Planck constant and μ_B is the Bohr magneton. Note that the electron Zeeman splitting at $B_V = 430$ mT is 0.04 meV only, which is much smaller than the inhomogeneous broadening of the exciton transitions. Comparing this g-factor value with the results of Refs. [21,26,30], we assign the signal oscillations to the precession of electron spins in a transverse magnetic field. The time-resolved FR technique does not allow directly determine the g-factor sign. However, we firmly assign it to positive based on the papers cited above. Additional confirmation for our identification of the electron spin coherence at a room temperature comes from the observation of the hole spin precession with smaller $g_h = 0.44$ at cryogenic temperatures, which we show below.

There are only two recent papers related to spin coherence in perovskite NCs at room temperature [27,28]. In both papers, the hole spin coherence was reported at room temperature for the $CsPbBr_3$ NCs, and we observe the electron spin beats. This demonstrates that photocharging in our samples is different from the previous reports.

The evaluated spin dephasing time T_2^* is about 60 ps being independent of the magnetic field strength, Figure 1e. This means that at a room temperature, it is not controlled by dispersion of g-factor, but rather by other spin relaxation mechanisms, among which phonon-assisted spin relaxation is most probable. The spectral dependence of the T_2^* time is also very weak, Figure 1c.

The FR amplitude also weakly depends on the magnetic field, Figure 1f. We check that the amplitude increases linearly with increasing pump power, whereas electron g-factor and spin dephasing time are weakly sensitive to the power density in the range P_{pump} = 3.8–12.7 W/cm^2 (Figure S2 in Supplementary Materials). This indicates that we perform experiments in a linear regime, despite using the laser with low repetition frequency of 25 kHz and relatively high peak power.

Similar results on electron spin coherence at room temperature are obtained for sample #2. Spin dynamics at various magnetic fields and magnetic field dependences of its parameters are shown in Figure S3 of the Supplementary Materials. The electron spin dephasing time is $T_{2,e}^* \approx 55$ ps and the electron g-factor is $g_e = 1.69 \pm 0.02$ being slightly smaller than that in the sample #1.

For sample #2, we measure the spin dynamics in a large temperature range by cooling the sample under laser illumination from 300 K down to 4 K in the magnetic field of $B_V = 410$ mT, see Figure 2a–c. In this experiment, the laser energy is adjusted at each temperature to the maximum of the FR amplitude in order to account for the temperature shift of the exciton/trion transition.

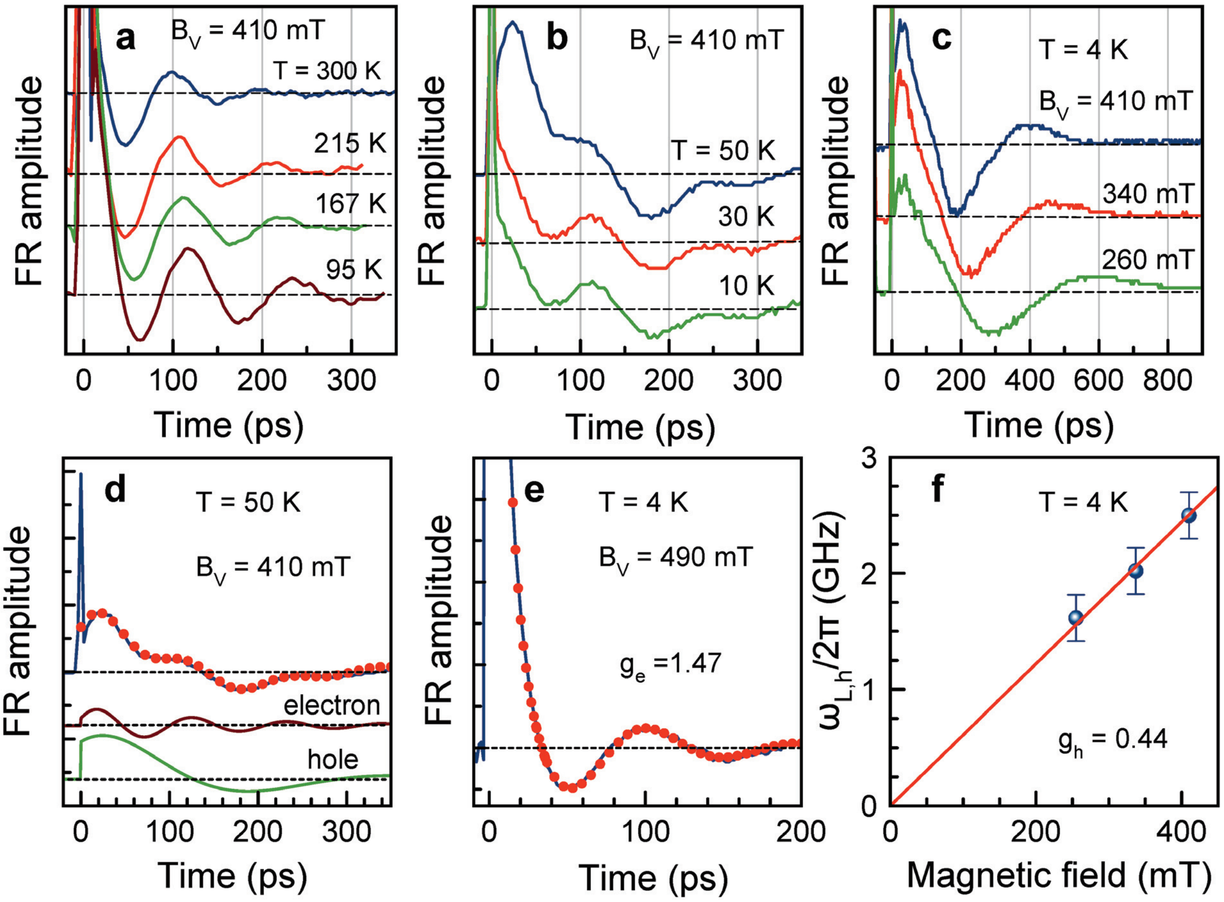

Figure 2. Spin dynamics of carriers in CsPbBr$_3$ NCs (sample #2) measured at different temperatures. (**a**) FR dynamics in the temperature range of $95 - 300$ K at $B_V = 410$ mT. (**b**) FR dynamics in the temperature range of $10 - 50$ K at $B_V = 410$ mT. (**c**) FR dynamics at different magnetic fields at $T = 4$ K. (**d**) FR dynamics at $B_V = 410$ mT and $T = 50$ K (blue line) and fit with Equation (2) (red dots). Lower panels show electron and hole contributions to the dynamics determined from the fit. (**e**) FR dynamics measured after thermal cycling: heating the sample from $T = 4$ K, keeping it at room temperature in the darkness for several hours, and cooling in the darkness to the temperature of 4 K (blue line). Fit with Equation (2) is shown by red dots. $P_{\text{pump}} = 12.7$ W/cm^2. (**f**) Magnetic field dependence of the Larmor precession frequency of holes (blue dots) and its linear fit (red line).

In the temperature range 95–300 K only one Larmor frequency related to the electrons is seen in the FR dynamics, Figure 2a. The Larmor precession frequency decreases with lowering temperature. At 50 K and below, a second oscillating component with lower Larmor frequency appears in the spin dynamics, Figure 2b,c. The magnetic field dependence of the lower Larmor frequency, which is evaluated by the fit with Equation (2), gives the g-factor $g_h = 0.44 \pm 0.01$, which we assign to holes (Figure 2f). Based on the results of Refs. [21,26,30], the hole g-factor is expected to be positive. The hole g-factor is independent of temperature in the range of 4–50 K, where the hole signal is detected, Figure 3f. The hole spin dephasing time is $T^*_{2,h} \approx 170$ ps at low temperatures and decreases down to 100 ps at 50 K, Figure 3g. We summarize the measured electron and hole spin dynamics parameters in Table 1. Note that in bulk CsPbBr$_3$ crystals both electron and hole spin components were observed only at cryogenic temperatures with comparable, but higher g factors (1.96 and 0.75, respectively) [18].

Table 1. Spin parameters measured for $CsPbBr_3$ perovskite NCs at different temperatures. T_2^* values are given for $B_V = 410$ mT.

	300 K	**4 K**
Electron g-factor, g_e	1.77	1.47
Hole g-factor, g_h	–	0.44
Electron spin dephasing time, $T^*_{2,e}$	60 ps	150 ps
Hole spin dephasing time, $T^*_{2,h}$	–	170 ps

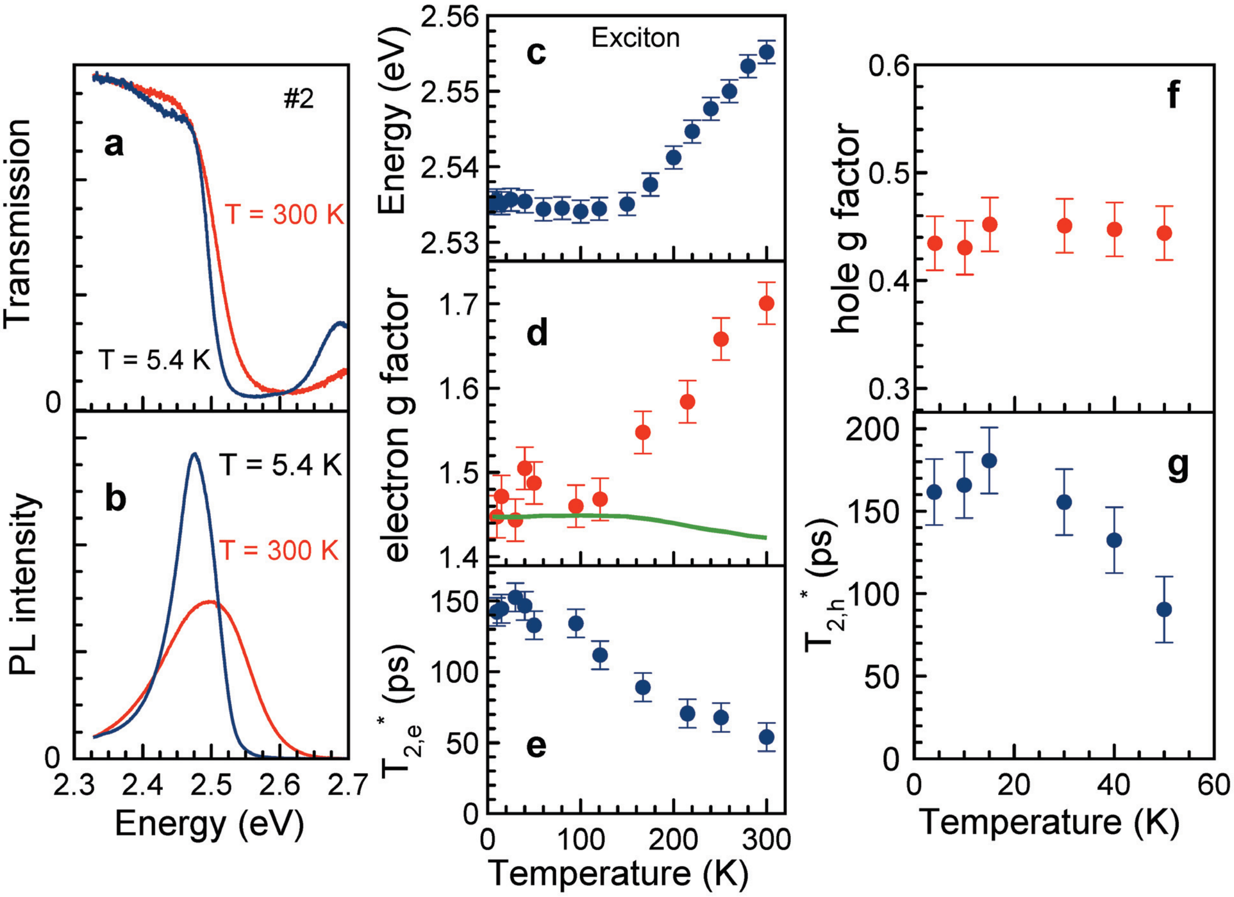

Figure 3. Temperature dependences of the parameters controlling spin dynamics in $CsPbBr_3$ NCs (sample #2). (**a**) Transmission spectra at $T = 5.4$ K and 300 K. (**b**) Photoluminescence spectra at $T = 5.4$ K and 300 K. (**c**) Temperature dependence of exciton energy evaluated from the absorption spectra (see Figure S1a). (**d**) Temperature dependence of electron g-factor (red circles). Green line shows model expectation accounting only for the temperature shift of the band gap. (**e**) Temperature dependence of electron spin dephasing time. (**f**) Temperature dependence of hole g-factor. (**g**) Temperature dependence of hole spin dephasing time. Data in panels (**d**–**g**) are measured at $B_V = 410$ mT and at $P_{pump} = 12.7\ W/cm^2$.

Let us turn to the temperature dependences of the electron spin parameters evaluated from the FR dynamics. The electron spin dephasing time increases from 55 ps at 300 K up to 150 ps at 4 K, Figure 3e. This is expected behavior, as phonon-assisted spin relaxation mechanisms loose their efficiency at cryogenic temperatures.

Temperature dependence of the electron g-factor is the most interesting and unexpected finding of this study. One can see in Figure 3d, that $g_e = 1.47$ at $T = 4$ K and stays constant at this value for the temperature increasing up to 120 K. However, with further temperature increase, it grows nearly linearly, reaching 1.69 at 300 K. This behavior qualitatively correlates with the temperature shift of the exciton energy (Figure 3c), which in turn reflects the temperature variation of the band gap energy.

We recently experimentally demonstrated (at cryogenic temperatures) and theoretically, that the electron g-factor in bulk lead halide perovskites has a universal dependence on the band gap energy [21], and its value decreases with growing the band gap energy. We take the energy shift of the exciton from Figure 3c and estimate the expected changes for $g_\mathrm{e}(T)$. The resulting dependence is shown by a green line in Figure 3d. One can see that the dependence is weak and small decrease in g_e at higher temperatures is expected. This is in strong contrast with what we find experimentally. Obviously, some other mechanisms are involved here, which have an origin that is to be disclosed in future studies. It will be important to clarify experimentally whether this temperature dependence of g_e reflects the properties of bulk perovskites or is specific for NCs. As we commented in the introduction, even for conventional semiconductors such as GaAs and CdTe, the temperature dependence of the electron g-factor is not fully understood. For GaAs, the possible temperature dependence of the interband matrix element was suggested [34], which in principle may be relevant for the perovskite semiconductors, but require solid experimental and/or theoretical proofs. Note that in Ref. [21] the universal dependence of the carrier g-factors on the band gap energy is derived assuming constant interband matrix elements. Another possible source of the g_e temperature dependence is the involvement of the states with larger k-vector [33]; however, its influence should be reconsidered for NCs with strong carrier confinement. Additionally, strong electron–phonon interaction in the perovskite semiconductors may lead to temperature-dependent modification of the energy spectrum and, consequently, of the carrier g-factors.

We show above in Figure 2a–c, that for NCs, which are cooled rather slow and under laser illumination, the hole signal appears below 50 K as a second Larmor precession frequency. In the case when the cooling from 300 K is performed in darkness and relatively fast (during about 20 min), the hole signal does not appear, and only the electron spin precession is seen at $T = 4$ K, Figure 2e. Obviously, photocharging of NCs either by electrons or by holes is responsible for this phenomenon [43]. Note that time-resolved FR is a very suitable technique for identifying the type of the resident carriers in colloidal NCs by measuring the Larmor precession of the specific carrier. We have demonstrated this for CdSe- and CdS-based colloidal NCs [44–46]. For CdS NCs, we have shown that the photocharging can develop dynamically from negative to positive [44]. The photocharging physics is complex and is determined by many factors (concentration and parameters of surface states, efficiency of Auger processes for electrons and holes, matrix in which NCs are embedded, lattice temperature, cooling and illumination conditions, etc.). Our results show that depending on illumination conditions during the cooling process we can realize either negatively photocharged NCs or coexistence of the negatively and positively charged NCs. In both cases, the presence of neutral (empty) NCs is also expected; however, these do not appear in the time-resolved FR experiments.

3.3. Differential Transmission and Optical Orientation Dynamics

To obtain further insight in the population and spin dynamics, we use the time-resolved differential transmission technique. The measurements were performed for sample #1 at room temperature and at zero magnetic field. The laser energy of $E_\mathrm{L} = 2.509$ eV is the same as in experiments with the time-resolved FR presented in Figure 1.

The population dynamics, measured with linearly polarized pump and probe beams, are shown in Figure 4a. Initially, about 20% of the signal amplitude decays with time $\tau_1 = 40$ ps and further signal decays with $\tau_2 = 2.2$ ns. We study the ensemble of $\mathrm{CsPbBr_3}$ NCs, where neutral NCs coexist with NCs charged by either electrons or holes. The neutral NCs gives rise to the dynamics of (neutral) excitons, and the charged NCs to the trion dynamics. Recombination dynamics of excitons in lead halide perovskite NCs at room temperature falls in the range of 1–2 ns [47–49]. Therefore, we assign the longer time of

2.2 ns in our NCs to the lifetime of excitons in neutral NCs. The shorter time of 40 ps can be assigned to trion lifetime in charged NCs, which is shortened by efficient Auger process. From the ratio of the amplitudes of the exciton and trion decays in Figure 4a we evaluate that about 20% of the NCs are charged and 80% stay neutral at room temperature.

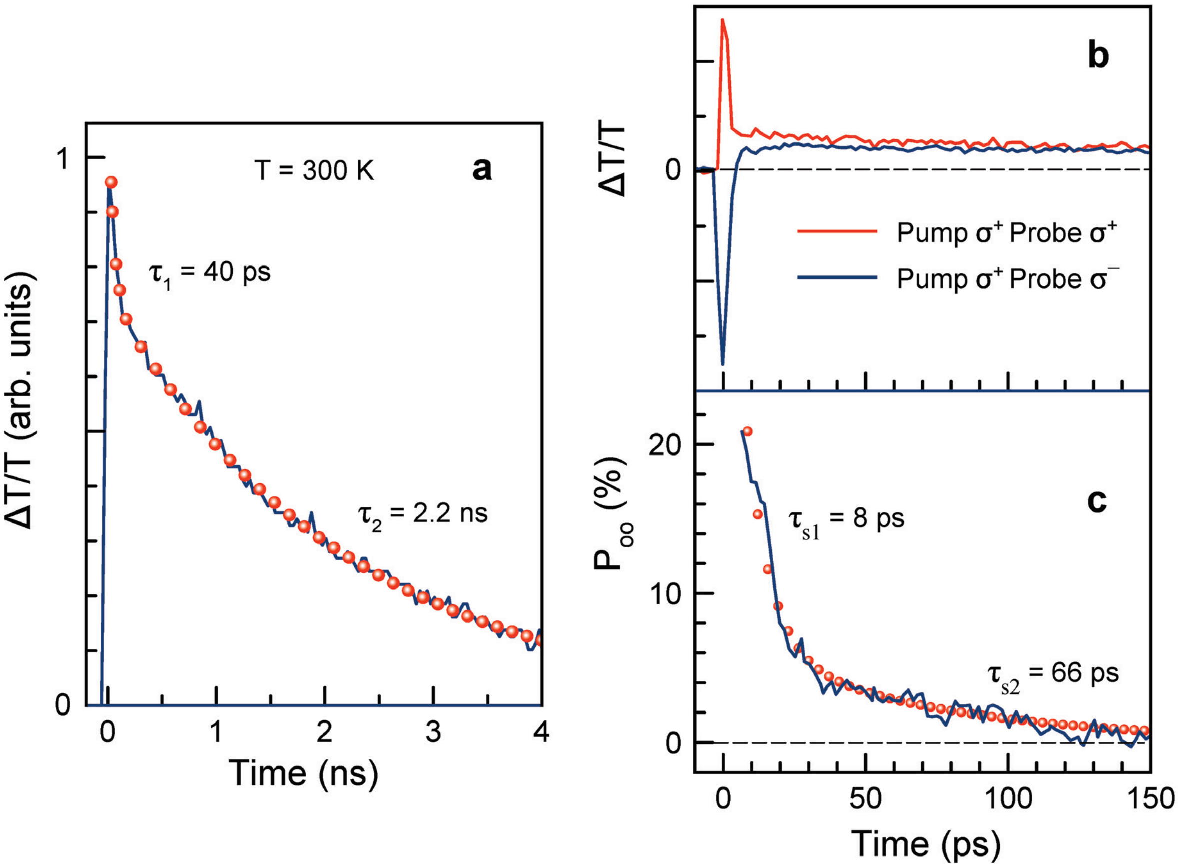

Figure 4. Time-resolved differential transmission measurements of CsPbBr$_3$ NCs (sample #1) at $T = 300$ K. (**a**) Population dynamics measured with linearly polarized pump ($P_{\text{pump}} = 5.1$ W/cm^2) and linearly polarized probe. Red dots show two-exponential fit. $E_{\text{L}} = 2.509$ eV. (**b**) Spin dynamics measured for σ^+ polarized pump and for either σ^+ (red line) or σ^- (blue line) polarized probe. $P_{\text{pump}} = 12.7$ W/cm^2. (**c**) Dynamics of optical spin orientation degree (blue line) calculated for data from panel (**b**). Dots show two-exponential fit.

Spin dynamics can be also addressed by the time-resolved differential transmission technique when the circularly polarized pump and probe are used. The circularly polarized pump, for which we take σ^+ polarization, photogenerates spin-polarized excitons/trions or charge carriers. Dynamics of their spin polarization are probed by transmission of either σ^+ or σ^- circularly polarized probe. The respective dynamics are shown in Figure 4b. These dynamics are similar to those measured in Refs. [19,50], except for a negative signal that we observe for a very short time. It is presumably related to the non-linear effects taking place for time-overlapping pump and probe pulses. The underlying mechanisms of carrier spin orientation are the same as in the time-resolved FR experiments and described in Ref. [37]. From these dynamics, we calculate the optical orientation degree using Equation (1), and these dynamics are displayed in Figure 4c. The $P_{\text{oo}}(t)$ dynamics have two spin relaxation times of $\tau_{\text{s1}} = 8$ ps and $\tau_{\text{s2}} = 66$ ps. The longer time coincides with $T_{2,\text{e}}^* = 60$ ps time that we measure by the time-resolved FR, Figure 1e. Based on that, we assign it to the spin relaxation of resident electrons in negatively charged NCs. The faster time of 8 ps can be either related to the spin relaxation of excitons in neutral NCs or to the hole spin relaxation in negatively charged trions. We suggest that the exciton spin relaxation is more probable here.

We are aware of only one report where the spin dynamics in perovskite ($CsPbI_3$) NCs have been measured by the time-resolved differential transmission [19]. Measured spin relaxation times of 3 ps at room temperature and 32 ps at cryogenic temperatures were attributed to charge carriers. In this experiment, the carriers were photogenerated with a large excess energy, as the laser photon energy was considerably detuned from the exciton resonance. This is an important difference from the conditions of our experiment, where the resonant excitation was used. In our experiment, we measured 66 ps at a room temperature for the spin relaxation dynamics of the resident electrons at the bottom of the conduction band.

Application of the time-resolved differential transmission technique to the bulk lead halide perovskites, such as $MAPbI_3$, $CsPbI_3$, $MAPbBr_3$, and $CsPbBr_3$ polycrystalline films, evidence very fast spin dynamics of <5 ps [11,20]. Note that the data for bulk structures should be taken with care when comparison with NCs is made, as zero-dimensional confinement strongly modifies the available spin relaxation mechanisms of carriers and excitons.

4. Conclusions

We have studied carrier spin dynamics in $CsPbBr_3$ perovskite nanocrystals by means of the time-resolved Faraday rotation and differential transmission techniques. Coherent spin dynamics in form of the Larmor spin precession of electrons and holes are provided by the NCs singly photocharged by these carriers. The photocharging process depends on whether the sample is cooled under laser illumination or in darkness. The coherent spin precession of electrons is observed in the temperature range from 4 K up to room temperature. Their spin dephasing time of 60 ps at room temperature is rather long compared to that for conventional semiconductors. Unexpected temperature dependence of the electron g-factor, which increases with growing temperature and with increasing the band gap energy, is found. The coherent spin dynamics of holes emerge at cryogenic temperatures of 4–50 K. Our results demonstrate that lead halide perovskite NCs are very interesting and promising materials for spintronics and information technologies exploiting spin-dependent phenomena.

Supplementary Materials: The following supporting information can be downloaded at: https://www.mdpi.com/article/10.3390/nano13172454/s1, Figure S1: photoluminescence and transmission spectra of the sample #2 measured in a temperature range 5.4–300 K; Figure S2: dependences of spin parameters on the pump power density in the sample #1; Figure S3: experimental data for time-resolved FR studies of the sample #2.

Author Contributions: Conceptualization, E.A.Z. and D.R.Y.; methodology, S.R.M., E.A.Z. and V.V.B.; validation, S.R.M., E.A.Z., E.V.K., V.V.B. and D.R.Y.; investigation, S.R.M., E.A.Z. and E.V.K.; writing—original draft preparation, E.A.Z. and D.R.Y.; writing—review and editing, S.R.M., E.A.Z., D.R.Y. and V.V.B.; supervision, D.R.Y. and E.A.Z.; project administration, D.R.Y. and V.V.B.; funding acquisition, D.R.Y. and V.V.B. All authors have read and agreed to the published version of the manuscript.

Funding: This research was funded by the Ministry of Science and Higher Education of the Russian Federation, Contract No. 075-15-2021-598 at the P. N. Lebedev Physical Institute.

Data Availability Statement: The data presented in this study are available on request from the corresponding author.

Acknowledgments: Samples for these studies were provided by D. N. Dirin and M. V. Kovalenko from ETH Zürich. We are thankful to M. O. Nestoklon and M. M. Glazov for fruitful discussions.

Conflicts of Interest: The authors declare no conflict of interest.

References

1. Jena, A. K.; Kulkarni, A.; Miyasaka, T. Halide perovskite photovoltaics: Background, status, and future prospects. *Chem. Rev.* **2019**, *5*, 3036–3103. [CrossRef]
2. Vinattieri, A.; Giorgi, G. (Eds.) *Halide Perovskites for Photonics*; AIP Publishing: Melville, NY, USA, 2021.
3. Vardeny, Z.V.; Beard, M.C. (Eds.) *Hybrid Organic Inorganic Perovskites: Physical Properties and Applications*; World Scientific: Singapore, 2022.
4. Wang, J.; Zhang, C.; Liu, H.; McLaughlin, R.; Zhai, Y.; Vardeny, S.R.; Liu, X.; McGill, S.; Semenov, D.; Guo, H.; et al. Spin-optoelectronic devices based on hybrid organic-inorganic trihalide perovskites. *Nat. Commun.* **2019**, *10*, 129. [CrossRef]
5. Ning, W.; Bao, J.; Puttisong, Y.; Moro, F.; Kobera, L.; Shimono, S.; Wang, L.; Ji, F.; Cuartero, M.; Kawaguchi, S.; et al. Magnetizing lead free halide double perovskites. *Sci. Adv.* **2020**, *6*, eabb5381. [CrossRef]
6. Kim, Y.-H.; Zhai, Y.; Lu, H.; Pan, X.; Xiao, C.; Gaulding, E.A.; Harvey, S.P.; Berry, J.J.; Vardeny, Z.V.; Luther, J.M.; et al. Chiral-induced spin selectivity enables a room-temperature spin light-emitting diode. *Science* **2021**, *371*, 1129. [CrossRef]
7. Kovalenko, M.V.; Protesescu, L.; Bondarchuk, M.I. Properties and potential optoelectronic applications of lead halide perovskite nanocrystals. *Science* **2017**, *358*, 745–750. [CrossRef]
8. Efros, A.L.; Brus, L.E. Nanocrystal quantum dots: From discovery to modern development. *ACS Nano* **2021**, *15*, 6192–6210. [CrossRef]
9. Meier, F.; Zakharchenya, B.P. (Eds.) *Optical Orientation*; North Holland: Amsterdam, The Netherlands, 1984.
10. Dyakonov, M.I. (Ed.) *Spin Physics in Semiconductors*; Springer International Publishing AG: Berlin/Heidelberg, Germany, 2017.
11. Giovanni, D.; Ma, H.; Chua, J.; Grätzel, M.; Ramesh, R.; Mhaisalkar, S.; Mathews, N.; Sum, T.C. Highly spin-polarized carrier dynamics and ultralarge photoinduced magnetization in $CH_3NH_3PbI_3$ perovskite thin films. *Nano Lett.* **2015**, *15*, 1553–1558. [CrossRef]
12. Nestoklon, M.O.; Goupalov, S.V.; Dzhioev, R.I.; Ken, O.S.; Korenev, V.L.; Kusrayev, Y.G.; Sapega, V.F.; de Weerd, C.; Gomez, L.; Gregorkiewicz, T.; et al. Optical orientation and alignment of excitons in ensembles of inorganic perovskite nanocrystals. *Phys. Rev. B* **2018**, *97*, 235304. [CrossRef]
13. Kopteva, N.E.; Yakovlev, D.R.; Yalcin, E.; Akimov, I.A.; Nestoklon, M.O.; Glazov, M.M.; Kotur, M.; Kudlacik, D.; Zhukov, E.A.; Kirstein, E.; et al. Giant optical orientation of exciton spins in lead halide perovskite crystals. *arXiv* **2023**, arXiv:2305.10875.
14. Zhang, C.; Sun, D.; Sheng, C.X.; Zhai, Y.X.; Mielczarek, K.; Zakhidov, A.; Vardeny, Z.V. Magnetic field effects in hybrid perovskite devices. *Nat. Phys.* **2015**, *11*, 427. [CrossRef]
15. Zhang, C.; Sun, D.; Yu, Z.-G.; Sheng, C.-X.; McGill, S.; Semenov, D.; Vardeny, Z.V. Field-induced spin splitting and anomalous photoluminescence circular polarization in $CH_3NH_3PbI_3$ films at high magnetic field. *Phys. Rev. B* **2018**, *97*, 134412. [CrossRef]
16. Canneson, D.; Shornikova, E.V.; Yakovlev, D.R.; Rogge, T.; Mitioglu, A.A.; Ballottin, M.V.; Christianen, P.C.M.; Lhuillier, E.; Bayer, M.; Biadala, L. Negatively charged and dark excitons in $CsPbBr_3$ perovskite nanocrystals revealed by high magnetic fields. *Nano Lett.* **2017**, *17*, 6177–6183. [CrossRef] [PubMed]
17. Odenthal, P.; Talmadge, W.; Gundlach, N.; Wang, R.; Zhang, C.; Sun, D.; Yu, Z.-G.; Vardeny, V.Z.; Li, Y.S. Spin-polarized exciton quantum beating in hybrid organic–inorganic perovskites. *Nat. Phys.* **2017**, *13*, 894. [CrossRef]
18. Belykh, V.V.; Yakovlev, D.R.; Glazov, M.M.; Grigoryev, P.S.; Hussain, M.; Rautert, J.; Dirin, D.N.; Kovalenko, M.V.; Bayer, M. Coherent spin dynamics of electrons and holes in $CsPbBr_3$ perovskite crystals. *Nat. Commun.* **2019**, *10*, 673. [CrossRef]
19. Strohmair, S.; Dey, A.; Tong, Y.; Polavarapu, L.; Bohn, B.J.; Feldmann, J. Spin polarization dynamics of free charge carriers in $CsPbI_3$ nanocrystals. *Nano Lett.* **2020**, *20*, 4724–4730. [CrossRef]
20. Zhou, M.; Sarmiento, J.S.; Fei, C.; Zhang, X.; Wang, H. Effect of composition on the spin relaxation of lead halide perovskites. *J. Phys. Chem. Lett.* **2020**, *11*, 1502–1507. [CrossRef]
21. Kirstein, E.; Yakovlev, D.R.; Glazov, M.M.; Zhukov, E.A.; Kudlacik, D.; Kalitukha, I.V.; Sapega, V.F.; Dimitriev, G. S.; Semina, M.A.; Nestoklon, M.O.; et al. The Landé factors of electrons and holes in lead halide perovskites: Universal dependence on the band gap. *Nat. Commun.* **2022**, *13*, 3062. [CrossRef]
22. Harkort, C.; Kudlacik, D.; Kopteva, N.E.; Yakovlev, D.R.; Karzel, M.; Kirstein, E.; Hordiichuk, O.; Kovalenko, M.V.; Bayer, M. Spin-flip Raman scattering on electrons and holes in two-dimensional $(PEA)_2PbI_4$ perovskites. *Small* **2023**, *19*, 2300988. [CrossRef]
23. Kirstein, E.; Yakovlev, D.R.; Glazov, M.M.; Evers, E.; Zhukov, E.A.; Belykh, V.V.; Kopteva, N.E.; Kudlacik, D.; Nazarenko, O.; Dirin, D.N.; et al. Lead-dominated hyperfine interaction impacting the carrier spin dynamics in halide perovskites. *Adv. Mater.* **2022**, *34*, 2105263. [CrossRef]
24. Belykh, V.V.; Skorikov, M.L.; Kulebyakina, E.V.; Kolobkova, E.V.; Kuznetsova, M.S.; Glazov, M.M.; Yakovlev, D.R. Submillisecond spin relaxation in $CsPb(Cl,Br)_3$ perovskite nanocrystals in a glass matrix. *Nano Lett.* **2022**, *22*, 4583–4588. [CrossRef]
25. Kirstein, E.; Kopteva, N.E.; Yakovlev, D.R.; Zhukov, E.A.; Kolobkova, E.V.; Kuznetsova, M.S.; Belykh, V.V.; Yugova, I.A.; Glazov, M.M.; Bayer, M.; et al. Mode locking of hole spin coherences in $CsPb(Cl,Br)_3$ perovskite nanocrystals. *Nat. Commun.* **2023**, *14*, 699. [CrossRef]
26. Grigoryev, P.S.; Belykh, V.V.; Yakovlev, D.R.; Lhuillier, E.; Bayer, M. Coherent spin dynamics of electrons and holes in $CsPbBr_3$ colloidal nanocrystals. *Nano Lett.* **2021**, *21*, 8481–8487. [CrossRef] [PubMed]
27. Crane, M.J.; Jacoby, L.M.; Cohen, T.A.; Huang, Y.; Luscombe, C.K.; Gamelin, D.R. Coherent spin precession and lifetime-limited spin dephasing in $CsPbBr_3$ perovskite nanocrystals. *Nano Lett.* **2020**, *20*, 8626–8633. [CrossRef]

28. Lin, X.; Han, Y.; Zhu, J.; Wu, K. Room-temperature coherent optical manipulation of hole spins in solution-grown, perovskite quantum dots. *Nat. Nanotechnol.* **2022**, *18*, 124. [CrossRef]
29. Kopteva, N.E.; Yakovlev, D.R.; Kirstein, E.; Zhukov, E.A.; Kudlacik, D.; Kalitukha, I.V.; Sapega, V.F.; Dirin, D.N.; Kovalenko, M.V.; Baumann, A.; et al. Weak dispersion of exciton Landè factor with band gap energy in lead halide perovskites: Approximate compensation of the electron and hole dependences. *arXiv* **2023**, arXiv:2301.12775.
30. Nestoklon, M.O.; Kirstein, E.; Yakovlev, D.R.; Zhukov, E.A.; Glazov, M.M.; Semina, M.A.; Ivchenko, E.L.; Kolobkova, E.V.; Kuznetsova, M.S.; Bayer, M. Tailoring the electron and hole Lande factors in lead halide perovskite nanocrystals by quantum confinement and halide exchange. *arXiv* **2023**, arXiv:2305.10586.
31. Oestreich, M.; Rühle, W.W. Temperature dependence of the electron Landè g-factor in GaAs. *Phys. Rev. Lett.* **1995**, *74*, 2315. [CrossRef] [PubMed]
32. Oestreich, M.; Hallstein, S.; Heberle, A.P.; Eberl, K.; Bauser, E.; Rühle, W.W. Temperature and density dependence of the electron Landè g factor in semiconductors. *Phys. Rev. B* **1996**, *53*, 7911. [CrossRef]
33. Zawadzki, W.; Pfeffer, P.; Bratschitsch, R.; Chen, Z.; Cundiff, S.T.; Murdin, B.N.; Pidgeon, C.R. Temperature dependence of the electron spin *g* factor in GaAs. *Phys. Rev. B* **2008**, *78*, 245203. [CrossRef]
34. Hübner, J.; Döhrmann, S.; Hägele, D.; Oestreich, M. Temperature-dependent electron Landè g factor and the interband matrix element of GaAs. *Phys. Rev. B* **2009**, *79*, 193307. [CrossRef]
35. Akkerman, Q.A.; Nguyen, T.P.T.; Boehme, S.C.; Montanarella, F.; Dirin, D.N.; Wechsler, P.; Beiglböck, F.; Rainò, G.; Erni, R.; Katan, C.; et al. Controlling the nucleation and growth kinetics of lead halide perovskite quantum dots. *Science* **2022**, *377*, 1406–1412.
36. Bujalance, C.; Caliò, L.; Dirin, D.N.; Tiede, D.O.; Galisteo-López, J.F.; Feist, J.; García-Vidal, F. J.; Kovalenko, M.V.; Míguez, H. Strong light-matter coupling in lead halide perovskite quantum dot solids. *arXiv* **2023**, arXiv:2306.10884.
37. Yakovlev, D.R.; Bayer, M. Coherent spin dynamics of carriers. In *Spin Physics in Semiconductors*; Dyakonov, M.I., Ed.; Springer International Publishing AG: Berlin/Heidelberg, Germany, 2017; Chapter 6, pp. 155–206.
38. Garcia-Arellano, G.; Trippé-Allard, G.; Legrand, L.; Barisien, T.; Garrot, D.; Deleporte, E.; Bernardot, F.; Testelin, C.; Chamarro, M.E.ergy tuning of electronic spin coherent evolution in methylammonium lead iodide perovskites. *J. Phys. Chem. Lett.* **2021**, *12*, 8272.
39. Yakovlev, D.R.; Crooker, S.A.; Semina, M.A.; Rautert, J.; Mund, J.; Dirin, D.N.; Kovalenko, M.V.; Bayer, M. Exciton-polaritons in $CsPbBr_3$ crystals revealed by optical reflectivity in high magnetic fields and two-photon spectroscopy. *arXiv* **2023**, arXiv:2307.07035.
40. Yang, Z.; Surrente, A.; Galkowski, K.; Miyata, A.; Portugall, O.; Sutton, R.J.; Haghighirad, A.A.; Snaith, H.J.; Maude, D.K.; Plochocka, P.; et al. Impact of the halide cage on the electronic properties of fully inorganic cesium lead halide perovskites. *ACS Energy Lett.* **2017**, *2*, 1621.
41. Shrivastava, M.; Krieg, F.; Mandal, D.; Poonia, A.K.; Bera, S.K.; Kovalenko, M.V.; Adarsh, K.V. Room-temperature anomalous coherent excitonic optical Stark effect in metal halide perovskite quantum dots. *Nano Lett.* **2022**, *22*, 808. [PubMed]
42. Biffi, G.; Cho, Y.; Krahne, R.; Berkelbach, T.C. Excitons and their fine structure in lead halide perovskite nanocrystals from atomistic GW/BSE calculations. *J. Phys. Chem. C* **2023**, *127*, 1891–1898.
43. Yakovlev, D.R.; Rodina, A.V.; Shornikova, E.V.; Golovatenko, A.A.; Bayer, M. Coherent spin dynamics of colloidal nanocrystals. In *Photonic Quantum Technologies: Science and Applications*; Benyoucef, M., Ed.; Wiley-VCH: Hoboken, NJ, USA, 2023.
44. Feng, D.H.; Yakovlev, D.R.; Pavlov, V.V.; Rodina, A.V.; Shornikova, E.V.; Mund, J.; Bayer, M. Dynamic evolution from negative to positive photocharging in colloidal CdS quantum dots. *Nano Lett.* **2017**, *17*, 2844–2851. [PubMed]
45. Hu, R.R.; Yakovlev, D.R.; Liang, P.; Qiang, G.; Chen, C.; Jia, T.Q.; Sun, Z.R.; Bayer, M.; Feng, D.H. Origin of two Larmor frequencies in the coherent spin dynamics of colloidal CdSe quantum dots revealed by controlled charging. *J. Phys. Chem. Lett.* **2019**, *10*, 3681–3687.
46. Hu, R.R.; Wu, Z.; Zang, Y.Y.; Yakovlev, D.R.; Liang, P.; Qiang, G.; Guo, J.X.; Jia, T.Q.; Sun, Z.R.; Bayer, M.; et al. Long-lived negative photocharging in colloidal CdSe quantum dots revealed by coherent electron spin precession. *J. Phys. Chem. Lett.* **2019**, *10*, 4994–4999. [PubMed]
47. Seth, S.; Ahmed, T.; Samanta, A. Photoluminescence flickering and blinking of single $CsPbBr_3$ perovskite nanocrystals: Revealing explicit carrier recombination dynamics. *J. Phys. Chem. Lett.* **2018**, *9*, 7007–7014. [PubMed]
48. Dey, A.; Rathod, P.; Kabra, D. Role of localized states in photoluminescence dynamics of high optical gain $CsPbBr_3$ nanocrystals, *Adv. Opt. Mater.* **2018**, *6*, 1800109.
49. Diroll, B.T.; Zhou, H.; Schaller, R.D. Low-temperature absorption, photoluminescence, and lifetime of $CsPbX_3$ (X = Cl, Br, I.n.nocrystals. *Adv. Funct. Mater.* **2018**, *28*, 1800945.
50. Li, Y.; Luo, X.; Liu, Y.; Lu, X.; Wu, K. Size- and Composition-Dependent Exciton Spin Relaxation in Lead Halide Perovskite Quantum Dots. *ACS Energy Lett.* **2020**, *5*, 1701–1708.

nanomaterials

Article

A High-Quality CdSe/CdS/ZnS Quantum-Dot-Based FRET Aptasensor for the Simultaneous Detection of Two Different Alzheimer's Disease Core Biomarkers

Xingchang Lu [1], Xiaoqi Hou [2,3,*], Hailin Tang [4], Xinyao Yi [1] and Jianxiu Wang [1,*]

[1] Hunan Provincial Key Laboratory of Micro & Nano Materials Interface Science, College of Chemistry and Chemical Engineering, Central South University, Changsha 410083, China
[2] School of Chemistry and Material Science, Hangzhou Institute for Advanced Study, University of Chinese Academy of Sciences, 1 Sub-Lane Xiangshan, Hangzhou 310024, China
[3] Key Laboratory of Intelligent Sensing Materials and Chip Integration Technology of Zhejiang Province, Hangzhou Innovation Institute, Beihang University, Hangzhou 310052, China
[4] SunYat-sen University Cancer Center, State Key Laboratory of Oncology in South China, Collaborative Innovation Center for Cancer Medicine, Guangzhou 510060, China
* Correspondence: houxiaoqi@ucas.ac.cn (X.H.); jxiuwang@csu.edu.cn (J.W.)

Abstract: The simultaneous detection of two different biomarkers for the point-of-care diagnosis of major diseases, such as Alzheimer's disease (AD), is greatly challenging. Due to the outstanding photoluminescence (PL) properties of quantum dots (QDs), a high-quality CdSe/CdS/ZnS QD-based fluorescence resonance energy transfer (FRET) aptasensor for simultaneously monitoring the amyloid-β oligomers (AβO) and tau protein was proposed. By engineering the interior inorganic structure and inorganic–organic interface, water-soluble dual-color CdSe/CdS/ZnS QDs with a near-unity PL quantum yield (>90%) and mono-exponential PL decay dynamics were generated. The π–π stacking and hydrogen bond interaction between the aptamer-functionalized dual-color QDs and gold nanorods@polydopamine (Au NRs@PDA) nanoparticles resulted in significant fluorescence quenching of the QDs through FRET. Upon the incorporation of the AβO and tau protein, the fluorescence recovery of the QDs-DNA/Au NRs@PDA assembly was attained, providing the possibility of simultaneously assaying the two types of AD core biomarkers. The lower detection limits of 50 pM for AβO and 20 pM for the tau protein could be ascribed to the distinguishable and robust fluorescence of QDs and broad spectral absorption of Au NRs@PDA. The sensing strategy serves as a viable platform for the simultaneously monitoring of the core biomarkers for AD and other major diseases.

Keywords: quantum dots; Aβ oligomers; tau protein; simultaneous detection; aptasensor

1. Introduction

Alzheimer's disease (AD) is a progressive and severe neurodegenerative disorder of the brain characterized by memory loss, cognitive dysfunction, behavioral disability, and irreversible brain damage, which drastically affects public health [1]. The pathological cascade of AD lasts for at least 10–15 years prior to the onset of clinical symptoms [2]. It has been confirmed that amyloid plaques and neurofibrillary tangles, which are formed largely by fibrillar forms of amyloid-β (Aβ) peptide and hyperphosphorylated tau protein, may contribute to the AD pathogenesis [3,4]. Among the various aggregated forms, the soluble Aβ oligomer (AβO), rather than the small Aβ monomer (AβM) and insoluble Aβ fibril (AβF), is the most neurotoxic form in vivo [5]. Thus, it is extremely desirable to monitor the core biomarkers of the AβO and tau protein for the point-of-care diagnosis and study of the pathogenesis of AD.

In recent years, numerous efforts have been made to develop reliable methods for the quantitative and accurate determination of AD biomarkers, including but not limited to electrochemistry [6,7], electrochemical luminescence [8,9], photo-electrochemistry [10,11], colorimetry [12,13], surface-enhanced Raman scattering [14], surface plasmon resonance [15], and so on. Recently, QD-based FRET and electrochemiluminescence resonance energy transfer (ECL-RET) systems have been constructed. For example, Jia's group reported a dual-wavelength ratiometric ECL-RET aptasensor for the detection of the Aβ protein [9], which exhibited a wider concentration range and superior sensitivity and selectivity for Aβ analysis. Most of the above methods aimed to assay one kind of AD biomarker, with either a low sensitivity or requirements for sophisticated instrumentation. It is known that almost all the major diseases are accompanied by the abnormal regulation of multiple biomarkers, and the detection of a single biomarker may cause a false diagnosis [16,17]. As an alternative, the fluorescence resonance energy transfer (FRET)-based methods, in which the energy from the excited fluorophore (energy donor) is transferred to the quencher (energy acceptor) in close proximity (within 10 nm), possesses a wide applicability in biological assays [18–23].

Colloidal quantum dots (QDs) serve as an unprecedented class of photo-emissive materials for optical biosensing due to their unique characteristics, such as their size-dependent fluorescent emission, broad excitation and narrow emission spectra, high emission brightness, and excellent optical and thermal stability [24–27]. Furthermore, the specific photophysical properties of QDs, such as their fluorescence blinking, quantum yield, temperature-dependent characteristics, etc., can affect their optical and optoelectronic applications [28–32]. Recently, tremendous advances in the fabrication of CdSe/CdS core/shell QDs with nearly ideal optical properties have been achieved [33,34]. However, these QDs were all synthesized in nonaqueous media and are not suitable for biosensing applications [35]. A variety of strategies have been proposed to construct water-soluble QDs, such as their encapsulation in micelles [36], coating with silica [37], and ligand exchange [38]. The first two strategies led to the formation of QDs of large hydrodynamic sizes, and the increased overall distance between the donor–acceptor pairs lowered the FRET efficiency, which limited the FRET-based biosensing applications [39]. By contrast, ligand exchange is a relatively simple procedure, and the compact QDs formed were better suited to FRET-based applications. It is worth noting that a large variety of surface traps usually existed on the water-soluble QDs [40,41]. To isolate these traps from the photo-generated excitons in the QDs, it was necessary to epitaxially grow an additional layer of inorganic shell with a large bandgap, such as a ZnS shell [42–44]. However, due to the large lattice mismatch (12%) between the CdSe core and ZnS shell, the intermediate layer of CdS was introduced to relieve the lattice strain [45]. Thus, the CdSe/CdS/ZnS core/shell/shell QDs acted as an ideal candidate for biosensing applications.

Gold nanorods (Au NRs) have been widely used in biological applications due to their high extinction coefficient and shape and size controllability [46,47]. It was found that the surface of Au NRs can be derived from various species, such as dopamine, and the resultant polydopamine-capped gold nanorods (Au NRs@PDA) were functionalized with amino, hydroxyl, and quinone groups [48]. These functional groups on the Au NRs@PDA then served as a bridge for the combination with single-stranded DNA through hydrogen bonding and π–π stacking [49–51]. Furthermore, the broad spectral absorption of the Au NRs@PDA provided the possibility of designing fluorescence-quenched assays.

Using dual-color QDs as energy donors and Au NRs@PDA as energy acceptors, a simple and sensitive FRET aptasensor for the simultaneous detection of the AβO and tau protein was proposed (Scheme 1). Two color-emitting CdSe/CdS/ZnS core/shell/shell QDs with ideal optical properties were synthesized and functionalized with aptamers to the AβO and tau protein, respectively. Through π–π stacking and hydrogen bond interaction, the QDs-DNA/Au NRs@PDA assembly was constructed, which triggered the FRET between the QDs-DNA and Au NRs@PDA due to their close proximity. However, the specific binding of the aptamers to the AβO and tau protein led to the detachment of the QDs-DNA from the surface of Au NRs@PDA. Thus, the quenched fluorescence signals were remarkably recovered. By monitoring the change in the fluorescence signals of the

QDs-DNA under single-wavelength excitation, the simultaneous detection of two different AD core biomarkers was achieved.

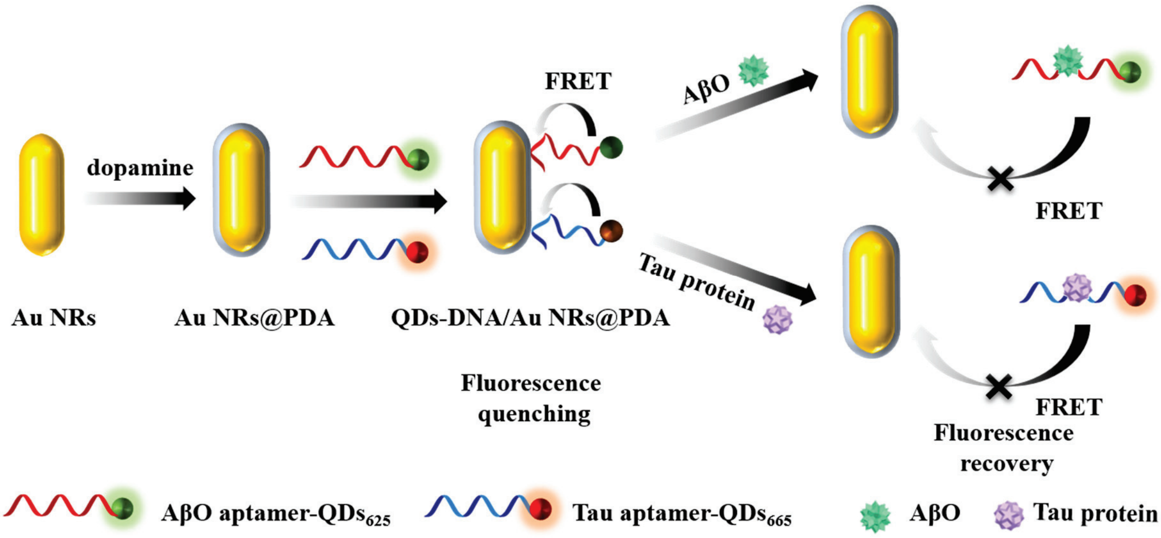

Scheme 1. Schematic illustration of the simultaneous detection of AβO and tau protein using the QDs-based FRET aptasensor.

2. Materials and Methods

2.1. Chemicals and Reagents

Silver nitrate ($AgNO_3$), SH-PEG-CH_3 (methoxy poly(ethylene glycol) thiol, MW = 5000), bovine serum albumin (BSA), selenium powder (Se, 200 mesh, 99.999%), cadmium oxide (CdO, 99.998%), and sulfur powder (S, 99.98%) were obtained from Sigma-Aldrich (St. Louis, MO, USA). Mercaptopropionic acid (MPA, >99%), tetramethylammonium hydroxide (TMAH, 25% *w*/*w* in methanol), myristic acid (98%), stearic acid (>90%), and 1-octadecene (ODE, 90%) were purchased from Alfa Aesar (Shanghai, China). 1,1,1,3,3,3-Hexafluoroisopropanol (HFIP) was acquired from Shanghai Macklin Biochemical Co., Ltd. (Shanghai, China). Hydrogen tetrachloroaurate trihydrate ($HAuCl_4 \cdot 3H_2O$), sodium borohydride ($NaBH_4$), cetyltrimethylammonium bromide (CTAB), dimethyl sulfoxide (DMSO), ascorbic acid, and other organic solvents were obtained from Sinopharm Chemical Reagent Co., Ltd. (Shanghai, China). All the chemicals were used directly, without any purification. Aβ (1–40) peptide (catalog number: HY-P0265) was purchased from MedChemExpress (Monmouth Junction, NJ, USA). Human tau protein (catalog number: orb392120) was purchased from Biorbyt (Cambridge, UK). The DNA aptamers were synthesized and purified by Sangon Biotechnology Co., Ltd. (Shanghai, China). The thiolated aptamers to the AβO and tau protein possessed the sequences of 5′-HS-$(CH_2)_6$-GCC TGT GTT GGG GCG GGT GCG and 5′-HS-$(CH_2)_6$-GCG GAG CGT GGC AGG-3′, respectively. A human serum sample was provided by the Sun Yat-sen University Cancer Center. Ultrapure water (18.2 MΩ cm,) was used to prepare the aqueous solutions throughout the experiments.

2.2. Instruments and Characterization

Transmission electron microscopic (TEM) images were taken using a Hitachi 7700 transmission electron microscope (Tokyo, Japan) with an accelerating voltage of 120 kV. The steady-state and transient photoluminescence spectra were measured using an Edinburgh Instruments FS5 spectrometer (Livingston, UK) with the excitation wavelengths at 405 nm and 450 nm, respectively. The absolute photoluminescence quantum yield of the QDs was measured using a QE65000 spectrometer equipped with an Ocean Optics FOIS-1 integrating sphere. The QD sample was gradiently diluted with an optical density below 0.1. Each diluted sample was measured at room temperature. The accuracy and stability of the measurement system were verified using organic dyes with known photoluminescence quantum yields. The ultraviolet-visible (UV-vis) spectra were monitored using an Agilent-Cary 60 spectrophotometer (Palo Alto, CA, USA). The zeta potential and hydrated particle size were measured at a neutral pH with a Malvern Zen 3600 Zetasizer (Malvern, UK). All the optical measurements were performed at room temperature.

2.3. Preparation of Water-Soluble Dual-Color CdSe/CdS/ZnS Core/Shell/Shell QDs

The alkanoate-coated CdSe/CdS/ZnS core/shell/shell QDs were synthesized according to the previous method [44]. The purification process of the core/shell/shell QDs can be described as follows. A total of 1 mL of the reaction mixture was mixed with 5 mL of ethyl acetate, and this was followed by centrifugation at 10,000 rpm for 3 min. The supernatant was removed, and the above procedure was repeated three times. After that, water-soluble mercaptopropionic acid (MPA)-capped CdSe/CdS/ZnS QDs were synthesized by exchanging the carboxylate ligands for MPA, following the reported protocol [52]. Briefly, 50 μL of MPA was added to 2 mL of purified QDs in chloroform. After ultrasonication for 10 min and centrifugation at 4000 rpm for 2 min, the precipitates were washed twice with hexane. Then, the precipitates were dried using high-purity argon to completely remove the organic solvent. Finally, the precipitates were dissolved in 610 μL of aqueous solution containing 10 μL of TMAH, and the concentration of the QDs was estimated to be 20 μM according to Lambert–Beer's law, in which the extinction coefficient is determined by Peng's group [53].

2.4. Fabrication of the Aptamer-Functionalized QDs

The aptamers to the AβO and tau protein were conjugated with the QDs via a ligand exchange process [41]. Briefly, 200 μL of 10 μM of the aptamer to AβO was mixed with 10 μL of tris (2-carboxyethyl) phosphine hydrochloride (TCEP, 20 mM) at room temperature for 1 h to break the $S-S$ bond between the thiolated aptamers, followed by incubation with 10 μL of the MPA-capped QDs_{625} (20 μM) that emit at 625 nm. The mixed solution was shaken overnight at room temperature under dark conditions, which allowed for the complete exchange of the thiol groups on the MPA-functionalized QDs with the thiolated aptamers. The resultant samples were purified by ultrafiltration using a centrifugal filter with a 50 kDa molecular weight cutoff (centrifugation at 8000 rpm for 2 min for three times). Finally, the upper phase containing the aptamer-capped QDs was redispersed in 2 mL of deionized water and stored at 4 °C for further use. The functionalization of the QDs_{665} that emit at 665 nm with the aptamer to the tau protein was performed in a similar way to that of the QDs_{625}.

2.5. Synthesis of Au NRs-CTAB

First, the CTAB-capped Au seeds were prepared according to the previous method [54]. Briefly, 7.5 mL of 0.1 M CTAB was mixed with 100 μL of 24 mM $HAuCl_4$, and the above solution was diluted with 9.4 mL of deionized water. Then, 0.6 mL of 10 mM ice-cold $NaBH_4$ was added under magnetic stirring. After vigorous stirring for 2 min, the seed solution was kept at room temperature and used within 3 h. Afterwards, the growth of the Au NRs was initiated by the introduction of the growth solution (100 mL of 0.1 M CTAB, 2 mL of 24 mM $HAuCl_4$, 2 mL of 0.5 M H_2SO_4, 350 μL of 10 mM $AgNO_3$, and 800 μL of 0.1 M ascorbic acid) into 240 μL of the seed solution under vigorous stirring. The above mixed solution was stirred for 2 min at 30 °C and then left to stand for 12 h. The precipitates were collected by centrifugation at 8000 rpm for 10 min and washed with deionized water more than three times to remove the surfactant and unreacted materials. The obtained Au NRs-CTAB was redispersed in 20 mL of deionized water with a concentration of 1 mg/mL.

2.6. Synthesis of Au NRs@PDA

The CTAB-capped Au NRs were unstable in alkaline conditions during dopamine self-polymerization. To solve this problem, a ligand exchange reaction, in which the CTAB layer on the Au NRs was replaced with $SH\text{-}PEG\text{-}CH_3$, was performed [50]. Briefly, 10 mL of the Au NRs-CTAB (1 mg/mL) was added into 1 mL of $SH\text{-}PEG\text{-}CH_3$ (5 mg/mL), followed by sonication in an ice bath for 2 h. By removing the supernatant through two centrifuging procedures at 8000 rpm for 10 min, the precipitates of the Au NRs-PEG were collected and dispersed in 10 mL of deionized water. Then, 2 mL of the obtained Au NRs-PEG was redispersed in 17 mL of tris-HCl solution (5 mM, pH 8.5), followed by the addition of 1 mL of 2 mg/mL dopamine and then sonication for 60 min. The Au NRs@PDA with various shell thicknesses were synthesized by simply changing the polymerization time (30, 60, and 90 min). Finally, by centrifuging twice at 8000 rpm for 10 min, the Au NRs@PDA was redispersed in 4 mL of deionized water with a concentration 0.5 mg/mL.

*2.7. Formation of Soluble Aβ*O

The treatment of the Aβ40 powder was carried out based on previous work [5]. Briefly, lyophilized Aβ peptide was dissolved in 1 mg/mL of HFIP and incubated overnight at room temperature. The above solution was sonicated for 30 min, and HFIP was evaporated under a gentle nitrogen stream. Then, the Aβ peptide was redissolved in dimethyl sulfoxide (DMSO) at a concentration of 1 mM and stored at −20 °C for later use. The AβO and Aβ fibrils (AβF) were obtained by incubating 100 µM of the pretreated Aβ in phosphate-buffered solution (20 mM, pH 7.4) in a thermostatic water bath at 37 °C for 24 h and 72 h in the dark, respectively. Based on the UV-vis spectra, the concentrations of AβO and AβF were determined and calculated as equivalent to the concentration of the pretreated Aβ peptide.

2.8. Simultaneous Detection of AβO and Tau Protein Using the FRET Aptasensor

To detect the AβO and tau protein simultaneously, 10 µL of the AβO-aptamer-functionalized QDs_{625} were mixed with 10 µL of the tau-protein-aptamer-functionalized QDs_{665}, and then 55 µL of 0.5 mg/mL Au NRs@PDA was introduced into the mixture to quench the fluorescence upon 30 min of incubation. In the presence of different concentrations of AβO (0, 100, 250, 500, 1000, 2000, 5000, and 10,000 pM) and tau protein (0, 50, 250, 750, 1000, 1500, 3000, and 5000 pM), the recovered fluorescence was recorded upon 120 min of incubation at room temperature. The fluorescence measurement conditions were as follows: excitation wavelength = 405 nm, excitation and emission slit width = 5.0 nm.

3. Results

3.1. Characterization of the QDs, QDs-DNA Conjugates, and Au NRs

Figure 1A–C shows the transmission electron microscopy (TEM) images of the two types of QDs and the corresponding Au NRs. Using CdSe QDs as the core with average diameters of 3.0 nm and 5.4 nm, the QDs_{625} and QDs_{665} were synthesized according to our previous report [44]. The alkanoate-coated CdSe/CdS/ZnS core/shell/shell QDs emitted at 625 nm (QDs_{625}) and 665 nm (QDs_{665}) and were excited at 405 nm, respectively. The QDs_{625} and QDs_{665} both possessed ideal optical properties toluene (Figure S1A–D) and showed well-controlled interfacial structures, with a small size distribution (Figures 1A,B and S2A,B). As evidenced by the EDS mapping image of Se, the CdSe was located in the center of the core/shell/shell structure, while Zn and S elements were distributed in the outer shell, indicating the well-controlled epitaxial growth of the shell (Figure S3). Moreover, the single crystalline structure of the QDs was observed (Figure S4). The hydrophilic ligand of MPA was used to convert the QDs into water-soluble forms [52,55]. After ligand exchange, the photoluminescence (PL) spectra were still narrow and symmetric, and the emission wavelengths and peak widths remained the same (Figure 1D). The QDs_{625} and QDs_{665} showed a near-unity PL quantum yield (>90%), and the transient PL spectra could be well-fitted by a mono-exponential function (Figure 1E, 1000 counts, goodness-of-fit < 1.30), indicating the elimination of the trap states accessible to the excited states. The CdSe/CdS/ZnS core/shell/shell QDs exhibited a high optical quality in both toluene and water media, which resulted from the additional layer of the inorganic ZnS shell with a large bandgap. The outermost shell could isolate the electron and hole wavefunctions from the environment, thus substantially improving the photostability of the QDs. The excellent optical stability of the water-soluble QDs (Figure S5A,B) provided the basis for their biological applications.

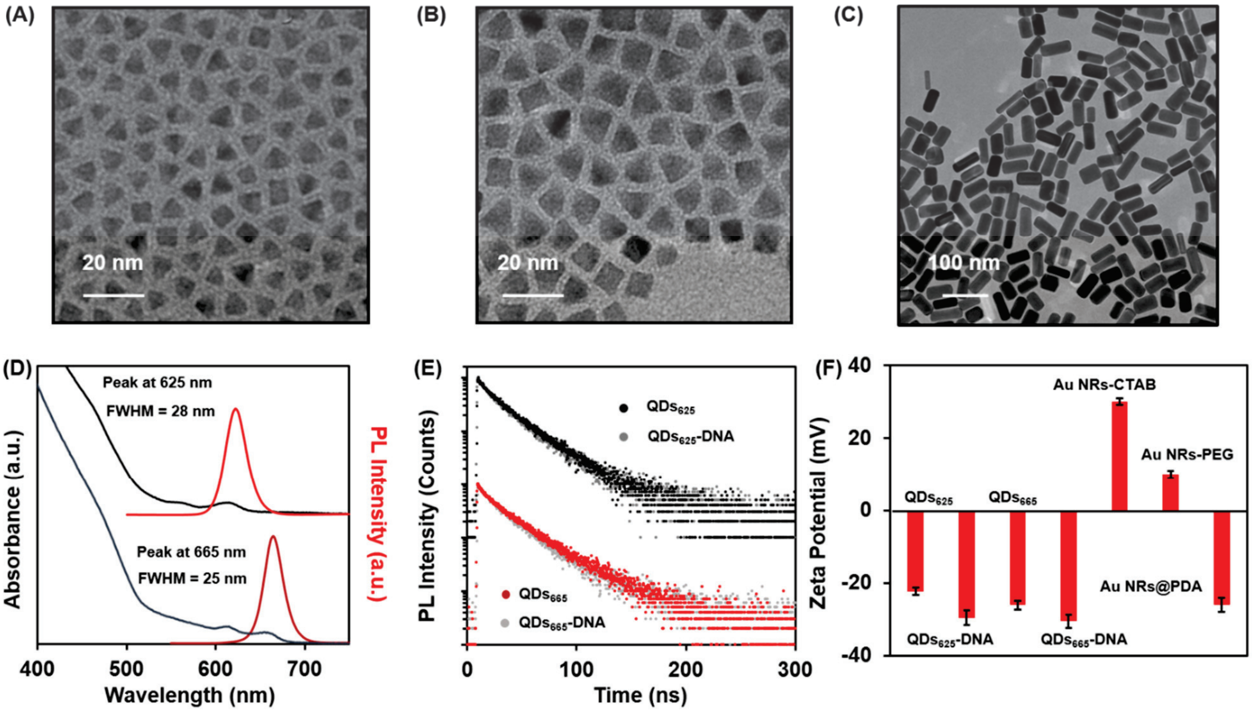

Figure 1. TEM images of (**A**) the alkanoate-coated QDs_{625}, (**B**) QDs_{665} in toluene, and (**C**) Au NRs-CTAB. (**D**) UV-vis absorption and fluorescence spectra of the QDs_{625}-DNA and QDs_{665}-DNA conjugates. The FWHM represented the full width at half maximum. (**E**) PL decay dynamics of QDs_{625} and QDs_{665} before and after conjugation with aptamers that were excited at 450 nm. (**F**) Zeta potentials of QDs_{625}, QDs_{625}-DNA, QDs_{665}, QDs_{665}-DNA, Au NRs-CTAB, Au NRs-PEG, and Au NRs@PDA.

Aptamers can be attached to QDs via ligand exchange between the thiol groups of MPA-functionalized QDs and the thiolated aptamers [56]. Notably, the PL decay dynamics and fluorescence intensities of the QDs_{625} and QDs_{665} were almost unchanged before and after conjugating them with thiolated aptamers (Figures 1E and S6A,B), indicating no additional surface defect states of the QDs upon their association with the aptamers and the preserved ideal optical quality of the QDs-DNA conjugates. Moreover, the successful conjugation of the aptamers to the QDs was confirmed by zeta potential measurements (Figure 1F). The QDs-DNA conjugates possessed a more negative zeta potential than the pure QDs due to the negatively charged phosphate backbone of the aptamers. Furthermore, the hydrodynamic diameter of the QDs_{625} or QDs_{665} functionalized with aptamers was slightly larger than that of the pure QDs (Figure S7A,B), further demonstrating the conjugation of the QDs with the aptamers.

The Au NRs@PDA served as an excellent fluorescence quencher of the QDs [47]. The CTAB-capped Au NRs were prepared by a modified silver-assisted seed growth method, and a typical uniform rod structure with an average diameter of 54 nm was attained (Figures 1C and S8). The Au NRs possessed wide absorption bands centered at 524 and 654 nm (Figure S9), which corresponded to the transverse and longitudinal surface plasmon resonance (SPR) of the Au NRs, respectively [46]. After the replacement of the CTAB with polyethylene glycol (PEG), the surface charge changed from +30.1 to +10.0 mV (Figure 1F), and a slight blue shift of the longitudinal SPR peak was obtained (Figure S9). After coating the PEG-functionalized Au NRs with PDA, the zeta potential changed to

−26.2 mV (Figure 1F), which was attributed to the abundant phenolic hydroxyl groups on the PDA shell.

3.2. Feasibility of the Proposed Aptasensor

As shown in Figure 2A, coating the surface of the Au NRs-PEG with PDA led to a redshift of the longitudinal SPR peak from 645 nm (black curve) to 668 nm (blue curve). In the meantime, the absorption spectrum of the Au NRs@PDA overlapped with the fluorescence spectrum of the QDs$_{625}$-DNA or QDs$_{665}$-DNA, providing the possibility of energy transfer from the QDs to the Au NRs@PDA. As expected, the QDs$_{625}$-DNA showed strong fluorescence upon excitation at 405 nm (black curve, Figure 2B). However, with the incorporation of the Au NRs@PDA, the fluorescence intensity of the QDs$_{625}$-DNA decreased by about 82% (red curve, Figure 2B). Simultaneously, the PL decay dynamics changed from a mono-exponential function (black curve, inset of Figure 2B) to double-exponential function (red curve, inset of Figure 2B). The additional short lifetime decay channel indicated the existence of the efficient nonradiative recombination of the excited states upon binding to the Au NRs@PDA, which led to the reduced PL quantum yield. The fluorescence quenching was induced by the distance-dependent FRET resulting from the binding of the QDs-DNA conjugates (donors) with the Au NRs@PDA nanoparticles (acceptors) via π–π stacking and hydrogen bonding. Due to the presence of amino, hydroxyl, and quinone groups on the PDA, the single-stranded DNA could be attached to the PDA surface. Upon the incubation of AβO with the QDs$_{625}$-DNA/Au NRs@PDA composites, the fluorescence of the QDs$_{625}$ was partially recovered (blue curve, Figure 2B). The specific binding between the AβO and its aptamer thus weakened the interaction between the QDs$_{625}$-DNA and Au NRs@PDA, and the detachment of the QDs$_{625}$-DNA from the surface of the Au NRs@PDA led to the recovery of the fluorescence signal. In the presence of AβO, the fraction of the short lifetime decay channel decreased significantly (blue curve, inset of Figure 2B) relative to that of the QDs$_{625}$-DNA/Au NRs@PDA composites, further demonstrating that the FRET between the QDs$_{625}$-DNA and Au NRs@PDA was destroyed to a large degree. In the case of the tau protein, similar results were attained for the QDs$_{665}$-DNA/Au NRs@PDA composites (Figure 2C). Therefore, the sensing protocol served as a reliable means of the simultaneous and accurate determination of the AβO and tau protein.

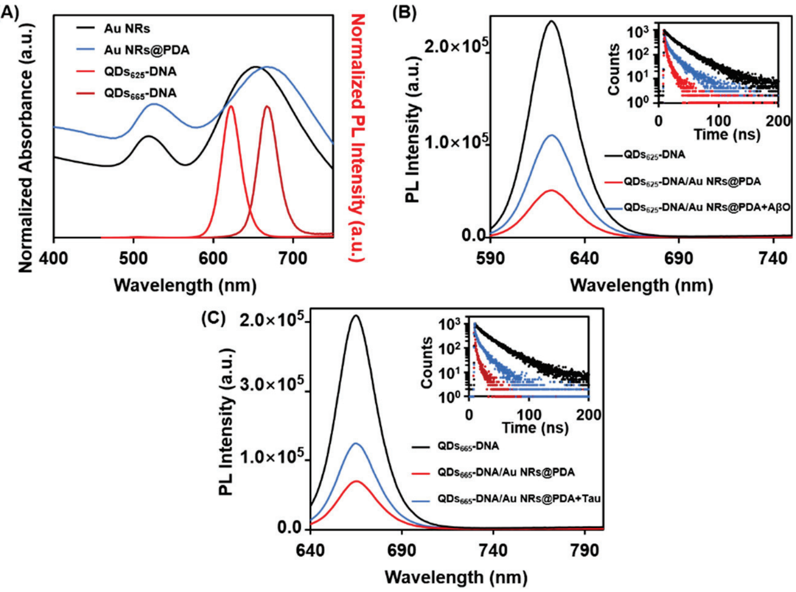

Figure 2. (**A**) The absorption spectra of Au NRs and Au NRs@PDA, and fluorescence spectra of QDs$_{625}$-DNA and QDs$_{665}$-DNA. Feasibility of the aptasensor for the (**B**) AβO and (**C**) tau protein. The insets in (**B**,**C**) show the corresponding PL decay dynamics excited at 450 nm. The concentrations of the AβO and tau protein were maintained at 5 nM and 2 nM, respectively.

3.3. Optimization of the Experimental Conditions

To achieve a better analytical performance, the self-polymerization time of the dopamine, concentration of the Au NRs@PDA, and incubation time for fluorescence quenching and recovery were optimized. The FRET efficiency was strongly dependent on the distance between donor–acceptor pairs and spectral overlap between the donor emission and acceptor absorption [57]. Notably, the absorption spectrum of the Au NRs@PDA and thickness of the PDA shell could be tuned by adjusting the self-polymerization time of the dopamine. In the weak alkaline medium, the Au NRs@PDA with a uniform and thin PDA shell was constructed via the in situ polymerization of dopamine for different time periods (30, 60, and 90 min for Figure 3A–C, respectively), and the inset histograms in Figure 3A–C show that the average PDA shell thicknesses were 5.2, 6.2, and 9.5 nm, respectively. The Au NRs@PDA with various shell thickness possessed the maximum absorption peaks at 650, 668, and 685 nm, respectively (Figure 3D). Next, the fluorescence quenching ability of the Au NRs@PDA with various shell thicknesses for the QDs_{625}-DNA was examined (Figure 3E). Remarkably, a larger fluorescence quenching efficiency was attained when the shell thickness of the PDA was 6.2 nm (red curve), which was accompanied by the significantly changed PL decay dynamics of the QDs_{625}-DNA (the inset red curve). However, in the case of the $PDA_{5.2\ nm}$, with a thin thickness, the PDA coating might not have been uniform, while the increased thickness of the $PDA_{9.5\ nm}$ might have led to the weakened FRET effect. Likewise, similar results were obtained for the QDs_{665}-DNA when the shell thickness of the PDA was maintained at 6.2 nm (Figure S10).

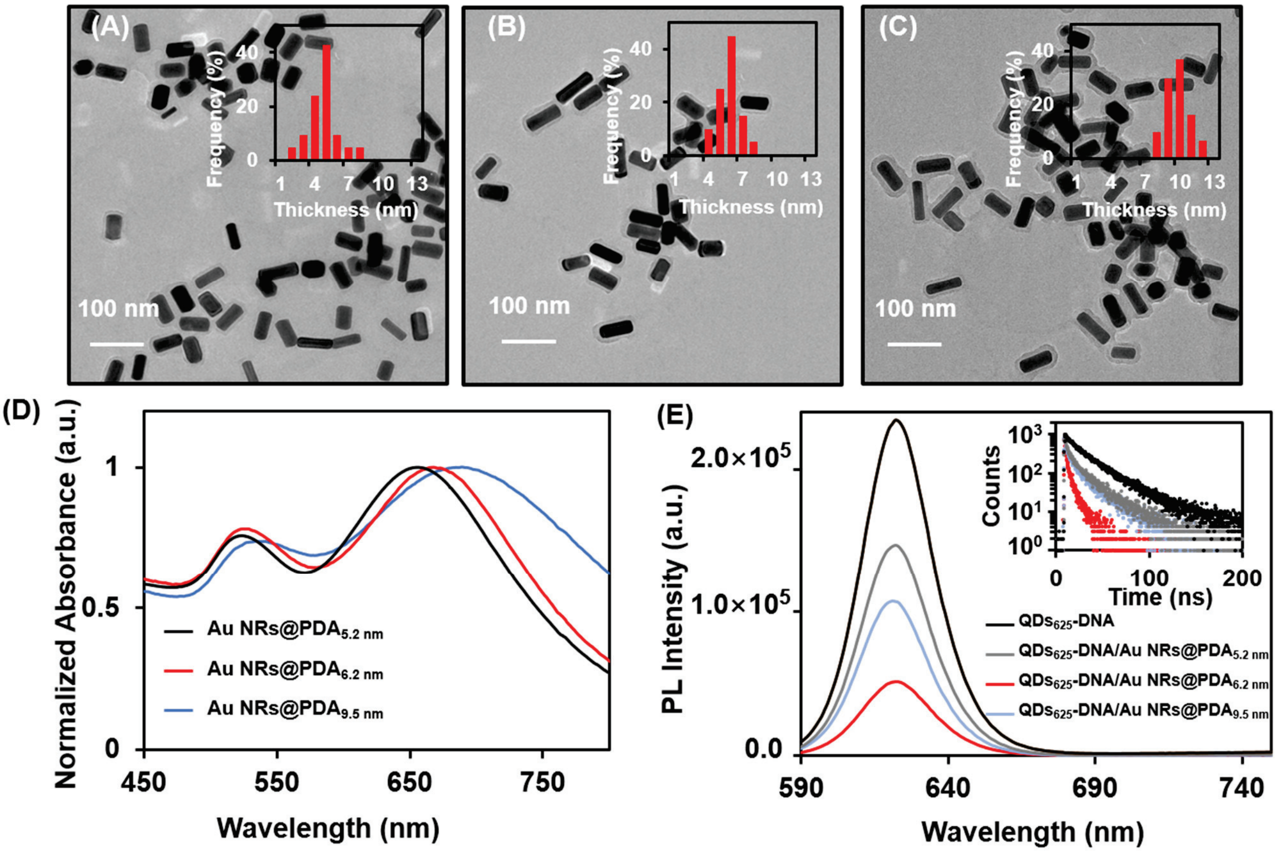

Figure 3. (**A**–**C**) TEM images of Au NRs@PDA with various shell thicknesses. The inset histograms show the average thickness of the PDA shell. (**D**) The absorption spectra of Au NRs@PDA with various shell thicknesses. (**E**) Fluorescence spectra of QDs_{625}-DNA in the absence and presence of Au NRs@PDA with various shell thicknesses. The inset shows the corresponding PL decay dynamics.

The concentration of the Au NRs@PDA was crucial for quenching the fluorescence of the QDs-DNA. As shown in Figure S11A, the fluorescence intensity of the QDs_{625}-DNA gradually decreased with the increase in the Au NRs@PDA concentration and began to level off after 25 μg/mL. Thus, 25 μg/mL of the Au NRs@PDA was used in the following experiments. Similarly, the fluorescence intensity of the QDs_{665}-DNA decreased with the increasing concentration of the Au NRs@PDA and plateaued at 20.8 μg/mL (Figure S11B). The incubation time also served as an important parameter for the fluorescence quenching and recovery. The fluorescence quenching of the QDs_{625}-DNA (Figure S12A) or QDs_{665}-DNA (Figure S12B) by the Au NRs@PDA became saturated at 30 min. With the incorporation of the AβO (Figure S12C) or tau protein (Figure S12D), the fluorescence recovery reached a maximum level at 120 min. Thus, the optimized incubation times for the fluorescence quenching and recovery were fixed at 30 min and 120 min, respectively.

3.4. Cross-Reactivity Analysis and Simultaneous Detection of the AβO and Tau Protein

The CdSe/CdS/ZnS QDs-based FRET aptasensor was capable of simultaneously determining the AβO and tau protein. First, the cross-reactivity between the AβO and tau protein was investigated. As shown in Figure 4A, the fluorescence intensity of theQDs_{625}-DNA increased upon the incorporation of AβO, while that of the QDs_{665}-DNA remained unchanged. Similarly, the existence of the tau protein only influenced the fluorescence intensity of the QDs_{665}-DNA. These results suggested no cross-reactivity between the AβO and tau protein. Under the optimum experimental conditions, the fluorescence intensities of the QDs_{625}-DNA and QDs_{665}-DNA excited at 405 nm gradually increased with the increasing concentrations of the AβO and tau protein, respectively (Figure 4B). The increased fluorescence intensity could be ascribed to the formation of a protein-aptamer complex, thus increasing the distance between the QDs-DNA and Au NRs@PDA and prohibiting the energy transfer from the QDs-DNA to Au NRs@PDA. The $F - F_0$ (where F and F_0 represent the integral fluorescence area of the QDs_{625}-DNA in the presence and absence of AβO, respectively) was found to be linearly proportional to the concentrations of AβO, ranging from 100 to 2000 pM (Figure 4C and the inset), and the linear regression equation was expressed as $F - F_0 = 287{,}972\ C_{A\beta O}$ (nM) + 149,804 ($R^2 = 0.9914$). The limit of detection (LOD) for AβO was estimated to be 50 pM based on the signal-to-noise ratio of 3. Likewise, a linear relationship between the $F - F_0$ (where F and F_0 represent the integral fluorescence area of the QDs_{665}-DNA in the presence and absence of the tau protein, respectively) was observed, and a concentration of the tau protein ranging from 50 to 1500 pM was attained with the linear regression equation of $F - F_0 = 576{,}773\ C_{tau}$ (nM) + 248,485 ($R^2 = 0.9904$) (Figure 4D and the inset). The LOD for the tau protein was calculated to be 20 pM. The relative standard deviation (RSD) was less than 5% for all the measurements, indicating the high precision and good repeatability of the proposed method. The CdSe/CdS/ZnS QDs-based FRET aptasensor for the assay of dual AD biomarkers possessed an excellent analytical performance, being comparable with or superior to the previously reported work (Table S1). Such a good performance could result from the outstanding fluorescence property of QDs and the high fluorescence quenching efficiency of Au NRs@PDA.

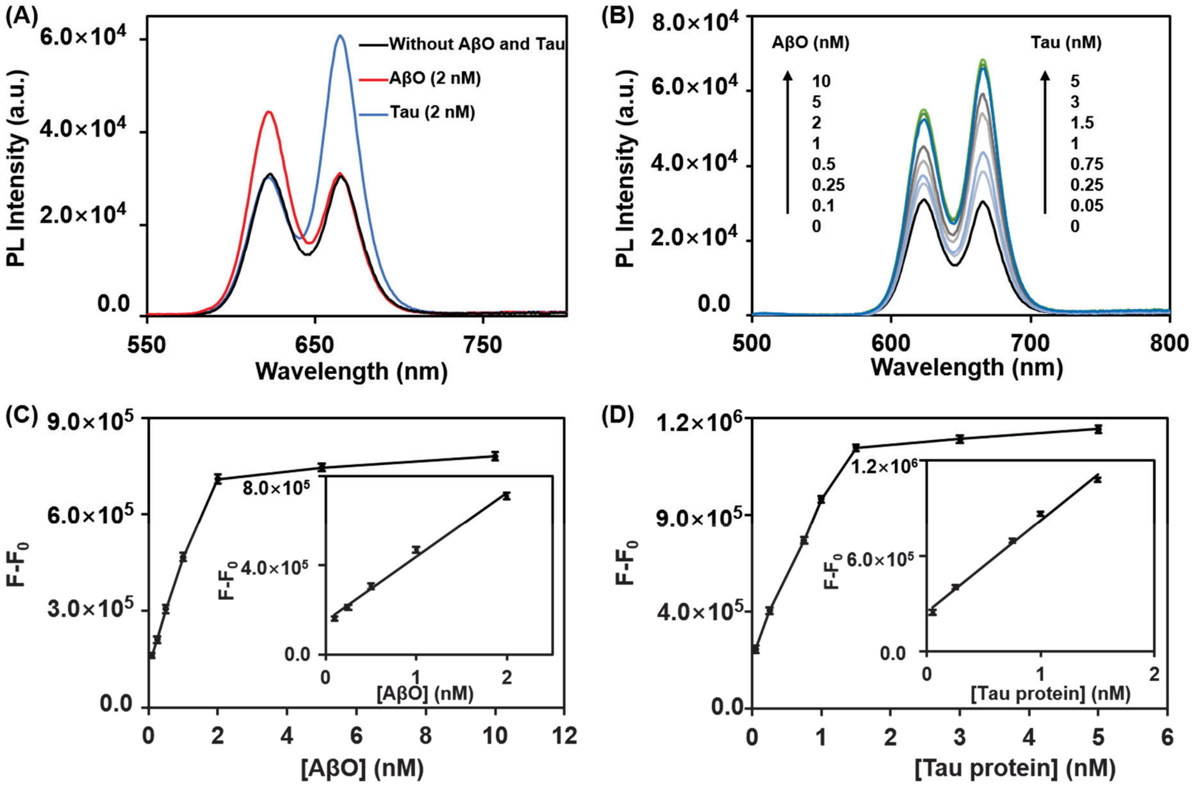

Figure 4. (**A**) Fluorescence spectra of QDs-DNA/Au NRs@PDA composites in the absence and presence of AβO or tau protein. (**B**) Fluorescence spectra of QDs-DNA/Au NRs@PDA composites upon incubation with different concentrations of AβO and tau protein. (**C**) Dependence of the $F - F_0$ for QDs_{625}-DNA on the concentrations of AβO. The inset shows the linear relationship with the concentrations of AβO from 100 to 2000 pM. (**D**) Dependence of the $F - F_0$ for QDs_{665}-DNA on the concentrations of tau protein. The inset shows the linear relationship with the concentrations of the tau protein from 50 to 1500 pM.

3.5. Selectivity of the FRET Aptasensor

To evaluate the specificity of the FRET aptasensor, the interfering species, such as BSA, AβM, and AβF, were investigated. The concentrations of the AβO and tau protein were maintained at 1.5 nM and 1 nM, respectively, while that of the interfering substances was 20 nM. As shown in Figure 5 and Figure S13, although the concentration of the interfering substances was much higher than that of the AβO and tau protein, no obvious fluorescence recovery of the QDs_{625}-DNA and QDs_{665}-DNA for the interfering species was obtained. The excellent specificity of the proposed method could be ascribed to the high binding affinity between the aptamer and AβO or tau protein.

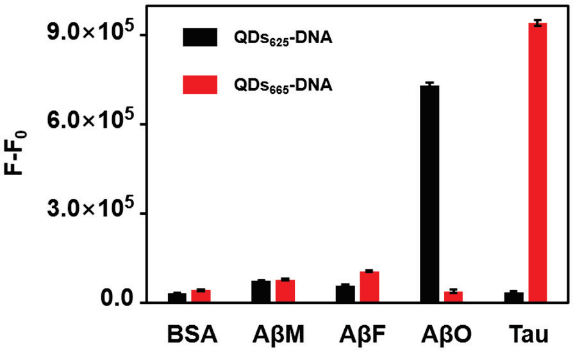

Figure 5. Selectivity of the FRET aptasensor.

3.6. Real Sample Analysis

To demonstrate the feasibility of the method for potential clinical applications, recovery assays for the AβO and tau protein were carried out. Various concentrations of AβO (200, 500, and 1500 pM) or tau protein (100, 500, and 1000 pM) were added to the 500-fold-diluted human serum samples, and the recovery values of 95–102% for AβO and 98–104% for tau protein were obtained (Table 1), indicating that the method was largely free from the matrix effect of the real sample. The CdSe/CdS/ZnS QDs-based FRET aptasensor thus holds great promise for the multiplexed detection of AD biomarkers in clinical samples.

Table 1. Determination of AβO and tau protein in human serum samples (n = 3).

Analytes	Spiked (pM)	Found (pM)	Recovery (%)	RSD (%)
AβO	200	190	95	3.59
	500	510	102	4.16
	1500	1470	98	2.35
tau protein	100	98	98	4.23
	500	520	104	3.62
	1000	1010	101	4.76

4. Conclusions

The simultaneous detection of dual types of AD core biomarkers was proposed based on a high-quality CdSe/CdS/ZnS QDs FRET aptasensor. Under the optimal conditions, the sensing strategy displayed an excellent analytical performance for the detection of the AβO and tau protein, and the detection limits of 50 pM and 20 pM were obtained, respectively. Compared with the previously reported fluorescent aptasensors, the proposed method possesses the following unique features. Firstly, the distinguishable and robust fluorescence signals of QDs and the broad spectral absorption of Au NRs@PDA provide the basis for the simultaneous detection of two types of AD core biomarkers. Secondly, the sensing protocol is simple and does not involve difficult separation procedures. Furthermore, the FRET aptasensor possesses a high flexibility for the assay of other target analytes using aptamers with different sequences. Given the advantages of its facile manipulation and high sensitivity and specificity, the aptasensor holds great promise for the point-of-care testing of core biomarkers related to AD and cancers.

Supplementary Materials: The following supporting information can be downloaded at: https://www.mdpi.com/article/10.3390/nano12224031/s1, Figure S1. Normalized fluorescence spectra and PL decay dynamics of QDs_{625} and QDs_{665} in toluene; Figure S2. Size distribution diagram of QDs_{625} and QDs_{665}; Figure S3. The EDS elemental mapping images of CdSe/CdS/ZnS core/shell/shell QDs; Figure S4. The high-resolution TEM image of CdSe/CdS/ZnS QDs; Figure S5. Normalized fluorescence intensity of the QDs (A) with the prolongation of the storage time in ambient condition and (B) at different temperatures; Figure S6. Normalized fluorescence spectra of QDs_{625} and QDs_{665} before and after conjugation with thiolated aptamers; Figure S7. The hydrodynamic diameters of QDs_{625} and QDs_{665} before and after conjugation with thiolated aptamers; Figure S8. Size distribution diagram of Au NRs; Figure S9. UV-vis absorption spectra of Au NRs and Au NRs-PEG; Figure S10. Fluorescence spectra of QDs_{665}-DNA in the absence and presence of Au NRs@PDA with various shell thicknesses and the corresponding PL decay dynamics; Figure S11. Fluorescence spectra of QDs_{625}-DNA and QDs_{665}-DNA in the presence of Au NRs@PDA with various concentrations; Figure S12. Influence of the incubation time on fluorescence quenching and recovery; Figure S13. Fluorescence spectra of the FRET aptasensor for assaying the targets and the related interfering species; Table S1. Comparison of the analytical performance of the proposed aptasensor with that of other fluorescent biosensors. References [58–61] are cited in the Supplementary Materials.

Author Contributions: X.L.: performing the experiments and writing the original draft. X.H.: writing, editing, conceptualization and funding acquisition. H.T.: providing the human serum samples. X.Y.: data analysis. J.W.: supervision and funding acquisition. All authors have read and agreed to the published version of the manuscript.

Funding: We thank the National Natural Science Foundation of China for their financial support of this work (No. 22076221, 21876208, 22105011).

Institutional Review Board Statement: Not applicable.

Informed Consent Statement: Not applicable.

Data Availability Statement: The data presented in this study are available on request from the corresponding author.

Conflicts of Interest: The authors declare that they have no conflict of interest.

References

1. Knopman, D.S.; Amieva, H.; Petersen, R.C.; Chételat, G.; Holtzman, D.M.; Hyman, B.T.; Nixon, R.A.; Jones, D.T. Alzheimer disease. *Nat. Rev. Dis. Primers* **2021**, *7*, 33. [CrossRef] [PubMed]
2. Masters, C.L.; Bateman, R.; Blennow, K.; Rowe, C.C.; Sperling, R.A.; Cummings, J.L. Alzheimer's disease. *Nat. Rev. Dis. Primers* **2015**, *1*, 15056. [CrossRef] [PubMed]
3. Panza, F.; Lozupone, M.; Logroscino, G.; Imbimbo, B.P. A critical appraisal of amyloid-β-targeting therapies for Alzheimer disease. *Nat. Rev. Neurol.* **2019**, *15*, 73–88. [CrossRef] [PubMed]
4. Congdon, E.E.; Sigurdsson, E.M. Tau-targeting therapies for Alzheimer disease. *Nat. Rev. Neurol.* **2018**, *14*, 399–415. [CrossRef] [PubMed]
5. Yin, Y.M.; Chen, G.F.; Gong, L.; Ge, K.Z.; Pan, W.Z.; Li, N.; Machuki, J.O.; Yu, Y.Y.; Geng, D.Q.; Dong, H.F.; et al. DNAzyme-powered three-dimensional DNA walker nanoprobe for detection amyloid β-peptide oligomer in living cells and In Vivo. *Anal. Chem.* **2020**, *92*, 9247–9256. [CrossRef] [PubMed]
6. Ngoc Le, H.T.; Park, J.; Chinnadayyala, S.R.; Cho, S. Sensitive electrochemical detection of amyloid beta peptide in human serum using an interdigitated chain-shaped electrode. *Biosens. Bioelectron.* **2019**, *144*, 111694. [CrossRef] [PubMed]
7. Song, Y.C.; Xu, T.L.; Zhu, Q.L.; Zhang, X.J. Integrated individually electrochemical array for simultaneously detecting multiple Alzheimer's biomarkers. *Biosens. Bioelectron.* **2020**, *162*, 112253. [CrossRef]
8. Qin, H.X.; Gao, X.; Yang, X.Y.; Cao, W.; Liu, S.F. A label-free and signal-on electrochemiluminescence strategy for sensitive amyloid-beta assay. *Biosens. Bioelectron.* **2019**, *141*, 111438. [CrossRef]
9. Wang, Y.F.; Zhang, Y.; Sha, H.; Xiong, X.; Jia, N. Design and biosensing of a ratiometric electrochemiluminescence resonance energy transfer aptasensor between a g-C_3N_4 nanosheet and Ru@MOF for amyloid-β protein. *ACS Appl. Mater. Interfaces* **2019**, *11*, 36299–36306. [CrossRef]
10. Zhang, J.L.; Zhang, X.C.; Gao, Y.; Yan, J.Y.; Song, W.B. Integrating CuO/g-C_3N_4 p-n heterojunctioned photocathode with MoS_2 QDs@Cu NWs multifunctional signal amplifier for ultrasensitive detection of AβO. *Biosens. Bioelectron.* **2021**, *176*, 112945. [CrossRef]
11. Gao, N.; Zhang, Y.F.; Gao, K.K.; Xie, J.D.; Liu, L.; Li, Y.Y.; Qiu, L.P.; Wei, Q.; Ma, H.M.; Pang, X.H. Ultrasensitive label-free photoelectrochemical immunosensor for the detection of amyloid β-protein based on Zn:SnO_2/SnS_2-Au nanocomposites. *Sens. Actuators B Chem.* **2020**, *308*, 127576. [CrossRef]
12. Deng, C.Y.; Liu, H.; Zhang, M.M.; Deng, H.H.; Lei, C.Y.; Shen, L.; Jiao, B.; Tu, Q.Y.; Jin, Y.; Xiang, L.; et al. Light-up nonthiolated aptasensor for low-mass, soluble amyloid-β_{40} oligomers at high salt concentrations. *Anal. Chem.* **2018**, *90*, 1710–1717. [CrossRef] [PubMed]
13. Hu, T.; Lu, S.S.; Chen, C.X.; Sun, J.; Yang, X.R. Colorimetric sandwich immunosensor for $A\beta_{(1\text{-}42)}$ based on dual anti-body-modified gold nanoparticles. *Sens. Actuators B Chem.* **2017**, *243*, 792–799. [CrossRef]
14. Zhang, X.; Liu, S.; Song, X.L.; Wang, H.W.; Wang, J.F.; Wang, Y.; Huang, J.D.; Yu, J.H. Robust and universal SERS sensing platform for multiplexed detection of Alzheimer's disease core biomarkers using PAapt-AuNPs conjugates. *ACS Sens.* **2019**, *4*, 2140–2149. [CrossRef]
15. Xia, N.; Liu, L.; Harrington, M.G.; Wang, J.X.; Zhou, F.M. Resonance detection of $A\beta_{(1\text{-}40)}$ and $A\beta_{(1\text{-}42)}$ peptides in cerebrospinal fluids with signal amplification by streptavidin conjugated to an N-terminus-specific antibody. *Anal. Chem.* **2010**, *82*, 10151–10157. [CrossRef]
16. Palmqvist, S.; Tideman, P.; Cullen, N.; Zetterberg, H.; Blennow, K.; The Alzheimer's Disease Neuroimaging Initiative; Dage, J.L.; Stomrud, E.; Janelidze, S.; Mattsson-Carlgren, N.; et al. Prediction of future Alzheimer's disease dementia using plasma phos-pho-tau combined with other accessible measures. *Nat. Med.* **2021**, *27*, 1034–1042. [CrossRef]
17. Kim, K.; Kim, M.J.; Kim, D.W.; Kim, S.Y.; Park, S.; Park, C.B. Clinically accurate diagnosis of Alzheimer's disease via multi-plexed sensing of core biomarkers in human plasma. *Nat. Commun.* **2020**, *11*, 119. [CrossRef]

18. Fang, W.K.; Liu, L.; Zhang, L.L.; Liu, D.; Liu, Y.; Tang, H.W. Detection of amyloid β oligomers by a fluorescence ratio strategy based on optically trapped highly doped upconversion nanoparticles-SiO_2@metal−organic framework microspheres. *Anal. Chem.* **2021**, *93*, 12447–12455. [CrossRef]
19. Zhang, X.J.; Hu, Y.; Yang, X.T.; Tang, Y.Y.; Han, S.Y.; Kang, A.; Deng, H.S.; Chi, Y.M.; Zhu, D.; Lu, Y. FÖrster resonance energy transfer (FRET)-based biosensors for biological applications. *Biosens. Bioelectron.* **2019**, *138*, 111314. [CrossRef]
20. Quan, K.; Yi, C.P.; Yang, X.H.; He, X.X.; Huang, J.; Wang, K.M. FRET-based nucleic acid probes: Basic designs and applications in bioimaging. *Trends Anal. Chem.* **2020**, *124*, 115784. [CrossRef]
21. Sheng, A.Z.; Wang, P.; Yang, J.Y.; Tang, L.F.; Chen, F.; Zhang, J. MXene coupled with CRISPR-Cas12a for analysis of endotoxin and bacteria. *Anal. Chem.* **2021**, *93*, 4676–4681. [CrossRef] [PubMed]
22. Zhao, Y.N.; Li, X.; Yang, Y.; Si, S.H.; Deng, C.Y.; Wu, H.Y. A simple aptasensor for $A\beta_{40}$ oligomers based on tunable mismatched base pairs of dsDNA and graphene oxide. *Biosens. Bioelectron.* **2020**, *149*, 111840. [CrossRef] [PubMed]
23. Zhang, Y.Y.; Zhao, J.W.; Yang, G.M.; He, Y.; Chen, S.H.; Yuan, R. Ultrasensitive detection of amyloid beta oligomers based on the "DD-A" FRET binary probes and quadrivalent cruciform DNA nanostructure-mediated cascaded amplifier. *ACS Appl. Mater. Interfaces* **2021**, *13*, 32013–32021. [CrossRef] [PubMed]
24. Chern, M.; Kays, J.C.; Bhuckory, S.; Dennis, A.M. Sensing with photoluminescent semiconductor quantum dots. *Methods Appl. Fluores.* **2019**, *7*, 012005. [CrossRef]
25. Medintz, I.; Uyeda, H.; Goldman, E.; Mattoussi, H. Quantum dot bioconjugates for imaging, labelling and sensing. *Nat. Mater.* **2005**, *4*, 435–446. [CrossRef]
26. Chan, W.C.W.; Nie, S.M. Quantum dot bioconjugates for ultrasensitive nonisotopic detection. *Science* **1998**, *281*, 2016–2018. [CrossRef]
27. Bruchez, M.J.; Moronne, M.; Gin, P.; Weiss, S.; Alivisatos, A.P. Semiconductor nanocrystals as fluorescent biological labels. *Science* **1998**, *281*, 2013. [CrossRef]
28. Magaryan, K.A.; Karimullin, K.R.; Vasil'eva, I.A.; Naumov, A.V. Analysis of the temperature dependence of the exciton luminescence spectra of cadmium selenide quantum dots grown in a liquid crystal matrix. *Opt. Spectrosc.* **2019**, *126*, 41–43. [CrossRef]
29. Karimullin, K.R.; Arzhanov, A.I.; Eremchev, I.Y.; Kulnitskiy, B.A.; Surovtsev, N.V.; Naumov, A.V. Combined photon-echo, luminescence and raman spectroscopies of layered ensembles of colloidal quantum dots. *Laser Phys.* **2019**, *29*, 124009. [CrossRef]
30. Hou, X.Q.; Kang, J.; Qin, H.Y.; Chen, X.W.; Ma, J.L.; Zhou, J.H.; Chen, L.P.; Wang, L.J.; Wang, L.W.; Peng, X.G. Engineering auger recombination in colloidal quantum dots via dielectric screening. *Nat. Commun.* **2019**, *10*, 1750. [CrossRef]
31. Rosen, S.; Schwartz, O.; Oron, D. Transient fluorescence of the off state in blinking CdSe/CdS/ZnS semiconductor nanocrystals is not governed by auger recombination. *Phys. Rev. Lett.* **2010**, *104*, 157404. [CrossRef] [PubMed]
32. Wegner, K.D.; Lanh, P.T.; Jennings, T.; Oh, E.; Jain, V.; Fairclough, S.M.; Smith, J.M.; Giovanelli, E.; Lequeux, N.; Pons, T.; et al. Influence of luminescence quantum yield, surface coating, and functionalization of quantum dots on the sensitivity of time resolved FRET bioassays. *ACS Appl. Mater. Interfaces* **2013**, *5*, 2881–2892. [CrossRef] [PubMed]
33. Chen, O.; Zhao, J.; Chauhan, V.P.; Cui, J.; Wong, C.; Harris, D.K.; Wei, H.; Han, H.S.; Fukumura, D.; Jain, R.K.; et al. Compact high-quality CdSe-CdS core-shell nanocrystals with narrow emission linewidths and suppressed blinking. *Nat. Mater.* **2013**, *12*, 445–451. [CrossRef] [PubMed]
34. Zhou, J.H.; Zhu, M.Y.; Meng, R.Y.; Qin, H.Y.; Peng, X.G. Ideal CdSe/CdS core/shell nanocrystals enabled by entropic ligands and their core size-, shell thickness-, and ligand-dependent photoluminescence properties. *J. Am. Chem. Soc.* **2017**, *139*, 16556–16567. [CrossRef]
35. Manner, V.W.; Koposov, A.Y.; Szymanski, P.; Klimov, V.I.; Sykora, M. Role of solvent-oxygen ion pairs in photooxidation of CdSe nanocrystal quantum dots. *ACS Nano* **2012**, *6*, 2371–2377. [CrossRef]
36. Gupta, R.; Peveler, W.J.; Lix, K.; Algar, W.R. Comparison of semiconducting polymer dots and semiconductor quantum dots for smartphone-based fluorescence assays. *Anal. Chem.* **2019**, *91*, 10955–10960. [CrossRef]
37. Goryacheva, O.A.; Guhrenz, C.; Schneider, K.; Beloglazova, N.V.; Goryacheva, I.Y.; Saeger, S.D.; Gaponik, N. Silanized luminescent quantum dots for the simultaneous multicolor lateral flow immunoassay of two mycotoxins. *ACS Appl. Mater. Interfaces* **2020**, *12*, 24575–24584. [CrossRef]
38. Wang, W.L.; Guo, Y.; Tiede, C.; Chen, S.Y.; Kopytynski, M.; Kong, Y.F.; Kulak, A.; Tomlinson, D.; Chen, R.; McPherson, M.; et al. Ultraefficient cap-exchange protocol to compact biofunctional quantum dots for sensitive ratiometric biosensing and cell imaging. *ACS Appl. Mater. Interfaces* **2017**, *9*, 15232–15244. [CrossRef]
39. Wu, Y.T.; Qiu, X.; Lindbo, S.; Susumu, K.; Medintz, I.L.; Hober, S.; Hildebrandt, N. Quantum dot–based FRET immunoassay for HER2 using ultrasmall affinity proteins. *Small* **2018**, *14*, 1802266. [CrossRef]
40. Wang, W.L.; Kong, Y.F.; Jiang, J.; Tian, X.; Li, S.; Akshath, U.S.; Tiede, C.; Hondow, N.; Yu, A.C.; Guo, Y.; et al. Photon induced quantum yield regeneration of cap-exchanged CdSe/CdS quantum rods for ratiometric biosensing and cellular imaging. *Nanoscale* **2020**, *12*, 8647–8655. [CrossRef]
41. Tong, P.; Zhao, W.W.; Zhang, L.; Xu, J.J.; Chen, H.Y. Double-probe signal enhancing strategy for toxin aptasensing based on rolling circle amplification. *Biosens. Bioelectron.* **2012**, *33*, 146–151. [CrossRef] [PubMed]

42. Wang, Q.B.; Xu, Y.; Zhao, X.H.; Chang, Y.; Liu, Y.; Jiang, L.J.; Sharma, J.; Seo, D.K.; Yan, H. A facile one-step in situ functionalization of quantum dots with preserved photoluminescence for bioconjugation. *J. Am. Chem. Soc.* **2007**, *129*, 6380–6381. [CrossRef] [PubMed]
43. Deka, S.; Quarta, A.; Lupo, M.G.; Falqui, A.; Boninelli, S.; Giannini, C.; Morello, G.; Giorgi, M.D.; Lanzani, G.; Spinella, C.; et al. CdSe/CdS/ZnS double shell nanorods with high photoluminescence efficiency and their exploitation as biolabeling probes. *J. Am. Chem. Soc.* **2009**, *131*, 2948–2958. [CrossRef] [PubMed]
44. Hou, X.Q.; Qin, H.Y.; Peng, X.G. Enhancing dielectric screening for auger suppression in CdSe/CdS quantum dots by epitaxial growth of ZnS shell. *Nano Lett.* **2021**, *21*, 3871–3878. [CrossRef] [PubMed]
45. Dabbousi, B.O.; Rodriguez-Viejo, J.; Mikulec, F.V.; Heine, J.R.; Mattoussi, H.; Ober, R.; Jensen, K.F.; Bawendi, M.G. (CdSe)ZnS core-shell quantum dots: Synthesis and characterization of a size series of highly luminescent nanocrystallites. *J. Phys. Chem. B* **1997**, *101*, 9463–9475. [CrossRef]
46. Ye, X.C.; Jin, L.H.; Caglayan, H.; Chen, J.; Xing, G.Z.; Zheng, C.; Doan-Nguyen, V.; Kang, Y.J.; Engheta, N.; Kagan, C.R.; et al. Improved size-tunable synthesis of monodisperse gold nanorods through the use of aromatic additives. *ACS Nano* **2012**, *6*, 2804–2817. [CrossRef]
47. Chen, H.Q.; Yuan, F.; Wang, S.Z.; Xu, J.; Zhang, Y.Y.; Wang, L. Aptamer-based sensing for thrombin in red region via fluorescence resonant energy transfer between $NaYF_4$:Yb,Er upconversion nanoparticles and gold nanorods. *Biosens. Bioelectron.* **2013**, *48*, 19–25. [CrossRef]
48. Choi, C.K.K.; Li, J.M.; Wei, K.C.; Xu, Y.J.; Ho, L.W.C.; Zhu, M.L.; To, K.K.W.; Choi, C.H.J.; Bian, L.M. A gold@polydopamine core–shell nanoprobe for long-term intracellular detection of microRNAs in differentiating stem cells. *J. Am. Chem. Soc.* **2015**, *137*, 7337–7346. [CrossRef]
49. Ye, Q.; Zhou, F.; Liu, W.M. Bioinspired catecholic chemistry for surface modification. *Chem. Soc. Rev.* **2011**, *40*, 4244–4258. [CrossRef]
50. Wang, J.; Gao, Y.H.; Liu, P.P.; Xu, S.H.; Luo, X.L. Core-shell multifunctional nanomaterial-based all-in-one nanoplatform for simultaneous multilayer imaging of dual types of tumor biomarkers and photothermal therapy. *Anal. Chem.* **2020**, *92*, 15169–15178. [CrossRef]
51. Liu, L.; Chang, Y.; Yu, J.; Jiang, M.S.; Xia, N. Two-in-one polydopamine nanospheres for fluorescent determination of beta-amyloid oligomers and inhibition of beta-amyloid aggregation. *Sens. Actuators B Chem.* **2017**, *251*, 359–365. [CrossRef]
52. Cao, Z.Y.; Shu, Y.F.; Qin, H.Y.; Su, B.; Peng, X.G. Quantum dots with highly efficient, stable, and multicolor electrochemiluminescence. *ACS Cent. Sci.* **2020**, *6*, 1129–1137. [CrossRef] [PubMed]
53. Yu, W.W.; Qu, L.H.; Guo, W.Z.; Peng, X.G. Experimental determination of the extinction coefficient of CdTe, CdSe, and CdS nanocrystals. *Chem. Mater.* **2003**, *15*, 2854–2860. [CrossRef]
54. Qiu, Y.; Liu, Y.; Wang, L.M.; Xu, L.G.; Bai, R.; Ji, Y.L.; Wu, X.C.; Zhao, Y.L.; Li, Y.F.; Chen, C.Y. Surface chemistry and aspect ratio mediated cellular uptake of Au nanorods. *Biomaterials* **2010**, *31*, 7606–7619. [CrossRef] [PubMed]
55. Aldana, J.; Wang, Y.A.; Peng, X.G. Photochemical instability of CdSe nanocrystals coated by hydrophilic thiols. *J. Am. Chem. Soc.* **2001**, *123*, 8844–8850. [CrossRef]
56. Hu, M.; He, Y.; Song, S.P.; Yan, J.; Lu, H.T.; Weng, L.X.; Wang, L.H.; Fan, C.H. DNA-bridged bioconjugation of fluorescent quantum dots for highly sensitive microfluidic protein chips. *Chem. Commun.* **2010**, *46*, 6126–6128. [CrossRef]
57. Tian, F.; Lyu, J.; Shi, J.Y.; Yang, M. Graphene and graphene-like two-denominational materials based fluorescence resonance energy transfer (FRET) assays for biological applications. *Biosens. Bioelectron.* **2017**, *89*, 123–135. [CrossRef]
58. Chen, W.; Gao, G.; Jin, Y.; Deng, C. A facile biosensor for $A\beta_{40}O$ based on fluorescence quenching of prussian blue nanoparticles. *Talanta* **2020**, *216*, 120930. [CrossRef]
59. Jiang, L.; Chen, B.; Chen, B.; Li, X.; Liao, H.; Huang, H.; Guo, Z.; Zhang, W.; Wu, L. Detection of Aβ oligomers based on magnetic-field-assisted separation of aptamer-functionalized Fe_3O_4 magnetic nanoparticles and $BaYF_5$:Yb,Er nanoparticles as upconver-sion fluorescence labels. *Talanta* **2017**, *170*, 350–357. [CrossRef]
60. Chen, L.; Lin, J.; Yi, J.; Weng, Q.; Zhou, Y.; Han, Z.; Li, C.; Chen, J.; Zhang, Q. A tyrosinase-induced fluorescence immunoassay for detection of tau protein using dopamine-functionalized $CuInS_2$/ZnS quantum dots. *Anal. Bioanal. Chem.* **2019**, *411*, 5277–5285. [CrossRef]
61. Huang, A.; Zhang, L.; Li, W.; Ma, Z.; Shuo, S.; Yao, T. Controlled fluorescence quenching by antibody-conjugated graphene oxide to measure tau protein. *R. Soc. Open Sci.* **2018**, *5*, 171808. [CrossRef] [PubMed]

nanomaterials MDPI

Review

Advances in Solution-Processed Blue Quantum Dot Light-Emitting Diodes

Sheng-Nan Li [1], Jia-Lin Pan [1], Yan-Jun Yu [1], Feng Zhao [1], Ya-Kun Wang [1,*] and Liang-Sheng Liao [1,2,*]

[1] Institute of Functional Nano & Soft Materials (FUNSOM), Jiangsu Key Laboratory for Carbon-Based Functional Materials & Devices, Soochow University, Suzhou 215123, China; lishengnan1004@163.com (S.-N.L.); jlpan1013@163.com (J.-L.P.); yuyanjun1998@163.com (Y.-J.Y.); fengzhao_lum@163.com (F.Z.)

[2] Macao Institute of Materials Science and Engineering, Macau University of Science and Technology, Taipa 999078, Macau SAR, China

* Correspondence: wangyakun@suda.edu.cn (Y.-K.W.); lsliao@suda.edu.cn (L.-S.L.)

Abstract: Quantum dot light-emitting diodes (QLEDs) have been identified as a next-generation display technology owing to their low-cost manufacturing, wide color gamut, and electrically driven self-emission properties. However, the efficiency and stability of blue QLEDs still pose a significant challenge, limiting their production and potential application. This review aims to analyse the factors leading to the failure of blue QLEDs and presents a roadmap to accelerate their development based on the progress made in the synthesis of II-VI (CdSe, ZnSe) quantum dots (QDs), III-V (InP) QDs, carbon dots, and perovskite QDs. The proposed analysis will include discussions on material synthesis, core-shell structures, ligand interactions, and device fabrication, providing a comprehensive overview of these materials and their development.

Keywords: blue QLED; II-V QD; III-V QD; carbon dot; perovskite QD

1. Introduction

Quantum dots (QDs) are an important low-dimensional semiconductor material characterized by dimensions that are not larger than twice the exciton Bohr radius of their corresponding pairs of bulk materials. The low-dimensional structure of QDs enables electron-hole radiative recombination by binding electrons and holes in a small space. Additionally, QDs can emit in a wide range, from visible to near-infrared, through the quantum confinement effect (QCE). These advantages make II-VI (CdSe, ZnSe), III-V (InP), and IV (Carbon dot) QDs attractive for various applications.

Among different kinds of QDs, CdSe has a photoluminescence quantum yield (PLQY) close to 100% and excellent photostability, making Cd-based light-emitting diodes highly efficient, with an external quantum efficiency (EQE) exceeding 20% [1]. However, the toxicity of Cd-based materials limits their commercial applications. Therefore, researchers have focused on developing heavy metal-free QDs, such as InP, ZnSe, and carbon dots (CDs). InP has a bandgap similar to that of CdSe but has a larger exciton Bohr radius. Although CDs are not suitable for display due to impurities and defect states, they show promise in bioimaging applications due to their good biocompatibility. The new perovskite QDs (PQDs) exhibit high color purity and PLQY. Additionally, PQD emission can be tuned through QCE and halogen composition, making them an attractive material for various applications.

QD light-emitting diodes (QLEDs) unite the advantages of low cost, solution processing, and low-temperature fabrication and production, which makes them stand out among other emitters [2–4]. Theoretically, QLEDs can achieve ultrahigh color purity, with the National Television System Committee standard of 140% [5].

Compared to red and green QLED devices, blue QLEDs have lower performance. For instance, using InP QLEDs as an example, blue InP QLEDs exhibit a luminance of <5000 cd m^{-2} and a maximum EQE of < 3% [6]. In contrast, red InP QLEDs can achieve an EQE, luminance, and T_{95} (the time for the brightness to drop to 95% of its initial value) of 22.2%, >110,000 cd m^{-2}, and >32,000 h, respectively [7]. Similarly, a green InP QLED can attain an EQE, luminance, and T_{50} (the time for the brightness to drop to 50% of its initial value) of 16.3%, >12,000 cd m^{-2}, and >1000 h, respectively [8]. Until now, red and green QLEDs have already satisfied the requirements for commercial applications, whereas blue QLEDs still have a long way to go. The reasons for this disparity include the fact that 1. blue QDs necessitate small particle sizes, which results in difficulties in synthesizing uniform QDs, and 2. the wide bandgap that makes exciton traps sensitive and results in nonradiative recombination. The synthesis methods for various types of QDs exhibit similarities. For example, Peng et al. synthesized InP QDs at low reaction temperatures by utilizing aliphatic amine ligands, which is a technique borrowed from the synthesis of II-VI QDs [9]. Similarly, Jang et al. utilized HF etching to prepare high-efficiency blue ZnTeSe QLEDs, achieving ZnSeTe QLEDs with a luminance of 88,900 cd m^{-2}, an EQE of 20.2%, and a T_{50} time of 15,850 h at 100 cd m^{-2} [10]. Thus, a comprehensive analysis of the synthetic methodology, surface ligand treatment, and device engineering of blue QDs is necessary for the advancement of blue QLEDs.

This review aims to provide an overview of blue QLEDs using II-VI QDs, III-V QDs, CDs, and PQDs. In Section 2, we introduce the properties, nucleation, and growth mechanisms of the aforementioned QD materials, as well as the principle of electroluminescence (EL) of QDs. Sections 3 and 4 focus on the synthesis and device engineering of II-VI (CdSe, ZnSe) and III-V (InP) inorganic QDs. In Section 5, we discuss the photoluminescence (PL) and EL prospects of CDs. Finally, in Section 6, we introduce newly developed PQDs from both QCE and mixed halogen perspectives. We hope that this review will provide researchers with a better understanding of the strengths and weaknesses of each type of QD, as well as the next steps for further improving the performance of blue QLEDs.

2. Properties of QDs

2.1. Quantum Confinement Effect

QCE is a phenomenon where the energy levels of a material become discrete when the particle is close to or smaller than the Bohr radius of the exciton (Figure 1). This phenomenon allows for the manipulation of the physical properties of semiconductor nanocrystals (NCs) by controlling their size. QDs are a type of NC, and their size can be precisely controlled, enabling tuning of their emission light from ultraviolet to infrared, which is a practical application of QCE [11].

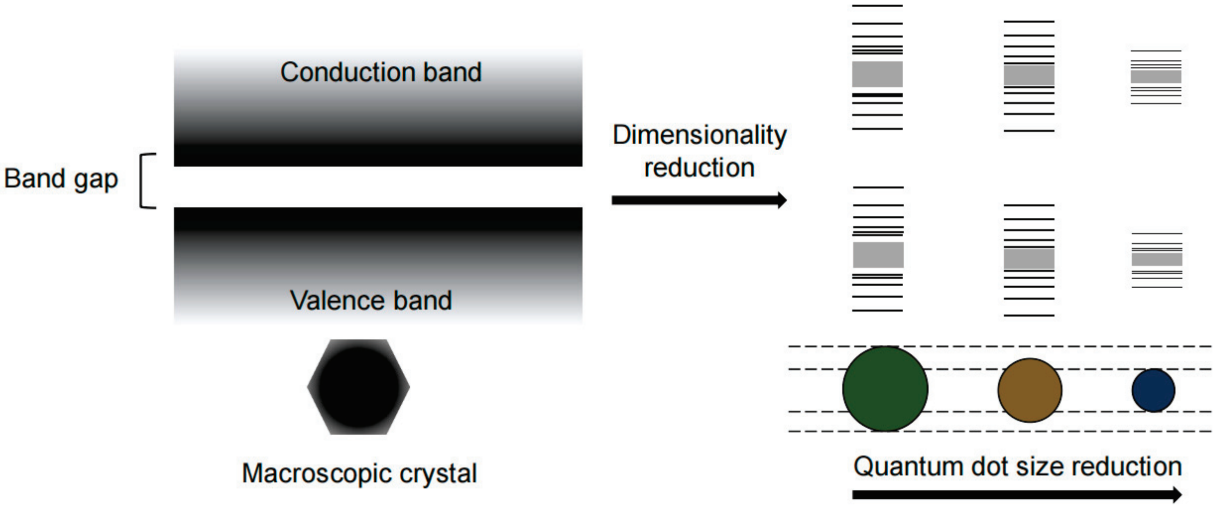

Figure 1. Schematic of QCE under different QD sizes.

2.2. Growth and Nucleation Mechanism of QDs

The minimization of Gibbs free energy is the chemical driving force for QD nucleation during synthesis. In the absence of a kinetic energy barrier, the total surface free energy of a crystallization system includes the area of each section (A_i) of each crystal in the solution and is related to the specific surface energy (σ_i). The relationship is shown in Equation (1).

$$\sum G_{surface} = \sum \sigma_i A_i \approx \sigma \sum A_i = minimum \quad (1)$$

The dangling bonds carried by the atoms on the crystal surface are the direct source of the crystal surface free energy. The surface Gibbs free energy decreases as the grain size increases. In addition to natural growth, appropriate ligands or specific solvent molecules can also reduce the number of dangling bonds [12].

The surface Gibbs free energy of NCs in Equation (1) decreases as size increases because of the reduced surface-to-volume atomic ratio. Therefore, the solubility of NCs decreases drastically as their size increases, which comes from the Gibbs-Thompson equation (Equation (2))

$$S_d = S_\infty exp(4\sigma V_m/dRT) \quad (2)$$

σ and V_m are the specific surface free energy and molar volume of the crystal, respectively, S_∞ is the solubility of the blocky crystal, S_d is the solubility of the crystal with diameter d, R is the gas constant, and T is the absolute temperature. In the process of NC nucleation and growth, larger crystals grow at the expense of smaller crystals due to the difference in surface energy between them, leading to the “size distribution out of focus” of NCs in the system [13]. This is because the smaller particles have a higher surface energy and tend to dissolve into the solution, while the larger particles have a lower surface energy and tend to absorb more monomers from the solution and grow further. This is the Oswald ripening process.

When the size of the studied NCs changes from the nanoscale to the micron scale, the surface-to-atom ratio decreases rapidly with increasing crystal size. This leads to the fact that the surface energy in the crystal is negligible compared to the total free energy of the system. Therefore, new methods are needed to study the crystallization process of NCs at the nanoscale. Peng’s group used a computer to deconvolve the absorption spectrum to obtain QD information on the size distribution. The method mentioned in the previous statement is known as the “deconvolution method”, which can be used to obtain the size distribution of QDs from their absorption spectra. Briefly, the ultraviolet–visible (UV–vis) absorption spectra of the samples were deconvoluted to obtain a series of contributing factors for the standard spectra. The corresponding particle size distribution profile can be obtained by adding the products of each contributing factor and the corresponding Gaussian particle size distribution of the standard sample [14].

2.3. Charge Transport and EL Properties of QDs

A typical QLED architecture is shown in Figure 2a, which contains an anode, a hole-injecting layer (HIL), a hole-transporting layer (HTL), a light-emitting layer (EML), an electron-transporting layer (ETL), an electron-injecting layer (EIL) and a cathode. The EL of QDs is generated by the radiative recombination of holes and electrons through the EML. QDs with long-chain ligands have insulating properties and make carrier injection difficult. To overcome this challenge and improve carrier injection efficiency, QDs require surface modification or ligand exchange with short chains. Furthermore, from a device perspective, the EML needs a HIL and EIL that reside between the electrode and the EML.

The implementation of a high mobility hole (electron) transporting layer (HTL/ETL) helps facilitate carrier recombination. However, the injection of electrons and holes into the EML does not always occur simultaneously. The conduction band shifts of the EML and ETL are typically much smaller than the valence band shifts of the EML and HTL. This discrepancy results in a build-up of excess electrons within the EML, leading to negatively charged QDs that are unable to undergo radial excitation (Figure 2b). Moreover, the accumulation of excess electrons can leak into the hole-transporting layers and cause a decrease in the device's lifetime [15,16]. Therefore, the fundamental principle in designing high-performance QLEDs is to focus on balancing charge injection and effective radiative recombination.

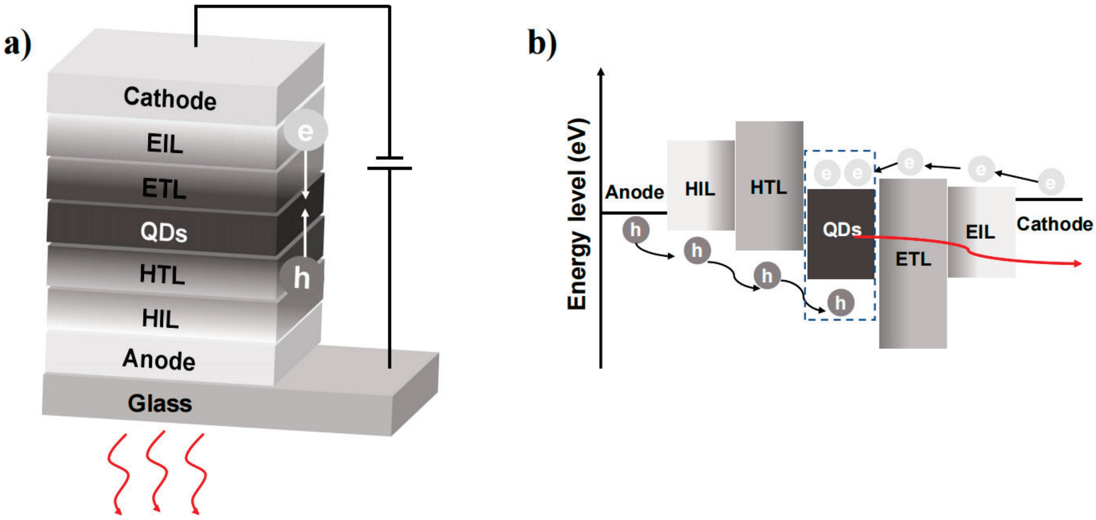

Figure 2. (**a**) The traditional structure of QLEDs. (**b**) Schematic of the processes of charge injection and charge recombination in an energy band diagram.

3. II-VI QDs

3.1. Cd-Based QDs

(1) Synthesis and modification of CdSe QDs

CdSe (1.74 eV), a direct bandgap semiconductor, has attracted extensive attention and in-depth study in the early stages of research [17–19]. The prenucleation of CdSe QDs is commonly achieved using the hot injection method. The injection of metal precursor solutions into different ligand systems can have a significant impact on the growth kinetics of CdSe QDs. Murray et al. utilized organometallic reagents for homogeneous nucleation by rapid injection into hot tri-n-octyl phosphine/tri-n-octyl phosphine oxide (TOP/TOPO)-liganded solvents [18]. Slow growth and annealing led to a uniform QD surface. As a result, nearly monodisperse (diameter <5% rms) samples were obtained. In another study, Talapin et al. introduced hexadecyl amine (HDA) into the TOP/TOPO system [20]. The ratio between TOPO and HDA strongly affected the growth kinetics of CdSe QDs. The initial particle size and growth rate of CdSe QDs decreased with increasing HDA content, which enabled better control of the dynamic growth of CdSe QDs. In addition, HDA not only solved the problem of the nonrepeatable shape of CdSe QDs in the TOP/TOPO system but also significantly improved the CdSe QD band-edge emitting efficiency at room temperature. The band-edge PLQY of CdSe QDs can be increased to 40–60% by surface passivation of inorganic (ZnS) or organic (alkylamine) shells (Figure 3a).

The QD core is covered by a wide-bandgap shell to reduce dangling bonds, passivate nonradiative surface sites, and improve PLQY. CdSe QD cores coated with CdS and ZnS thin shell layers can increase the PLQY by more than 50% [21]. However, a thin shell is not the perfect choice for QDs because of the loss or denaturation of ligands during solvent transfer, which will lead to incomplete passivation of surface defects and thus affect the PLQY. To address the instability of ligands in thin-shell QDs, Chen's group developed giant shell QDs (g-QDs) [22]. The ultrathick shell completely isolated the core from the QD surface. The thick shell effectively acted as a spacer between adjacent QDs and suppressed distance-dependent interactions between particles, such as Förster resonance energy transfer [23,24]. As a result, g-QDs had strong chemical stability and high photostability in photobleaching, which improved blinking behavior (Figure 3b) [24,25]. Multiple growths of one shell layer on the core can result in the accumulation of interlayer defects. Further design of a multishell structure with alloying can release the stress caused by a lattice mismatch between the core and shell, which can result in high-quality QDs with low defect densities. Moreover, energy level matching between the QDs and the transport layer can be realized by adjusting the composition of the QDs. Liu et al. successfully designed CdZnSe/ZnSeS/ZnS/CdZnS QDs (Figure 3c) to achieve efficient blue emission [26]. On the condition that the CdZnSe/ZnSeS/ZnS double shell structure enables high PLQY, a layer of CdZnS with a narrow band gap is added to promote the holes that inject the EML (Figure 3d).

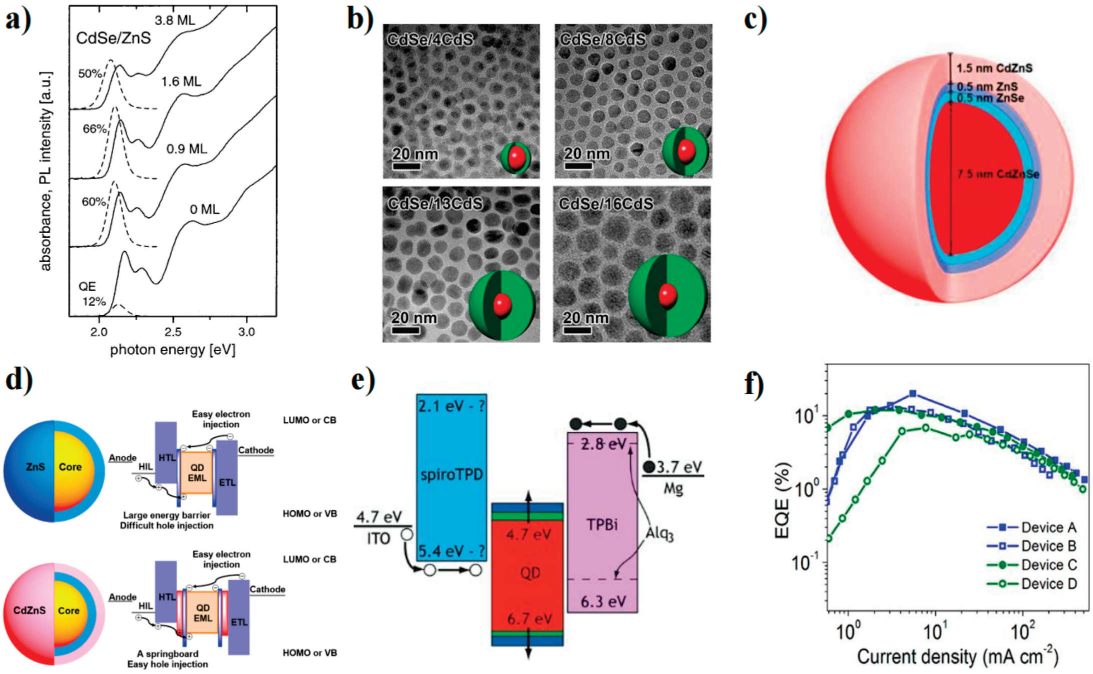

Figure 3. (**a**) UV–vis absorption (solid lines) and PL spectra (dashed lines) of CdSe QDs before and after deposition of ZnS shells of different thicknesses [20]. Copyright 2001, American Chemical Society. (**b**) TEM images of CdSe/xCdS QDs [25]. Copyright 2012, American Chemical Society. (**c**) The corresponding core/shell structure of CdZnSe/ZnSeS/ZnS/CdZnS QDs [26]. Copyright 2022, Wiley-VCH. (**d**) Multishell structure QD and an energy diagram in a conventional QLED [26]. Copyright 2022, Wiley-VCH. (**e**) All-organic QLED device structures of the energy diagram [27]. Copyright 2009, American Chemical Society. (**f**) EQE—current density curve of the blue CdSe/ZnS QLED [28]. Copyright 2017, American Chemical Society.

(2) Blue CdSe-based QLEDs

Since the first report of CdSe QLEDs in 1994, a series of explorations on on-device application and synthesis have been developed [17,29–33]. Initially, the device structure was simple, where QDs were used as both the emissive and transport layers, resulting in poor PLQY [17]. As OLED devices progressed, researchers borrowed the transport layer design and tried to prepare all-organic devices by inserting QDs between two organic transport layers (Figure 3e) [27]. However, this structure is not ideal due to concerns about the stability of organic devices. While all-inorganic devices exhibit greater thermal and chemical stability, there are still issues with inorganic metal oxides, such as complex surface defects and a lack of research on the physical mechanism of exciton formation. Currently, the most widely used and efficient devices are organic–inorganic hybrid devices, where organic compounds (such as PEDOT:PSS, poly-TPD, PVK, and TFB) are used in the HIL and HTL, while inorganic metal oxides (such as ZnO and ZnMgO) are used in the ETL and the EML is placed in the middle position. Various typical structures were summarized in Qi's article [19,34]. Over more than a decade of development, the performance of blue QLEDs has rapidly improved. At present, the Cd-based blue QLED performance can reach EQE = 19.8%, maximum luminance (L_{max}) = 62,600 cd m^{-2}, and T_{50} > 10,000 h (Figure 3f). Qian et al. introduced ZnO as an ETL and fabricated blue QLEDs with an EQE of 0.22% by using an organic–inorganic hybrid structure [29]. Subsequently, Wang et al. increased the EQE of blue QLEDs to 19.8% (excluding tandem devices; the EQE for current tandem blue QLEDs is 24%) [28,35–42]. During this period of rapid development, blue QLED performance was optimized from three aspects (Table 1): (1) core-shell structure and ligand engineering to reduce nonradiative recombination (Auger recombination and Förster resonance energy transfer, etc.), (2) device interface engineering to avoid interlayer charge accumulation, and (3) the electron-blocking layer to balance the charge and promote radiation recombination due to the deep HOMO level of blue QDs, making hole injection more difficult than electron injection.

Table 1. Device performance summary of the representative blue CdSe-based QLEDs.

QD	PLQY	Device Performance					
		λ (nm)	EQE (%)	Luminance (cd m^{-2})	CIE (x, y)	Device Structure	Ref
CdZnSe/ZnSeS/ZnS/CdZnS	77.3%	476	8.40%	12,000	(0.11, 0.13)	ITO/PEDOT:PSS/TFB/QD/ZnMgO/Al	[26]
CdSe/ZnSe	73%		8.05%	62,600		ITO/PEDOT:PSS/TFB/QD/ZnO/Al	[35]
CdSe/ZnS	87%	468	19.80%	4890	(0.136, 0.078)	ITO/PEDOT:PSS/PVK/QD/ZnO/Al	[28]
CdZnS/ZnS	82%	448	12.40%	3694	(0.152, 0.024)	ITO/PEDOT:PSS/PVK/QD/ZnO/Al	[36]
CdSe/ZnS		455	10.70%	≈5000	(0.16, 0.02)	ITO/PEDOT:PSS/PVK/QD/ZnO/Al	[38]
ZnCdS/ZnS	70%	443	12.20%	7600	(0.14, 0.02)	ITO/PEDOT:PSS/TFB/QD/ZnO/Al	[39]
$Zn_xCd_{1-x}S$/ZnS	100%	445	3.80%	4100		ITO/TFB/QD/ZnO/Al	[37]
CdZnS/ZnS	98%	452	7.1%	2624	(0.153, 0.027)	ITO/PEDOT:PSS/PVK/QD/ZnO/Al	[40]
$Cd_{1-x}Zn_xS$/ZnS		437	1.7%	2250	(0.17, 0.02)	ITO/PEDOT:PSS/ploy-TPD/QD/TPBi/LiF/Al	[41]
CdSe/ZnS		470	0.22%	4200		ITO/PEDOT:PSS/ploy-TPD/QD/ZnO/Al	[29]
ZnCdS/$Cd_xZn_{1-x}S$/ZnS	100%	445	18%	6768		ITO/PEDOT:PSS/PVK/QD/ZnO/Al	[43]
ZnCdSe/ZnS//ZnS	92%	479	16.2%	14,100	(0.119, 0.154)	ITO/PEDOT:PSS/TFB/QD/PMMA/ZnO/Al	[44]

3.2. ZnSe-Based QDs

(1) Synthesis and modification of ZnSe-based QDs

ZnSe has emerged as a promising alternative to Cd-based materials in the blue region due to its nontoxicity and appropriate bandgap (2.7 eV). Margaret's group studied ZnSe QD growth and investigated how to control the properties of the QDs [45]. They synthesized monodisperse and highly luminescent ZnSe QDs in an HDA/TOPO coordination solvent and achieved tunable band-edge fluorescence between 2.8 and 3.4 eV at room temperature. Moreover, high-brightness ZnSe QDs with a PLQY of 72% and high reproducibility were obtained by non-injection [46]. Yu et al. synthesized ZnSe QDs with uniform size and controlled shape by heating a mixture of $Zn(Ac)_2$, Se powder, oleic acid, and liquid paraffin instead of direct injection of the Se source. This method avoided the use of dangerous and unstable alkyl phosphines, such as TOPO [47]. Zheng et al. developed water-synthesized glutathione-capped ZnSe and $Zn_{1\text{-}x}Cd_xSe$ alloy QDs with adjustable fluorescence emission between 360 and 500 nm and a high PLQY of 50% (Figure 4a) [48]. This is also the first study to directly synthesize blue QDs in an aqueous solution. Although element doping can adjust the ZnSe bandgap, nontoxic elements such as Te, Mn, and Cu are more suitable for doping than Cd [49,50]. The optimal choice for achieving ZnSe QD blue light emission is to form an alloy with ZnTe (2.25 eV). Lesnyak et al. proposed a simple one-step water synthesis of glutathione covering $ZnSe_{1-x}Te_x$ QDs, which avoided the complexity of multistage preparation and achieved a PLQY of 20% [47].

ZnSe and ZnS are commonly used as shell layers to improve the PLQY and brightness of QDs. Dong et al. proposed a two-step synthesis method to synthesize ZnSe/ZnS QDs in the 390–460 nm range under mild conditions (150 °C) [51]. Recently, Yang's group also reported a seed-mediated double-shell strategy in which two ZnS shells were prepared by two different shell-forming steps to obtain ZnSe/ZnS/ZnS core-shell QDs with high PLQY and good stability. Lad et al. synthesized ZnSe and ZnSe/ZnS QDs by a high-temperature wet chemical route and found four excited states ($1S^e - 1S_{3/2}$, $1S^e{-}1S^h_{\frac{3}{2}}$, $1P^e{-}1P^h_{\frac{3}{2}}$, and $1S^e - 1S^{SO}$) [52]. The four excited states vary with the ZnS shell layer thickness, which can visually reflect how the electronic energy level of the ZnSe QD changes.

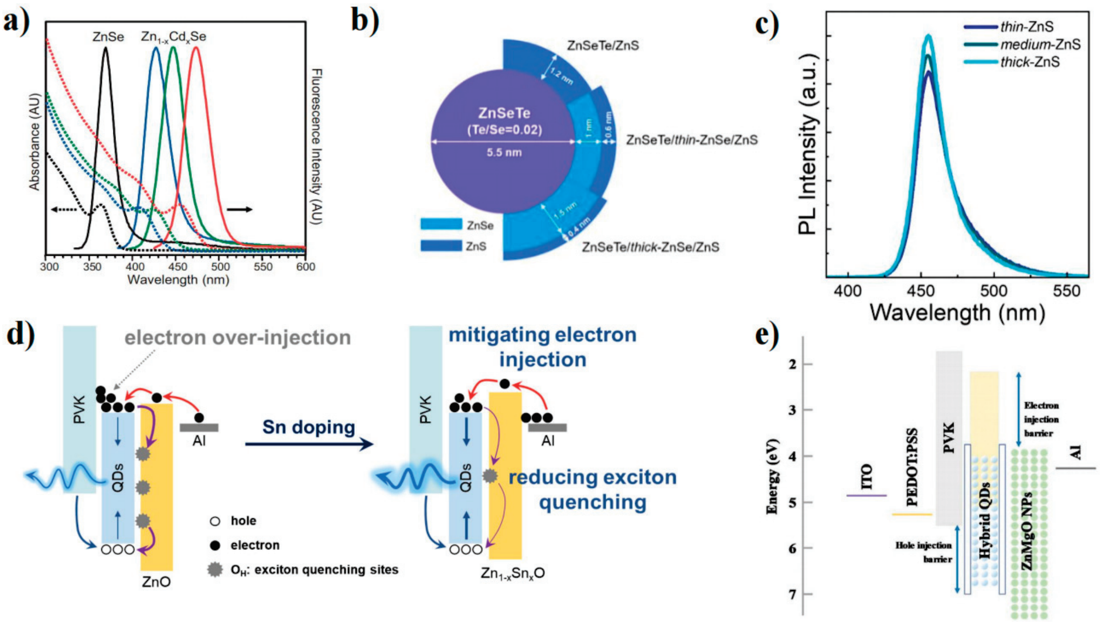

Figure 4. (**a**) UV–vis absorption (dashed lines) and PL spectra (solid lines) of ZnSe and $Zn_{1-x}Cd_xSe$ alloyed QDs [48]. Copyright 2007, Wiley-VCH. (**b**) Schematic of ZnSeTe core to double shells of ZnSeTe/thin-, medium-, and thick-ZnSe/ZnS C/S/S QDs [53]. Copyright 2017, American Chemical Society. (**c**) PL spectra of ZnS outer shell thickness-dependent C/S/S QDs [54]. Copyright 2021, Elsevier B. V (**d**) Carrier injection and recombination mechanism for these deep-blue-emitting devices [55]. Copyright 2022, American Chemical Society. (**e**) Device and energy level structure of QLEDs with hybrid QDs [56]. Copyright 2020, Wiley-VCH.

(2) Blue ZnSe-based QLEDs

Jang et al. investigated the synthesis of binary and ternary ZnSe-based QDs. Specifically, they explored the effects of increasing the thickness of the ZnSe shell and adjusting the Se/Te ratio in ZnSeTe on the performance of the blue QLED (Figure 4b). To further enhance device performance, ZnSe was introduced between the ZnSeTe and ZnS interfaces, resulting in the successful fabrication of high-performance blue ZnSeTe/ZnSe/ZnS QLEDs. Furthermore, Lee et al. adopted a two-step method to synthesize ZnSeTe/ZnSe/ZnS QDs and tuned the thickness of the ZnSe inner shell and the ZnS shell to investigate the effect on the performance of blue QLEDs (Figure 4c). Their results indicated that the thickness modulation of the ZnSe inner shell not only influenced the growth of the ZnS shell but also affected the peak wavelength, color purity, and PLQY of the QDs. Additionally, as the thickness of the ZnS shell increased, the injection of electrons was found to be more effectively suppressed relative to holes, resulting in improved charge balance and enhanced EQE.

To improve the efficiency and stability of blue ZnSe-based QLEDs, researchers have also explored various aspects, such as device structures, surface passivation, material preparation, and simulation of ZnSe-based QDs (Table 2) [57]. Currently, there are two main approaches to developing ZnSe-based QLEDs: on the one hand, the EML is doped to mitigate the electron leakage current, which is caused by the high intrinsic electron mobility of ZnSe QDs; on the other hand, the ETL is doped to regulate the energy band and reduce the electron mobility while suppressing the surface defect states. Cho et al. utilized P-type semiconductors (TCTA and TPD) to dope ZnSe (Figure 4e) [56]. Hybrid QDs were found to effectively prevent electron overflow from the hole transport materials and improve the hole current characteristics due to the p-type doping effect. ZnO is commonly used as the

ETL in blue-light devices. Efforts have been made to optimize the physical properties of ZnO NPs by doping elements such as Mg, Li, Cl, S, Al, and Ga [58–64]. Gao et al. reported the use of Sn-doped ZnO, which not only reduced the exciton quenching sites on the metal oxide surface caused by OH but also decreased the electron mobility and slowed down the over injection of electrons (Figure 4d) [55]. Kim et al. modulated the emission wavelength of ZnSeTe to 457 nm by adding Te. They fabricated a double-QD EML with graded chloride content in the LED to facilitate hole transport. The resulting device has high efficiency (EQE = 20.2%), high brightness (L_{max} = 88,900 cd m^{-2}), and a long operating life (T_{50} = 15,850 h at 100 cd m^{-2}) [10]. This is the best performance of an inorganic blue QLED at present.

Table 2. Device performance summary of the representative blue ZnSe-based QLEDs.

QD	PLQY	Device Performance					
		λ (nm)	EQE (%)	Luminance (cd m^{-2})	CIE (x, y)	Device Structure	Ref
ZnSeTe/ZnSe/ZnS	93%	455	18.60%	12,654	(0.128, 0.109)	ITO/PEDOT:PSS/PVK/QD/ZnMgO/Al	[54]
ZnSe/ZnS	95%	443	13.60%	1031	(0.17, 0.03)	ITO/PEDOT:PSS/PVK/QD/$Zn_{1-x}Sn_xO$/Al	[55]
ZnSe/ZnS	95%	445	12.20%	570	(0.16, 0.03)	ITO/PEDOT:PSS/PVK/QD/ZnMgO/Al	[65]
ZnSe/ZnS	55%	434	6.88%	450	(0.166, 0.013)	ITO/PEDOT:PSS/PVK/QD/ZnMgO/Al	[56]
ZnSe/ZnS/ZnS	56%	446	2.62%	106	(0.16, 0.02)	ITO/ZnO/QD/CBP/HAT-CN/Al	[66]
ZnSeTe/ZnSe/ZnSeS/ZnS	84%	445	9.50%	2904	(0.148, 0.048)	ITO/PEDOT:PSS/PVK/QD/m-ZnMgO/Al	[58]
ZnSeTe/ZnSe/ZnS	100%	460	20.20%	88,900		ITO/PEDOT:PSS/TFB/QD Cl(f)/Cl(l)/ZnMgO/Al	[10]
ZnSeTe/ZnSe/ZnS	70%	441	4.2%	1195	(0.153, 0.027)	ITO/PEDOT:PSS/PVK/QD/ZnMgO/Al	[53]
ZnSe/ZnS	48%	430	7.83%	2250	(0.169, 0.023)	ITO/PEDOT:PSS/PVK/QD/ZnO/Al	[67]
ZnSe/ZnS		441		1170	(0.16, 0.15)	Al/MoO3/TCTA/CBP/QD/ZnO/ITO	[68]
ZnSe/ZnS	40%	425	0.65%			ITO/PEDOT:PSS/PVK/QD/ZnO/Al	[57]

4. III-V QDs

4.1. Development of InP QD Synthesis

InP QDs are promising candidates for heavy-metal-free QDs because of their wider spectral range, narrow PL linewidth, and high PLQY properties, which are achieved through control of the size distribution of the InP core and engineering of the heterostructure. Previous studies on the synthesis of InP QDs aimed to obtain products with mild reaction conditions, controllable size, and high PLQY. However, the high reactivity of atoms or ions and large reaction barriers in the chemical pathways for the crystal formation of III-V QDs complicate their nucleation and growth processes. To overcome the high reaction barrier of InP QDs, researchers generally used highly reactive $(SiMe_3)_3P$ as the P precursor due to its high reactivity [69–71]. In 1994, Nozik et al. first used $InCl_3$ and $(SiMe_3)_3P$ to synthesize InP QDs [70]. In 1994, Nozik et al. first used $InCl_3$ and $(SiMe_3)_3P$ to synthesize InP QDs. Similar to the synthesis of II-VI QDs, the concentration of ligands in a noncoordinating solvent can change the reactivity of Cd and Zn precursors, resulting in the formation of high-quality QDs [70,72]. The effect of ligand concentration on the reactivity of III-V precursors is more significant. Peng et al. reduced the InP nucleation time from days to hours by using octadecene (ODE) as a noncoordinating solvent and fatty acids as ligands [73]. Lucey et al. also synthesized InP QDs with better monodispersity in ODE by using indium carboxylate and $(SiMe_3)_3P$ without surfactants or ligand solvents [74]. We can observe the lattice edges of the QD from the high-resolution transmission electron microscopy (HRTEM) of a single InP QD (Figure 5a). However, some studies suggest that a similar nucleation process in a noncoordinating solvent can also be obtained when the coordination effect of the solvent is much weaker than that of the introduced strong ligand. Xu's group used fatty acid lipids (methyl myristate and dibutyl sebacate) as weakly coordinating solvents, as well as a more reactive indium precursor (trimethylindium) and a proton reagent to accelerate the synthesis [75]. The nucleation process produced QDs with a narrow size (2.5 nm). The results showed that high-boiling esters can act as effective, weakly coordinating solvents to control the nucleation process. Peng et al. used aliphatic amines as activating reagents to improve the reactivity of indium carboxylate and reduce the reaction temperature of the synthesis [9]. InP/ZnS QDs with controllable size distributions were successfully synthesized over a wide spectral range (450–750 nm) (Figure 5b). In addition to controlling the InP QD size to tune its emission wavelength, changing the thickness ratio between the core and shell can also perform spectral modulation. Yang et al. made the PL spectra of InP QDs cover the entire visible spectrum (350–800 nm) by changing the ratio of InP:ZnS [76].

Compared with the smaller Bohr radius (4.6 nm) of CdSe QDs, the InP system has obvious intrinsic advantages (the Bohr radius is 9.6 nm). However, the development of InP QDs in the blue region is not ideal, mainly because it is difficult to find suitable reaction conditions and precursors to control the growth of InP QDs. Shen et al. reported a colloidal approach mediated by zinc halide to improve the performance of blue-emitting InP/ZnS QDs [77]. The high reaction rate of blue InP QDs was attributed to both P and In precursors, and the use of tris(dimethylamino)phosphine ($(DMA)_3P$) as the P precursor could suppress the QD size distribution (Figure 5c). Excess I^- was found to increase the reactivity of In^{3+} and could be used to accelerate the cleavage of In-X compared to Cl^- [78]. Furthermore, excess I^- could be combined with oleylamine (OAM) and adsorbed on the surface of InP QDs as a passivation agent, which suppressed the size distribution and reduced surface defects. Thus, an amine halide passivation layer was formed by a ZnS halide-mediated colloidal approach, leading to a PLQY of 76.1%. Due to the highly toxic and flammable nature of $(DMA)_3P$, Yu et al. replaced it with the inorganic solid metal phosphorus, sodium phosphaethynolate (NaOCP), to synthesize InP QDs (Figure 5d). Inorganic solid phosphine source synthesized InP QDs with a modulable PL emission range of 465–620 nm. The PLQYs of blue (465 nm), green (533 nm), and red (620 nm) QDs were found to be 43%, 97%, and 95%, respectively [79].

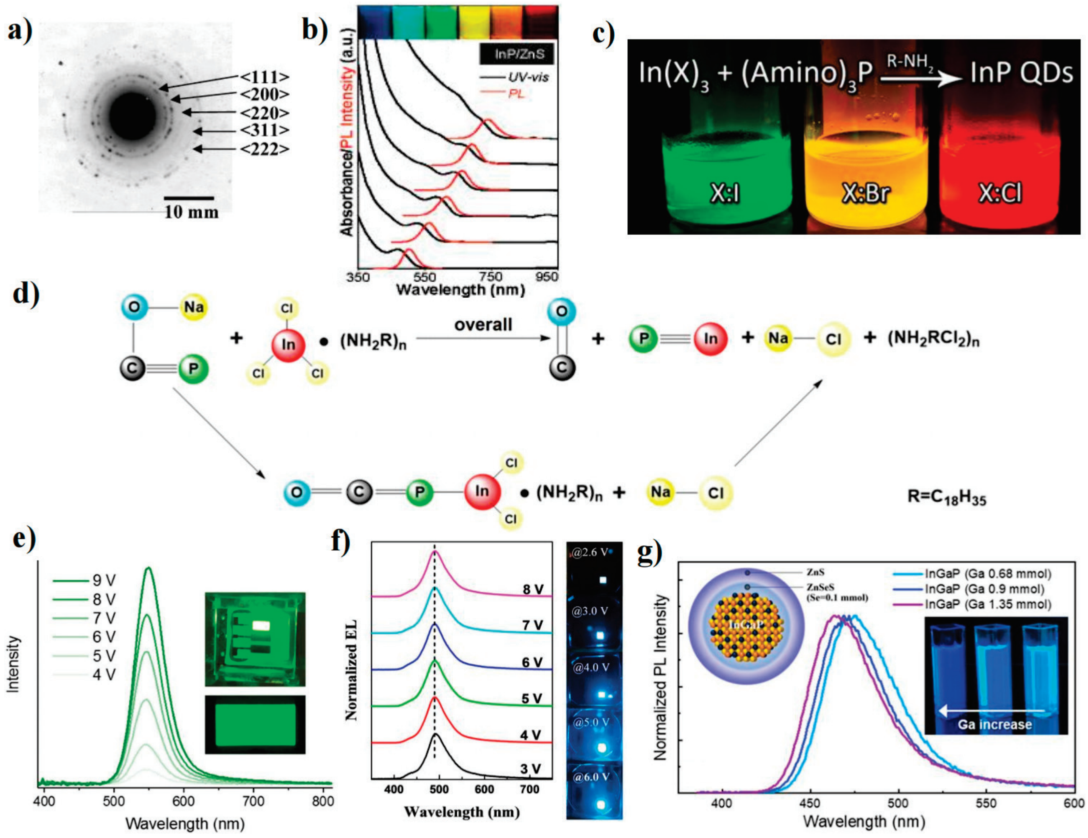

Figure 5. (**a**) HRTEM image of an InP QD [74]. Copyright 2005, American Chemical Society. (**b**) UV–vis absorption and PL spectra of different sized InP/ZnS core/shell QDs [9]. Copyright 2007,

American Chemical Society. (**c**) Schematic of the synthesis of InP QDs from indium halide and aminophosphine precursors [78]. Copyright 2015, American Chemical Society. (**d**) Schematic for the formation of InP QDs by using $InCl_3$ and NaOCP [79]. Copyright 2021, American Chemical Society. (**e**) Voltage-dependent EL spectra of the green QLED [8]. Copyright 2017, Nature Publishing Group. (**f**) EL spectra at different voltages [80]. Copyright 2020, American Chemical Society. (**g**) Normalized PL spectra of InGaP QDs [81]. Copyright 2020, American Chemical Society.

4.2. Blue InP-Based QLEDs

In recent years, InP QLEDs have made significant progress in both red and green emissions [82,83]. Red InP QLEDs, for example, achieved an EQE of 21.4% and a luminance of >100,000 cd m^{-2} [84]. Similarly, Green InP QLEDs have demonstrated an EQE of 16.3% after passivation with different alkyl diamines and zinc halides (Figure 5e) [85]. Despite these successes, the development of blue InP QLEDs has been slower. This is mainly due to two factors: (1) the low PLQY of QD-assembled light-emitting films and (2) the low carrier injection and transport processes. To address these challenges, several strategies have been proposed. For example, Zhang et al. synthesized thick-shell blue InP/ZnS/ZnS QDs using a wide bandgap ZnS shell to effectively prevent electron transition from the core to the shell and achieved emission from InP QDs at 468 nm. The EQE of these QLEDs was found to reach 1.7% [86]. Du et al. introduced a GaP bridging layer to reduce the lattice mismatch between the InP core and the ZnS shell, resulting in InP/GaP/ZnS quantum dots with thick ZnS shells that exhibited high PLQY (≈81%). QLEDs fabricated using these QDs achieved a L_{max} of 3120 cd m^{-2} and an EQE of 1.01% (Figure 5f) [80]. To improve carrier injection in blue InP QLEDs, Tan et al. introduced an electric dipole layer (EDL) (MoO_3) with a deep conduction band sandwiched between PEDOT:PSS and PVK to generate voids from PEDOT:PSS. The dipole-induced embedded electric field in the forward direction of the HIL to PVK balances the carrier injection by enhancing hole injection. The p-type doping effect of MoO_3 increased the carrier concentration of the interfacial PVK and reduced the trap density, thereby increasing its hole mobility. This approach improved the EQE of the blue InP QLED from 1.0% to 2.1% [87]. Based on Tan's work, Mei et al. developed a strategy for light extraction. Specifically, they extracted light from the waveguide mode to the air mode by using a thin HTL, a high-refractive-index substrate, and substrate surface roughening. The thin HTL and high-refractive-index substrate facilitated the transport of light from the waveguide mode to the substrate mode. The substrate surface was then roughened to further extract light from the enhanced substrate mode into the air mode. This approach improved the EQE of the blue InP QLED from 2.1% to 2.8% and currently represents the highest efficiency for InP blue light emission [6].

The development of InP-based ternary compounds for blue emission has been identified as a significant area of research. In particular, InGaP ternary QDs have emerged as promising candidates for the development of high-quality blue QLEDs [88]. Previous studies have reported on the synthesis of InGaP QDs using two Ga precursors (gallium oleate and gallium acetylacetonate), but the resulting PLQY was low (≈20%) even after the growth of a ZnS shell layer [89]. More recent work by Kim et al. has shown that cation exchange of In^{3+} and Ga^{3+} followed by double growth of the ZnSe inner shell and ZnS outer shell can result in InGaP/ZnSeS/ZnS QDs with tunable blue emission in the 465–475 nm range (depending on the Ga ratio) (Figure 5g). The 465 nm sample showed a high PLQY of 80%, and the corresponding QLED exhibited excellent performance with a L_{max} of 1038 cd m^{-2} and an EQE of 2.5% [81]. The development of InGaP ternary QDs holds great promise for the realization of high-quality blue QLEDs.

5. Carbon Dots

5.1. Photoluminescence of Carbon Dots

Carbon dots (CDs) are a type of carbon-based nanomaterial that possess at least one dimension less than 10 nm. The isolation of CDs within single-walled carbon nanotubes

(SWNTs) by Xu et al. (Figure 6a) sparked significant interest in their potential applications in optics, leading to numerous studies on their properties [90–96]. CDs possess a range of advantageous characteristics, such as low cost, low toxicity, good biocompatibility, simple preparation processes, tunable fluorescence emission (Figure 6b), and photochemical stability.

A vast range of raw materials, including laboratory-produced chemicals and natural products, have been used for the synthesis of CDs. This has resulted in a diverse range of components and structures used to prepare CDs, making it difficult to develop a unified theory by comparing the results reported in the literature. The complexity of CDs and the various factors that affect their luminescence processes have also made it challenging to deduce a reasonable PL mechanism. The luminescence of CDs is primarily determined by three characteristics: (1) the material is primarily composed of carbon, (2) carbonization or cross-linking processes are needed, and (3) the kernel luminescence is a carbon-based structure, which is the sp^2/sp^3 conjugated structure [97–99]. At present, the PL mechanism of CDs is mainly summarized in four aspects: (1) the QCE or conjugate π domain determined by the carbon core [100]; (2) the surface state, which is determined by the hybridization of the carbon backbone and the linked chemical groups; and (3) the molecular state, which is determined only by the fluorescent molecules attached to the surface or interior of CDs; and (4) the crosslinked enhanced emission (CEE) effect [101].

Yan et al. synthesized large-scale colloidal graphene QDs with uniform and tunable sizes through a solubilization strategy [102]. The oxidation of polyphenylene dendritic precursors synthesized by stepwise solution chemistry results in fused graphene moieties, which are stabilized through multiple 2′,4′,6′-trialkyl phenyl groups covalently attached to the edges of the graphene moieties. The bandgap of graphene could be further reduced by increasing its size or chemically functionalizing it to tune its redox potential. In some cases, heteroatom doping can have a more significant effect on the wavelength modulation of CDs than particle size. Yang et al. investigated the use of nitrogen-based precursors (DMF, urea, ethanamide, and formamide) in a solvent-free reaction to achieve multicolor (505–650 nm) fluorescence emission. They revealed that the fluorescence properties of CDs were dependent not only on their particle size but also on their degree of graphitization. The content of C-O and C=N functional groups on the surface of CDs played a synergistic role in constructing multicolor fluorescent CDs [103].

In the absence of group modification, blue-emitting CDs are more easily attainable than longer wavelength-emitting CDs [104–106]. However, this does not necessarily imply that the performance of the blue CD-LED is better. The aggregation-induced quenching (ACQ) phenomenon can cause a significant decrease in the fluorescence intensity of CDs in the solid state, leading to a serious change in the spectral characteristics [107]. Ding et al. gradually tuned CDs from blue to red with bright and stable light under the excitation of single-wavelength UV light by silica gel column chromatography [108]. These samples exhibited similar particle size distributions and graphite structures in their carbon nuclei, but their surface states changed gradually. The authors found that the incorporation of oxygen into the surface structure of CDs led to a decrease in the bandgap of these CDs (Figure 6c), resulting in a redshift of the emission peak from 440 to 625 nm.

Recently, Cao's group confirmed two precise fluorophore structures, DAP and AHP, in o-phenylenediamine (O-PD) CDs [109]. They also extracted two green compounds (G-CD, G-CD 1, and G-CD 2) and one blue compound (B-CD). DAP, G-CD, and B-CD were mixed with polyvinylpyrrolidone (PVP) powder and ethanol to produce a white LED with a color rendering coefficient of up to 87 (Figure 6d). In a study conducted by Yang's group in 2014, branched polyethylene-imine (PEI) was utilized as a model system to synthesize carbon dots (CDs) by crosslinking with carbon tetrachloride [110]. As a result, the PL of the CDs was found to be significantly enhanced, which was attributed to the reduced vibration and rotation of PEI. This study demonstrated the first instance of cross-linked enhanced emission at the nonconjugated polymerization point.

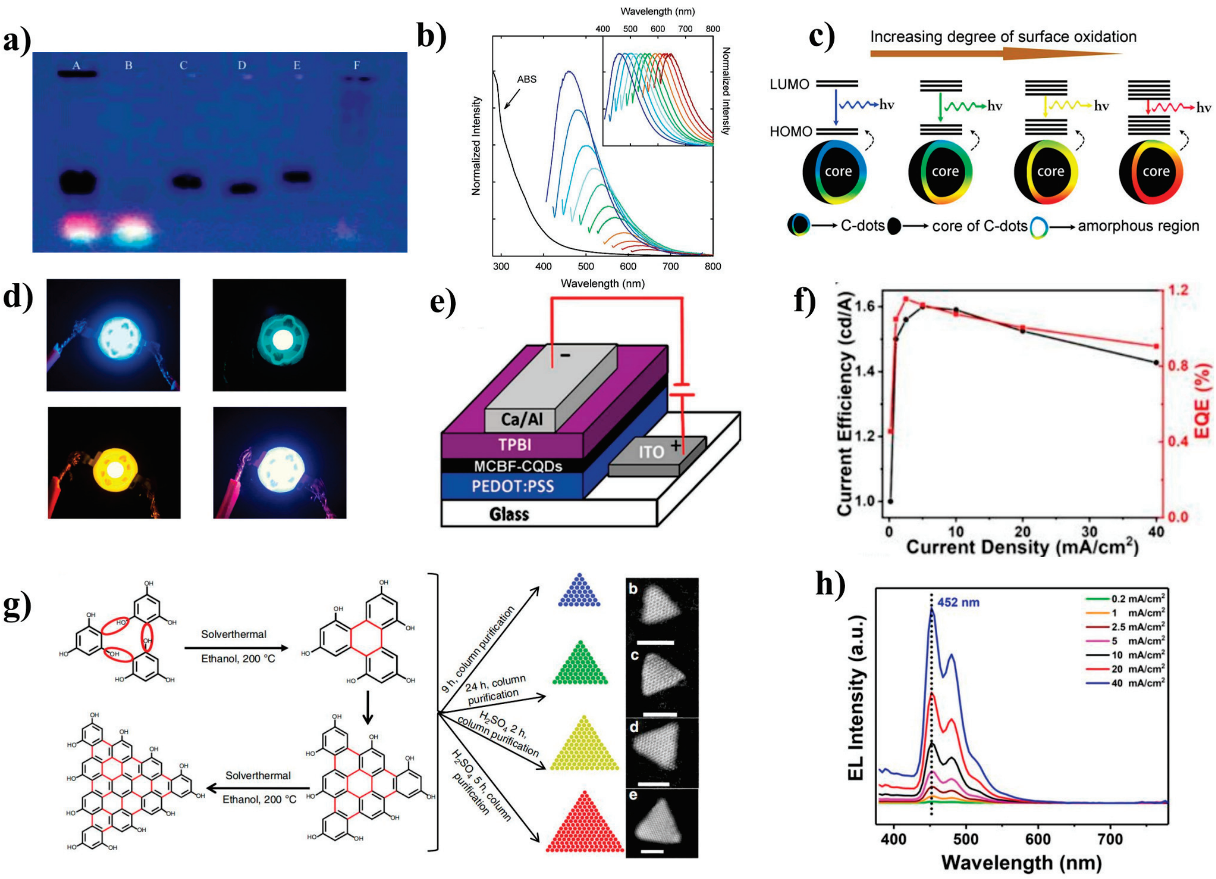

Figure 6. (**a**) Electrophoretic profile in 1% agarose gel under 365 nm UV light [90]. Copyright 2004, American Chemical Society. (**b**) UV–vis absorption and PL spectra of CDs [97]. Copyright 2006, American Chemical Society. (**c**) Model for the tunable PL of CDs with different degrees of oxidation [108]. Copyright 2006, American Chemical Society. (**d**) Optical photographs of blue, green, yellow, and white LEDs [109]. Copyright 2022, Elsevier B.V. (**e**) The device structure of MCBF: CDs-LED [111]. Copyright 2017, Wiley-VCH. (**f**) EQE values (red solid line) and current efficiency (black solid line) of WLEDs [112]. Copyright 2021, Wiley-VCH. (**g**) Synthesis route and HAADF-STEM images of triangular CDs [113]. Copyright 2018, Nature Publishing Group. (**h**) EL emission spectra of the blue CD-LED at different current densities [114]. Copyright 2021, Wiley-VCH.

5.2. Electroluminescence of Carbon Dots

CD electroluminescent devices have a more complex luminescence mechanism than inorganic QDs. The device structure of CD-LEDs is similar to that of inorganic QLEDs, such as ITO/PEDOT:PSS/EML/TPBi/LiF/Al (Figure 6e) [111,114,115]. The largest difference lies in the EML. If CD materials are prepared as the EML of the device alone, the luminescence will be low due to aggregation fluorescence quenching. To overcome this issue, CDs are usually incorporated into host materials (such as PVK, CBP, poly-TPD, etc.) to serve as the EML [113,116–118]. Host materials not only improve the dispersion of CDs and reduce aggregation fluorescence quenching but also have wider bandgaps that facilitate Förster resonance energy transfer to excite CD luminescence. For example, Wang et al. demonstrated the first preparation of a white CD-LED, which obtained only 0.083% EQE. However, when PVK was used as the host material, the EQE of the white light device was improved by up to 1.18% (Figure 6f) [112,119]. Additionally, Kwon et al. achieved energy transfer from the CBP host to the GQD guest [100]. The energy levels of graphene QDs are located inside the CBP, so charge carriers are injected into the CBP and then transferred from the CBP to the GQD, leading to valuable EL.

Moreover, CDs usually have a broad full width at half maximum (FWHM) emission spectrum due to their structure and surface defects. However, Yuan et al. designed triangular-shaped CQDs (T-CQDs) (Figure 6g) through structural engineering, which greatly weakened electron-phonon coupling and reduced surface defects, resulting in negligible trap-state free exciton emission [113]. These triangular CQDs achieved narrow-bandwidth emission from blue to red (FWHM = 30 nm), with a PLQY of 54–72%, L_{max} = 4762 cd m^{-2}, and current efficiency (CE) = 5.11 cd A^{-1}.

Furthermore, Sargent's group explored the effect of oxygen-containing functional groups on spectral broadening using density functional theory [120]. They found that electron coupling to molecular vibration and distortion is the reason for the wide emission spectra. The bandgap vibrations of COOH-CD and NH_2-CD were compared, and due to the strong polarization effect caused by the COOH functional group, its rotation relative to the base plane affects the positioning degree of the wave function, resulting in the broadening of the spectra.

5.3. Blue Carbon Dot Light-Emitting Diodes

The performance of blue CD-LEDs is currently not as good as that of inorganic QLEDs in terms of device luminance, lifetime, EQE, and color purity due to the intrinsic properties of CD materials [117,121]. However, recent research has shown promising results. In 2019, Sargent's group reported the synthesis of excellent blue CDs using a solution method with citric acid and diaminonaphthalene, resulting in blue CD-LEDs with a L_{max} of 5240 cd m^{-2} and an EQE of 4.04% [120]. Passivating the surface of the CDs with diaminonaphthalene reduced the trap state and increased the PLQY to 70% ± 10%, while decreasing the proportion of oxygen-containing functional groups led to a significant reduction in the FWHM (35 nm). The wide spectra of CD devices have been a significant obstacle in the development of monochromatic devices. However, in 2021, Kang et al. synthesized strongly blue-emitting O and N codoped CDs by the hydrothermal method from perylene-3,4,9,10-tetracarboxylic dianhydride (PTCDA) and 2,3-diamino phenazine (DAP) [119]. The incorporation of these CDs into PVK to form the EML resulted in CD-LEDs emitting at 452 nm, which closely matches the CIE coordinates of the standard pure blue color (0.14, 0.08) specified in NTSC 1953, achieving a purer blue LED (Figure 6h).

6. Perovskite QDs

The luminescence properties of perovskite materials vary greatly in different dimensions. Unlike conventional two-dimensional materials that require only a few atomic layers thin to exhibit QCE, perovskite materials can form a natural quantum well structure even with two-dimensional layers due to the isolation of the perovskite layer by long-chain molecular groups. However, the quantum effect of perovskite material depends heavily on the thickness of the perovskite in each layer. While three-dimensional perovskites have high electron mobility, their low film coverage and high defect density have hindered the preparation of high-efficiency devices. Quasitwo-dimensional states lie between two and three dimensions and are a combination of polyphase three- and two-dimensional perovskite layers. Several studies have shown that quasitwo-dimensional structures can combine the advantages of both two- and three-dimensional perovskites, but there remain significant challenges in their development.

PQDs are a type of zero-dimensional perovskite material that exhibits QCE and quantization of near band-edge states when their size is smaller than the Bohr radius. PQDs, similar to other inorganic QDs such as CdSe, InP, and ZnSeTe, exhibit a high PLQY, a narrow emission linewidth, and controllable growth regulation. Two primary methods for achieving deep blue emission in PQDs have emerged. The first approach involves adjusting the size of the PQDs using the ligand-assisted reprecipitation process to control QCE, as demonstrated by Rogach et al. in 2015. By manipulating the temperature, they modulated the emission spectrum of $CH_3NH_3PbBr_3$ QDs (1.8–3.6 nm) from 475 nm to 520 nm [122]. The second approach involves introducing Cl to modulate the emission wavelength by controlling the ratio of Br/Cl halogens. Kovalenko et al. synthesized $CsPbX_3$ and achieved emission spectra throughout the visible region of 410–700 nm by changing the halogen ratio [123,124]. The resulting $CsPbX_3$ QDs displayed narrow emission line widths of 12–42 nm, a wide gamut of up to 140% of the NTSC color standard, and a high PLQY of up to 90%.

6.1. Quantum Confinement Effect of Perovskite QDs

One approach to achieving spectral modulation in PQD technology is to adjust the bandgap of the PQDs through QCE. This method requires precise control of the crystal growth of the PQDs, which ideally should be close to the Bohr radius. Yang et al. attempted to enhance size uniformity and reduce crystal defects by using ice water and liquid nitrogen to temporarily halt QD growth during synthesis [125]. Ultrafast thermodynamically controlled QDs (UFTDC-QDs) were synthesized using this method and were found to reduce the injection barrier compared to ice water and liquid nitrogen treatment as a control variable for UFTDC (Figure 7a). Perovskite LED (PeLED) prepared on this basis achieved an EQE of 3.66%, a L_{max} of 2100 cd m^{-2} at 460 nm, and a T_{50} of 288 s.

Temperature is not the only factor that can control the reaction process. Mathews et al. used octyl phosphonic acid (OPA) ligands to modulate the growth rate of PQDs [126]. This approach effectively decoupled the PQD nucleation and growth stages, and the reaction duration was determined by preventing PQD growth with the addition of the dodecyl dimethyl ammonium bromide (DDAB) ligand. This method achieved $CsPbBr_3$ QD emission wavelengths between 501 and 517 nm. Pradhan et al. reported on $CsPbBr_3$ QDs with adjustable wide window sizes [127]. The size and shape of the QDs could be precisely controlled by changing the concentration of the alkylammonium bromide reagent without altering the reaction temperature or the ligand. Cao's group also investigated the use of macromolecule (6-amino-6-deoxy) beta-cyclodextrin (6A-βCD) as a new cationic ligand to replace the OAM [128]. The spatial hindrance and cage junction of 6A-βCD effectively limited the size of $CsPbBr_3$ QDs in three dimensions, achieving blue emission of 400–500 nm (Figure 7b), with a PLQY up to 72.4%.

In addition to the use of large volumes of organic ligands to inhibit PQD growth during the growth process, adjusting the growth environment of the crystal is another approach. Yu et al. found that Sb^{3+} inhibited the further growth of ultrasmall $CsPbBr_3$ QDs (2.2–2.9 nm) [129]. The doping of Sb^{3+} reduced the surface energy, improved the lattice energy, passivated defect states, and increased the PLQY to 73.8% (Figure 7c). Zhang et al. designed a polymer gel network by irradiating acrylamide monomers in dimethyl sulfoxide under UV light [130]. The polymer gel controlled the concentration of supersaturated ions and extended the crystallization time to form 1.1 ± 0.2 nm $CsPbBr_3$ QDs. Due to excellent surface passivation and QCE, the $CsPbBr_3$ QDs achieved a spectrum ranging from 433 nm to 512 nm. The obtained PQDs can emit high-quality blue light with an FWHM of 14 nm and a PLQY of 74%.

6.2. Blue Perovskite QDs of Mixed Halogens

The high surface area to volume ratio of small-sized blue PQDs results in a large number of Br- vacancy (VBr) defects on their crystal surface, which adversely affects their optical properties. Achieving efficient deep blue light emission from pure bromine chalcogenides is therefore challenging. To address this issue, a compositional modality of mixing halide (Cl/Br) perovskite has been employed to widen the band gap in the blue spectral region. The Cl/Br ratio can be easily adjusted to tune the band gap, leading to improved optical properties.

Zeng et al. reported the first QLED based on all-inorganic ($CsPbX_3$, X = Cl, Br, and I) PQDs, achieving broad spectra from orange to blue (Figure 7d) [131]. Similarly, He et al. synthesized $CsPbCl_{3-x}Br_x$ (x = 0.0–2.5) QDs using a modified ligand-assisted reprecipitation method and obtained blue emissions with different Br compositions by changing the $PbCl_2$ to $PbBr_2$ ratio in the precursor [132]. The value of x can be adjusted to precisely control the band gap of $CsPbCl_{3-x}Br_x$ (x = 0.0–2.5) QDs between 2.54 and 3.06 eV (Figure 7e). However, changes in Cl content can result in changes in halide vacancies and energy states, leading to unbalanced charge injection and an increase in nonradiative sites, causing significant efficiency roll-off. Cl^- vacancies are the primary source of mixed halide (Br/Cl) PeLED trap states. To address this issue, we developed a strategy for the passivation of Cl^- vacancies in $CsPb(Br_xCl_{1-x})_3$ QDs using a nonpolar solvent-soluble organic halide [N-dodecyl ammonium thiocyanate (DAT)] (Figure 7f) [133]. Density functional theory calculations showed that the SCN group filled the Cl^- vacancy, removing the electron trap in the bandgap, resulting in a stable (~470 nm) and highly efficient (EQE = 6.3%) blue PeLED.

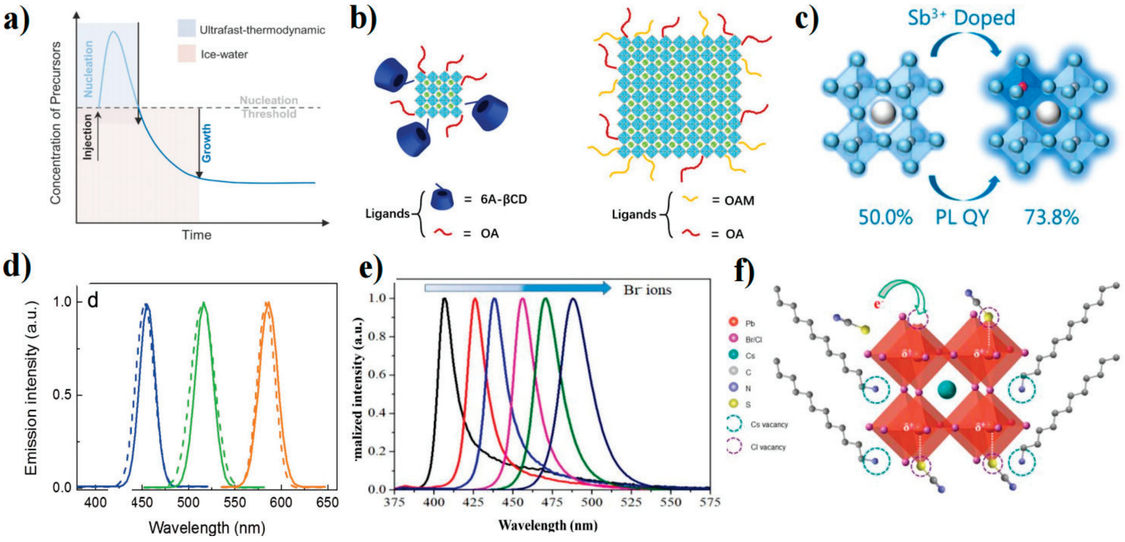

Figure 7. (**a**) La Mer model of PQD growth guidance in IW and UFTDC cooling processes [117]. Copyright 2021, American Chemical Society. (**b**) Growth schematic for ultrasmall $CsPbBr_3$ QDs and large $CsPbBr_3$ nanocubes [118]. Copyright 2021, Wiley-VCH. (**c**) Schematic of the PLQY change after Sb^{3+} doping [129]. Copyright 2019, American Chemical Society. (**d**) EL spectra (straight line) and PL spectra (dashed line) of $CsPbX_3$ QDs [131]. Copyright 2015, Wiley-VCH. (**e**) Normalized PL spectra of $CsPbCl_{3-x}Br_x$ (x = 0.0–2.5) QDs [132]. Copyright 2021, Elsevier B.V. (**f**) Illustration of Cl^- vacancy-induced Coulomb trap site formation, electron trapping, and self-assembly of organic thiocyanate (RSCN) on the defect sites in MHP [133]. Copyright 2020, American Chemical Society.

The long chains of insulating ligands hinder the radiative recombination of charges in QDs, reducing the efficiency of PeLEDs. To overcome this limitation, Kovalenko and Kim et al. utilized di-dodecyl dimethylammonium halides (DDAX) as short ligands, which enabled the PQDs to self-reconstruct into a stable formation by surface passivation from OA or OAM to DDA^+. Surface passivation using DDAX significantly increased the PLQY of PQDs to 50.2% in the deep blue light region at 467 nm [124,134].

7. Conclusions and Outlook

QLEDs have experienced unprecedented advances as a new generation of light-emitting components, especially for red and green QLEDs. However, efficient blue QLEDs remain a challenge. In this review, we summarized the development of II-VI (CdSe, ZnSe) QDs, III-V (InP) QDs, CDs, and PQDs (mainly $CsPbX_3$) in blue light devices.

Cd-based QDs with great success in achieving high-performance LEDs have inspired researchers to develop solution synthesis of other types of inorganic QDs, with a particular focus on heavy metal-free QDs. The experience gained from the synthesis, ligand modifications, core-shell engineering and device preparation of Cd-based QDs provides a reference for the development of other heavy metal-free QDs.

ZnSe-based QDs have advantages in achieving blue light emission due to their large band gap. In addition to exploiting the QCE, spectral tuning can be achieved by doping Te elements. This offers ZnSe-based QDs a large scope for emission tuning from violet to green. However, the doping of Te significantly broadens the FWHM and makes the spectrum asymmetric. Therefore, achieving high EQE and high color purity will be the next step for blue ZnSe-based QLEDs.

Blue InP QDs face a challenge in achieving deep blue light emission (<470 nm) due to their small core size (<2 nm). The current InP blue QLED efficiency is below 3%. InP can emit in the deep blue range by introducing Ga elements. InGaP QLEDs were reported to emit at 469 nm with an EQE of 2.5%. It is foreseeable that ternary InGaP is the direction of InP-based QD blue light.

From the display perspective, the ACQ effect limits CD luminescence in the solid state, which can only be solved by synthesizing anti-burst CDs and doping them into host materials. Although CD-LEDs are not currently comparable to inorganic QLEDs, CD luminescence has the potential for developing bioimaging applications due to its nontoxic and biocompatible characteristics.

Perovskite QDs have a peculiar crystal structure that enables efficient luminescence. Multicolor luminescence can be achieved by the QCE and modulation of halogen composition. However, deep blue PQDs usually require Br/Cl codoping, which leads to phase separation due to the migration of halogen ions under an electric field. Although several strategies have been proposed to improve PQDs, such as adjusting the halogen ratio, A$^-$ and B$^-$site doping, and chemical environment regulation, structural instability and poor lifetime remain challenges that PQDs must overcome.

Here, we discussed four representative QDs in material synthesis, core-shell structures, ligand interactions, and device fabrication. We hope to introduce a variety of representative QD materials to help readers understand the problems and solutions encountered in the development of blue QLEDs. As RGB's most important and difficult part, blue light requires more researchers' continued attention and efforts.

Funding: This research was funded by the National Natural Science Foundation of China (NSFC) (62175171, 61961160731 and 62205230), China Postdoctoral Science Foundation (2021TQ0230, 2021M690114), Suzhou Key Laboratory of Functional Nano & Soft Materials, Collaborative Innovation Center of Suzhou Nano Science & Technology, the 111 Project, Joint International Research Laboratory of Carbon-Based Functional Materials and Devices. This project is also funded by the Collaborative Innovation Center of Suzhou Nano Science and Technology (CIC-Nano).

Data Availability Statement: Not applicable.

Conflicts of Interest: The authors declare no conflict of interest.

References

1. Wu, Q.; Gong, X.; Zhao, D.; Zhao, Y.B.; Cao, F.; Wang, H.; Wang, S.; Zhang, J.; Quintero-Bermudez, R.; Sargent, E.H.; et al. Efficient Tandem Quantum-Dot LEDs Enabled by An Inorganic Semiconductor-Metal-Dielectric Interconnecting Layer Stack. *Adv. Mater.* **2022**, *34*, 2108150. [CrossRef] [PubMed]
2. Zhao, J.; Chen, L.; Li, D.; Shi, Z.; Liu, P.; Yao, Z.; Yang, H.; Zou, T.; Zhao, B.; Zhang, X.; et al. Large-area patterning of full-color quantum dot arrays beyond 1000 pixels per inch by selective electrophoretic deposition. *Nat. Commun.* **2021**, *12*, 4603. [CrossRef] [PubMed]
3. Dai, X.; Deng, Y.; Peng, X.; Jin, Y. Quantum-Dot Light-Emitting Diodes for Large-Area Displays: Towards the Dawn of Commercialization. *Adv. Mater.* **2017**, *29*, 1607022. [CrossRef] [PubMed]
4. Yang, Z.; Gao, M.; Wu, W.; Yang, X.; Sun, X.W.; Zhang, J.; Wang, H.-C.; Liu, R.-S.; Han, C.-Y.; Yang, H.; et al. Recent advances in quantum dot-based light-emitting devices: Challenges and possible solutions. *Mater. Today* **2019**, *24*, 69–93. [CrossRef]
5. Zhang, J.; Wang, L.; Zhang, X.; Xie, G.; Jia, G.; Zhang, J.; Yang, X. Blue light-emitting diodes based on halide perovskites: Recent advances and strategies. *Mater. Today* **2021**, *51*, 222–246. [CrossRef]
6. Mei, G.; Tan, Y.; Sun, J.; Wu, D.; Zhang, T.; Liu, H.; Liu, P.; Sun, X.W.; Choy, W.C.H.; Wang, K. Light extraction employing optical tunneling in blue InP quantum dot light-emitting diodes. *Appl. Phys. Lett.* **2022**, *120*, 091101. [CrossRef]
7. Li, H.; Zhang, W.; Bian, Y.; Ahn, T.K.; Shen, H.; Ji, B. ZnF_2-Assisted Synthesis of Highly Luminescent InP/ZnSe/ZnS Quantum Dots for Efficient and Stable Electroluminescence. *Nano Lett.* **2022**, *22*, 4067–4073. [CrossRef]

8. Chao, W.-C.; Chiang, T.-H.; Liu, Y.-C.; Huang, Z.-X.; Liao, C.-C.; Chu, C.-H.; Wang, C.-H.; Tseng, H.-W.; Hung, W.-Y.; Chou, P.-T. High efficiency green InP quantum dot light-emitting diodes by balancing electron and hole mobility. *Commun. Mater.* **2021**, *2*, 96. [CrossRef]
9. Xie, R.; Battaglia, D.; Peng, X. Colloidal InP Nanocrystals as Efficient Emitters Covering Blue to Near-Infrared. *J. Am. Chem. Soc.* **2007**, *129*, 15432–15433. [CrossRef]
10. Kim, T.; Kim, K.H.; Kim, S.; Choi, S.M.; Jang, H.; Seo, H.K.; Lee, H.; Chung, D.Y.; Jang, E. Efficient and stable blue quantum dot light-emitting diode. *Nature* **2020**, *586*, 385–389. [CrossRef]
11. Ioannou, D.; Griffin, D.K. Nanotechnology and molecular cytogenetics: The future has not yet arrived. *Nano Rev.* **2010**, *1*, 5117.
12. Peng, X. An essay on synthetic chemistry of colloidal nanocrystals. *Nano Res.* **2009**, *2*, 425–447.
13. Peng, X.; Wickham, J.; Alivisatos, A.P. Kinetics of II–VI and III–V Colloidal Semiconductor Nanocrystal Growth: "Focusing" of Size Distributions. *J. Am. Chem. Soc.* **1998**, *120*, 5343–5344. [CrossRef]
14. Thessing, J.; Qian, J.; Chen, H.; Pradhan, N.; Peng, X. Interparticle Influence on Size/Size Distribution Evolution of Nanocrystals. *J. Am. Chem. Soc.* **2007**, *129*, 2736–2737. [CrossRef] [PubMed]
15. Li, Z.; Wei, J.; Wang, F.; Tang, Y.; Li, A.; Guo, Y.; Huang, P.; Brovelli, S.; Shen, H.; Li, H. Carrier Dynamics in Alloyed Chalcogenide Quantum Dots and Their Light-Emitting Devices. *Adv. Energy Mater.* **2021**, *11*, 2101693. [CrossRef]
16. Shin, D.H.; Lampande, R.; Kim, S.J.; Jung, Y.H.; Kwon, J.H. Understanding the Origin of Degradation of InP-Quantum Dot Light-Emitting Diodes. *Adv. Electron. Mater.* **2022**, *8*, 2200256. [CrossRef]
17. Colvin, V.L.; Schlamp, M.C.; Alivisatos, A.P. Light-emitting-diodes made from cadmium selenide nanocrystals and a semiconducting polymer. *Nature* **1994**, *370*, 354–357. [CrossRef]
18. Murray, C.B.; Noms, D.J.; Bawendi, M.G. Synthesis and Characterization of Nearly Monodisperse CdE (E = S, Se, Te) Semiconductor Nanocrystallites. *J. Am. Chem. Soc.* **1993**, *115*, 8706–8715. [CrossRef]
19. Supran, G.J.; Shirasaki, Y.; Song, K.W.; Caruge, J.-M.; Kazlas, P.T.; Coe-Sullivan, S.; Andrew, T.L.; Bawendi, M.G.; Bulović, V. QLEDs for displays and solid-state lighting. *MRS Bull.* **2013**, *38*, 703–711. [CrossRef]
20. Talapin, D.V.; Rogach, A.L.; Kornowski, A.; Haase, M.; Weller, H. Highly Luminescent Monodisperse CdSe and CdSe/ZnS Nanocrystals Synthesized in a Hexadecylamine−Trioctylphosphine Oxide−Trioctylphospine Mixture. *Nano Lett.* **2001**, *1*, 207–211. [CrossRef]
21. Peng, X.; Schlamp, M.C.; Kadavanich, A.V.; Alivisatos, A.P. Epitaxial Growth of Highly Luminescent CdSe/CdS Core/Shell Nanocrystals with Photostability and Electronic Accessibility. *J. Am. Chem. Soc.* **1997**, *119*, 7019–7029. [CrossRef]
22. Chen, Y.; Vela, J.; Htoon, H.; Casson, J.L.; Werder, D.J.; Bussian, D.A.; Klimov, V.I.; Hollingsworth, J.A. "Giant" Multishell CdSe Nanocrystal Quantum Dots with Suppressed Blinking. *J. Am. Chem. Soc.* **2008**, *130*, 5026–5027. [CrossRef] [PubMed]
23. Kundu, J.; Ghosh, Y.; Dennis, A.M.; Htoon, H.; Hollingsworth, J.A. Giant nanocrystal quantum dots: Stable down-conversion phosphors that exploit a large stokes shift and efficient shell-to-core energy relaxation. *Nano Lett.* **2012**, *12*, 3031–3037. [CrossRef] [PubMed]
24. Hanson, C.J.; Hartmann, N.F.; Singh, A.; Ma, X.; DeBenedetti, W.J.I.; Casson, J.L.; Grey, J.K.; Chabal, Y.J.; Malko, A.V.; Sykora, M.; et al. Giant PbSe/CdSe/CdSe Quantum Dots: Crystal-Structure-Defined Ultrastable Near-Infrared Photoluminescence from Single Nanocrystals. *J. Am. Chem. Soc.* **2017**, *139*, 11081–11088. [CrossRef]
25. Pal, B.N.; Ghosh, Y.; Brovelli, S.; Laocharoensuk, R.; Klimov, V.I.; Hollingsworth, J.A.; Htoon, H. 'Giant' CdSe/CdS core/shell nanocrystal quantum dots as efficient electroluminescent materials: Strong influence of shell thickness on light-emitting diode performance. *Nano Lett.* **2012**, *12*, 331–336. [CrossRef]
26. Liu, B.; Guo, Y.; Su, Q.; Zhan, Y.; Chen, Z.; Li, Y.; You, B.; Dong, X.; Chen, S.; Wong, W.Y. Cadmium-Doped Zinc Sulfide Shell as a Hole Injection Springboard for Red, Green, and Blue Quantum Dot Light-Emitting Diodes. *Adv. Sci.* **2022**, *9*, 2104488. [CrossRef]
27. Anikeeva, P.O.; Halpert, J.E.; Bawendi, M.G.; Bulović, V. Quantum Dot Light-Emitting Devices with Electroluminescence Tunable over the Entire Visible Spectrum. *Nano Lett.* **2009**, *9*, 2532–2536. [CrossRef]
28. Wang, L.; Lin, J.; Hu, Y.; Guo, X.; Lv, Y.; Tang, Z.; Zhao, J.; Fan, Y.; Zhang, N.; Wang, Y.; et al. Blue Quantum Dot Light-Emitting Diodes with High Electroluminescent Efficiency. *ACS Appl. Mater. Interfaces* **2017**, *9*, 38755–38760. [CrossRef]
29. Qian, L.; Zheng, Y.; Xue, J.; Holloway, P.H. Stable and efficient quantum-dot light-emitting diodes based on solution-processed multilayer structures. *Nat. Photonics* **2011**, *5*, 543–548. [CrossRef]
30. Loudon, J.C.; Mathur, N.D.; Midgley, P.A. Charge-ordered ferromagnetic phase in $La_{(0.5)}Ca_{(0.5)}MnO_3$. *Nature* **2002**, *420*, 797–800. [CrossRef]
31. Zhao, J.; Bardecker, J.A.; Munro, A.M.; Liu, M.S.; Niu, Y.; Ding, I.-K.; Luo, J.; Chen, B.; Jen, A.K.-Y.; Ginger, D.S. Efficient CdSe/CdS Quantum Dot Light-Emitting Diodes Using a Thermally Polymerized Hole Transport Layer. *Nano Lett.* **2006**, *6*, 463–467. [CrossRef] [PubMed]
32. Cho, K.-S.; Lee, E.K.; Joo, W.-J.; Jang, E.; Kim, T.-H.; Lee, S.J.; Kwon, S.-J.; Han, J.Y.; Kim, B.-K.; Choi, B.L.; et al. High-performance crosslinked colloidal quantum-dot light-emitting diodes. *Nat. Photonics* **2009**, *3*, 341–345. [CrossRef]
33. Caruge, J.M.; Halpert, J.E.; Wood, V.; Bulović, V.; Bawendi, M.G. Colloidal quantum-dot light-emitting diodes with metal-oxide charge transport layers. *Nat. Photonics* **2008**, *2*, 247–250. [CrossRef]
34. Qi, H.; Wang, S.; Jiang, X.; Fang, Y.; Wang, A.; Shen, H.; Du, Z. Research progress and challenges of blue light-emitting diodes based on II–VI semiconductor quantum dots. *J. Mater. Chem. C* **2020**, *8*, 10160–10173. [CrossRef]

35. Shen, H.; Gao, Q.; Zhang, Y.; Lin, Y.; Lin, Q.; Li, Z.; Chen, L.; Zeng, Z.; Li, X.; Jia, Y.; et al. Visible quantum dot light-emitting diodes with simultaneous high brightness and efficiency. *Nat. Photonics* **2019**, *13*, 192–197. [CrossRef]
36. Lee, K.-H.; Han, C.-Y.; Kang, H.-D.; Ko, H.; Lee, C.; Lee, J.; Myoung, N.; Yim, S.-Y.; Yang, H. Highly Efficient, Color-Reproducible Full-Color Electroluminescent Devices Based on Red/Green/Blue Quantum Dot-Mixed Multilayer. *ACS Nano* **2015**, *9*, 10941–10949. [CrossRef]
37. Shen, H.; Bai, X.; Wang, A.; Wang, H.; Qian, L.; Yang, Y.; Titov, A.; Hyvonen, J.; Zheng, Y.; Li, L.S. High-Efficient Deep-Blue Light-Emitting Diodes by Using High Quality $Zn_xCd_{1-x}S$/ZnS Core/Shell Quantum Dots. *Adv. Funct. Mater.* **2014**, *24*, 2367–2373. [CrossRef]
38. Yang, Y.; Zheng, Y.; Cao, W.; Titov, A.; Hyvonen, J.; Manders, J.R.; Xue, J.; Holloway, P.H.; Qian, L. High-efficiency light-emitting devices based on quantum dots with tailored nanostructures. *Nat. Photonics* **2015**, *9*, 259–266. [CrossRef]
39. Shen, H.; Cao, W.; Shewmon, N.T.; Yang, C.; Li, L.S.; Xue, J. High-efficiency, low turn-on voltage blue-violet quantum-dot-based light-emitting diodes. *Nano Lett.* **2015**, *15*, 1211–1216. [CrossRef]
40. Lee, K.-H.; Lee, J.-H.; Song, W.-S.; Ko, H.; Lee, C.; Lee, J.-H.; Yang, H. Highly Efficient, Color-Pure, Color-Stable Blue Quantum Dot Light-Emitting Devices. *ACS Nano* **2013**, *7*, 7295–7302. [CrossRef]
41. Kwak, J.; Bae, W.K.; Lee, D.; Park, I.; Lim, J.; Park, M.; Cho, H.; Woo, H.; Yoon, D.Y.; Char, K.; et al. Bright and efficient full-color colloidal quantum dot light-emitting diodes using an inverted device structure. *Nano Lett.* **2012**, *12*, 2362–2366. [CrossRef]
42. Shen, H.; Lin, Q.; Cao, W.; Yang, C.; Shewmon, N.T.; Wang, H.; Niu, J.; Li, L.S.; Xue, J. Efficient and long-lifetime full-color light-emitting diodes using high luminescence quantum yield thick-shell quantum dots. *Nanoscale* **2017**, *9*, 13583–13591. [CrossRef]
43. Wang, O.; Wang, L.; Li, Z.; Xu, Q.; Lin, Q.; Wang, H.; Du, Z.; Shen, H.; Li, L.S. High-efficiency, deep blue ZnCdS/$Cd_xZn_{1-x}S$/ZnS quantum-dot-light-emitting devices with an EQE exceeding 18%. *Nanoscale* **2018**, *10*, 5650–5657. [CrossRef]
44. Lin, Q.; Wang, L.; Li, Z.; Shen, H.; Guo, L.; Kuang, Y.; Wang, H.; Li, L.S. Nonblinking Quantum-Dot-Based Blue Light-Emitting Diodes with High Efficiency and a Balanced Charge-Injection Process. *ACS Photonics* **2018**, *5*, 939–946. [CrossRef]
45. Hines, M.A.; Guyot-Sionnest, P. Bright UV-Blue Luminescent Colloidal ZnSe Nanocrystals. *J. Phys. Chem. B* **1998**, *102*, 3654–3657. [CrossRef]
46. Yu, K.; Hrdina, A.; Zhang, X.; Ouyang, J.; Leek, D.M.; Wu, X.; Gong, M.; Wilkinson, D.; Li, C. Highly-photoluminescent ZnSe nanocrystals via a non-injection-based approach with precursor reactivity elevated by a secondary phosphine. *Chem. Commun.* **2011**, *47*, 8811–8813. [CrossRef]
47. Liu, Y.; Tang, Y.; Ning, Y.; Li, M.; Zhang, H.; Yang, B. "One-pot" synthesis and shape control of ZnSe semiconductor nanocrystals in liquid paraffin. *J. Mater. Chem.* **2010**, *20*, 4451–4458. [CrossRef]
48. Zheng, Y.; Yang, Z.; Ying, J.Y. Aqueous Synthesis of Glutathione-Capped ZnSe and $Zn_{1-x}Cd_xSe$ Alloyed Quantum Dots. *Adv. Mater.* **2007**, *19*, 1475–1479. [CrossRef]
49. Pradhan, N.; Battaglia, D.M.; Liu, Y.; Peng, X. Efficient, Stable, Small, and Water-Soluble Doped ZnSe Nanocrystal Emitters as Non-Cadmium Biomedical Labels. *Nano Lett.* **2007**, *7*, 312–317. [CrossRef]
50. Shen, H.; Wang, H.; Li, X.; Niu, J.Z.; Wang, H.; Chen, X.; Li, L.S. Phosphine-free synthesis of high quality ZnSe, ZnSe/ZnS, and Cu-, Mn-doped ZnSe nanocrystals. *Dalton Trans.* **2009**, 10534–10540. [CrossRef]
51. Dong, B.; Cao, L.; Su, G.; Liu, W. Facile synthesis of highly luminescent UV-blue emitting ZnSe/ZnS core/shell quantum dots by a two-step method. *Chem. Commun.* **2010**, *46*, 7331–7333. [CrossRef] [PubMed]
52. Lad, A.D.; Mahamuni, S. Effect of ZnS shell formation on the confined energy levels of ZnSe quantum dots. *Phys. Rev. B* **2008**, *78*, 125421. [CrossRef]
53. Jang, E.P.; Han, C.Y.; Lim, S.W.; Jo, J.H.; Jo, D.Y.; Lee, S.H.; Yoon, S.Y.; Yang, H. Synthesis of Alloyed ZnSeTe Quantum Dots as Bright, Color-Pure Blue Emitters. *ACS Appl. Mater. Interfaces* **2019**, *11*, 46062–46069. [CrossRef]
54. Lee, S.-H.; Song, S.-W.; Yoon, S.-Y.; Jo, D.-Y.; Kim, S.-K.; Kim, H.-M.; Kim, Y.; Park, S.M.; Yang, H. Heterostructural tailoring of blue ZnSeTe quantum dots toward high-color purity and high-efficiency electroluminescence. *Chem. Eng. J.* **2022**, *429*, 132464. [CrossRef]
55. Gao, M.; Tu, Y.; Tian, D.; Yang, H.; Fang, X.; Zhang, F.; Shen, H.; Du, Z. Alleviating Electron Over-Injection for Efficient Cadmium-Free Quantum Dot Light-Emitting Diodes toward Deep-Blue Emission. *ACS Photonics* **2022**, *9*, 1400–1408. [CrossRef]
56. Cho, H.; Park, S.; Shin, H.; Kim, M.; Jang, H.; Park, J.; Yang, J.H.; Han, C.W.; Baek, J.H.; Jung, Y.S.; et al. Highly Efficient Deep Blue Cd-Free Quantum Dot Light-Emitting Diodes by a p-Type Doped Emissive Layer. *Small* **2020**, *16*, 2002109. [CrossRef] [PubMed]
57. Xiang, C.; Koo, W.; Chen, S.; So, F.; Liu, X.; Kong, X.; Wang, Y. Solution processed multilayer cadmium-free blue/violet emitting quantum dots light emitting diodes. *Appl. Phys. Lett.* **2012**, *101*, 053303. [CrossRef]
58. Han, C.-Y.; Lee, S.-H.; Song, S.-W.; Yoon, S.-Y.; Jo, J.-H.; Jo, D.-Y.; Kim, H.-M.; Lee, B.-J.; Kim, H.-S.; Yang, H. More Than 9% Efficient ZnSeTe Quantum Dot-Based Blue Electroluminescent Devices. *ACS Energy Lett.* **2020**, *5*, 1568–1576. [CrossRef]
59. Hu, Y.; Zeng, H.; Du, J.; Hu, Z.; Zhang, S. The structural, electrical and optical properties of Mg-doped ZnO with different interstitial Mg concentration. *Mater. Chem. Phys.* **2016**, *182*, 15–21. [CrossRef]
60. Kim, H.M.; Geng, D.; Kim, J.; Hwang, E.; Jang, J. Metal-Oxide Stacked Electron Transport Layer for Highly Efficient Inverted Quantum-Dot Light Emitting Diodes. *ACS Appl. Mater. Interfaces* **2016**, *8*, 28727–28736. [CrossRef]
61. Cao, S.; Zheng, J.; Zhao, J.; Yang, Z.; Li, C.; Guan, X.; Yang, W.; Shang, M.; Wu, T. Enhancing the Performance of Quantum Dot Light-Emitting Diodes Using Room-Temperature-Processed Ga-Doped ZnO Nanoparticles as the Electron Transport Layer. *ACS Appl. Mater. Interfaces* **2017**, *9*, 15605–15614. [CrossRef]

62. Wang, S.; Guo, Y.; Feng, D.; Chen, L.; Fang, Y.; Shen, H.; Du, Z. Bandgap tunable $Zn_{1-x}Mg_xO$ thin films as electron transport layers for high performance quantum dot light-emitting diodes. *J. Mater. Chem. C* **2017**, *5*, 4724–4730. [CrossRef]
63. Zhang, L.; Zhu, X.; Wang, Z.; Yun, S.; Guo, T.; Zhang, J.; Hu, T.; Jiang, J.; Chen, J. Synthesis of ZnO doped high valence S element and study of photogenerated charges properties. *RSC Adv.* **2019**, *9*, 4422–4427. [CrossRef] [PubMed]
64. Jiang, W.; Chae, H. Efficiency Enhancement of Tris(dimethylamino)-phosphine-Based Red Indium Phosphide Quantum-Dot Light-Emitting Diodes via Chlorine-Doped ZnMgO Electron Transport Layers. *J. Phys. Chem. C* **2020**, *124*, 25221–25228. [CrossRef]
65. Gao, M.; Yang, H.; Shen, H.; Zeng, Z.; Fan, F.; Tang, B.; Min, J.; Zhang, Y.; Hua, Q.; Li, L.S.; et al. Bulk-like ZnSe Quantum Dots Enabling Efficient Ultranarrow Blue Light-Emitting Diodes. *Nano Lett.* **2021**, *21*, 7252–7260. [CrossRef]
66. Yang, Z.; Wu, Q.; Zhou, X.; Cao, F.; Yang, X.; Zhang, J.; Li, W. A seed-mediated and double shell strategy to realize large-size ZnSe/ZnS/ZnS quantum dots for high color purity blue light-emitting diodes. *Nanoscale* **2021**, *13*, 4562–4568. [CrossRef]
67. Wang, A.; Shen, H.; Zang, S.; Lin, Q.; Wang, H.; Qian, L.; Niu, J.; Song Li, L. Bright, efficient, and color-stable violet ZnSe-based quantum dot light-emitting diodes. *Nanoscale* **2015**, *7*, 2951–2959. [CrossRef]
68. Ji, W.; Jing, P.; Xu, W.; Yuan, X.; Wang, Y.; Zhao, J.; Jen, A.K.Y. High color purity ZnSe/ZnS core/shell quantum dot based blue light emitting diodes with an inverted device structure. *Appl. Phys. Lett.* **2013**, *103*, 053106. [CrossRef]
69. Trentler, T.J.; Hickman, K.M.; Goel, S.C.; Viano, A.M.; Gibbons, P.C.; Buhro, W.E. Solution-Liquid-Solid Growth of Crystalline III-V Semiconductors: An Analogy to Vapor-Liquid-Solid Growth. *Science* **1995**, *270*, 1791–1794. [CrossRef]
70. Mikik, I.; Sprague, J.R.; Curtis, C.J.; Jones, K.M.; Machol, J.L.; Nozik, A.J. Synthesis and Characterization of InP, Gap, and $GaInP_2$ Quantum Dots. *J. Phys. Chem.* **1995**, *99*, 7754–7759.
71. Guzelian, A.A.; Katari, J.E.B.; Kadavanich, A.V.; Banin, U.; Hamad, K.; Juban, E.; Alivisatos, A.P. Synthesis of Size-Selected, Surface-Passivated InP Nanocrystals. *J. Phys. Chem.* **1996**, *100*, 7212–7219. [CrossRef]
72. Peng, Z.A.; Peng, X. Nearly Monodisperse and Shape-Controlled CdSeNanocrystals via Alternative Routes Nucleation and Growth. *J. Am. Chem. Soc.* **2002**, *124*, 3343–3353. [CrossRef] [PubMed]
73. Battaglia, D.; Peng, X. Formation of High Quality InP and InAs Nanocrystals in a Noncoordinating Solvent. *Nano Lett.* **2002**, *2*, 1027–1030. [CrossRef]
74. Lucey, D.W.; MacRae, D.J.; Furis, M.; Sahoo, Y.; Cartwright, A.N.; Prasad, P.N. Monodispersed InP Quantum Dots Prepared by Colloidal Chemistry in a Noncoordinating Solvent. *Chem. Mater.* **2005**, *17*, 3754–3762. [CrossRef]
75. Xu, S.; Kumar, S.; Nann, T. Rapid Synthesis of High-Quality InP Nanocrystals. *J. Am. Chem. Soc.* **2006**, *128*, 1054–1055. [CrossRef]
76. Yang, X.; Zhao, D.; Leck, K.S.; Tan, S.T.; Tang, Y.X.; Zhao, J.; Demir, H.V.; Sun, X.W. Full visible range covering InP/ZnS nanocrystals with high photometric performance and their application to white quantum dot light-emitting diodes. *Adv. Mater.* **2012**, *24*, 4180–4185. [CrossRef]
77. Shen, W.; Tang, H.; Yang, X.; Cao, Z.; Cheng, T.; Wang, X.; Tan, Z.; You, J.; Deng, Z. Synthesis of highly fluorescent InP/ZnS small-core/thick-shell tetrahedral-shaped quantum dots for blue light-emitting diodes. *J. Mater. Chem. C* **2017**, *5*, 8243–8249. [CrossRef]
78. Tessier, M.D.; Dupont, D.; De Nolf, K.; De Roo, J.; Hens, Z. Economic and Size-Tunable Synthesis of InP/ZnE (E = S, Se) Colloidal Quantum Dots. *Chem. Mater.* **2015**, *27*, 4893–4898. [CrossRef]
79. Yu, P.; Shan, Y.; Cao, S.; Hu, Y.; Li, Q.; Zeng, R.; Zou, B.; Wang, Y.; Zhao, J. Inorganic Solid Phosphorus Precursor of Sodium Phosphaethynolate for Synthesis of Highly Luminescent InP-Based Quantum Dots. *ACS Energy Lett.* **2021**, *6*, 2697–2703. [CrossRef]
80. Zhang, H.; Ma, X.; Lin, Q.; Zeng, Z.; Wang, H.; Li, L.S.; Shen, H.; Jia, Y.; Du, Z. High-Brightness Blue InP Quantum Dot-Based Electroluminescent Devices: The Role of Shell Thickness. *J. Phys. Chem. C* **2020**, *11*, 960–967. [CrossRef]
81. Kim, K.-H.; Jo, J.-H.; Jo, D.-Y.; Han, C.-Y.; Yoon, S.-Y.; Kim, Y.; Kim, Y.-H.; Ko, Y.H.; Kim, S.W.; Lee, C.; et al. Cation-Exchange-Derived InGaP Alloy Quantum Dots toward Blue Emissivity. *Chem. Mater.* **2020**, *32*, 3537–3544. [CrossRef]
82. Zhang, H.; Hu, N.; Zeng, Z.; Lin, Q.; Zhang, F.; Tang, A.; Jia, Y.; Li, L.S.; Shen, H.; Teng, F.; et al. High-Efficiency Green InP Quantum Dot-Based Electroluminescent Device Comprising Thick-Shell Quantum Dots. *Adv. Opt. Mater.* **2019**, *7*, 1801602. [CrossRef]
83. Sun, Z.; Wu, Q.; Wang, S.; Cao, F.; Wang, Y.; Li, L.; Wang, H.; Kong, L.; Yan, L.; Yang, X. Suppressing the Cation Exchange at the Core/Shell Interface of InP Quantum Dots by a Selenium Shielding Layer Enables Efficient Green Light-Emitting Diodes. *ACS Appl. Mater. Interfaces* **2022**, *14*, 15401–15406. [CrossRef] [PubMed]
84. Li, Y.; Hou, X.; Dai, X.; Yao, Z.; Lv, L.; Jin, Y.; Peng, X. Stoichiometry-Controlled InP-Based Quantum Dots: Synthesis, Photoluminescence, and Electroluminescence. *J. Am. Chem. Soc.* **2019**, *141*, 6448–6452. [CrossRef]
85. Won, Y.H.; Cho, O.; Kim, T.; Chung, D.Y.; Kim, T.; Chung, H.; Jang, H.; Lee, J.; Kim, D.; Jang, E. Highly efficient and stable InP/ZnSe/ZnS quantum dot light-emitting diodes. *Nature* **2019**, *575*, 634–638. [CrossRef]
86. Zhang, W.; Ding, S.; Zhuang, W.; Wu, D.; Liu, P.; Qu, X.; Liu, H.; Yang, H.; Wu, Z.; Wang, K.; et al. InP/ZnS/ZnS Core/Shell Blue Quantum Dots for Efficient Light-Emitting Diodes. *Adv. Funct. Mater.* **2020**, *30*, 2005303. [CrossRef]
87. Tan, Y.; Zhang, W.; Xiao, X.; Sun, J.; Ma, J.; Zhang, T.; Mei, G.; Wang, Z.; Zhao, F.; Wu, D.; et al. Enhancing hole injection by electric dipoles for efficient blue InP QLEDs. *Appl. Phys. Lett.* **2021**, *119*, 221105. [CrossRef]
88. Srivastava, V.; Kamysbayev, V.; Hong, L.; Dunietz, E.; Klie, R.F.; Talapin, D.V. Colloidal Chemistry in Molten Salts: Synthesis of Luminescent $In_{1\text{-}x}Ga_xP$ and $In_{1\text{-}x}Ga_xAs$ Quantum Dots. *J. Am. Chem. Soc.* **2018**, *140*, 12144–12151. [CrossRef]

89. Wegner, K.D.; Pouget, S.; Ling, W.L.; Carriere, M.; Reiss, P. Gallium—A versatile element for tuning the photoluminescence properties of InP quantum dots. *Chem. Commun.* **2019**, *55*, 1663–1666. [CrossRef]
90. Xu, X.; Ray, R.; Gu, Y.; Ploehn, H.J.; Gearheart, L.; Raker, K.; Scrivens, W.A. Electrophoretic Analysis and Purification of Fluorescent Single-WalledCarbon Nanotube Fragments. *J. Am. Chem. Soc.* **2004**, *126*, 12736–12737. [CrossRef]
91. Chien, C.T.; Li, S.S.; Lai, W.J.; Yeh, Y.C.; Chen, H.A.; Chen, I.S.; Chen, L.C.; Chen, K.H.; Nemoto, T.; Isoda, S.; et al. Tunable photoluminescence from graphene oxide. *Angew. Chem. Int. Ed. Engl.* **2012**, *51*, 6662–6666. [CrossRef] [PubMed]
92. Jiang, K.; Sun, S.; Zhang, L.; Lu, Y.; Wu, A.; Cai, C.; Lin, H. Red, green, and blue luminescence by carbon dots: Full-color emission tuning and multicolor cellular imaging. *Angew. Chem. Int. Ed. Engl.* **2015**, *54*, 5360–5363. [CrossRef] [PubMed]
93. Lim, S.Y.; Shen, W.; Gao, Z. Carbon quantum dots and their applications. *Chem. Soc. Rev.* **2015**, *44*, 362–381. [CrossRef] [PubMed]
94. Xin, Q.; Shah, H.; Nawaz, A.; Xie, W.; Akram, M.Z.; Batool, A.; Tian, L.; Jan, S.U.; Boddula, R.; Guo, B.; et al. Antibacterial Carbon-Based Nanomaterials. *Adv. Mater.* **2019**, *31*, 1804838. [CrossRef] [PubMed]
95. Hutton, G.A.M.; Martindale, B.C.M.; Reisner, E. Carbon dots as photosensitisers for solar-driven catalysis. *Chem. Soc. Rev.* **2017**, *46*, 6111–6123. [CrossRef] [PubMed]
96. Ding, H.; Zhou, X.-X.; Wei, J.-S.; Li, X.-B.; Qin, B.-T.; Chen, X.-B.; Xiong, H.-M. Carbon dots with red/near-infrared emissions and their intrinsic merits for biomedical applications. *Carbon* **2020**, *167*, 322–344. [CrossRef]
97. Sun, Y.-P.; Zhou, B.; Lin, Y.; Wang, W.; Fernando, K.A.S.; Pathak, P.; Meziani, M.J.; Harruff, B.A.; Wang, X.; Wang, H.; et al. Quantum-Sized Carbon Dots for Bright and Colorful Photoluminescence. *J. Am. Chem. Soc.* **2006**, *128*, 7756–7757. [CrossRef]
98. Eda, G.; Lin, Y.Y.; Mattevi, C.; Yamaguchi, H.; Chen, H.A.; Chen, I.S.; Chen, C.W.; Chhowalla, M. Blue photoluminescence from chemically derived graphene oxide. *Adv. Mater.* **2010**, *22*, 505–509. [CrossRef]
99. Liu, F.; Jang, M.H.; Ha, H.D.; Kim, J.H.; Cho, Y.H.; Seo, T.S. Facile synthetic method for pristine graphene quantum dots and graphene oxide quantum dots: Origin of blue and green luminescence. *Adv. Mater.* **2013**, *25*, 3657–3662. [CrossRef]
100. Kwon, W.; Kim, Y.H.; Lee, C.L.; Lee, M.; Choi, H.C.; Lee, T.W.; Rhee, S.W. Electroluminescence from graphene quantum dots prepared by amidative cutting of tattered graphite. *Nano Lett.* **2014**, *14*, 1306–1311. [CrossRef]
101. Zhu, S.; Song, Y.; Shao, J.; Zhao, X.; Yang, B. Non-Conjugated Polymer Dots with Crosslink-Enhanced Emission in the Absence of Fluorophore Units. *Angew. Chem. Int. Ed. Engl.* **2015**, *54*, 14626–14637. [CrossRef] [PubMed]
102. Yan, X.; Cui, X.; Li, L.-S. Synthesis of Large, Stable Colloidal Graphene Quantum Dots with Tunable Size. *J. Am. Chem. Soc.* **2010**, *132*, 5944–5945. [CrossRef] [PubMed]
103. Wei, S.; Yin, X.; Li, H.; Du, X.; Zhang, L.; Yang, Q.; Yang, R. Multi-Color Fluorescent Carbon Dots: Graphitized sp(2) Conjugated Domains and Surface State Energy Level Co-Modulate Band Gap Rather Than Size Effects. *Chem. Eur. J.* **2020**, *26*, 8129–8136. [CrossRef]
104. Wu, Z.L.; Liu, Z.X.; Yuan, Y.H. Carbon dots: Materials, synthesis, properties and approaches to long-wavelength and multicolor emission. *J. Mater. Chem. B* **2017**, *5*, 3794–3809. [CrossRef] [PubMed]
105. Zhao, B.; Ma, H.; Zheng, M.; Xu, K.; Zou, C.; Qu, S.; Tan, Z.a. Narrow-bandwidth emissive carbon dots: A rising star in the fluorescent material family. *Carbon Energy* **2022**, *4*, 88–114. [CrossRef]
106. Ren, J.; Malfatti, L.; Innocenzi, P. Citric Acid Derived Carbon Dots, the Challenge of Understanding the Synthesis-Structure Relationship. *C* **2021**, *7*, 2. [CrossRef]
107. Ren, J.; Stagi, L.; Innocenzi, P. Fluorescent carbon dots in solid-state: From nanostructures to functional devices. *Prog. Solid State Chem.* **2021**, *62*, 100295. [CrossRef]
108. Ding, H.; Yu, S.B.; Wei, J.S.; Xiong, H.M. Full-Color Light-Emitting Carbon Dots with a Surface-State-Controlled Luminescence Mechanism. *ACS Nano* **2016**, *10*, 484–491. [CrossRef]
109. Cao, L.; Zan, M.; Chen, F.; Kou, X.; Liu, Y.; Wang, P.; Mei, Q.; Hou, Z.; Dong, W.-F.; Li, L. Formation mechanism of carbon dots: From chemical structures to fluorescent behaviors. *Carbon* **2022**, *194*, 42–51. [CrossRef]
110. Zhu, S.; Wang, L.; Zhou, N.; Zhao, X.; Song, Y.; Maharjan, S.; Zhang, J.; Lu, L.; Wang, H.; Yang, B. The crosslink enhanced emission (CEE) in non-conjugated polymer dots: From the photoluminescence mechanism to the cellular uptake mechanism and internalization. *Chem. Commun.* **2014**, *50*, 13845–13848. [CrossRef]
111. Yuan, F.; Wang, Z.; Li, X.; Li, Y.; Tan, Z.; Fan, L.; Yang, S. Bright Multicolor Bandgap Fluorescent Carbon Quantum Dots for Electroluminescent Light-Emitting Diodes. *Adv. Mater.* **2017**, *29*, 1604436. [CrossRef] [PubMed]
112. Wang, X.; Wang, B.; Wang, H.; Zhang, T.; Qi, H.; Wu, Z.; Ma, Y.; Huang, H.; Shao, M.; Liu, Y.; et al. Carbon-Dot-Based White-Light-Emitting Diodes with Adjustable Correlated Color Temperature Guided by Machine Learning. *Angew. Chem. Int. Ed. Engl.* **2021**, *60*, 12585–12590. [CrossRef] [PubMed]
113. Yuan, F.; Yuan, T.; Sui, L.; Wang, Z.; Xi, Z.; Li, Y.; Li, X.; Fan, L.; Tan, Z.; Chen, A.; et al. Engineering triangular carbon quantum dots with unprecedented narrow bandwidth emission for multicolored LEDs. *Nat. Commun.* **2018**, *9*, 2249. [CrossRef] [PubMed]
114. Wang, X.; Ma, Y.; Wu, Q.; Wang, Z.; Tao, Y.; Zhao, Y.; Wang, B.; Cao, J.; Wang, H.; Gu, X.; et al. Ultra-Bright and Stable Pure Blue Light-Emitting Diode from O, N Co-Doped Carbon Dots. *Laser Photonics Rev.* **2021**, *15*, 2000412. [CrossRef]
115. Xu, J.; Miao, Y.; Zheng, J.; Wang, H.; Yang, Y.; Liu, X. Carbon dot-based white and yellow electroluminescent light emitting diodes with a record-breaking brightness. *Nanoscale* **2018**, *10*, 11211–11221. [CrossRef]
116. Lee, S.H.; Kim, D.Y.; Lee, J.; Lee, S.B.; Han, H.; Kim, Y.Y.; Mun, S.C.; Im, S.H.; Kim, T.H.; Park, O.O. Synthesis of Single-Crystalline Hexagonal Graphene Quantum Dots from Solution Chemistry. *Nano Lett.* **2019**, *19*, 5437–5442. [CrossRef]

117. Zhang, X.; Zhang, Y.; Wang, Y.; Kalytchuk, S.; Kershaw, S.V.; Wang, Y.; Wang, P.; Zhang, T.; Zhao, Y.; Zhang, H.; et al. Color-Switchable Electroluminescence of Carbon Dot Light-Emitting Diodes. *ACS Nano* **2013**, *7*, 11234–11241. [CrossRef]
118. Kim, D.H.; Kim, T.W. Ultrahigh current efficiency of light-emitting devices based on octadecylamine-graphene quantum dots. *Nano Energy* **2017**, *32*, 441–447. [CrossRef]
119. Wang, F.; Chen, Y.H.; Liu, C.Y.; Ma, D.G. White light-emitting devices based on carbon dots' electroluminescence. *Chem. Commun.* **2011**, *47*, 3502–3504. [CrossRef]
120. Yuan, F.; Wang, Y.-K.; Sharma, G.; Dong, Y.; Zheng, X.; Li, P.; Johnston, A.; Bappi, G.; Fan, J.Z.; Kung, H.; et al. Bright high-colour-purity deep-blue carbon dot light-emitting diodes via efficient edge amination. *Nat. Photonics* **2019**, *14*, 171–176. [CrossRef]
121. Ding, Y.; Zhang, F.; Xu, J.; Miao, Y.; Yang, Y.; Liu, X.; Xu, B. Synthesis of short-chain passivated carbon quantum dots as the light emitting layer towards electroluminescence. *RSC Adv.* **2017**, *7*, 28754–28762. [CrossRef]
122. Huang, H.; Susha, A.S.; Kershaw, S.V.; Hung, T.F.; Rogach, A.L. Control of Emission Color of High Quantum Yield $CH_3NH_3PbBr_3$ Perovskite Quantum Dots by Precipitation Temperature. *Adv. Sci.* **2015**, *2*, 1500194. [CrossRef] [PubMed]
123. Protesescu, L.; Yakunin, S.; Bodnarchuk, M.I.; Krieg, F.; Caputo, R.; Hendon, C.H.; Yang, R.X.; Walsh, A.; Kovalenko, M.V. Nanocrystals of Cesium Lead Halide Perovskites ($CsPbX_3$, X = Cl, Br, and I): Novel Optoelectronic Materials Showing Bright Emission with Wide Color Gamut. *Nano Lett.* **2015**, *15*, 3692–3696. [CrossRef] [PubMed]
124. Shynkarenko, Y.; Bodnarchuk, M.I.; Bernasconi, C.; Berezovska, Y.; Verteletskyi, V.; Ochsenbein, S.T.; Kovalenko, M.V. Direct Synthesis of Quaternary Alkylammonium-Capped Perovskite Nanocrystals for Efficient Blue and Green Light-Emitting Diodes. *ACS Energy Lett.* **2019**, *4*, 2703–2711. [CrossRef]
125. Yan, C.; Luo, C.; Li, W.; Peng, X.; Cao, J.; Zeng, X.; Gao, Y.; Fu, X.; Chu, X.; Deng, W.; et al. Thermodynamics-Induced Injection Enhanced Deep-Blue Perovskite Quantum Dot LEDs. *ACS Appl. Mater. Interfaces* **2021**, *13*, 57560–57566. [CrossRef]
126. Brown, A.A.M.; Vashishtha, P.; Hooper, T.J.N.; Ng, Y.F.; Nutan, G.V.; Fang, Y.; Giovanni, D.; Tey, J.N.; Jiang, L.; Damodaran, B.; et al. Precise Control of $CsPbBr_3$ Perovskite Nanocrystal Growth at Room Temperature: Size Tunability and Synthetic Insights. *Chem. Mater.* **2021**, *33*, 2387–2397. [CrossRef]
127. Dutta, A.; Dutta, S.K.; Das Adhikari, S.; Pradhan, N. Tuning the Size of $CsPbBr_3$ Nanocrystals: All at One Constant Temperature. *ACS Energy Lett.* **2018**, *3*, 329–334. [CrossRef]
128. Kong, X.; Wu, Y.; Xu, F.; Yang, S.; Cao, B. Ultrasmall $CsPbBr_3$ Quantum Dots with Bright and Wide Blue Emissions. *Phys. Status Solidi RRL* **2021**, *15*, 2100134. [CrossRef]
129. Zhang, X.; Wang, H.; Hu, Y.; Pei, Y.; Wang, S.; Shi, Z.; Colvin, V.L.; Wang, S.; Zhang, Y.; Yu, W.W. Strong Blue Emission from Sb^{3+}-Doped Super Small $CsPbBr_3$ Nanocrystals. *J. Phys. Chem. Lett.* **2019**, *10*, 1750–1756. [CrossRef]
130. Yang, H.; Feng, Y.; Tu, Z.; Su, K.; Fan, X.; Liu, B.; Shi, Z.; Zhang, Y.; Zhao, C.; Zhang, B. Blue emitting $CsPbBr_3$ perovskite quantum dot inks obtained from sustained release tablets. *Nano Res.* **2019**, *12*, 3129–3134. [CrossRef]
131. Song, J.; Li, J.; Li, X.; Xu, L.; Dong, Y.; Zeng, H. Quantum Dot Light-Emitting Diodes Based on Inorganic Perovskite Cesium Lead Halides ($CsPbX_3$). *Adv. Mater.* **2015**, *27*, 7162–7167. [CrossRef] [PubMed]
132. Xun, J.; Deng, J.; Shen, W.; Li, M.; He, R. Rapid synthesis of highly stable all-inorganic perovskite nanocrystals exhibiting strong blue luminescence. *J. Alloys Compd.* **2021**, *872*, 159612. [CrossRef]
133. Zheng, X.; Yuan, S.; Liu, J.; Yin, J.; Yuan, F.; Shen, W.-S.; Yao, K.; Wei, M.; Zhou, C.; Song, K.; et al. Chlorine Vacancy Passivation in Mixed Halide Perovskite Quantum Dots by Organic Pseudohalides Enables Efficient Rec. 2020 Blue Light-Emitting Diodes. *ACS Energy Lett.* **2020**, *5*, 793–798. [CrossRef]
134. Shin, Y.S.; Yoon, Y.J.; Lee, K.T.; Jeong, J.; Park, S.Y.; Kim, G.H.; Kim, J.Y. Vivid and Fully Saturated Blue Light-Emitting Diodes Based on Ligand-Modified Halide Perovskite Nanocrystals. *ACS Appl. Mater. Interfaces* **2019**, *11*, 23401–23409. [CrossRef] [PubMed]

MDPI AG
Grosspeteranlage 5
4052 Basel
Switzerland
Tel.: +41 61 683 77 34

Nanomaterials Editorial Office
E-mail: nanomaterials@mdpi.com
www.mdpi.com/journal/nanomaterials

Academic Open
Access Publishing

mdpi.com

ISBN 978-3-7258-4458-6